Decovalex-2011: Quintessa and University of Edinburgh Contribution to Task A

Decovalex-2011: Quintessa and University of Edinburgh Contribution to Task A

A technical report to NDA RWMD

Alex Bond

Steven Benbow

James Wilson

Chris McDermott

Myles English

QRS-1378J-R9

V1.0

29/2/2012

Quintessa

Document History

Title:	Decovalex-2011: Quintessa and University of Edinburgh Contribution to Task A
Subtitle:	A technical report to NDA RWMD
Client:	NDA RWMD
Document Number:	QRS-1378J-R9
Version Number:	V1.0 **Date:** 29/2/2012
Notes:	For Issue
Prepared by:	Alex Bond, Steven Benbow, James Wilson, Chris McDermott, Myles English
Reviewed by:	Peter Robinson
Approved by:	Alex Bond

Quintessa Limited
The Hub, 14 Station Road
Henley-on-Thames
Oxfordshire RG9 1AY
United Kingdom

Tel: +44 (0) 1491 636246
Fax: +44 (0) 1491 636247
info@quintessa.org
www.quintessa.org
www.quintessa-online.com

Executive Summary

The DECOVALEX-2011 project is the fifth round of an international co-operative research programme for geological radioactive waste disposal, specifically considering the DEvelopment of COupled models and their VALidation against EXperiments. The overall objective of DECOVALEX is the development of scientific methodologies for evaluation of Thermal-Hydraulic-Mechanical and Chemical (THMC) processes in numerical models and to demonstrate how these can be applied to detailed and performance assessment calculations.

Quintessa, in conjunction with the University of Edinburgh (UoE), has contributed to Task A of DECOVALEX-2011 on behalf of the UK Nuclear Decommissioning Authority, Radioactive Waste Management Directorate (NDA RWMD). This task was concerned with the evaluation of numerical modelling capabilities for simulating coupled THMC processes in argillaceous rocks. More specifically, work was focussed on attempting to model and better understand the complex results of the Mont Terri Rock Laboratory Ventilation Experiment, which was constructed in the Opalinus Clay close to the Swiss-French border. Under NDA RWMD's classification of geological environments potentially suitable for radioactive waste disposal, the Opalinus Clay falls under the general category of 'low-strength sedimentary'. As such, the work presented here is of direct relevance to the ongoing NDA RWMD research programme.

During this project the following key elements have been achieved.

- The combination of expert consultancy and a University enabled both the successful completion of the modelling tasks and the training of a PhD student for future radioactive waste management expertise.
- Two different numerical methods and international codes were applied and their application developed (Finite Element: OpenGeoSys and Finite Volume / Mixed Element: QPAC). Experimental results on different spatial scales were used as benchmarks for code comparison and validation of process models and codes.

Within the remit of Task A the following was accomplished:

- Multi-phase flow modelling of laboratory experiments with successful reproduction of experimental observations.
- Multi-phase flow modelling and fully coupled mechanical deformation of a large scale field experiment, including successful blind prediction of experimental responses.

- Excellent reproduction of observations of the non-reactive geochemical evolution associated with the field experiment through tracer transport modelling based on the variably saturated hydro-mechanical response.
- Good reproduction of the observed reactive geochemical evolution associated with the field experiment through reactive transport modelling based on the coupled hydro-mechanical response.

While some uncertainties remain, the work has illustrated that it is possible to construct predictive models of ventilation for hydro-mechanical-chemical processes in the Opalinus Clay, and arguably argillaceous materials in general, under ventilation conditions.

Contents

1 Introduction

1.1 The DECOVALEX-2011 Project

The DECOVALEX-2011 project (acronym for DEvelopment of COupled models and their VALidation against EXperiments) is an international research project designed to:

- support development of computer simulators;
- investigate and implement suitable algorithms for THM and THMC modelling;
- compare model calculations with results from field and laboratory experiments;
- design new experiments to support code development; and
- apply THM (and THMC) modelling to performance and safety assessment of nuclear waste facilities.

The technical project work is composed of three tasks (A-C):

- Task A: Investigation and application of experimental results from the Mont Terri Rock Laboratory for the Ventilation Experiment.
- Task B: Pillar stability and fracturing near excavation rock surfaces with specific reference to field investigations conducted by SKB in a granitic rock.
- Task C: Modelling of fluid flow and rock stress evolution (together with contaminant transport) in fractured rock masses with reference to the Bergetov Tunnel, Czech Republic.

Quintessa, in conjunction with the University of Edinburgh (UoE), have contributed to the project through Task A. This contribution was funded by the UK Nuclear Decommissioning Authority (Radioactive Waste Management Directorate – NDA RWMD). The work discussed in this report was predominantly conducted in the period April 2008 to November 2011.

1.2 Task A Objectives

Argillaceous host rocks for geological disposal of nuclear waste are being considered as a viable option for safe long term storage and final disposal. In order to assess the safety implications, it is important to have a substantive understanding of the major processes operating in argillaceous rocks and the implications of the coupling of these processes. Construction of such waste facilities will lead to drying, heating, re-saturating and the potential for chemical alteration of the host rocks.

The main objective of Task A of DECOVALEX-2011 was to examine the hydro-mechanical and chemical changes that occur in argillaceous host rocks, especially in

relation to the ventilation of drifts constructed for the waste storage. The Mont Terri Rock Laboratory is constructed in a stiff argillaceous deposit, the Opalinus Clay, close to the Swiss-French border. The significance of the study lies in the fact that all drifts and tunnels in the repository will be subjected to ventilation effects to some extent during the operational phase of the facility. Argillaceous rocks with their high water content, dependency on electrostatic forces for their strength and the presence of a large surface area for the sorption of both cations and anions are expected to be especially sensitive to ventilation effects. Understanding these effects can be regarded as fundamental scientific underpinning to support the assessment of the medium and long term integrity of these facilities.

Under NDA RWMD's classification of geological environments potentially suitable for radioactive waste disposal, the Opalinus Clay falls under the general category of 'low-strength sedimentary' (NDA, 2010). As such, the work presented here is of direct relevance to the ongoing NDA RWMD research programme.

1.3 Codes

Quintessa used QPAC (Quintessa, 2010) to address the Task. QPAC is a highly flexible multi-physics code using a Control Volume or Mixed Element formulation developed and wholly owned by Quintessa Ltd (www.quintessa.org/qpac). The code uses a 'model-as-input' paradigm, where all aspects of existing quality assured process models (e.g. multi-phase flow, thermal heat transfer) can be modified by the user, and new process models can be quickly created, without changing the QPAC code. Application to date has been extremely broad, addressing complex coupled thermal, hydraulic, mechanical and chemical problems in radioactive waste, hydrogeology and CO_2 storage and impacts.

UoE used RockFlow-GeoSys (currently referred to as OpenGeoSys or OGS). OpenGeoSys is a scientific open source project developed and maintained primarily by UFZ Leipzig (www.opengeosys.net) designed to for the development of numerical methods for the simulation of thermo-hydro-mechanical-chemical (THMC) processes in porous and fractured media. Application areas of OGS are currently CO_2 sequestration, geothermal energy, water resources management, hydrology, and waste deposition. A summary of the mathematical formulation for OGS and process models used in this project are given in Appendix C.

1.4 Report Structure

The report is structured largely to follow the evolution of the task;

- Section 2 discusses the Ventilation Experiment itself and the Task A structure

- Section 3 discusses 'Step 0' – the initial benchmarking exercise and limited validation exercise
- Section 4 discusses 'Step 1' – the initial hydro-mechanical modelling of the Ventilation Experiment
- Section 5 discusses 'Step 2' – the 'advanced' hydro-mechanical modelling of the Ventilation Experiment including the predictive analysis.
- Section 6 discusses 'Step 3' – the non-reactive transport modelling using Step 2 as a basis
- Section 7 discusses 'Step 4' – the reactive transport modelling using Step 2 and 3 as a basis
- Section 8 summarises the conclusions of the modelling.

This report presents a synthesis of the internal reports produced at each stage of the project and intends to show the evolution of the modelling activities and approaches through the project duration.

2 Task A: Mont Terri Ventilation Experiment

2.1 Short Description

The Mont Terri Underground Research Laboratory (URL) is located near a security gallery of a motorway tunnel in northern Switzerland (Bossart and Nussbaum, 2007). It is at a depth of about 400 meters in Opalinus clay, which is a stiff layered Mesozoic clay of marine origin. After the excavation of niches in 1996, a new gallery was excavated in 1998, followed by a micro-tunnel of 1.3m in diameter in early 1999. The ventilation experiment took place in a 10 m long section of this micro-tunnel as represented on Figure 2-1.

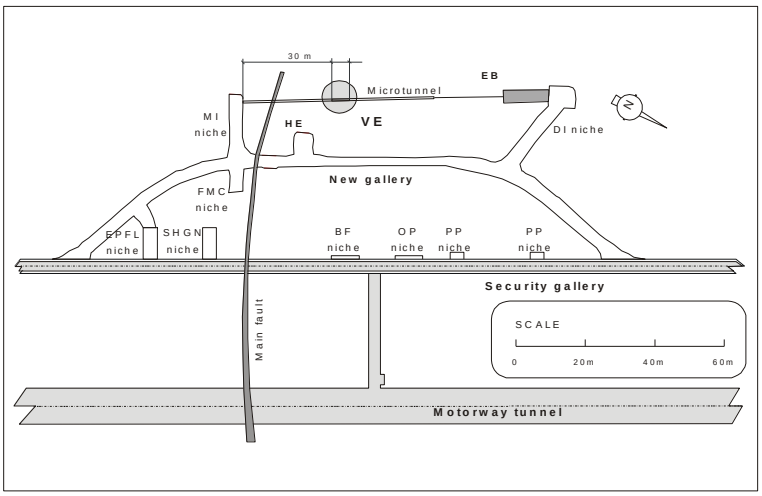

Figure 2-1. Location of the micro-tunnel in Mont Terri

After its excavation, the micro-tunnel was left without control of the ambient relative humidity for approximately 4 years. After this period doors were installed in order to create a section of 10 m length, where the air inflow and the relative humidity could be controlled and monitored (Figure 2-1). The micro-tunnel was then subjected to two wetting-drying cycles. The first cycle lasted from the 8th of July 2002 to the 29th of January 2004 (Phase 1). First 100% relative humidity inflowing air wetted the micro-tunnel and then during a desaturation period, 2% relative humidity air flowed into the tunnel. This first cycle was then followed by a second cycle, and a final resaturation which continued until 2010 (Phase 2), although data is only available until April 2007. The corresponding total sequence of prescribed relative humidity is illustrated on Figure 2-3 (curve RH-in, in red).

The micro-tunnel has been intensively instrumented with relative humidity sensors, pore pressure sensors and displacements sensors. Moreover, two water pans have been installed in order to record the evolution of their mass loss due to the ventilation. Their locations are indicated on Figure 2-2. The variation of the relative humidity with time, at different points along the micro-tunnel, is shown in Figure 2-3.

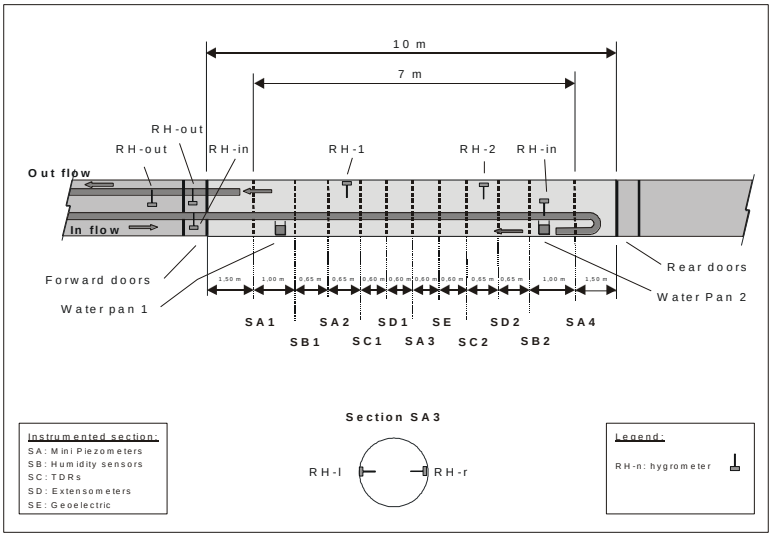

Figure 2-2. Controlled ventilation section in the micro-tunnel, and relative humidity measurement locations.

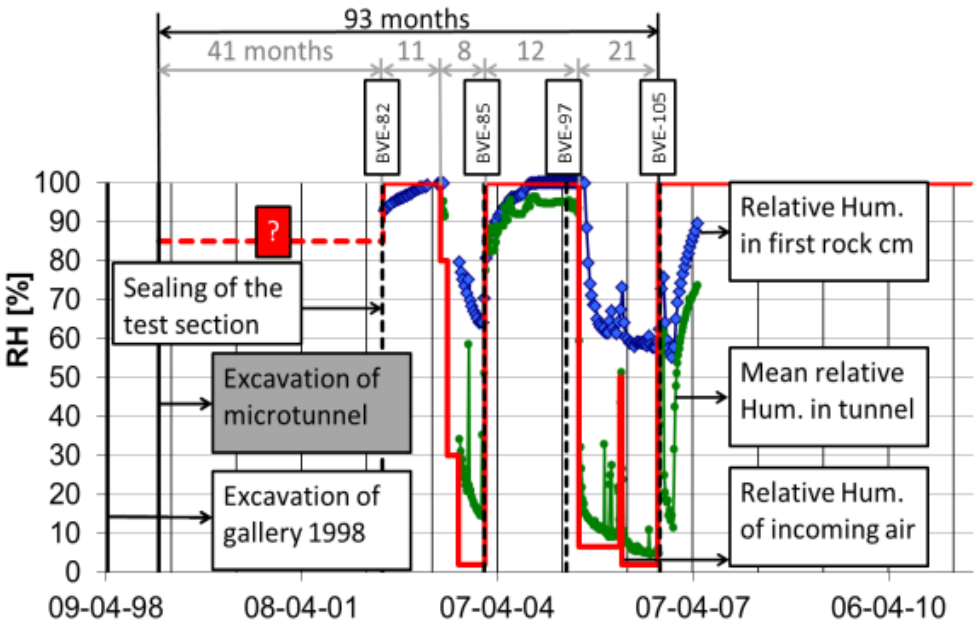

Figure 2-3. Relative humidity history of the test section (from Garitte *et al.* 2012).

2.2 Task Structure

A discussion of the main Mont Terri Ventilation Experiment (VE) can be found in Garitte and Gens (2008) and more a detailed overview of the data is given in Appendix A. Quintessa and UoE were two of several teams working under Task A, which included significant contributions from Commissariat à l'Energie Atomique (CEA), Japanese Atomic Energy Agency (JAEA) and the Chinese Academey of Sciences (CAS), however most of the work and results of the other teams will not be discussed in this report. The task itself was run by technical staff from Universidad Politécnica de Catalunya (UPC) and at the time of writing a number of academic papers are in preparation as part of the task output (Bond *et al.* 2012a,b; Garritte *et al.* 2012; Millard *et al.* 2012; and Zhang *et al.* 2012).

Task A considers five different 'steps' in the project, each looking at different aspects of the (VE), loosely covering the three different time phases of the ten year project:

- Step 0: Modelling of a laboratory drying test relevant to the VE.
- Step 1: Simple hydro-mechanical modelling from the start of Phase 0 to the end of Phase 1 of the VE using Step 0 parameterisation initially, followed by additional calibration and preparation for Step 2.
- Step 2: Advanced hydro-mechanical modelling up to the end of Phase 2. This step the modelling teams were provided only with only boundary condition data for Phase 2 in order to provoke a blind prediction of Phase 2 observations. Step 2 also included investigation of potential Engineered Damage Zone (EDZ) effects, material property evolution, heterogeneity and anisotropy as required.
- Step 3: Hydro-mechanical and non-reactive geochemical model of the full experiment. Phases 0-2.
- Step 4: Hydro-mechanical and reactive geochemical model of the full experiment (optional task). Phases 0-2.

The intention of the task structure was to loosely replicate a typical site investigation process. Step 0 covers initial laboratory investigation and code benchmarking, before testing the small-scale laboratory parameterisation at a larger spatial scale during Step 1. Step 2 then tests the ability of the modellers and codes to blindly predict hydro-mechanical behaviour over an extended time period. Steps 3 and 4 then consider more advanced studies once the confidence in the fundamental hydro-mechanical understanding has reached a sufficiently advanced point. The original task schedule is shown in Figure 2-4.

It should be emphasised that the task work was very much collaborative effort and that once the initial models had been built for Step 1, and good agreement across the modelling teams had been found, that different areas of investigation were assigned to

different teams. As such, this report is only a partial record of the full range of work performed under the task.

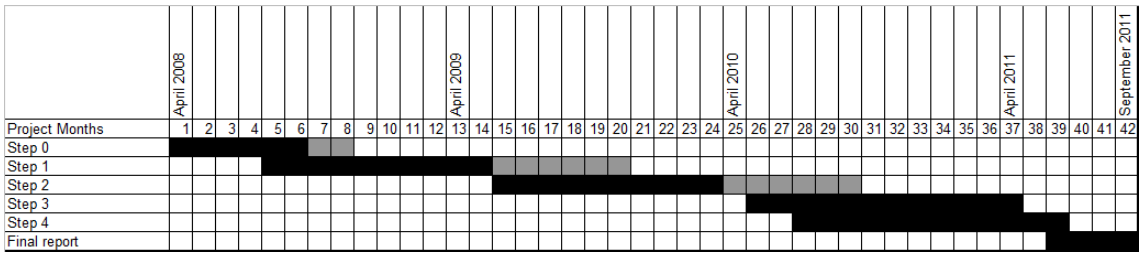

Figure 2-4. Original Task A Work Schedule.

Experimental data for the experiments were released in stages. All the available drying test data was released for Step 0 and all the hydro-mechanical Phase 1 data for the Ventilation Experiment released at the start of Step 1. At the start of Step 2 only information on the boundary condition evolution (applied relative humidity and air flow rate) was released for Phase 2 of the VE. However, because most of the teams were struggling to create models that reflected the true experimental boundaries, some additional tunnel relative humidity data was made available to the teams, sufficient to characterise the tunnel and the system water mass-balance, mid-way through Step 2. The geochemical data for all of the experiment duration were released at the start of Step 3. The Phase 2 hydro-mechanical data was only released after the final workshop meeting in November 2011 where a number of the teams' predictions were tested against this data.

3 Step 0: Laboratory Drying Test

3.1 Drying Test – Short Description

A summary of the Step 0 data is given in Appendix A, but a brief summary of the experimental setup is provided here. This complimentary experiment to the main ventilation experiment has been discussed in some detail by Garitte *et al.* (2010, 2012), Floria *et al.* (2002) and complemented by supporting data from Muñoz *et al.* (2003).

The drying test was a well constrained laboratory experiment where three cylindrical samples of Opalinus Clay (~101 mm diameter, ~278.5 mm height) were placed in a controlled drying chamber along with an evaporation pan, axial direction oriented vertically. The experiment is illustrated schematically in Figure 3-1. Chamber relative humidity and airflow was monitored continuously throughout the 142 day experiment. The samples were covered such that the upper circular surface only could lose water through evaporation. The samples and evaporation pan were also weighed continuously such that water loss could be monitored. Samples were removed and dissected at 21, 99 and 142 days so that the water content profile vertically from the evaporation surface could be monitored.

From this combination of data a continuous record of water loss for each sample as a function of the chamber conditions could be established, along with the sample water content profiles at 21, 99 and 142 days.

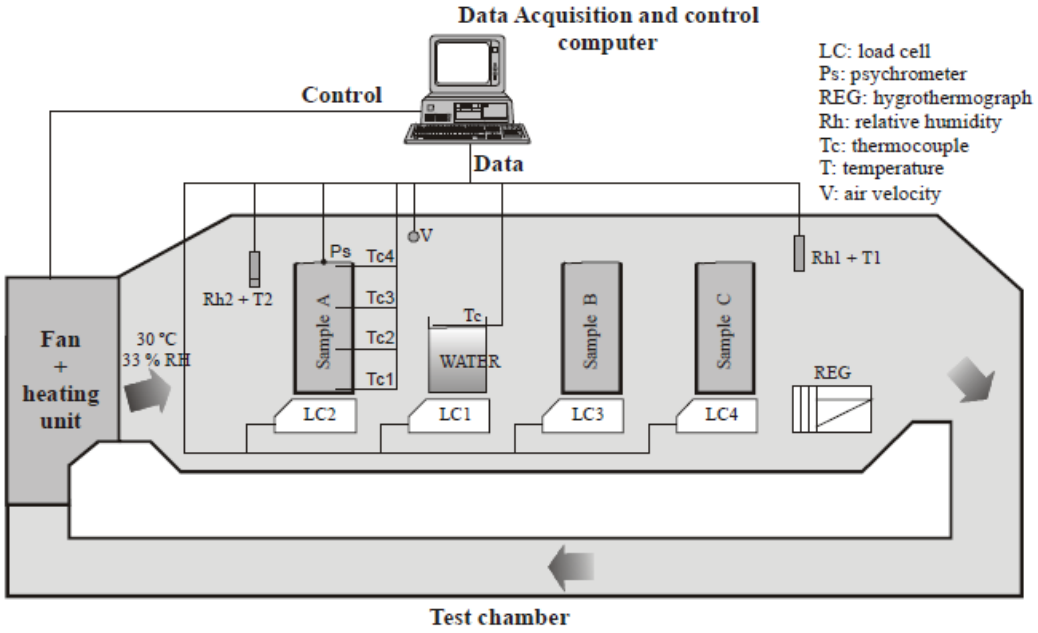

Figure 3-1. Schematic illustration of the Drying Test (from Floria *et al.* 2002)

3.2 Modelling Approach

As discussed in Garitte *et al.* (2012), this experiment was used as a precursor modelling exercise by DECOVALEX in order to reduce uncertainty and build confidence in codes, process models and hydraulic parameterisation before attempting the full ventilation experiment. The experiment also provided a useful role in understanding the possibilities for upscaling processes and parameters from the laboratory scale to the field scale.

Given the objectives of the task, it was decided that Quintessa and UoE would not directly coordinate their approaches to ensure that as wide a range as possible of unconstrained approaches and parameterisation could be presented for task A. The approach taken was for Quintessa and UoE to each produce an initial build, ensure basic consistency between the models and results using standard sets of process models and then move on to explore different aspects of the problem independently:

- Quintessa would look at aspects of variability and heterogeneity in understanding the results using a full process model suitable for Step 1.
- UoE would focus on the parameterisation of the hydraulic process model.

For later Steps, where the cases become more complex, it was planned that Quintessa and UoE will adopt a more structured approach and target specific areas of uncertainty, in conjunction with the other teams.

3.3 Quintessa - Step 0

The following sections describe the conceptual model, mathematical models, implementation and results for the Quintessa modelling.

3.3.1 Conceptual Model

The geometry and temporal evolution of the samples was taken explicitly, as described in Appendix A. As discussed in Appendix A, the following data are available:

- relative humidity in the drying chamber at two locations;
- temperature in the drying chamber at two locations;
- temperature at different elevations in Sample A;
- weight of each sample with time during the experiment, and hence directly inferred water loss with time; and
- water content (by mass) for samples at different elevations when the samples were removed from the drying chamber.

Several key conceptual points can be inferred from the data and setup that significantly impact on the approach to modelling the problem.

The key result is that the cumulative water loss from each sample is different over the time periods for which more than one sample was drying (Figure A6). Given that the physical environments of the samples are measured to be the same, it must be concluded that the physical properties of the three samples are slightly different, either in terms of initial conditions or effective bulk parameterisation. Following this logic, it must be recognised that the water content curves in (Figure A8) are in fact from three different samples at three different times, not the evolution of a single sample.

However, it is observed that the closer a sample is to the heater, the faster it appears to dry (Figure A2 and A8). In this study it was assumed this is simply a coincidence, the measurements in the drying chamber are representative, and that it is differences in the properties of the samples that cause differences in water loss rates.

Given this fundamental assumption on the behaviour of the samples the modelling approach was:

1. Model an individual sample using the observed conditions in the drying chamber as boundary conditions with the aim of getting the best 'average' fit to the observed data. This is referred to as the reference case.
2. Conduct some sensitivity analyses to attempt to obtain fits to the data optimised for each sample, with a view to understanding what magnitude of variability may be causing the different results.

For the purposes of minimising the complexity of the analysis, in each case we will be assuming that each sample can be represented as a homogenous body.

3.3.2 Physical Relationships

In summary the physical process models included in this model were:

- Multi-phase flow in porous media (air, liquid water, water vapour) (Bond and Benbow, 2009).
- Thermal conduction and convection/advection (Bond, 2010).
- Poro-elasticity (Bond *et al.*, 2009).

Full multi-phase flow incorporating water, air and water vapour was employed and the constitutive equations for gases (g consisting of j gas phases) and water (w) over all flowing phases (i) are given below:

$$\frac{\partial}{\partial t}(\theta\rho_i S_i) = -\nabla\cdot(\rho_i \mathbf{u}_i) + q_i$$

$$\mathbf{u}_i = -\frac{\mathbf{k}_i}{\mu_i}\nabla(p_i + \rho_i g z) \qquad 3.1$$

$$\mathbf{k}_i = k_{r,i}(S_i)\mathbf{k}$$

$$\psi = p_{g_j} - p_w$$

where subscript i denotes the phase, ρ is the density (kg m^{-3}), $\mathbf{u}$ is the volumetric flux (m s^{-1}), q is an external mass source (kg s^{-1}), S is the saturation (-), k is the intrinsic permeability (m^2), k_r is the relative permeability (-), ψ is the capillary pressure (Pa).

The vapour mass fluxes (kg s^{-1} m^{-2}) for diffusion and advection in bulk gas are

$$\mathbf{u}_{v,diff} = -D_v(S_g)\nabla\rho_v$$

$$\mathbf{u}_{v,adv} = \mathbf{u}_g\rho_v \qquad 3.2$$

Where D_v is the effective diffusivity of water vapour (m^2 s^{-1}), which is assumed to be a function of bulk gas saturation. For this case the effective vapour diffusivity was assumed to be the gas saturated effective vapour diffusivity multiplied by the total gas saturation.

The thermal conduction model utilised the typical formulation

$$\begin{aligned}\frac{dQ_H}{dt} &= F_{HC} + S,\\ Q_H &= V\rho cT,\\ F_{HC} &= A\nabla\cdot(\Gamma\nabla T).\end{aligned} \qquad 3.3$$

where T (K) is the temperature and ρ (kg m^{-3}), c (J kg^{-1} K^{-1}) and Γ (W m^{-1} K^{-1}) are the density, specific heat capacity and thermal conductivity of the medium respectively in the relevant compartment which has volume V (m^3).

Convection of heat via the movement of fluid in a porous medium adds a contribution to the heat flux

$$F_{HF} = Aq_F\rho_F c_F T \qquad 3.4$$

where the F subscript is used to denote transfer in the fluid, q_F (m s^{-1}) is the Darcy velocity across the interface, ρ_F (kg m^{-3}) is the fluid density, and c_F (J kg^{-1} K^{-1}) is the specific heat capacity of the fluid.

The poro-elastic mechanical solves the classical elastic constraint equation

$$\frac{d\boldsymbol{\sigma'}}{d\boldsymbol{\varepsilon}} = \boldsymbol{C} \qquad 3.5$$

where $\boldsymbol{\sigma'}$ is the effective stress tensor, $\boldsymbol{\varepsilon}$ is the strain tensor and $\boldsymbol{C}$ is the elastic coefficient tensor. Effective stress in the principal directions (n) is related to total stress and the effective pore fluid pressure P (MPa) as follows, noting that the effective shear stress components are equal to the total shear stress components

$$\sigma'_n = \sigma_n - P \qquad 3.6$$

By default we assume that the effective pore pressure can be related to individual fluid pressures using Bishop's formulation (Bishop, 1959)

$$P = \sum_i (S_i p_i)^{n_i} \qquad 3.7$$

where n is a fitting coefficient, which for this study took the typical value of 1.

While the full multi-phase flow, thermal and mechanical processes were not explicitly required for Step 0, it was felt to be beneficial to include them at this stage to make the development of the Step 1 and 2 models (Garitte & Gens, 2008) less complex. For later steps, the existing tracer transport and reactive chemical transport modules will also be employed.

It should be noted that one of QPAC's most important features is the ability to quickly, easily and robustly couple and decouple processes in a given modelling problem. Figure 3-2 schematically shows the coupling between modules used in this case and the key conservation variables.

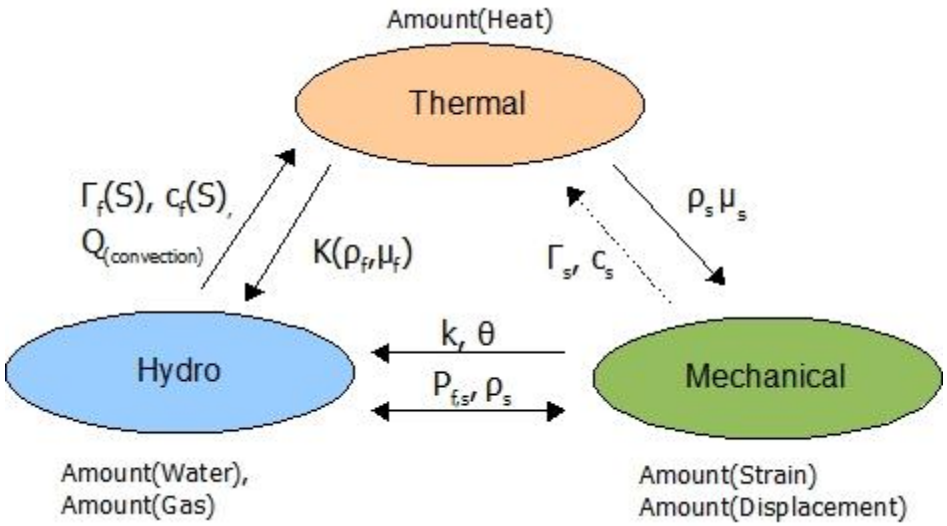

Figure 3-2: Interaction of Parameters across the THM System: subscript 'f' denotes fluid and 's' denotes solid phases

The intrinsic permeability is linked to porosity change and pore fluid pressure linked to effective stress to provide the hydro-mechanical coupling (Table 3-1). The thermal process model is coupled to the hydraulic evolution through changes in fluid content changing bulk thermal properties, through advective transfer of heat as fluids migrate and the latent heat of vaporisation/condensation of water vapour (Table 3-1).

3.3.3 Discretisation and Boundary Conditions

Figure 3-3 shows the schematic layout of the problem as implemented in QPAC. Spatial discretisation was achieved through a cylindrical grid with a single compartment in the radial direction, with a single outer interface representing the radial boundary condition, and interfaces lying at the following vertical elevations with compartments occupying the space in between.

0.0, 25, 50, 75, 100, 125, 150, 175, 200, 225, 250, 265, 278.5 [mm]

The bottom and top interfaces were parameterised as boundaries as shown in Figure 3-3. The model grid is shown in Figure 3-3. Grid convergence testing was carried out on this model and the discretisation found to be sufficiently refined that the results were representative.

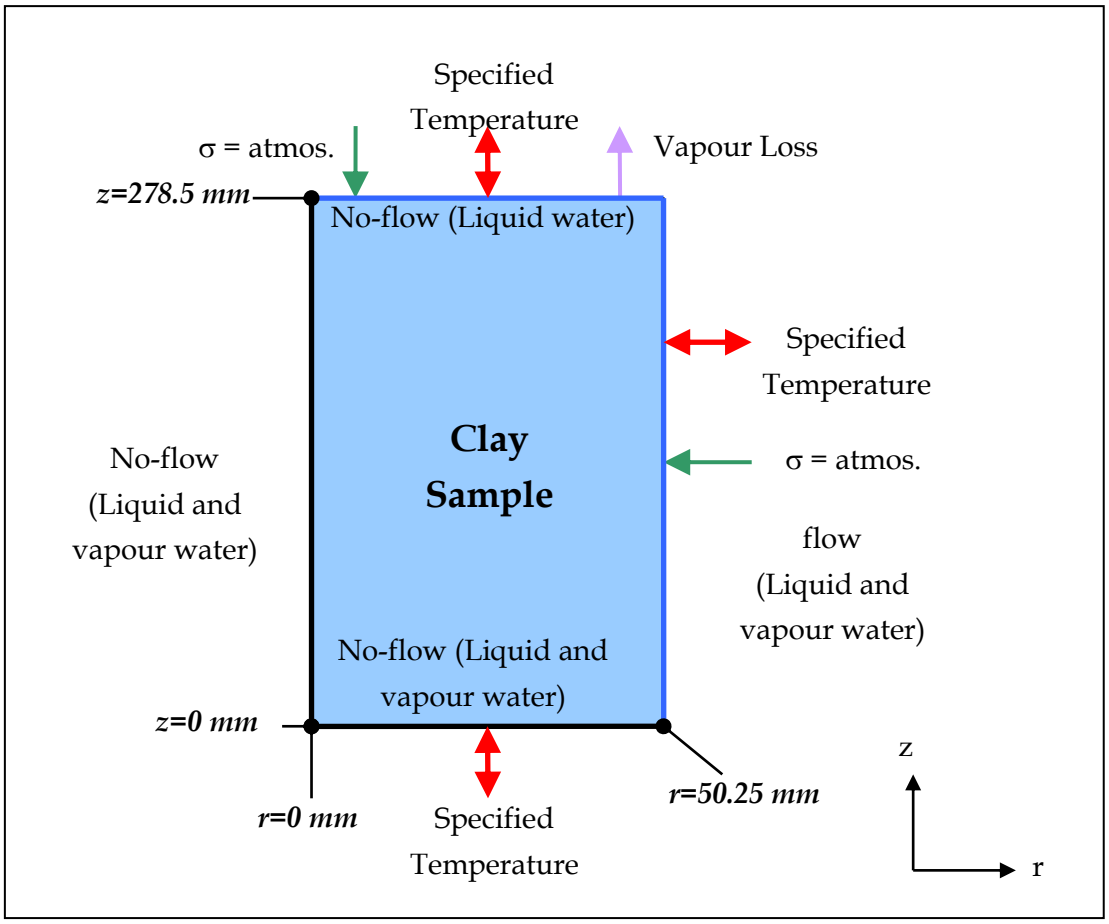

Figure 3-3. Schematic layout of QPAC Step 0 model. Note the thick black lines on the inner radius and base of model denote zero displacement boundaries.

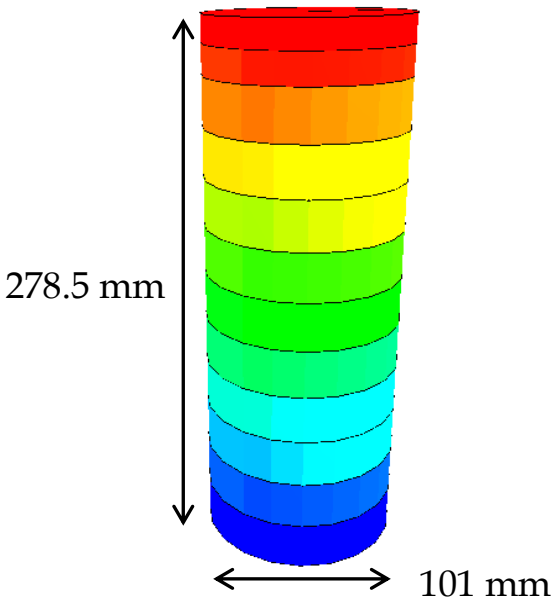

Figure 3-4. Drying test QPAC grid. Volumes are coloured by centroid elevation (m).

Successful treatment of the surface condition for water in both the drying test and the ventilation experiment is clearly important in ensuring a good representation of the interface between the air filled void (tunnel or drying chamber) and the porous medium. The drying test represented a controlled set of data where options for representing these conditions, before attempting the more complex ventilation experiment.

Two general approaches for defining the liquid water boundary condition were examined in QPAC based on the available data and conceptual understanding of the experiments. The first used Kelvin's Law to define an equivalent water pressure (p_l) at the surface, representative of the air relative humidity (RH) in the tunnel or drying chamber:

$$p_l = p_a - \frac{RT}{M_w}\rho_l \ln(RH) \qquad 3.8$$

Where p_a is the air pressure (Pa), R is the ideal gas constant (J mol^{-1} K^{-1}), T is the temperature (K), M_w is the molar mass of water (kg/mol), ρ_l is the density of water (kg m^{-3}) and RH is the relative humidity in the air expressed as a fraction (-). This boundary condition is best described as a time-variant Dirichlet condition, and will be referred to as the 'pressure' variant in the remainder of this report.

The second used an empirical relationship which correlated the observed open pan evaporation rate in each experiment ($F_f(RH)$, kg m^{-2} s^{-1}), versus the relative humidity in tunnel or drying chamber. For each experiment a simple functional relationship was derived between the two observations. Note that changes in air circulation rate, which might be reasonably assumed to affect the local rate of evaporation, were neglected under the assumption that mixing of the air was relatively rapid. The function was then scaled by the fractional effective area of the free liquid water assumed to be present at the rock surface. The assumption was that this fractional effective area could be described by the product of the porosity (θ), water saturation (S_w) at the top of the sample, hence the effective water loss flux could be described as.

$$F_e = \theta S_w X F_f(RH) \qquad 3.9$$

where X is a penalty coefficient (-) that enables additional scaling of the flux based on additional factors not covered in the fractional area term. Clearly this formulation requires a good estimate of the saturation at the evaporation surface to function adequately. Dependent on the model formulation, there are a number of approaches that can be adopted to achieve this, the most obvious being a high degree of spatial discretisation up to the evaporation surface. In mathematical terms, this type of condition is a weak form of 'mixed' condition, whereby a time variant Neumann flux ($F_f(RH)$) is scaled by properties internal to the model. This boundary condition is best described as a time-variant Neumann condition, and will be referred to as the 'flux' variant in the remainder of this report.

Both of these models assume that mixing in the air above the surface is relatively rapid compared with the loss from the porous medium, and hence there is no need to consider any boundary layer effects.

In the default formulation used for QPAC vapour is considered explicitly as a distinct phase and hence the surface condition for the water vapour had to be handled separately from the liquid water condition. The surface boundary condition for vapour was simply water vapour diffusion continuity equation using the relative humidity in the tunnel or drying chamber to define the water vapour density as a time variant Dirichlet condition thus;

$$\rho_v = 10^{-3} \exp\left(a - \frac{b}{T}\right) RH \qquad 3.10$$

where ρ_v is the vapour density (kg m^{-3}), a is an empirical constant (19.891 (-)), b is an empirical constant (4975.9(K)) (Rutqvist *et al.*, 2003).

There reference QPAC model used the pressure based condition for the liquid water, and the flux-based method as a variant. Relative humidity was evaluated from the experimental data using a 7 day moving average to eliminate the rapid oscillations (see Appendix A)

The temperature boundaries were a specified temperature, using the reported drying chamber temperatures as it changes with time. This was achieved through a simple lookup function taken directly from the experimental data.

3.3.4 Parameter Values – Reference Case

The full Multi-Phase Flow (MPF) formulation was used in this case as it was felt that gas pressurisation could be important to the model results and was examined during the calibration process, even though ultimately it was not included and the model runs identically just using the Richard's Equation (RE) module (gas pressure is assumed to be constant and hence gas infinitely mobile). It is also noted that the temperature parameterisation for this case is largely irrelevant (the samples appear to remain in reasonable thermal equilibrium with the drying temperature) and hence some default clay parameterisation has been used.

Key parameters were subject to calibration in order to achieve a best 'mean' fit, and these are clearly marked in the table below

Table 3-1. List of Input Parameters for Step 0 (reference case)

Parameter	Unit	Value	Source
Acceleration due to	m s^{-2}	9.81	Gettys *et al.* (1989)

Parameter	Unit	Value	Source
gravity g			
Young's Modulus (Clay) E	GPa	2.5	Estimated value – case insensitive
Poissons Ratio (Clay) ν	-	0.3	Estimated value – case insensitive
Reference Porosity (Clay) θ_0	-	0.16	Estimated 'mean' porosity to give mean starting water contents reported by Floria *et al.* (2002) across all three samples.
Initial Stress (Radial)	atmosphere (bar)	1	Floria *et al.* (2002)
Initial Stress (Vertical)	atmosphere (bar)	1	Floria *et al.* (2002)
Initial Water Pressure	atmosphere (bar)	1	Floria *et al.* (2002)
Initial Temperature	degrees C	22	Garitte and Gens (2008)
Bulk Specific Heat Capacity C_b	J kg^{-1} K^{-1}	$(C_{water} WC\ F_{vapour} + C_{vapour} WC\ (1-F_{vapour}) + C_{clay})/(1+WC)$ WC = Mass water content, F_{vapour} = fraction of water as vapour	Linear scaling from 3 different components, liquid water, water vapour and clay
C_{water}	J kg^{-1} K^{-1}	4181.3	Gettys *et al.* (1989)
C_{clay}	J kg^{-1} K^{-1}	1850	Default value – insensitive to this case
C_{vapour}	J kg^{-1} K^{-1}	1100	Gettys *et al.* (1989)
Thermal Conductivity Γ	W m^{-1} K^{-1}	$((A1-A2) / (1+\exp((S_w-x0)/dx)) + A2)$ x 1 [W m-1 K-1] $A1$ = 0.6 $A2$ = 1.2 $x0$ = 0.65 dx = 0.1	Used relationship for bentonite, determined to be broadly representative for this case
Reference Water Density	kg m^{-3}	1000	Assumption
Reference Water Pressure	atmosphere (bar)	1	Assumption
Relative Permeability Air $k_{r,A}$	-	Gas Saturation	Gas is assumed to be largely passive to water saturation.
Relative Permeability Water $k_{r,w}$	-	$S_{wr}^{(1/2)}\ (1-(1-S_{wr}^{(1/\lambda)})^{\lambda})^{2}$ Where S_{wr} is the reduced saturation and λ is a fitting parameter = 0.3	λ was calibrated within the range given in Muñoz *et al.* (2003).

Parameter	Unit	Value	Source
Intrinsic Permeability k	m^2	k_0 $((\theta^3)/(1-\theta)^2)((1-\theta_0)^2/(\theta_0)^3)$ where k_0 = 1.6875e-19 m^2	k_0 is a fitting parameter bounded by the ranges discussed in Muñoz *et al.* (2003).
Reference Vapour Diffusivity D_v	$m^2\ s^{-1}$	2.5e-6	Claesson & Sallfors (2005) and calibrated
Suction pressure Ψ	MPa	Determined by constraint solution to: $0 = S_{wr}(1- F_{vapour}) - ((1 + (\Psi / P_0)^{(1/(1-\lambda))})^{-\lambda})((1-(\Psi / P_S))^{\lambda_s})$ where P_0 = 3.9 (Mpa) λ = 0.128 (-) P_S = 700 (Mpa) λ_s= 2.73 (-)	Muñoz *et al.* (2003)
Initial Water Saturation	-	0.999	Floria *et al.* (2002)
Dry grain density ρ_m	$kg\ m^{-3}$	2700	Derived and calibrated value from initial conditions quoted in Floria *et al.* (2002). Consistent with Bock (2001)
Henrys Law Constant	$Pa\ m^3\ mol^{-1}$	0 (dissolution disabled)	Not required

3.3.5 Results – Reference Case

There were only two sets of results identified for key comparison (Garitte and Gens, 2008):

1. Water contents from each elevation in each sample as they were removed from the drying chamber.
2. Total water loss rates from each sample.

Comparison between the reference case and the experimental results are shown below, again it is emphasised that the intention is to produce a 'mean' set of results that represent the general behaviour of the three samples, not replicate the apparent differences in physical properties.

The key observation for the result is that the QPAC calculations, as intended, fall within the range of responses for the experimental data. QPAC tends to over-estimate the water loss for sample C and indeed the water contents calculated in QPAC show a higher degree of desaturation than the experimental results. Sample B shows a similar degree of fit as C, but with an over-estimation of water saturation, while Sample A shows a higher degree of water loss than calculated by QPAC, and indeed the water contents calculated by QPAC are higher than the experimental results from Sample A. It should be noted that the water loss rates from Sample A are so high, that it might suggest (as implied, but not positively confirmed in Floria *et al.*, 2002) that Sample A may have a higher starting water content (presumably through a higher initial porosity) than the other samples.

The interesting feature of the water content results that is not replicated is the sharp desaturation front shown at early times in Sample C. This feature was found to be extremely difficult to replicate using the 'typical' parameterisation discussed in Muñoz *et al.* 2003) while retaining good results for the other two samples. In contrast it was relatively easy to get broadly consistent results for Samples A and B in terms of water content, although as already discussed Sample A shows much higher water losses than the other two samples, perhaps due to differing initial conditions.

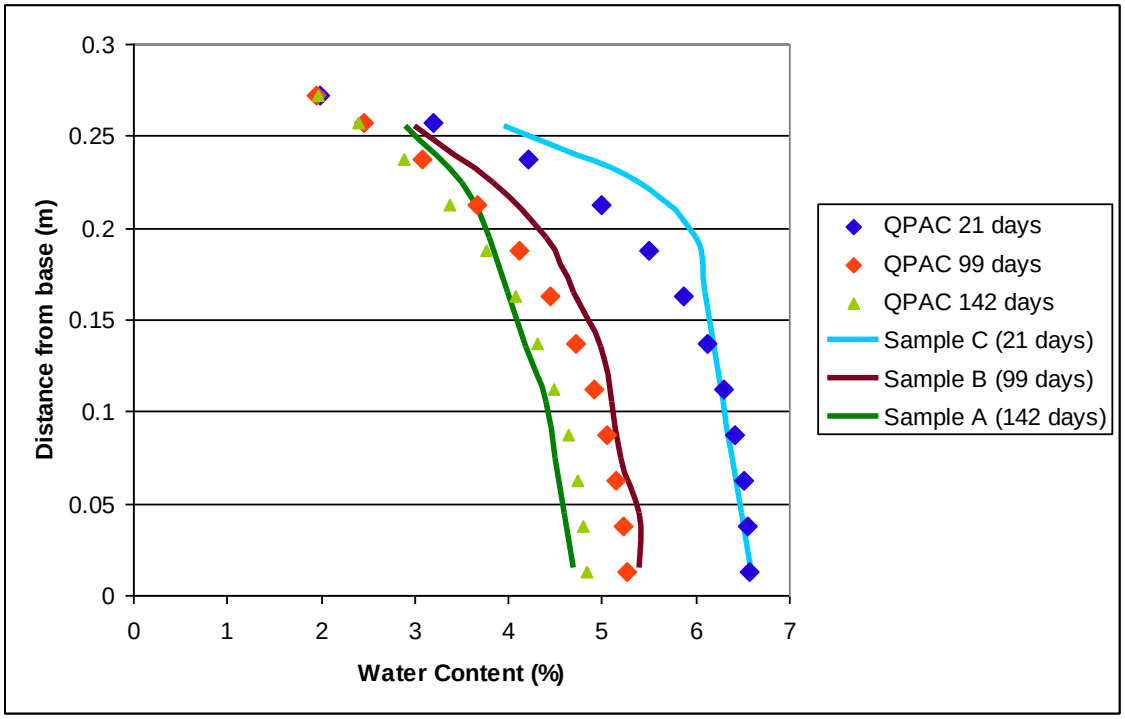

Figure 3-5. Water content with elevation for the QPAC reference case and the experimental results from the three samples

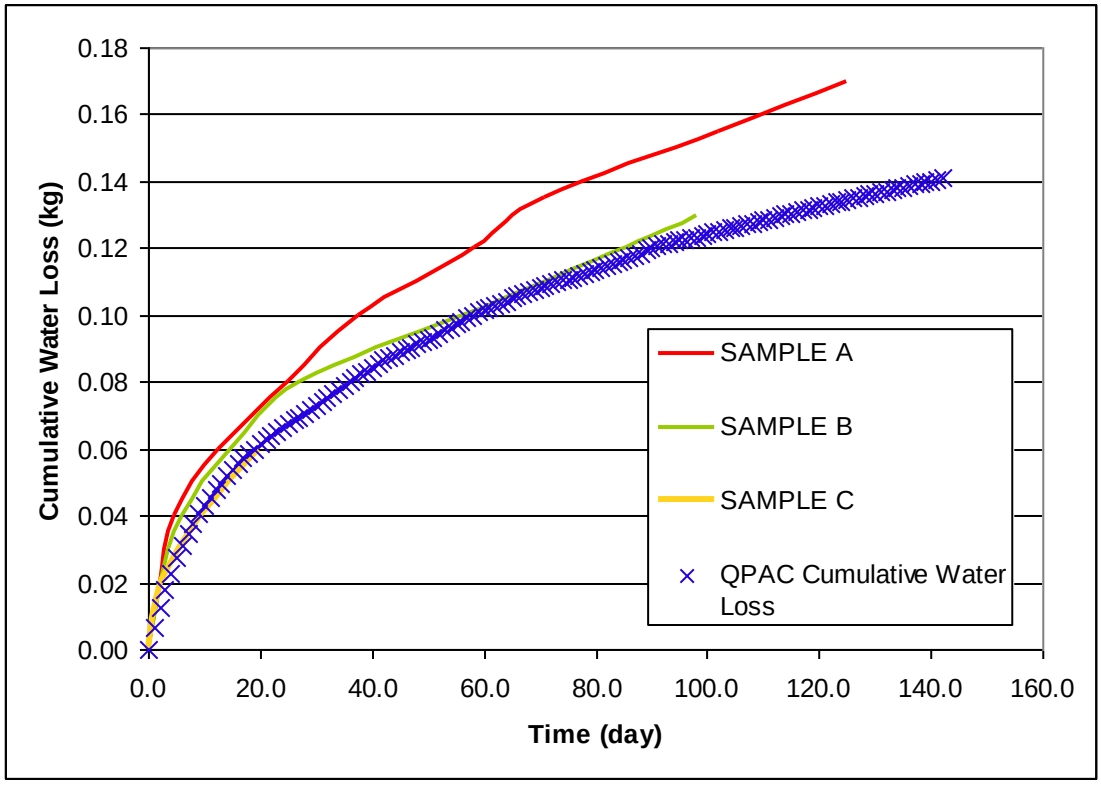

Figure 3-6. Total water loss for the QPAC reference case and the experimental results from the three samples

3.3.6 Alternative Cases – Sample Specific Fits.

Sample A

Good fits could be achieved for water content for Sample A (142 days) by slightly increasing the k_0 value in Table 3-1 to 3.0e-19 m^2. This gave a better match versus the water loss rates, however the calculated values were slightly too low. By increasing the porosity to 0.166, increasing the solid density to 2750 kg m^{-3} and hence the initial water content to 7.2% (Floria, *et al.* 2002) a better fit was achieved.

It is noted that the Sample A water loss measurement data is quite noisy (Figure A6) a great deal of high frequency, large amplitude (± 0.05) variation and that the smoothed water loss curve for sample A shows a number of 'steps', which may be indicative of sample heterogeneity. The result here therefore represents a 'best fit' water loss curve for a homogenous parameterisation to the smoothed data.

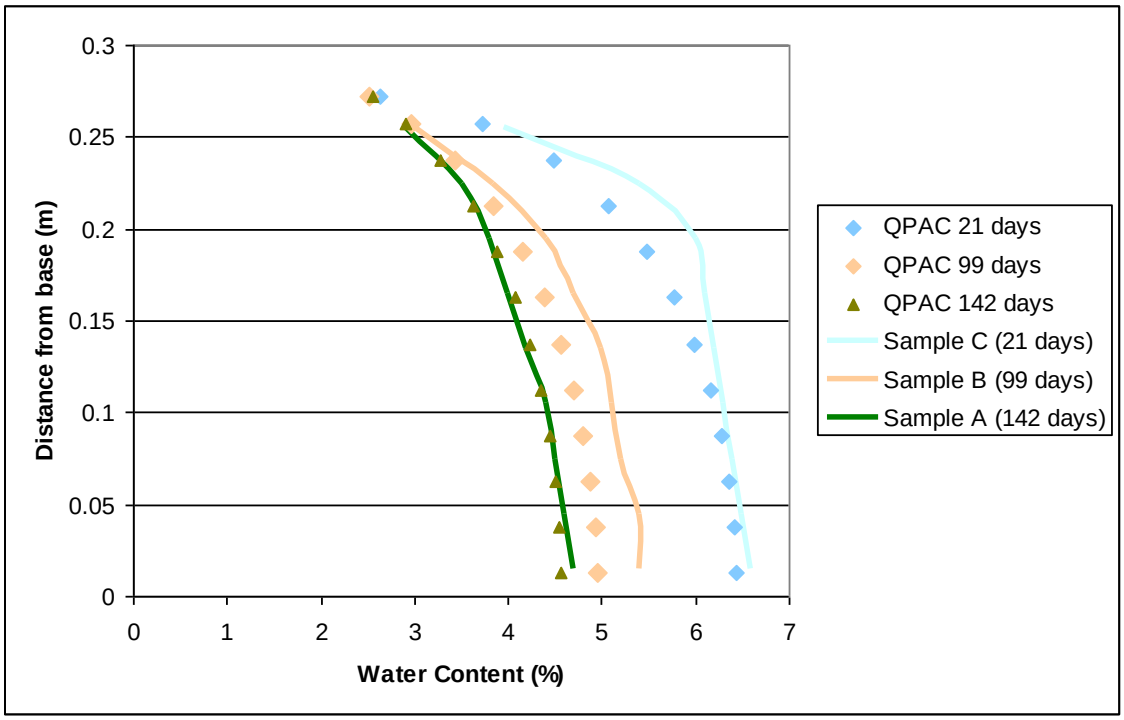

Figure 3-7. Water content with elevation for the QPAC model optimised for Sample A and the experimental results from the three samples. Note results at 21 and 99 days are shown in washed-out colours because their results are not directly relevant

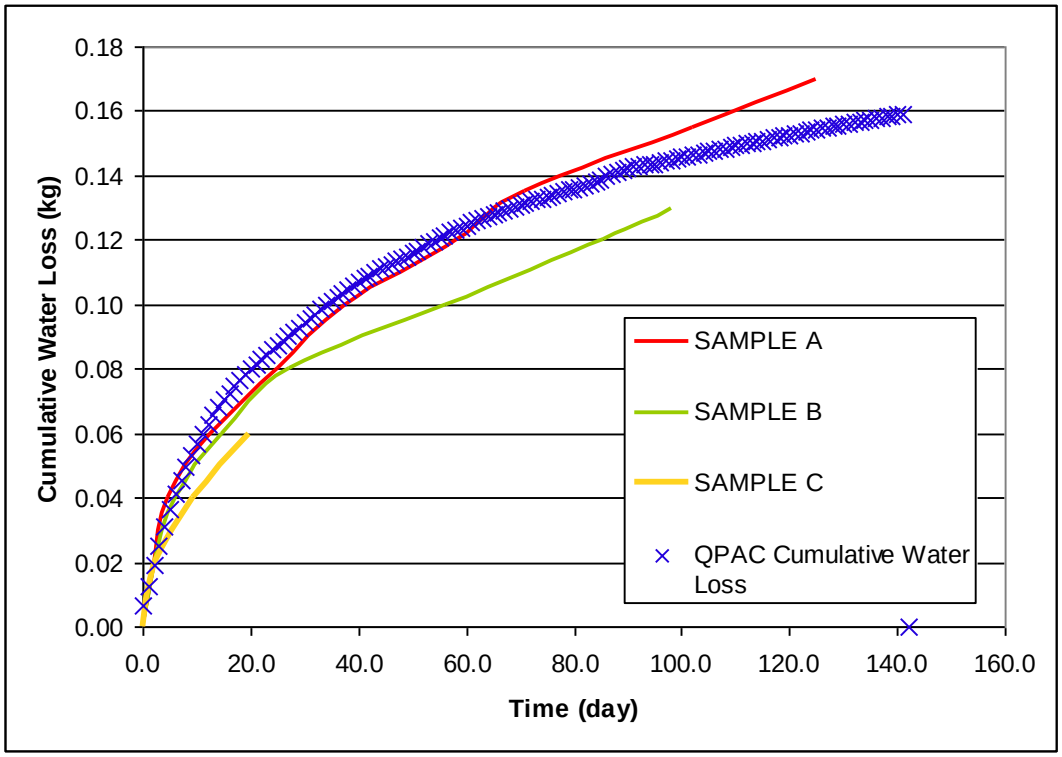

Figure 3-8. Total water loss for the QPAC model optimised for Sample A and the experimental results from the three samples

Sample B

The fit to sample B was felt to be sufficiently good in the reference case, and hence no further effort was spent on this sample.

Sample C

As already discussed, Sample C shows a very sharp change in water content close to the upper surface not seen in the other samples. After a considerable amount of calibration, it was established that this feature could be best represented through changing the k_0 value in Table 3-1 to 1.125e-18 m² and changing the λ factor in the relative permeability curve to 0.2. From the results of Muñoz *et al.* (2003) this would be consistent with the presence of some form of discontinuity present, perhaps only in the upper portion of the sample. The calibrated results are shown below.

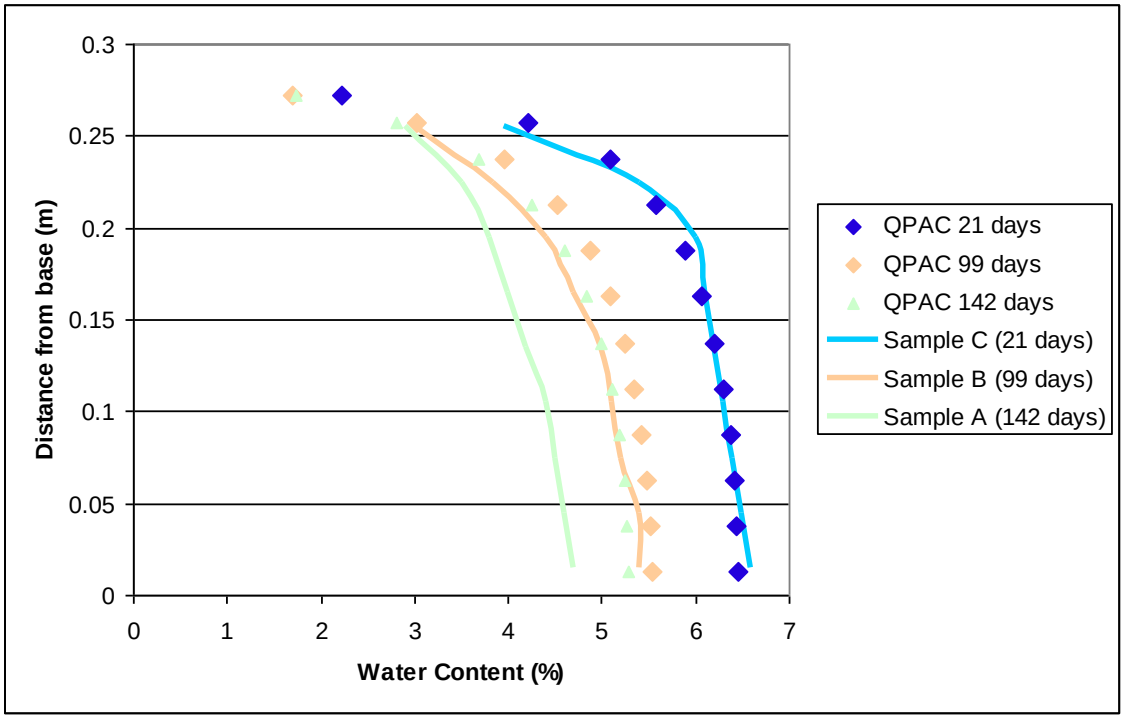

Figure 3-9. Water content with elevation for the QPAC model optimised for Sample C and the experimental results from the three samples. Results at 99 and 142 days are shown in washed-out colours because their results are not directly relevant

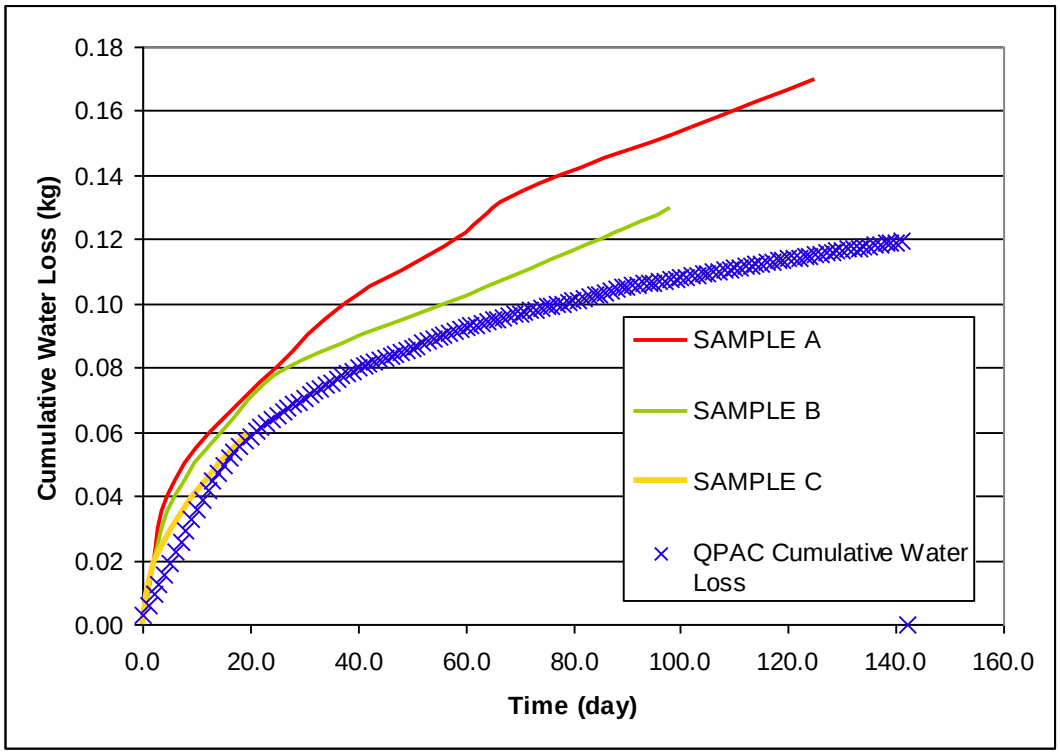

Figure 3-10. Total water loss for the QPAC model optimised for Sample C and the experimental results from the three samples

3.3.7 Sensitivity Results

A small number of sensitivity cases were run, focussing primarily on the role of discretisation and numerical formulation on the modelling results. These exercises varied the grid density and permitted the air relative permeability to drop with increasing water saturation.

The grid discretisation results showed conclusively that the grid selected was reasonable, and that increasing grid densities did not significantly change the results, only lengthened the run-time of the case. Reducing the grid density by a factor of 1.5 did start to impact on the results and at a reduction factor of 2, the results were severely compromised by a coarse discretisation.

Applying a simple phase interference model to air relative permeability (i.e. relative permeability being equal to air saturation) had no significant effect on the results, however using a tighter relationship with air relative permeability equal to the square of air saturation did start to retard water loss from the sample. The results with significant reduction in air relative permeability did not seem to significantly improve the form of the results, hence it was concluded that air was most accurately represented as a passive phase for this case.

Adjusting the liquid water condition to use the 'flux' based condition on the upper surface was also tried. The equivalent outputs for the calculation using the specified flux upper boundary condition are shown in Figure 3-11 using a penalty factor X (equation 4.2) of 1 and an implied free evaporation rate at zero relative humidity ($Ff(RH=0)$) of 1.1 g/day/cm^2 reducing linearly to zero at a relative humidity of 100%. While there are some small differences, the basic result is equivalent. Simple parametric sensitivity studies showed that functionally identical results can be produced with only minor adjustments to the parameterisation of intrinsic permeability, relative permeability or vapour diffusivity, all of which well within the accepted bounds of data uncertainty for this case and are sufficiently similar to those given in Table 3-1 to not warrant further discussion.

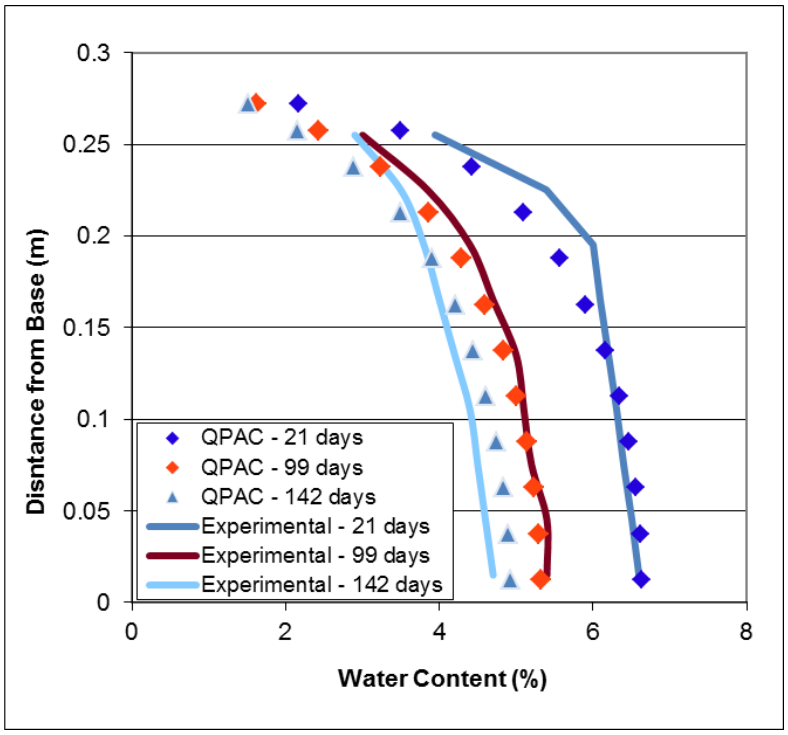

Figure 3-11. Comparison of calculated water contents for the three samples in the Drying Test versus the calculated QPAC results using the flux based upper boundary condition.

A key numerical point, is that in order for the flux version of the case to work adequately, estimation of the water saturation at the upper surface of the sample needs to be accurate. Because a finite volume approximation was adopted in this case, primary variables are calculated at compartment centres, hence no water saturation was calculated at the boundary. In this case this was addressed through estimating a boundary water saturation using the inferred water saturation profile through the upper half of the model via an automatic, dynamic high-order polynomial fit and using this directly in the water flux calculation.

The required parameter changes to make one solution equivalent to the other are sufficiently small relative to other uncertainties, that the difference between the two boundary condition approaches is effectively negligible for the drying experiment. However it is recognised that this congruence of approaches may not generally be true, and caution should be adopted in different environments.

3.3.8 Summary Remarks

The Step 0 analysis was completed successfully using QPAC and a full thermal-hydraulic-mechanical formulation and provided a sound basis for moving on to the later steps. The work demonstrated that fully consistent results could be obtained across all the samples, if modest assumptions regarding sample heterogeneity were

adopted, although there is no direct evidence of this heterogeneity. The work also showed that, for this case, the results were largely insensitive to assumptions regarding the formulation of the upper boundary condition. Such a conclusion should be taken with caution because the air flow rates through the drying apparatus were thought to be sufficiently fast to eliminate significant boundary layer effects on the drying surface.

3.4 University of Edinburgh – Step 0

3.4.1 Model Design

Physical Processes

As discussed in Appendix C, the numerical model for this case utilised a hydraulic-only formulation, incorporating pressure-driven multi-phase flow of air and water in porous media.

Geometry

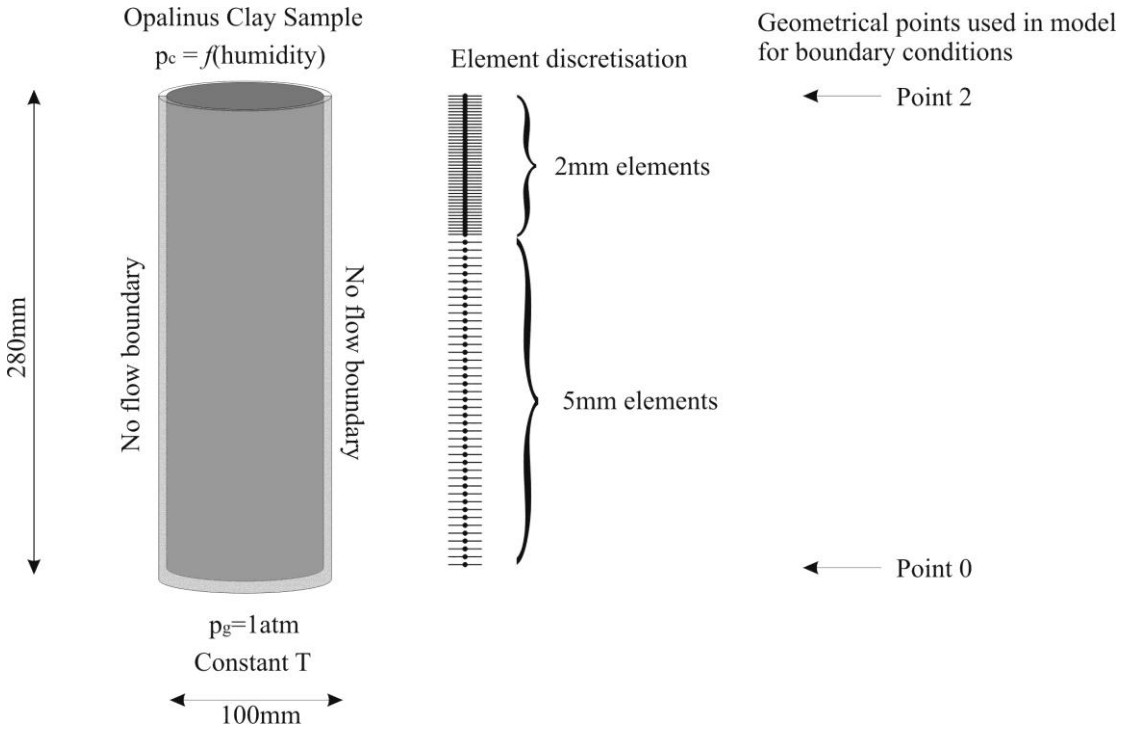

Figure 3-12. Model design, mesh representation and geometrical points for modelling.

The model comprised 80 elements and 81 nodes.

Initial Conditions

The sample was initially fully saturated with respect to water with water and air at atmospheric pressure.

Fluid (Water and Air) Properties

Table 3-2. Physical properties for fluids in the OpenGeoSys calculation

	Water	Air
Density (kg m^{-3})	1000	Evaluated Analytically (see equation C8)
Viscosity (Pa s)	1.0e-3	1.8e-5
Specific Heat Capacity (J K^{-1} kg^{-1})	4162	101
Thermal Conductivity (J m^{-1} K^{-1})	0.6	0.026

Time Control

The model used a total of 2272 time steps of 1.5 hours each. Consistent with the experiment, the total length of time simulated was 142 days.

Boundary Conditions, Relative Humidity.

As per Munoz *et al.* (2003) the model uses the pressure based condition (Equation 3.1) discussed in the QPAC Step 0 parameterisation. The change in relative humidity in the drying chamber of the samples is given by Floría *et al. (*2002), see Figure 3-13 below. The relative humidity in the model is approximated by a time dependent function presented as the plotted line graph in Figure 3-13.

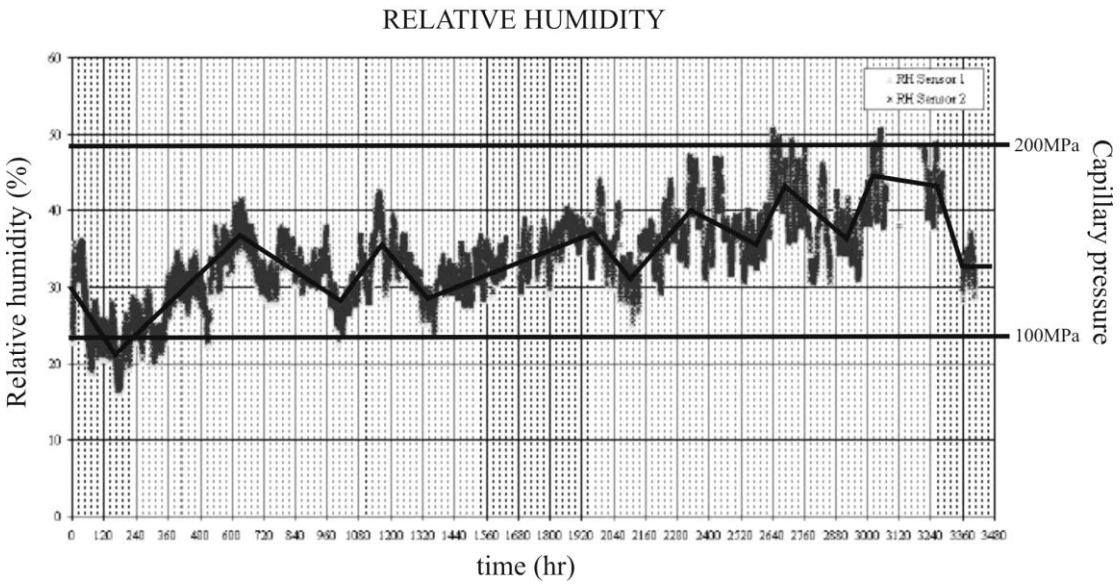

Figure 3-13. Superposition of measured humidity, and model function of humidity against capillary suction pressure.

Capillary pressure and saturation relationship

Several authors have investigated both the drying path and wetting path of the opalinus clay. Following the data by Gens (2000); Munoz *et al.* (2003); Villar (2007); Zhang and Rothfuchs (2005) Figure 3-14 presents the best fit of the experimentally measured capillary pressure and saturation curves. Several models exist to match this curve, including the Brooks Corey and Van Genuchten approximations. In OpenGeoSys the option exists to enter the measured curves or different formulas attempting to represent the data. One key issue is the inclusion of air entry pressure, the fact that air will enter the pores of a sample naturally by a drainage type effect if the pores are large enough. This is determined experimentally. After fitting with several functions the modified Van Genuchten law presented by Ippisch *et al. (*2006) was found to fit the data most accurately. Also presented in Table 3-3 is the data used by Munoz *et al. (*2003), as this was used as a comparison for other groups working on Task A.

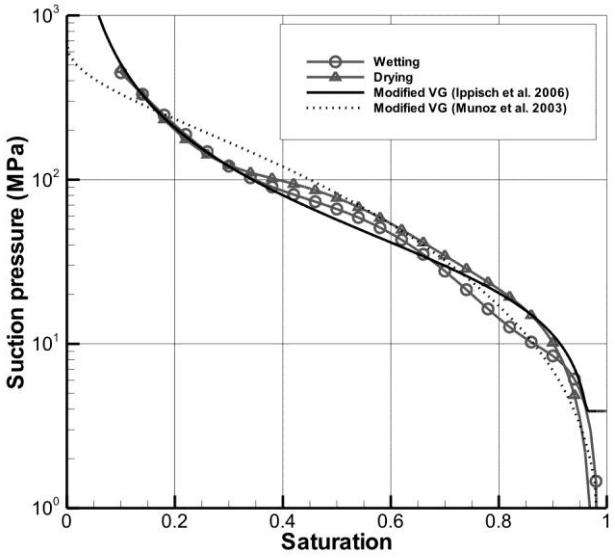

Figure 3-14. Experimentally measured capillary pressure suction values against saturation, and fitted capillary function.

Table 3-3 : Parameters used for fitting capillary pressure vs saturation data.

Munoz *et al.*(2003)		Ippisch *et al.* (2006)	
Parameter	**Value**	**Parameter**	**Value**
S_e	0-1.0	S_e	0-1.0
P	3.9 MPa	P	3.9 MPa
λ	0.128	λ (m)	0.44
Ps	700 MPa	$\frac{1}{1-\lambda}$ (n)	1.78
λ_s	2.73	α	3.57E-08
S_{rl}	0	S_{rl}	0
S_{max}	0.975	S_{max}	0.975

Material medium properties

Porosity of samples

The porosity of the sample effects the mass flux of water from the sample to the drying chamber, the amount of water available in the sample, and the calculation of the moisture content from the degree of saturation. In the literature provided, several authors give estimates of the porosity of the Opalinus clay. Particularly Munoz *et al. (*2003) assumes in his estimates of relative permeability, a porosity of 19.2%. Compared to the range of values offered for Opalinus clay, e.g. Nagra (2002b) p246, this value is in the upper range of measured values, is however not out of the range and fits the mass flux data best of all. For the modelling work a porosity of 19% was assumed.

The water content at 100% saturation was taken to be 8%. Data from Floría *et al. (*2003) gave values of above 6.9% for incomplete saturation. The conversion of saturation to moisture content (expressed as a fraction rather than percentage) is given as

$$s = 0.08\, w \qquad 3.11$$

Relative Permeabilities

The drying test results as presented by Floría, *et al. (*2003) formed the target fitting of the numerical model in order to determine realistic parameters for the further model fitting and development for the further stages in the project steps. It was found that the drying saturation of the samples was very sensitive to the relative permeability curve. In particular given that the upper boundary condition set the saturation between 30% to 40% depending on the humidity, the permeability of the system at this saturation was one of the most sensitive parameters.

Theoretically the function used to describe the capillary pressures and the relative permeability curves should have the same fitting parameters. However it was found

that fitting both the capillary pressure function and the relative permeability curves using the same parameter set was not possible whilst still maintaining the distinctive shape of the drying curve. This suggests an inconsistency in the use of the standard capillary pressure and relative permeability models in the Opalinus clay. However the models for relative permeability provided useful mathematical functions to generate comparative relative permeability curves.

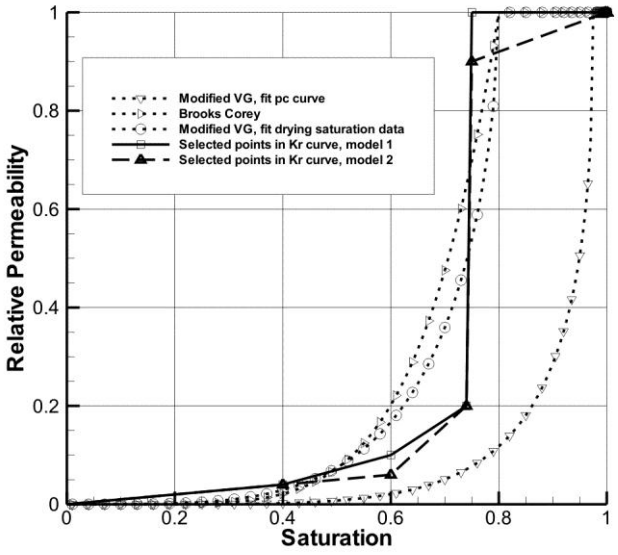

Figure 3-15. Relative permeability curves

3.4.2 Calibration and Results

A number of attempts were made to fit the drying curves as presented by Floría *et al. (*2003). A particular feature of the drying curves was the breakdown in permeability at around 80 to 90% saturation. This effect was also noted in Munoz *et al. (*2003), p22 at 95%. To fit the experimental data and demonstrate this sharp drop in permeability a sharp drop in the relative permeability at around 80% saturation was necessary. This is represented in Figure 3-14 in the two curves marked as "Selected points in the Kr curve". In these cases the whole Kr curve is represented in the model by the few points given. The results of the comparison to the drying data are presented in Figure 3-16. Here marked on Figure 3-16, it can be seen that the drying curve shape for sample C is quite accurately represented.

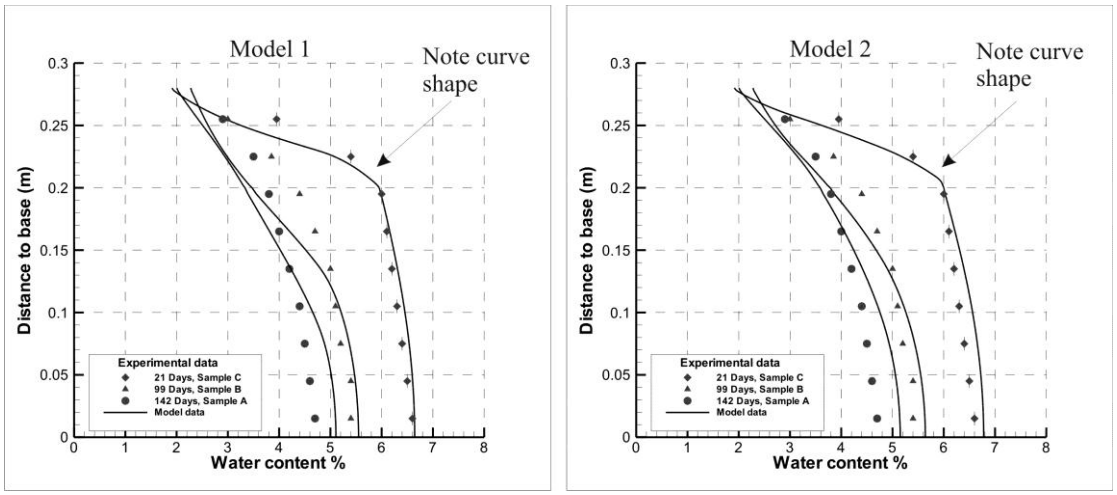

Figure 3-16. Selected Kr models 1 & 2

As stated the standard Krel models were not able to represent this irregularity in the shape of curve A. However they were able to get close to the general shape of the curves, as illustrated in Figure 3-17.

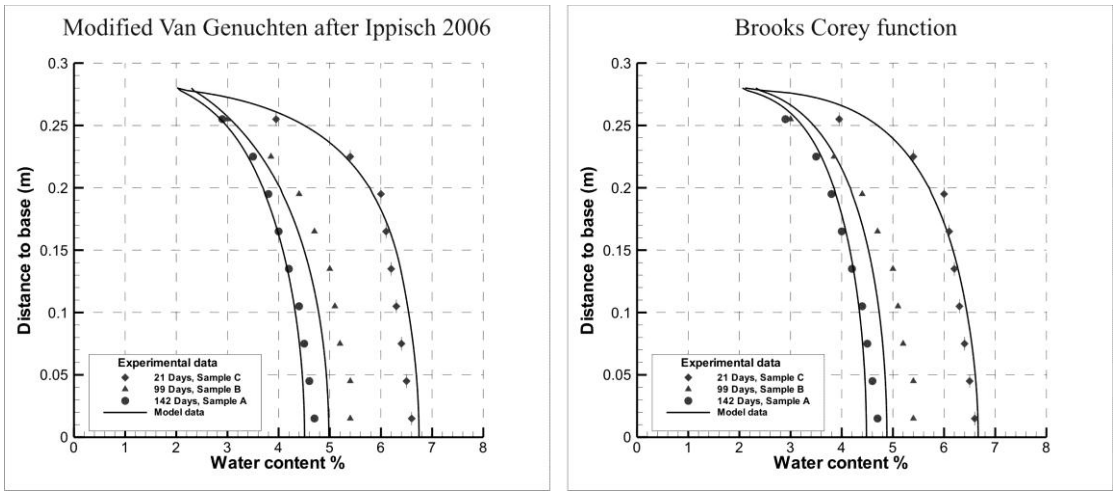

Figure 3-17. Comparison of the drying curves predicted by two Krel functions.

Table 3-4 : Parameters used in fitting experimental results, attempt to match irregular shape of drying curve A.

Mod Van Genuchten parameter	Value	Brooks Corey Parameter	Value
S_e	0-1.0	S_e	0-1.0
P	3.9 MPa	P	3.9 MPa
λ (m)	0.6	λ	0.78
$\frac{1}{1-\lambda}$ (n)	2.5		
α	3.57E-08		
S_{rl}	0	S_{rl}	0
S_{max}	0.8	S_{max}	0.8
Intrinsic saturated permeability	3.2×10^{-20} m^2	Intrinsic saturated permeability	3.2×10^{-20} m^2

Examining the relative permeability curves in Figure 3-15 the difference in permeability in the boundary cell dominated by the relative permeability at between 30% to 40% saturation becomes apparent. The effect of this difference is best seen in Figure 3-18.

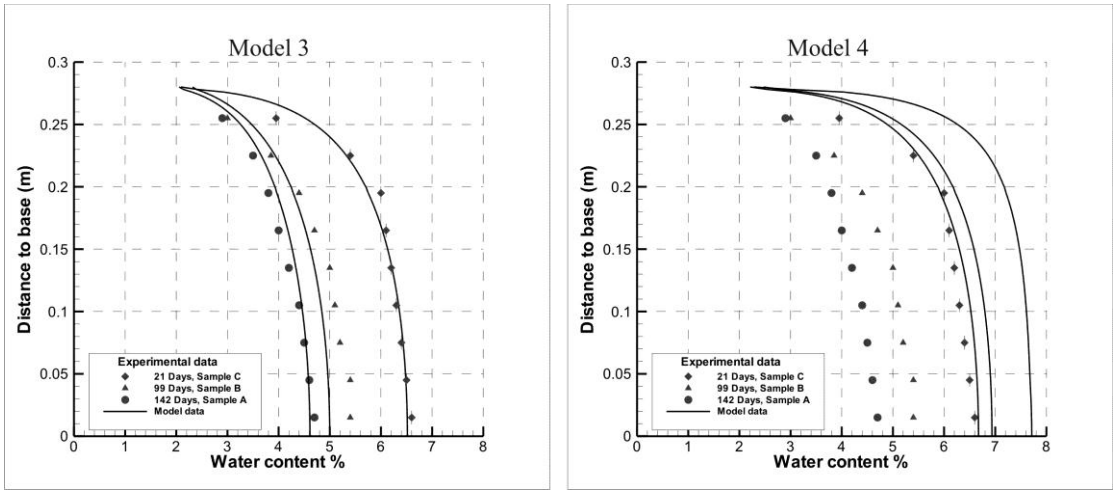

Figure 3-18. Effect of the change in the Krel curve.

Model 3 and model 4 both use the modified Van Genuchten relative permeability curve expected to be derived from the fitting of the capillary pressure data, Table 3-3, and Figure 3-15, curve "Modified VG, fit pc curve". Model 4 uses the intrinsic

permeability values predicted from Table 3-4, $3.2\times10^{-20}m^2$, model 3 uses a fitted permeability of $2.6\times10^{-19}m^2$.

The main differences in the Krel curves are twofold,

1. the rapid drop in permeability predicted by sample C is not represented
2. the difference in relative permeability typical boundary condition saturation is approximately a factor of 10.

Summarising this point, the permeability assumed at the boundary as a product of the saturated intrinsic permeability and the relative permeability has a significant influence on the fitting of the experimental results.

The last point considered here in matching the curves is the effect of the boundary conditions on the drying curves. Figure 3-19 presents a model fitting where the suction at the boundary conditions has been reduced slightly. Again a good fit to the experimental results can be derived.

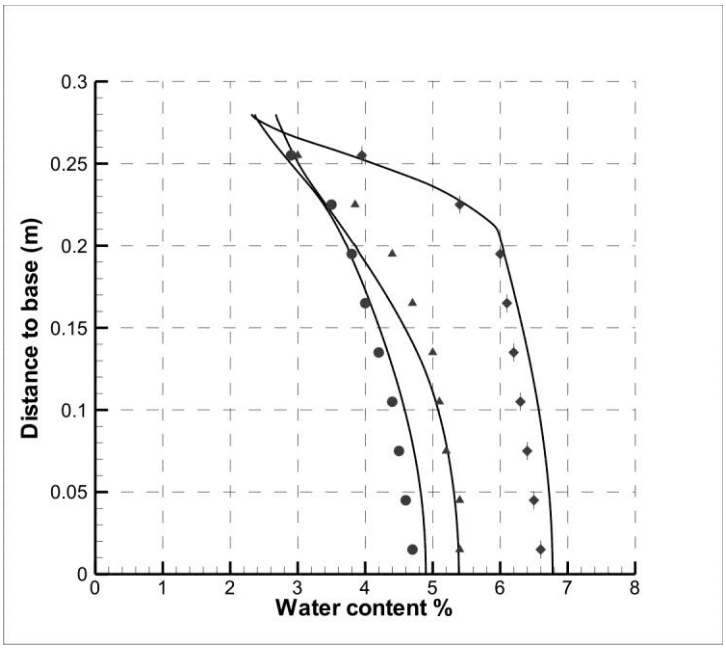

Figure 3-19. $k_{sat} = 2.8\times10^{-20}$.

The mass flux data for two of the fits are presented below, Brooks Corey function from Figure 3-17 and the modified Van Genuchten from Figure 3-18.

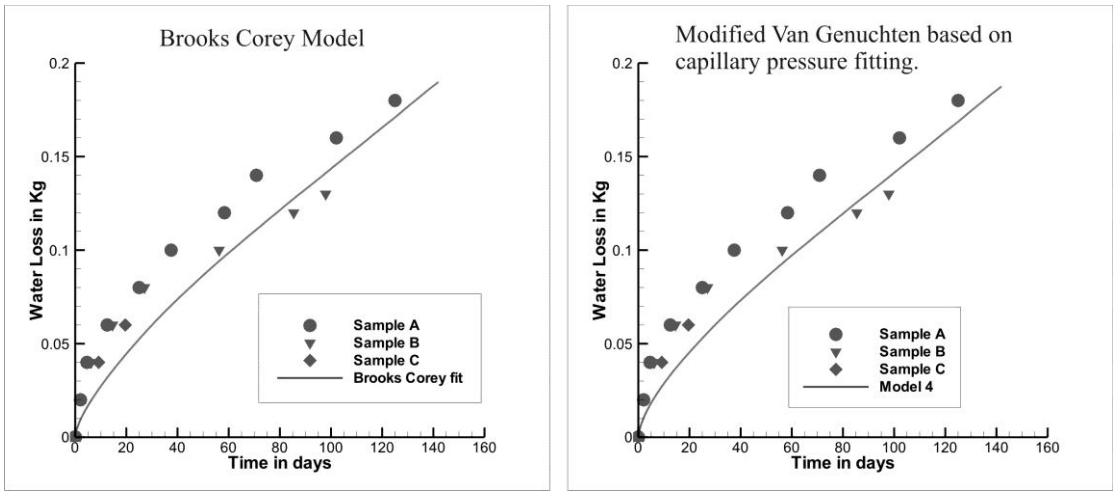

Figure 3-20. Comparison of measured water loss and modelled water loss.

The best fit relative permeability for air was found to be very similar in all models, and is presented in for the Brooks Corey model as an example.

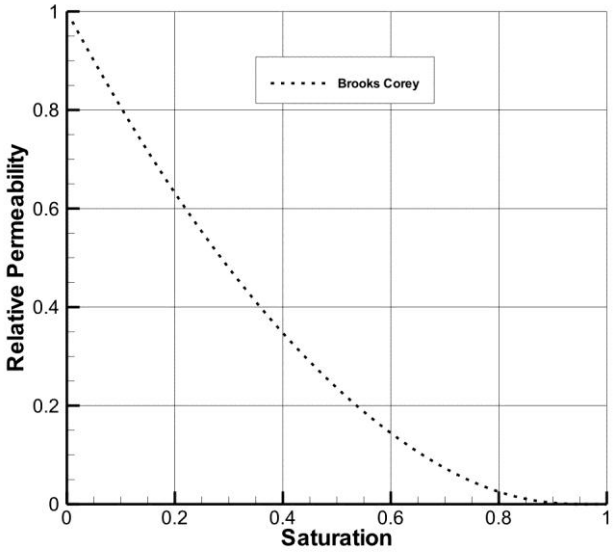

Figure 3-21. Brooks Corey relative permeability for air model.

3.4.3 Discussion of results

A general fitting of all three samples was achieved using a single set of modelling parameters. The exact representation of the individual curves for all samples was not possible using a single set of parameters and suggests that sample heterogeneity may play a role in the differences as well as the usual experimental tolerances to be expected. However because there are little direct data allowing the assumption of sample heterogeneity, hence for the UoE analysis consistent samples have been assumed in this case.

The drying characteristics of the samples where found to be very sensitive to the selection of the relative permeability curve, and no unique solution to the drying problem could be identified, rather a series of good fits depending on the choice of the relative permeability model and the assumption of the initial saturated permeability of the sample. All the model parameters were within the range stipulated in the literature available and noted as having been measured at one time or another for Opalinus clay.

Given the range in parameters available from the literature and noted in the modelling, it is with caution that extra processes, such as chemical osmosis, are to be entered into the consideration of the ventilation experiments. Additional processes may bring more realistic mathematical representation of the processes operating, but may actually not bring an improved prediction of behaviour.

3.5 Comparison of Quintessa and UoE Results

The two models have both been able to replicate the Step 0 results with a good degree of accuracy using similar parameter sets. The key difference between the two models is in the treatment of the upper evaporation boundary condition and the consequent impact on parameter sensitivity adjacent to this upper boundary.

It has been noted that water vapour dominates the water migration processes (see Figure 3-22). Because water vapour migration is not directly sensitive to the intrinsic permeability and relative permeability and water vapour is extremely mobile even at low gas saturations it seems likely that this difference in boundary formulations causes the difference in parameter sensitivity between the two models for the upper boundary.

As a consequence the QPAC model showed no significant sensitivity to the low water saturation relative permeabilities at the upper boundary, while the OpenGeoSys model clearly did show such sensitivities. Either approach would seem to be valid, however it is clear that differences in approach to the treatment of this boundary may have implications in later steps where the specific impact of this boundary may be less clear.

As a further point of context, it was noted across the teams (Garitte *et al.* 2012) that it was possible to change formulation by including and excluding water vapour as an

explicit process, adjusting the relative permeability functions to compensate. The results of Quintessa and UoE were consistent with the parameterisation and physical assumptions of other teams as well as being consistent with each other (Garitte *et al.* 2010).

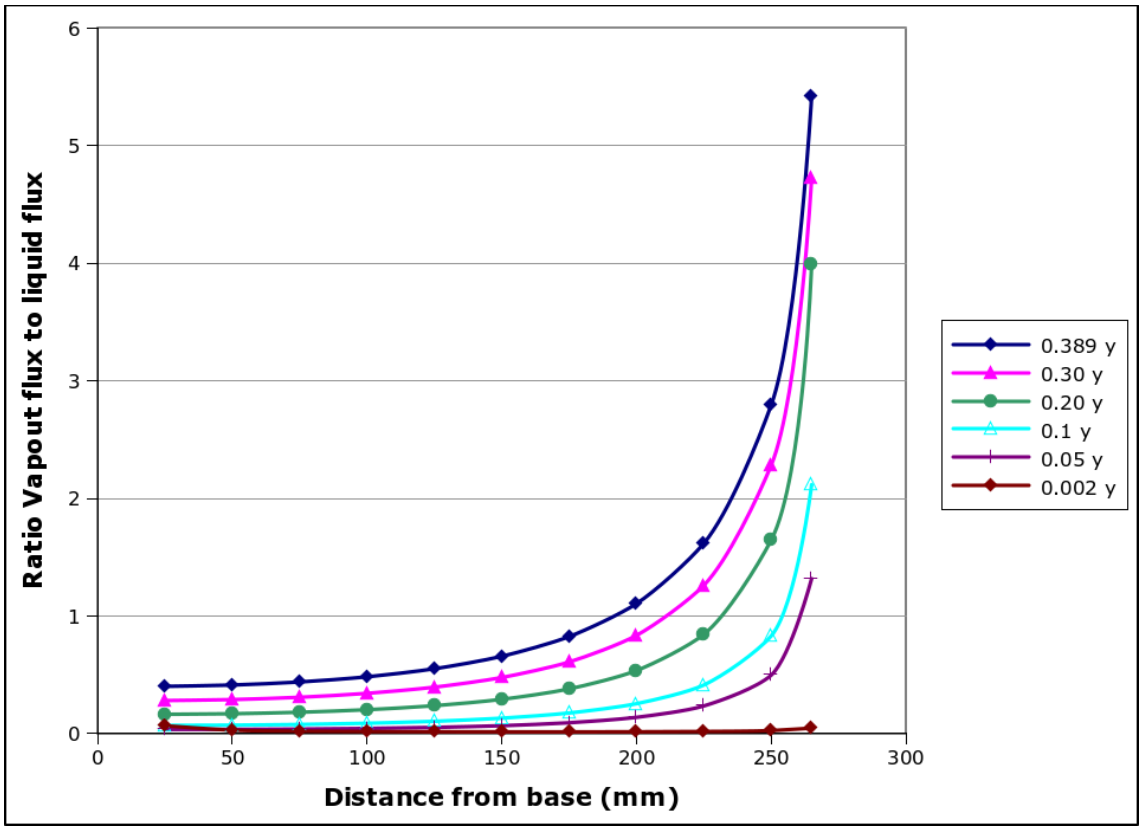

Figure 3-22 Ratio of water vapour flux to liquid water flux with elevation from the base of the sample at different model output times (QPAC best fit case)

4 Step 1: Ventilation Experiment Phase 1

The primary purpose of Step 1 was to provide an opportunity to calibrate initial models to two relatively short periods of wetting and drying (Phase 1) of the VE tunnel in order to:

- Take the processes and parameterisation from Step 0 as an initial model setup – this is also interesting as a laboratory to field upscaling exercise.
- Gain confidence that the models are behaving appropriately as hydraulic-only or hydro-mechanical cases without dealing with the complexity of the full experimental run.
- Calibrate against 'Phase 0', the early period of the tunnel where for approximately 4 years the relative humidity and hence the water drainage from the tunnel is not accurately known.
- Perform some initial conceptual and parameter uncertainty modelling to understand the relative importance of different processes and the degree to which the experimental data is understood conceptually.
- Identify any additional process modelling required to represent the full VE case in Step 2.

This section discusses the reference conceptual model for the Ventilation Experiment, the adopted modelling approach and the results of these initial model builds.

4.1 Data and Conceptual Model

The following data are available for comparison with models in Phase 1:

- relative humidity in the tunnel at two locations, including the input and output relative humidities along with air flow rates through the tunnel;
- pan evaporation time-series data in the tunnel;
- inferred water balance from the tunnel using the above information;
- water contents in three radial borehole cores, one constructed at the end of Phase 0 and the others at the end of Phase 1;
- time-series relative humidities and water pressures in radial boreholes for water unsaturated and saturated conditions respectively;
- partial time series for extensiometers mounted radially between the tunnel wall and approximately 2 m into the host rock;

From this data and the understanding gained during Step 0, the tentative general hydro-mechanical conceptual model for the system during Phase 1 and 2 can be described as follows.

1. A known rate of air with a defined relative humidity is input into the sealed section of the tunnel.
2. Interaction between the water vapour in the tunnel and the unlined tunnel host-rock results in vapour exchange between the tunnel and the host-rock. Evaporation of liquid water from the tunnel surface may also occur depending on local tunnel relative humidity.
3. Water vapour leaves the tunnel via a measurement gauge for relative humidity and air rate. The difference between this and point 1 above constitutes the tunnel water balance.
4. Loss of water from the host-rock to the tunnel as vapour causes a reduction in water pressure and saturation as air invades the formation from the host-rock.
5. The reduction in liquid pressure and relative humidity around the tunnel causes liquid water and water vapour (where present) to migrate towards the tunnel.
6. Desaturation and reduction in fluid pressure causes reduction in pore volume and limited shrinkage of some of the rock skeleton, causing a local net drop in volume of the host-rock.
7. The volume change of the host-rock causes localised stress changes and coupling with the hydraulic evolution through a reduction in porosity, which creates a coupling with fluid pressures and intrinsic permeability.

No significant temperature changes were observed during the experiment, and the modelling teams were instructed to assume that the case was effectively isothermal.

The processes described above are illustrated in Figure 4-1. The dominant processes, and those which have been represented by the modelling teams in DECOVALEX are therefore: vapour diffusion in, and advection by, air in porous media and engineered volumes; viscous dominated multi-phase flow of air and water in porous media; and poro-mechanical deformation of the host-rock.

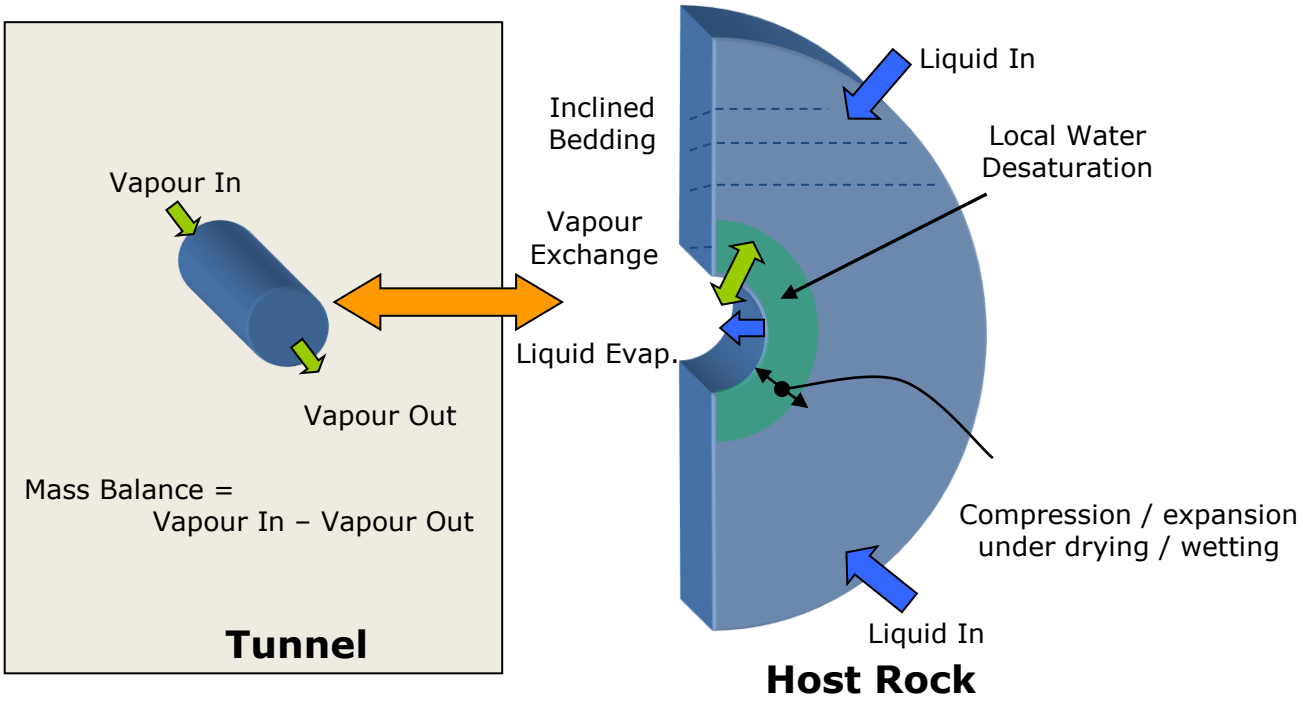

Figure 4-1. Schematic conceptual model of the hydro-mechanical system.

The results of the VE during Phase 1 can be summarised as follows – see Appendix B for more detail

- During Phase 0 (Figure 4-2) uncontrolled drying of the tunnel takes place leading to a zone of moderate water desaturation approximately 25 cm into the tunnel wall. Water pressures are above suction levels at a distance of approximately 1 m radially into the host rock. Within 2 m of the tunnel wall, water pressures reach a maximum of 1 MPa, versus the undisturbed conditions of 1.85 MPa.
- During the 'wetting' portion of Phase 1 (relative humidity in the tunnel raised to 100%), net recharge of the rock occurs, pore pressures are assumed to rise with the consequent observation that net expansion of the rock is observed between the tunnel wall and the end of the extensiometers 2 m radially into the rock. Expansion occurs very shortly or instantaneously after the change in tunnel conditions.
- During the 'drying' portion of Phase 1 (Figure 4-2), net loss of water from the rock occurs with a consequent contraction observed in the extensiometers – again this occurs almost immediately after the change in tunnel conditions. Similarly there are observed drops in saturated water pressure at a distance of 2 m into the rock. Critically these pressure changes occur almost immediately on

the tunnel conditions changing, implying negligible hydraulic diffusion lag between the tunnel and 2 m into the rock. Borehole measurements indicate a significant drop in water content at the end of this drying phase out to approximately 0.5 m from the tunnel wall.

- The data shows little in the way of trend along the tunnel or around the circumference, in other words the case appears to largely respect an inclined 1D cylindrical symmetry.

The overall impression therefore is of significant and very rapid changes in pressure and stress state radially (as witnessed by the extensiometer data), at a significant distance from the tunnel, while the zones of desaturation remain relatively limited in extent.

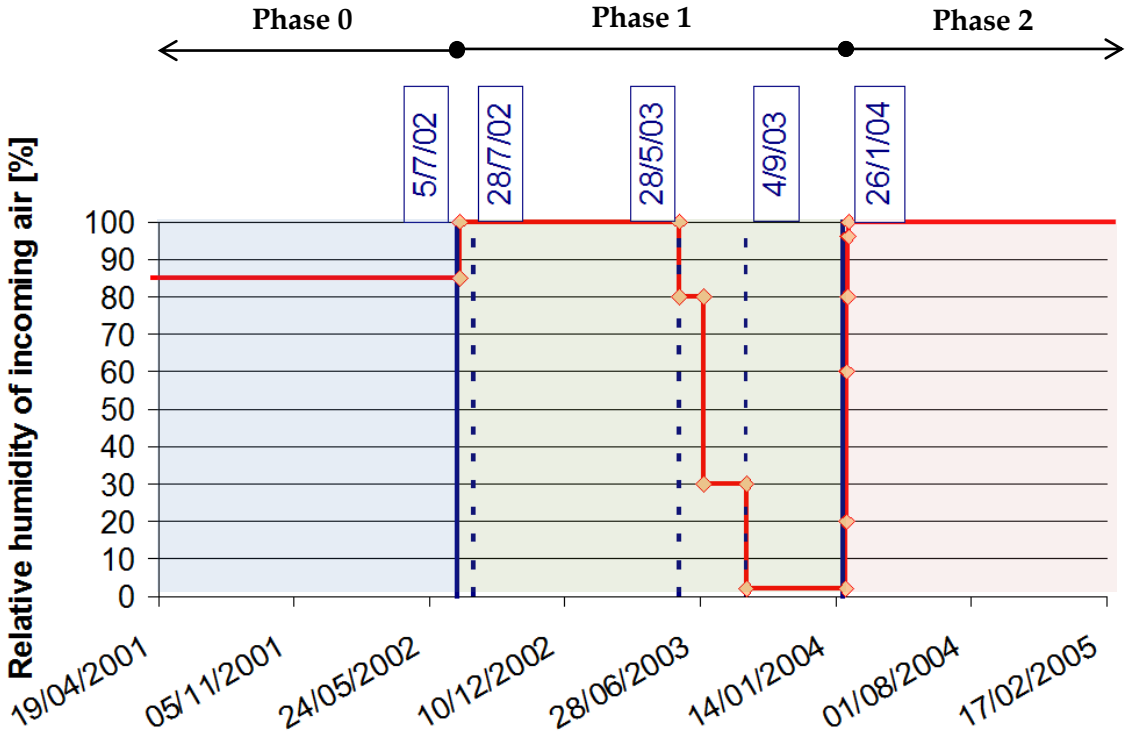

Figure 4-2. Applied relative humidity in the isolated section of the tunnel.

4.2 Modelling Approach

Given the overall objectives of the Step and the excellent agreement between codes for Step 0, it was decided that Quintessa and UoE would coordinate their approaches to ensure that as wide a range as possible of unconstrained approaches and parameterisation could be presented for Task A. It was also recognised that at this point in the project, the UoE PhD student Myles English required some training on

multi-phase flow modelling in general and OpenGeoSys in particular, having only been available from the end of Step 0, hence the approach taken was:

- Quintessa to focus on understanding the coupled hydro-mechanical problem and better methods for representing the complexity of the tunnel boundary condition. Quintessa would aim to provide the main input to Step 1 while UoE allowed their PhD student to become familiar with the case and multi-phase flow modelling in general.
- UoE would build on the Step 0 work to trial different representations of the Opalinus clay system mainly as training for Myles English. It was expected that UoE contribution to this step would be relatively minor, with the main effort directed for Step 2 and 3.

As the UoE Step 1 results were primarily a training exercise and did not substantially contribute to the understanding of the VE, for the sake of brevity they are only discussed in outline.

4.3 Quintessa Step 1 Reference Model

4.3.1 Process Model, Parameterisation and Domain

The QPAC model used the same process model and parameterisation as Step 0 (Section 3.3.4 and Table 3-1) except that thermal component was not used, due to relatively rapid heat transfer by conduction in comparison with the fluid movement, which effectively prevented any thermal variation being seen in the model.

The interpretation of the available data indicated there was very little in the way of structural variation, hence a 2D inclined cylindrical geometry was felt to be appropriate for this initial model. The grid is shown in Figure 4-3, and represented the full 10 m length of the tunnel as a single compartment, with 45 compartments in the radial direction (60 m total) spaced with approximately geometrically increasing radial size starting from 2.5 mm, and 5 equally spaced compartments around a 180 degree vertical symmetry through the centre of the tunnel assumed.

Grid convergence tests were conducted with significantly refined grids, and the above discretisation was found to be sufficiently converged around the tunnel without adding the burden of many more compartments.

Changing this model to 1D or 3D variant was a trivial exercise, allowing for discretisation along the tunnel or in the angular direction around the tunnel with a change to a single line of input. The impacts on the model to such changes were evaluated as part of the sensitivity analysis.

4.3.2 Boundary conditions

The following boundary conditions were applied:

1. Outside Radial Boundary: Zero deviatoric stress, constant hydrostatic fluid pressure, assuming 1.85 MPa at the elevation of the centre of the tunnel.
2. Front and Back (perpendicular to tunnel): Symmetry condition.
3. Angular boundaries (parallel to tunnel): Symmetry condition.
4. Tunnel boundary: Removal of the estimated ambient stress field to represent tunnel construction, 'flux' based boundary condition for liquid water (Equation 3.2).

The relative humidity used was a simple piecewise approximation to the measured tunnel relative humidity (Garitte & Gens, 2008), Appendix B. A best fit for initial conditions (start of Phase 1) was obtained using a relative humidity of 0.7, rather than the 0.85 as originally estimated by Garitte & Gens, (2008). Note that this approach implicitly assumes that the water vapour in the tunnel is well-mixed and that the measured relative humidities are representative of the moisture that the tunnel walls are exposed to.

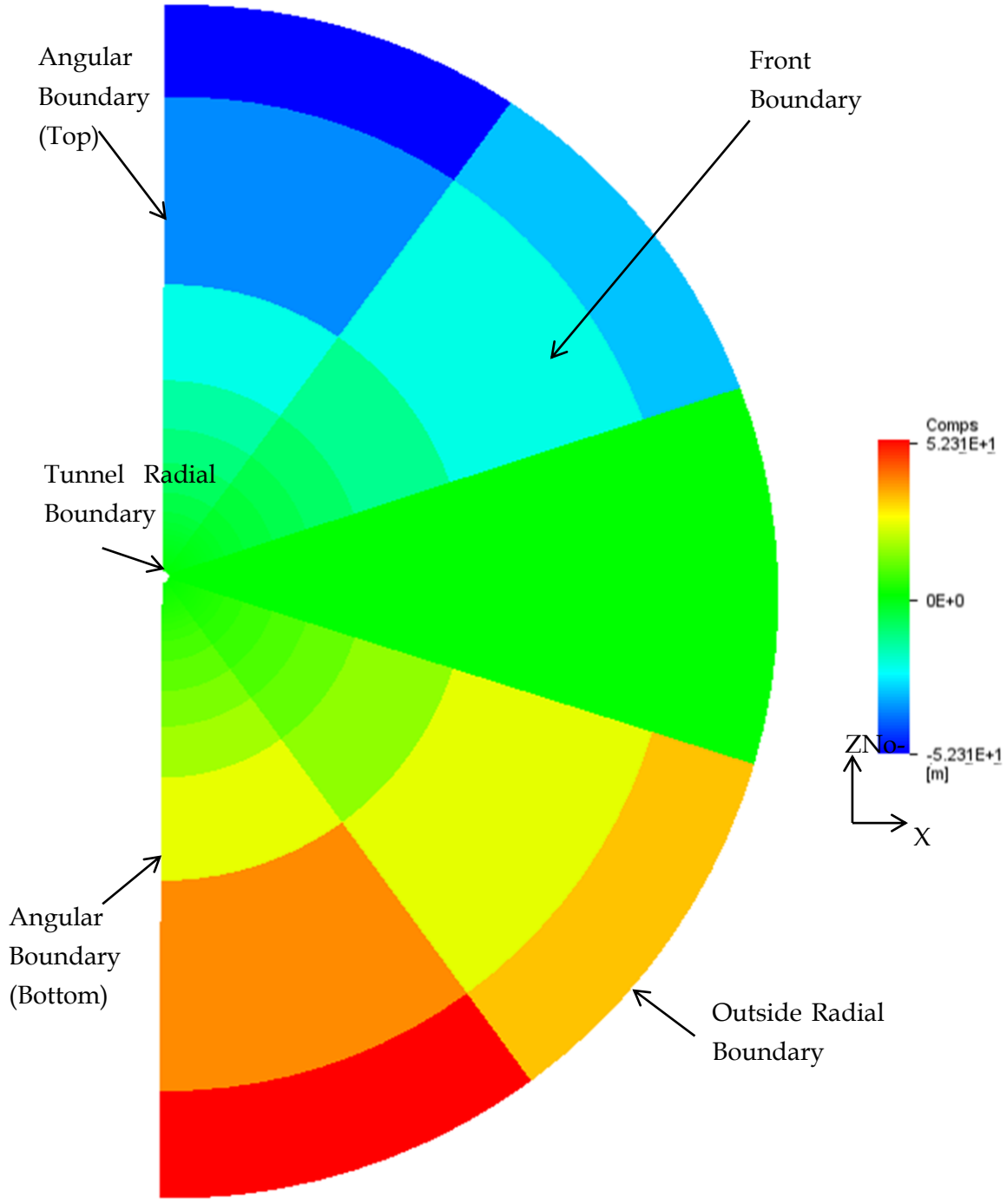

Figure 4-3 Compartmental structure of the model, coloured by elevation to emphasize compartment boundaries - image looks along the axis of the tunnel

4.3.3 Reference Results

The following results are presented as an indication of general performance and not as a result of a detailed calibration exercise. The objective was to provide a general calibration primarily by adjusting the unknown Phase 0 conditions that could be used to identify key uncertainties and provide a basis for a more complete model as part of Step 2. It should be noted that while the 2D model was used for the reference case, very little variation was seen around the angular coordinate, save for hydrostatic water pressure at the outer edges of the model.

4.3.4 Water Balance

A calculated water balance has been provided by the Task A organisers which evaluates the net water loss from the tunnel. For Phase 1 data is only available after the drying phase took place (second half of Phase 1 – see Figure 4-2). Two estimates of the water balance are provided arising from the imbalance in airflow into the tunnel and that which came out through the outflow tunnel – clearly some leakage has occurred. The upper estimate ('Qout=Qin') is probably the most realistic as it assumes the 'lost' air has the same relative humidity as that seen in the outflow pipe, while the lower estimate ('Qout=Qout') assumes this lost air is dry and contains no water vapour. Figure 4-4 shows the results obtained in comparison with the experimental data.

Clearly the QPAC results are a good match for the upper estimate, but arguably the rate of loss is too high at early times.

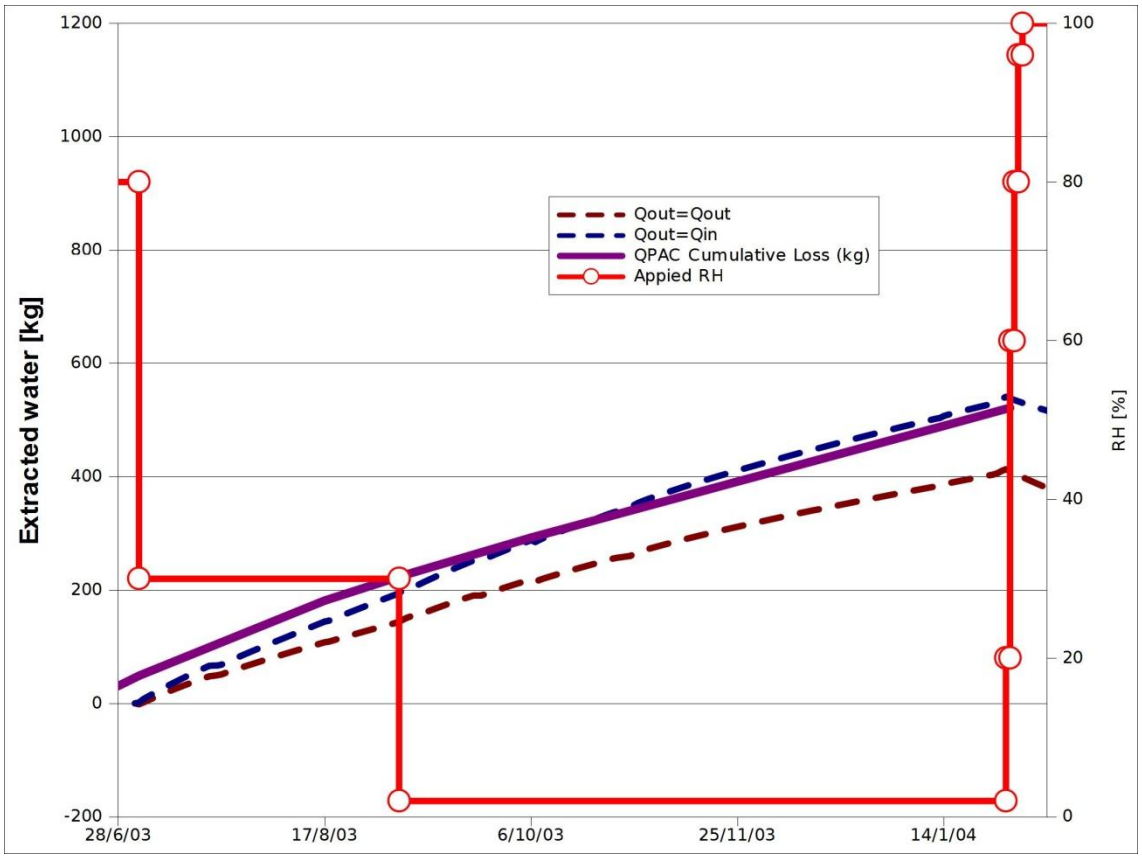

Figure 4-4. Water balance for the second half of Phase 1.

4.3.5 Water Content

Numerous radial boreholes were constructed at different times during the VE for different purposes, three of which were cored during Phase 1 and the water contents measured at different points. BVE82 was constructed at the end of Phase 0 and BVE85 and 86 at the end of Phase 1. Boreholes BVE82 and 85 show a very similar bulk porosity while 86 shows a significantly higher bulk porosity hence the saturated water content for BVE86 is nearly a full percentage point different from the other boreholes. This difference clearly illustrates the variation seen in the Opalinus clay and thus makes close comparison with larger-scale experimental results difficult. The default parameterisation of the model has been setup to lie closer to the porosity shown by BVE82 and 85 (which in turn are very similar to the Step 0 drying test values). The comparison is shown below, the QPAC results should be compared with BVE86. BVE85 and BVE82 are shown for reference (Figure 4-5).

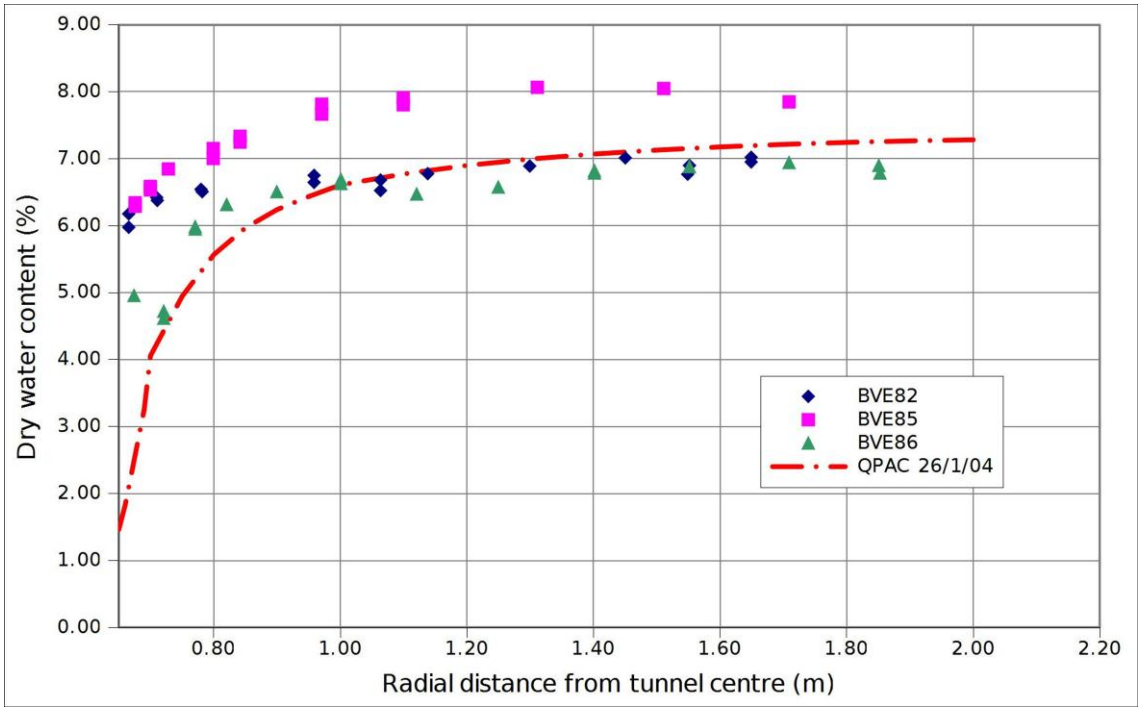

Figure 4-5. Observed and computed water contents for the start and end of Phase 1

The QPAC results bear a good comparison with the experimental results, showing a very similar profile. It is noted that while BVE85 and 86 are offset, a very similar curve shape is seen in both cases which is well reflected by the QPAC results – it appears that the zone of desaturation is being estimated well by the numerical calculations, although arguably drying close to the tunnel is too strong.

4.3.6 Pressure and Relative Humidity

Dynamic measurements of the fluid state were taken using conventional pressure transducers for fully saturated groundwater conditions and using humidity meters in unsaturated conditions. Piezometers and humidity meters were installed in backfilled radial boreholes out to a total distance of approximately 2.7 m (~ 2 m into the tunnel wall). In addition, so-called 'surface' relative humidity meters were installed 2 cm into the tunnel surface and then backfilled behind flush with the tunnel wall using concrete.

Comparison is made between the calculated relative humidities and the experimental data at two points down the tunnel, one close to the air inflow and the other close to the outflow (Figure 4-6). While comparisons away from the tunnel wall seem reasonable, the model predicts significantly lower relative humidities at the tunnel wall. This is consistent with the observations that the water contents close to the tunnel wall seem a little too low, however the relative humidity gradients calculated near the tunnel wall are extremely steep. To get the observed relative humidity using the QPAC model, one only needs to move an additional 1.5 cm into the host rock.

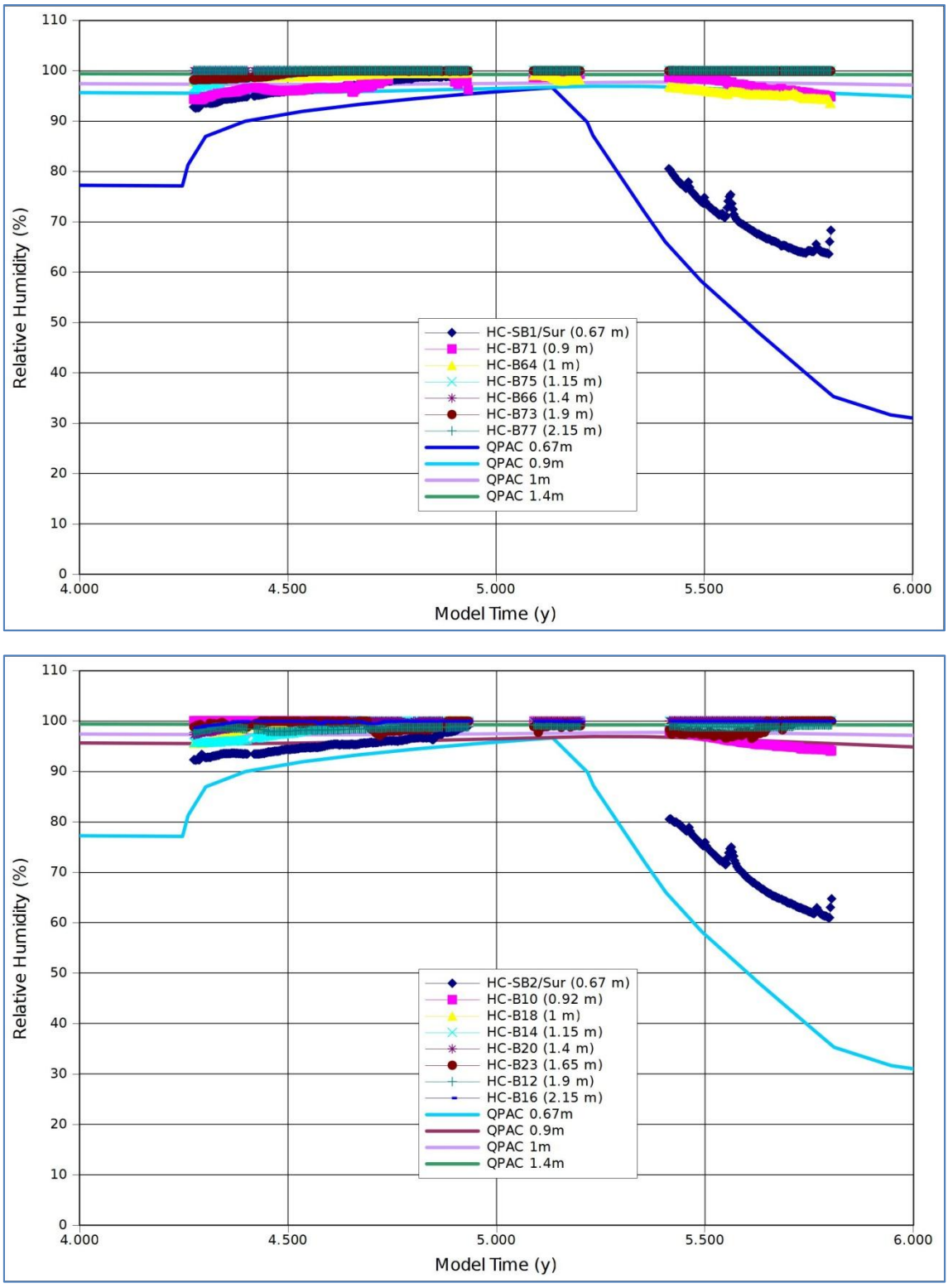

Figure 4-6. Relative humidity, experimental versus computed during Phase 1. The two plots refer to measurements taken close to the air inflow (top) and close to the air outflow (bottom)

This suggests that measurements at the tunnel wall may be susceptible to error caused by the method of installation. If the concrete used to fix the measurement devices in place significantly retards water or vapour migration, it seems quite likely that the relative humidities recorded are too high in comparison with the remainder of the tunnel wall, hence this comparison should perhaps be treated with some caution until the experimental aspects of these surface relative humidity installations can be examined further.

In terms of water pressure, saturated water conditions are only consistently observed at a total radius of 2 m or greater. Figure 4-8 shows the comparison of water pressures (QPAC water pressures are truncated at zero to be consistent with the experimental apparatus). The experimental data show pressures greater than atmospheric from between 2 and 2.8 m radius and greater while the QPAC results give pressures greater than atmospheric at approximately 2 m radius, a little too low.

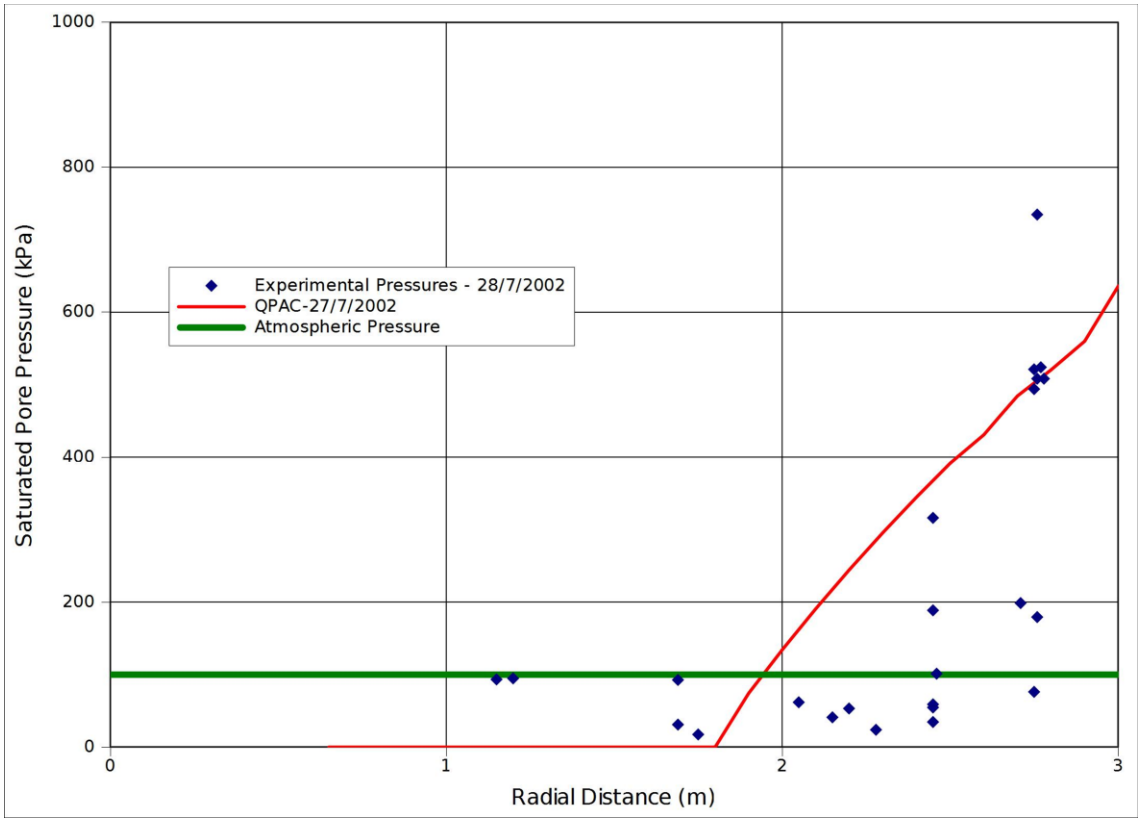

Figure 4-7: Comparison of modelled and experimental pressures at the start of Phase 1

This is a reasonable result, but needs to be put into context with the other results. Given that the water balance for Phase 1 is sensible it suggests that desaturation and pressure drops in general are too focussed around the tunnel in the numerical model in comparison with the experimental data.

However there are complications when considering the transient water pressure data. In Figure 4-8 it is quite clear that upon entering the drying phase that an immediate pressure response is seen at a radius of 2 m. The QPAC numerical results show no rapid response, just a slow decrease in pressure due to the general drawdown caused by the ventilation (not shown on the figure) because the hydraulic diffusivity of the system is such that any pressure response should take months or years to migrate through the system to this radius (and the model does indeed show this when run over long periods). This means that either this pressure response is a function of a rapid process not represented in the model, for example as a result of some kind of poro-mechanical effect, or the borehole itself is acting to transmit pressure and affect the results.

Also there is an initial response after installation (early times) showing a sudden rise in water pressure up to an equilibrium value. This is probably just a settling effect, but it illustrates the borehole construction has significantly perturbed the system at least locally, and the local borehole hydraulic systems may not be in equilibrium as the system is stressed.

It would appear that the experimental water pressures are questionable at the present level of system understanding and should be treated with a great deal of caution as they are clearly inconsistent with the simple Step 0 and 1 conceptual model.

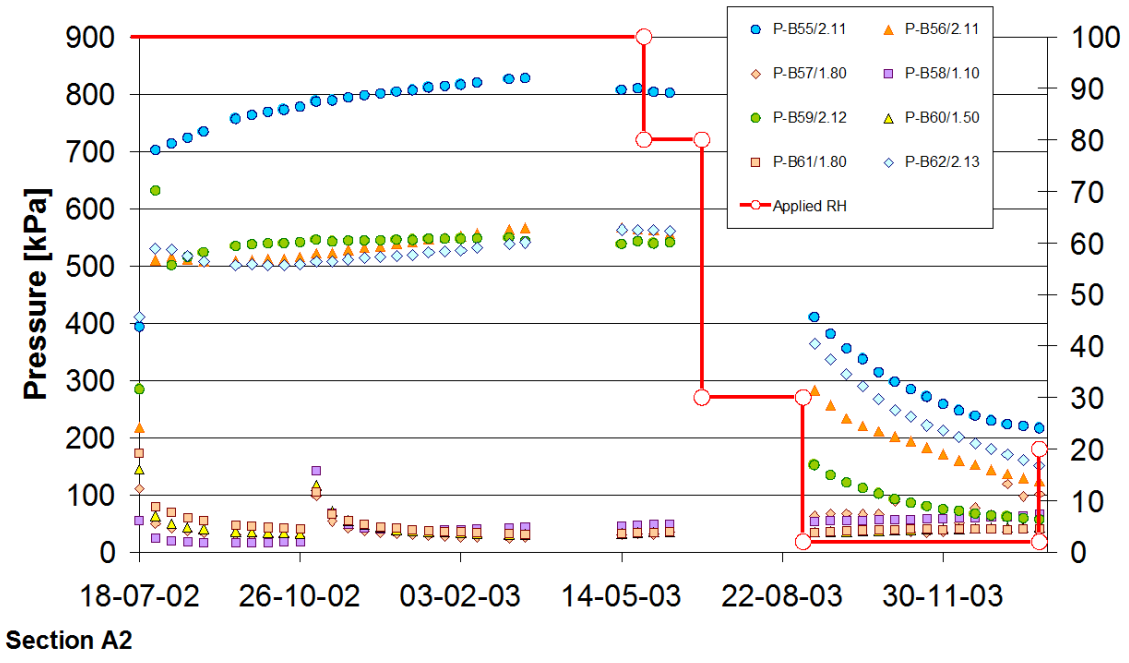

Figure 4-8. Saturated water pressures (> 1 atm pressure) measured at section A2 in the micro tunnel at depths of 1.5 to 2.12 m from the tunnel wall (see legend) during Phase 1. From Gens and Garitte (2008). Also shown in Figure B10.

4.3.7 Relative Displacements

Relative displacements between the tunnel wall and notionally 'fixed' point 2 m radially into the rock mass are calculated through the poro-elastic mechanical model. These displacements arise from pore pressure changes in the clay and are conceptualised to be elastic and reversible, consistent with standard approaches in soil mechanics. It is an interesting observation that according to poro-elastic theory that it is not the tunnel wall that undergoes displacement with the inner end of the borehole being 'fixed' (Carranza-Torres and Zhao, 2009). Rather, the impact of the pore pressures is to redistribute stresses in the tunnel wall such that the displacements occur in the wall rock, while the tunnel wall itself does not move. Hence in all these cases it is in fact the end point of the borehole, and attached extensiometer, that should move. The QPAC mechanical module accurately reflects such behaviour. However, should any of the deformation be plastic, as might arise from weakened rock associated with any EDZ, then the tunnel wall can then move. Such an observation may give an insight into the correct conceptual model for the mechanical processes in this case.

The experimental results show quite considerable variation depending on the borehole being examined, although the variation does not appear to be systematic. We compare the QPAC relative displacements versus the range of reliable extensiometer measurements available (Figure 4-9). For simplicity we plot only the horizontal radial displacement as there was little or no variation depending on the angular orientation.

The QPAC results clearly match the form of behaviour observed, although the magnitudes are a little small. Given that the model is parameterised using a relatively small value of Young's modulus for intact Opalinus Clay, this suggests that EDZ effects may be important, reducing the stiffness of the clay over at least part of the volume of interest. Alternatively it may suggest some alternative modes of deformation may be taking place. In any event, the mechanical model requires some additional investigation.

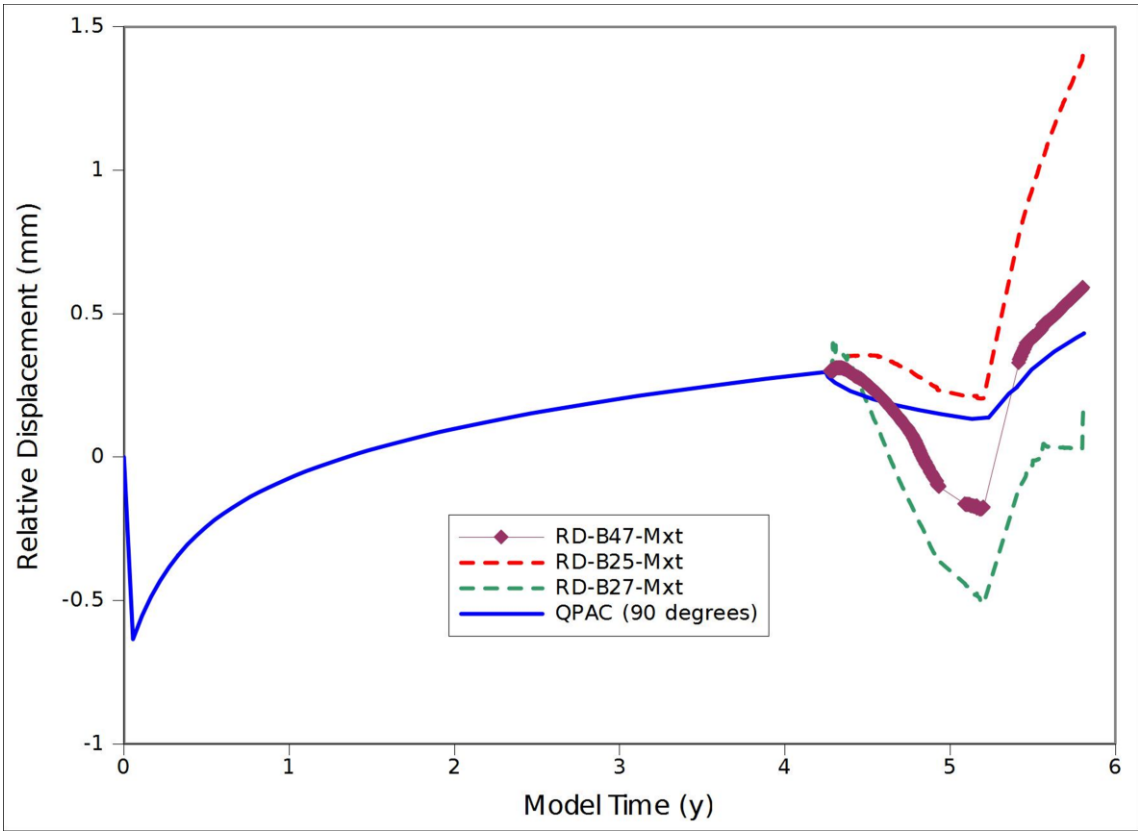

Figure 4-9. Relative displacements compared between the experimental data and QPAC results. Time is in years since model start.

4.4 Sensitivity Analyses

The following sensitivity analyses were conducted, and their impacts discussed briefly in the following sections:

- Phase 0 tunnel relative humidity.
- Opalinus Clay intrinsic permeability.
- Water vapour diffusivity.
- Subsuming vapour transport into the liquid water flow model.
- Young's Modulus for the Opalinus Clay.

It is noted that the specification of Task A suggests that the possible implications of the EDZ, anisotropy and heterogeneity be examined as there are clearly geological features that would suggest such behaviour. However, given there is little evidence from the hydraulic and mechanical data to reinforce such variation, and there are no clear deviations to compare against, it seemed more prudent to try and obtain a baseline understanding without unnecessary complexity. Such features may become important

when considering the possible impacts of boreholes and other engineering structures in Step 2.

Sensitivity analyses were conducted using a slightly simplified version of the full model, in that the angular discretisation was reduced to a single compartment, turning this case into a true 1D cylindrical geometry. The reference results showed that the gravitational component has a negligible impact on the results, hence sensitivity calculations could be performed much faster (~2 minutes per run) without invalidating the results.

4.4.1 Phase 0 Tunnel Relative Humidity

The tunnel relative humidity during Phase 0 were set to 0.6 and 0.85 respectively in two separate sensitivity runs, compared to 0.7 in the reference case.

Reducing the Phase 0 relative humidity to 0.6 has a number of marked impacts on the results:

- Water contents are reduced slightly close to the tunnel wall (~10% drop)
- Total water loss from the tunnel during Phase 1 is reduced by approximately 10%, this is because there is less water close to the tunnel wall when drying does take place in Phase 1.
- Water pressures are reduced close to the tunnel wall (-41 MPa versus –65 MPa at the end of Phase 0) and the distance at which 1 atmosphere water pressure occurs increases slightly from approximately 2 m to 2.05 m
- Relative displacements during the initial wetting portion of Phase 1 are significantly increased (factor of ~1.5) presumably because disproportionately higher suctions (and hence much lower pore pressures) have been developed close to the tunnel wall, which are then available for release once wetting takes place.

Increasing the Phase 0 relative humidity to 0.85 has almost exactly the opposite effect to a similar magnitude. In both cases the major observable change versus the available data is in the Phase 1 water balance and the change in the early relative displacements. Neither of these sensitivity cases significantly improved the comparison with the available data.

4.4.2 Intrinsic Permeability

For these sensitivity cases the reference intrinsic permeability was varied between 0.5 and 2 times the reference case value. Scaling values of 0.5, 0.75, 1.25, 1.5 and 2 were run. The results can be summarised as follows:

- Significant effects were seen mainly on the calculated water balance, with second-order impacts seen in the water contents and water pressures.
- Increasing the reference intrinsic permeability by a factor of two leads to a 20% increase in total water loss from the system by the end of Phase 1, while reducing the intrinsic permeability by a factor of two gives approximately 10% reduction in water loss. The reduction in permeability is just about acceptable in terms of a calibration, but the factor of two increase gives rise to a net water loss that is too far away from the available data.
- Impacts on water pressure (and implicitly relative humidity) and water contents are sufficiently minor and tend to be distributed across the whole zone of interest, hence they do not to significantly impact the loose calibration already conducted.
- The radius at which water pressure reach atmospheric do vary significantly across the range of intrinsic permeabilities tested, being at 1.7 m from the tunnel centre at the lowest intrinsic permeability and up to 2.3 m at the highest. These values bracket the reference case (as is to be expected) with the reference case and highest permeability results being closest to the experimental data.

4.4.3 Water vapour diffusivity

Water vapour diffusivity was changed from 2.5e-6 $m^2\ s^{-1}$ to 1e-5 $m^2\ s^{-1}$, 5e-6 $m^2\ s^{-1}$ and 1e-6 $m^2\ s^{-1}$. The covers a reasonable range of potential effective vapour diffusivities given uncertainty in the pore system tortuosity (effectively a value of 5 for the reference case). Results were analogous to the equivalent changes in intrinsic permeability with significant changes to the water balance observed, but only relatively minor and distributed changes to water contents and water pressures. Doubling the diffusivity led to an increase in water loss of approximately 20%, while a halving of diffusivity gave a reduction in by approximately 10%. Water pressures were largely unchanged in contrast, with the atmospheric pressure contour remaining at approximately 2 m from the tunnel centre in all cases for the end of Phase 0. In terms of the calculated water contents, changes were similarly small, although arguably the lower diffusivity case gave rise to a water content distribution that was slightly flatter at the end of Phase 0 and slightly more consistent with the available data.

4.4.4 Subsuming water vapour representation

Sensitivity tests turning the vapour transport on and off (using the calibrated Step 0 parameterisation used by UoE) showed very similar results except for two issues:

- Water contents close to the wall don't drop as much (4% minimum), but this also means that the relative humidities don't get as low as observed. This

indicated that the water contents are not consistent with the measured suctions (and vice versa), hence it was considered prudent to revisit the water retention curves during Step 2.

- The pressure fronts do move further into the saturated rock mass, but still don't show the variation seen in the borehole data.

4.4.5 Young's Modulus

Young's modulus for the Opalinus clay was varied from 2.5 GPa to 10 and 1 GPa in order to understand its sensitivity to the scale of mechanical deformation and any impacts on the hydro-mechanical coupling. The range reflects the fullest possible range of experimental values as discussed in Bock (2001).

As one would expect the major impact is on the degree of expansion and contraction observed as the pore pressures changes, with a 1 GPa Young's modulus increasing the deformation to a level more consistent with the experimental observations. In contrast a value of 10 GPa virtually eliminated any significant deformation during Phase 1.

Interestingly there was a small effect on the hydraulic behaviour due to these changes. Total water losses for Phase 1 altered by approximately 5 % across this sensitivity analysis, primarily through the intrinsic permeability changes caused by the construction of the tunnel in the first instance. Reducing the Young's modulus allows for greater deformation of the rock mass and hence a larger rise in net porosity (and hence permeability using Kozensky's model – see Table 3-1) as the tunnel walls converge post-construction and start to drain. Thus, using this simple elastic model decreasing Young's modulus tends to increase permeability close to the tunnel and hence increase drainage. The effect in comparison with other parameter uncertainty is quite small.

4.5 Summary Comments

The Step 1 QPAC model a relatively simple hydro-mechanical model designed to investigate the degree of complexity that is reasonable to expect in a 'final' implementation. The bulk fluid results and the generalities of the displacements seem to match the system reasonably well, although perhaps the model is a little too dry adjacent to the tunnel, at the expense of having too much water at a greater radial distance. Given that the model is using the Step 0 parameterisation, with only minor adjustment to account for the unknown boundary conditions during Phase 0, the results are surprisingly good and the results largely robust to parametric uncertainty.

Some details of behaviour notably the spatial variability in the displacement response and the measured very fast fluid responses cannot be replicated with the current

process set. Indeed the conceptual model for the system does not account for such rapid variations, hence the numerical model cannot be expected address them.

While it is tempting to take the fluid pressure measurements at face value, however there are some anomalies that makes them questionable and hence in need of some interpretation.

1. The initial response after installation shows a sudden rise in water pressure up to an equilibrium value. This is probably just a settling effect, but it illustrates the borehole construction has significantly perturbed the system at least locally.

2. The pressure response to the drying signal is very similar to that of the mechanical deformation, i.e. there is a sudden drop in pressure once the relative humidity drops below 0.85. Given the low hydraulic diffusivity of the system, this seems to be more likely to be a mechanical effect than a purely hydraulic effect. The model and hand calculations would suggest that such pressure drops to hydraulic only processes would be confined to within 50 cm of the tunnel wall during Phase 1, not out to 1.5 m.

It seems possible therefore that the boreholes are significantly influencing the measurements. It implies either some sort of hydraulic bypass (e.g. a leak) or some mechanical effect enhanced by the presence of the borehole. Further consideration of these issues were held over until Step 2 where a coordinated response amongst the teams could be developed.

Further calibration of the Step 1 QPAC model was not attempted because it was recognised that in order to satisfy the requirements of Step 2, major additions to the model would be required for the predictive calculations. To this end, the Step 1 model was halted and development started on the upgraded model (Section 5)

4.6 University of Edinburgh Step 1 Modelling

The following sections describe the progress made towards the Step 1 model using OpenGeoSys. Due to the use of this Step as a training exercise for the UoE PhD student, they are presented in outline only.

4.6.1 Model Geometry

The VE was assumed to be symmetrical about a vertical plane through the tunnel's axis and so only half the domain needed to be considered. For this work, the boundary condition at the tunnel wall was calculated from the sensor data (Figure 4-10) in the tunnel rather than the relative humidity of the air tunnel input in order to make it consistent with the use a 2D model. In this sense the tunnel has been excluded from the model and is represented solely as a boundary condition.

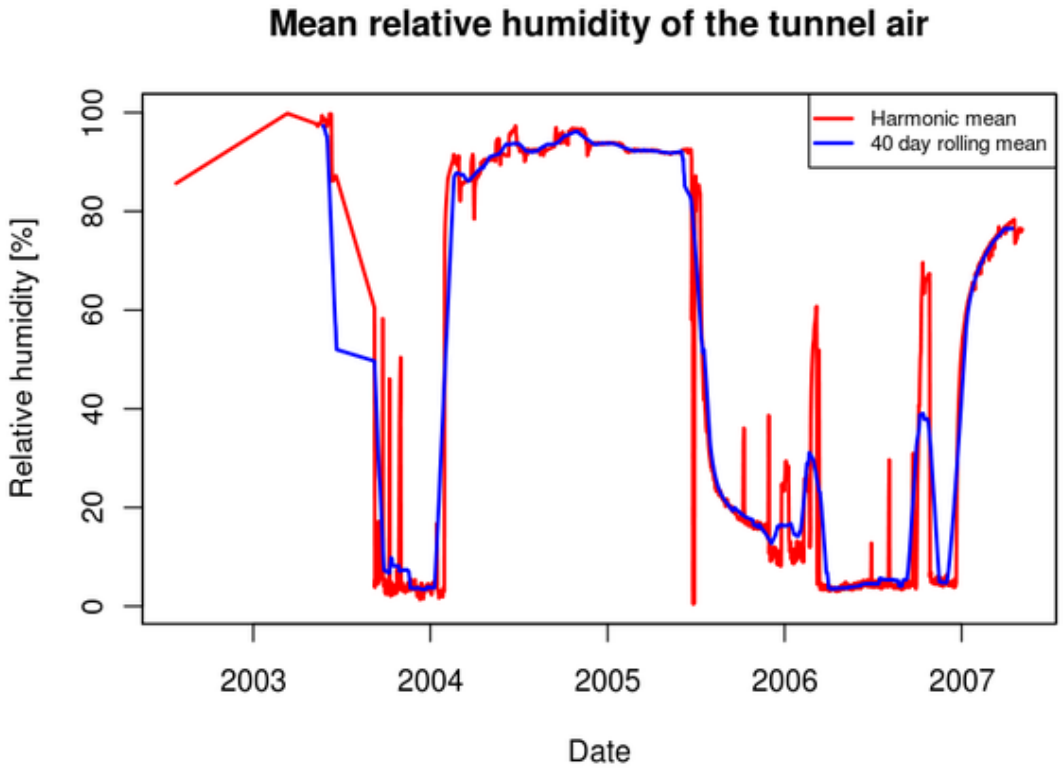

Figure 4-10: Applied relative humidity boundary.

At this stage UoE had two models in use, differing mainly in their spatial extent from the tunnel. The small model was semi-circular encompassing a 4m radius from the tunnel wall (Figure 4-11) while the large model was rectangular, 65 m wide by 120 m tall (Figure 4-12). The large mesh was comprised of 4146 nodes making 7932 elements with increasing mesh refinement towards the tunnel (Figure 4-13).

The lengthy runtime of the larger model (discussed later) meant that a complete Phase 0-1 run was not possible, but it was recognised that the smaller model suffered from boundary effects, limiting the utility of both these results. The model results were sufficient to allow a qualitative overview of the behaviour of the system to be gained, but not encourage detailed cross-comparison with the experimental data – this would be developed in Step 2.

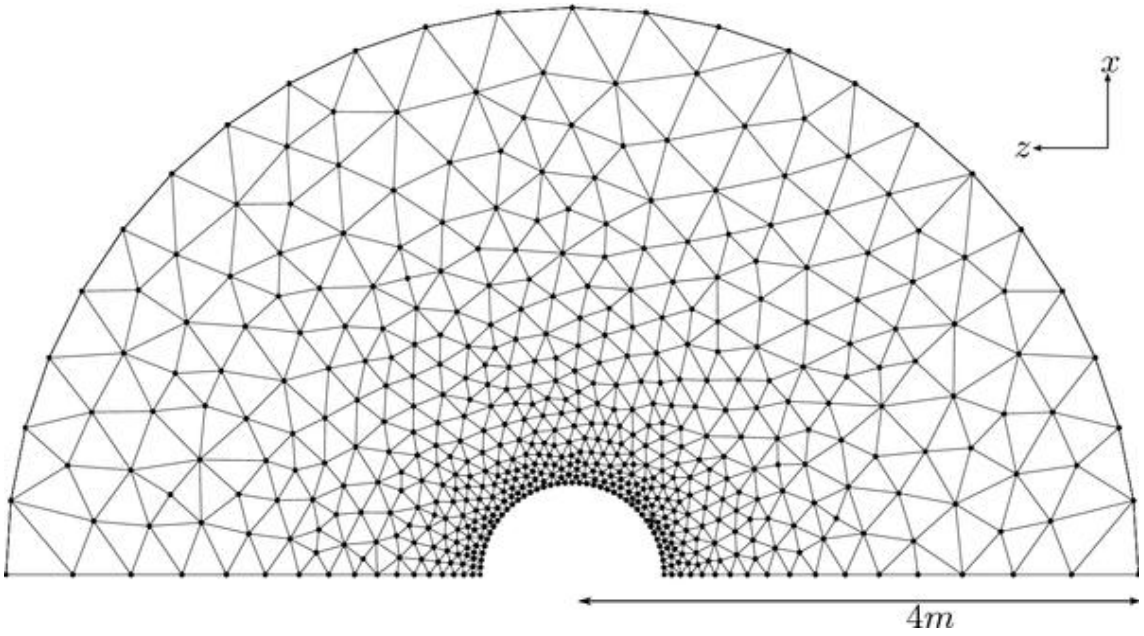

Figure 4-11. Test mesh of 4m radius

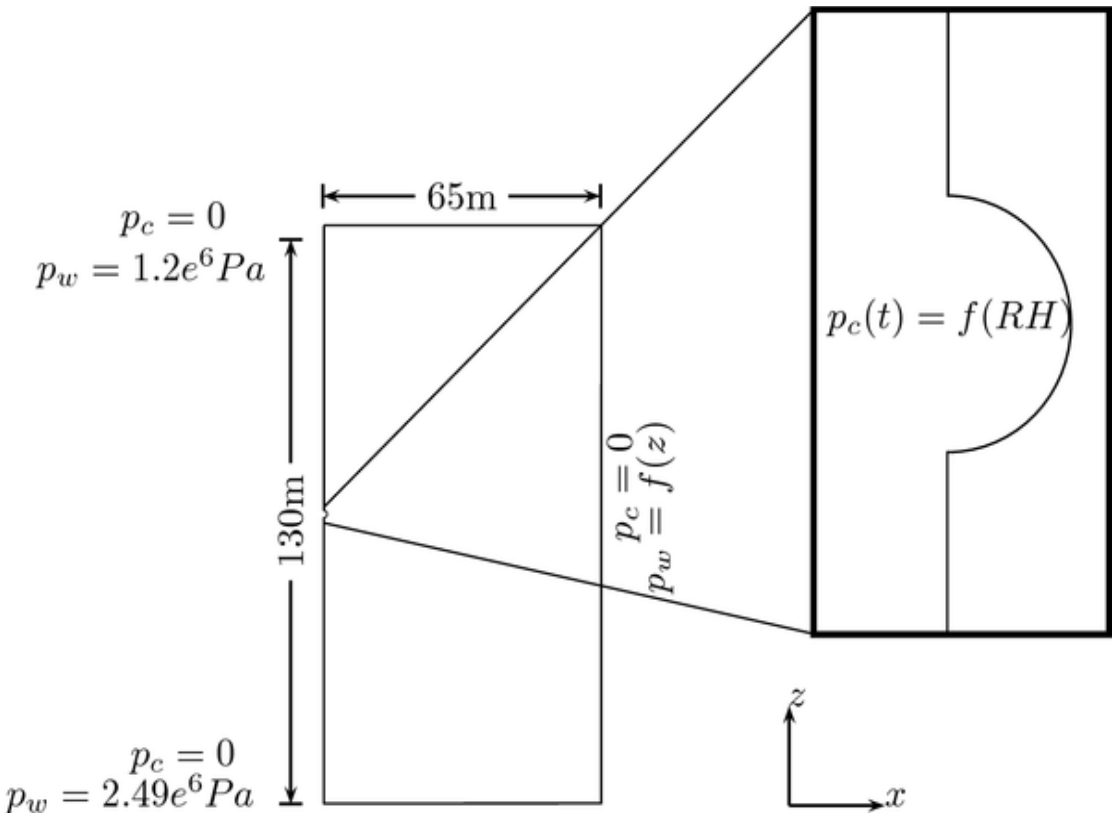

Figure 4-12. Model domain and boundary conditions

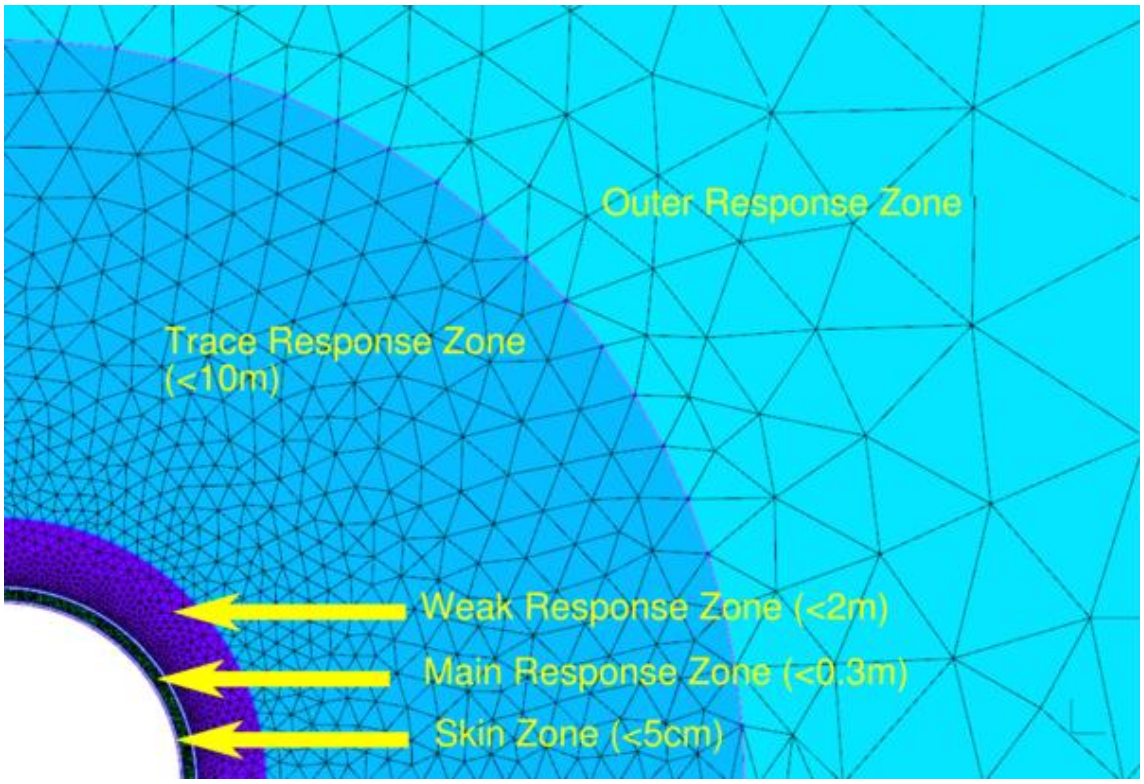

Figure 4-13. Detail showing zones of mesh refinement. (Zone thickness in brackets).

4.6.2 Parameterisation

The clay is initially saturated with respect to water, so capillary pressure is set to zero, water pressure is hydrostatic ($p_w = \rho_w \times g \times$ depth) and the gas pressure is assigned to effect this. The fluid properties remain the same as for Step 0 and the parameters for Opalinus Clay arrived at in Step 0 are also used utilising the reference relative permeability and capillary curves of Munoz *et al.* (2003) and Section 3.4.2.

4.6.3 Boundary Conditions

The only time varying boundary condition is at the tunnel wall. The relative humidity (RH) at the tunnel wall is calculated by the rolling mean of representative sensors (Figure 5.1) and this is converted into capillary pressure by (after Muñoz *et al.*, 2003):

$$p_c = ln(RH) \cdot \rho_w \frac{RT}{M_w}. \qquad 4.1$$

where ρ_w is the density of the water at 20°C, R is the universal gas constant, T is the thermodynamic temperature, Mw is the molar mass of water. This is equivalent to the 'pressure' condition given in Section 3.3.3. A relative humidity of 0.85 is assumed during Phase 0.

4.6.4 Issues

Parallel Processing

As programmed, the implementation of the monolithic pressure-pressure scheme for multiphase flow in OGS runs on one computer processing core. The runtime for this model with the full domain, on normal hardware, was approximately 18 days and is too long for practical sensitivity analysis as originally planned. By using domain decomposition the problem may be split up into several subdomains and each run on a separate core for the assembly and solving stages of the program execution. A parallel implementation of this scheme was tested for Step 1, however it is clear that a good parallel preconditioner for the solver is needed. PETSc is an Open Source collection of solvers and preconditioners and can provide the needed functionality and work was carried forward to Step 2 to access these tools from OGS.

Time Stepping

Specifying the time step lengths explicitly for this model is not satisfactory in OGS because if one step fails to converge then the absolute time is thrown off by the length of that timestep. An automatic time stepping scheme is used and for the most part works well in choosing the longest time step length that is likely to converge. Where the tunnel boundary condition changes rapidly however, an over-optimistic value for the time step is chosen and much (real) time is wasted while successively smaller intervals are tested (Figure 4-14).

An efficient automatic time stepping scheme could reduce the excessive runtime considerably and was taken forward as a focus of development for Step 2.

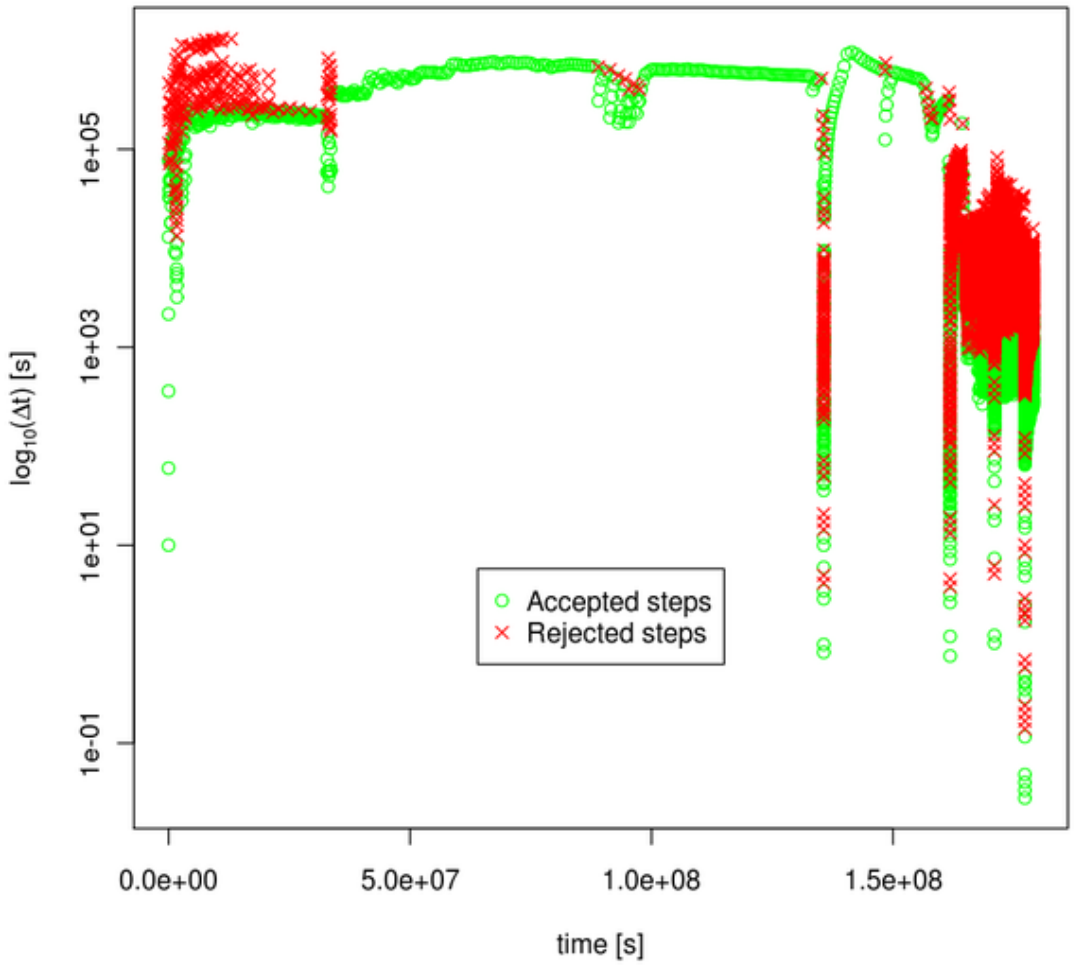

Figure 4-14. Time stepping scheme inefficiency shown by the high incidence of non-convergence ('Rejected steps') during periods of changing conditions.

4.6.5 Representation of the Tunnel

In order to examine the feasibility of including a better representation of the tunnel in the model, some experimentation has been done with a 3D slice using tetrahedral elements to allow discretisation along the tunnel axis. This lead to poorly shaped elements distal to the tunnel where the slice is thin and the other two dimensions of the elements are large. If the slice was thicker there would be many more elements along the tunnel wall, because the mesh is finer there, leading to long run times

Investigation was planned for Step 2 in the use of prismatic elements which would make the refinement more stable and reduce run-times. Also following the Quintessa work where the impact of gravity on the main results was found to be negligible in the

QPAC 2D model and largely indistinguishable from a simpler 1D model (Section 4.3), consideration was given to implementing this case as a 1D cylindrical model for rapid parameter and process investigation for Step 2.

4.6.6 Mechanical Processes

Following the initial QPAC results, no mechanical processes have been modelled as the coupling to the main hydraulic problem is relatively weak, hence for the purposes of training it was decided that it would be more efficient to focus on hydraulic only processes at this stage. It should be noted that poro-elastic processes have been implemented as part of the scheme in OpenGeoSys and was not expected to be difficult include as part of Step 2, however in the context of training and the work of other teams it was not considered to be a priority.

4.7 Main Results

Even though the smaller test model has had had limited calibration and hence cannot be used for accurate quantitative use it succeeds in reproducing the general responses of the hydraulic system around the VE. For example, Figure 4-15 shows that the shape of the relative humidity predicted by the model over time correlates fairly well with HC-SB2 while water content in the rock at the start of Phase 1, shown in Figure 4-16, is slightly underestimated.

4.8 Summary Comments

Two initial models were developed by UoE of the VE for Step 1. The models, while limited through run-time and boundary condition issues, fulfilled the requirement for training of the UoE PhD student. Furthermore, the initial results were encouraging in that they reproduced the broad features of the VE system during Phase 1.

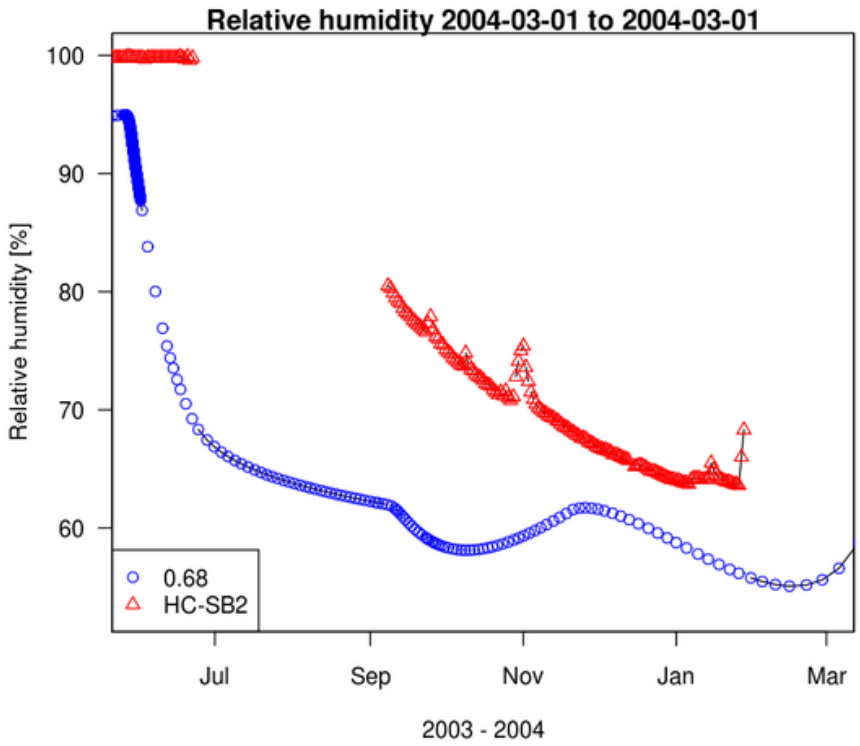

Figure 4-15. Predicted model relative humidity compared with HC-SB2.

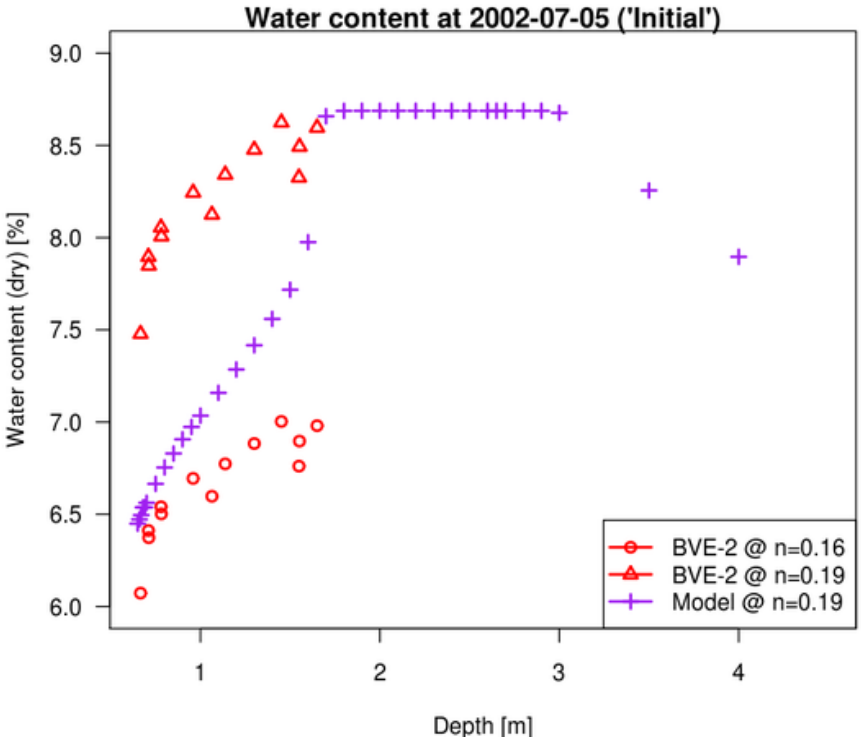

Figure 4-16. Water content before the VE (n is porosity).

5 Step 2: 'Advanced' Hydro-Mechanical Modelling

5.1 Objectives and Issues

For Step 2 teams were given only a small amount of additional data; comprising only air inflow and applied relative humidity data for the tunnel for Phase 1 and 2; and asked to model the remainder of the experiment (Phase 2) without reference to the field observations during this period (Appendix B), i.e. the true experimental boundary conditions on the tunnel. This restriction in data was intended to reflect that during the operation of an open clay tunnel, the air flow rate and input relative humidity would be known by the site operator, but the hydraulic response in the tunnel would not. The primary problem this created was that the tunnel wall boundary condition used during Step 1 relies on the measured tunnel relative humidities at the tunnel wall or in the tunnel as bulk (dependent on approach), and this information was not initially supplied.

Three general solutions to the problem were considered as part of general task discussions:

1. An empirical approach using Phase 1 data to relate applied relative humidity to observed humidities in the tunnel.
2. A simplified model of the tunnel system considering only the water vapour mass balance, allowing tunnel relative humidities to be calculated dynamically as part of the model solve.
3. A full continuum fluid dynamics (CFD) approach where air movement and water vapour migration in the tunnel are calculated explicitly and coupled to the porous media calculations.

Recognising the potential difficulty for some modelling teams in extending their codes to cover the additional processes required for options 2 and 3, the organisers made available just the observed tunnel relative humidities to allow progress while developments were made, which also enabled the mass balance to be calculated for Phase 2. However taking the data early was optional, and the Quintessa team did not take the data until much later in Step 2 (April 2010) as a partial check of the accuracy of the prediction. Observations in the host-rock were held back until November 2011 where the accuracy of those teams who made predictions could be assessed.

In addition to predictions for Phase 2, teams were to investigate any additional uncertainties or sensitivities they felt worthy of investigation primarily using Phase 1

data including, but not limited to; anisotropy; heterogeneity; EDZ effects; boundary conditions etc.

It should be noted that due to the complexity and many different avenues for investigation for Step 2, that this task continued until the end of the project in parallel with Step 3 and 4, rather than halting in 2010 as originally envisaged (Figure 2-4).

5.2 Modelling Approach

Quintessa and UoE chose to take two differing but complementary approaches to Step 2.

Using the existing QPAC model Quintessa would attempt to construct an abstracted representation of the tunnel such that the true experimental boundary conditions of the system could be represented, perform a full calibration against Phase 1 data and make predictions on the evolution of the system during Phase 2. Various sensitivity and uncertainty investigations would be conducted during this period.

Recognising that a great deal of overlapping work had already been conducted amongst the team members of Task A, a decision was taken by UoE that for Steps 2 and 3 they would attempt to construct the simplest possible model of the hydro-mechanical tunnel system using OpenGeoSys that could reproduce the observations. The intention here would be to demonstrate the minimum complexity model one could sensibly apply to such a system – an area not directly investigated by other teams. UoE would also attempt to develop a simplified tunnel model to enable predictive analysis, however this would be an extended process recognising that this was a relatively more difficult task to accomplish on OpenGeoSys than in QPAC.

5.3 Quintessa Step 2 Analysis

5.3.1 QPAC Tunnel Model

The QPAC implementation developed the existing Step 1 model and utilised an additional sub-system to represent the tunnel. The two sub-systems would then be linked hydraulically via evaporation and vapour diffusion to create a single fully coupled model. Given that the Step 1 model showed no major variation in the angular direction, the reference host-rock model was simplified to a 1D cylindrical geometry with a notional axial thickness of 10 m to represent the full length of the isolated section of the tunnel (discretisation in the radial direction only), noting that the dimensionality of the grid could be changed very simply and could be tested as part of the model build process.

The tunnel model was designed to accommodate the features induced by the interaction air flow and water vapour that might be reasonably expected to exist. These features were:

1. An 'active' zone and a 'passive' zone in the radial direction; the active zone interacting with the tunnel wall and the passive zone not doing so (and hence not interacting with the active zone), only transporting the vapour associated with the injected air. The passive zone may be zero-sized.
2. Water vapour migration in the active zone is diffusive both radially and axially with an advective component along the axis of the tunnel caused by the local air velocity.
3. Any impact of turbulent mixing of the air can be considered through enhanced radial diffusion, acting to more quickly equilibrate water vapour radially in the tunnel.
4. A velocity distribution for air parallel to the tunnel axis may be defined locally.
5. Interaction between the outer tunnel and the porous media through evaporation of liquid water and vapour diffusion.

The primary objective of including such features was to allow the impact of the uncertainty in the above conceptual and parametric uncertainty to be explored in a single model, and hence deliver a more predictive model with a good understanding of the likely errors that might be produced from the assumptions on the detailed air flow. This model is illustrated in Figure 5-1.

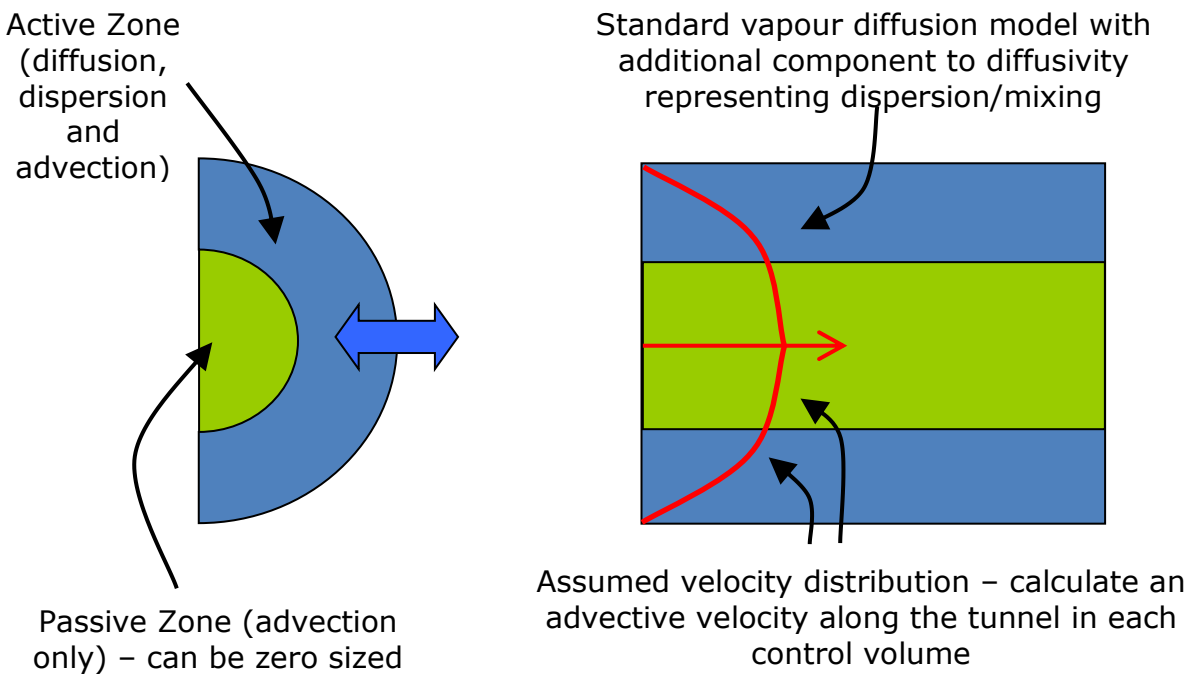

Figure 5-1. Schematic illustration of the conceptual model for QPAC abstracted tunnel model.

The numerical implementation is extremely simple, consisting of a mass balance of water vapour in each compartment and migration through diffusion in air and advection by air using equations 3.2. Discretisation was set to be consistent with the axial and angular discretisation in the porous medium sub-system. Radial discretisation was 6 compartments with the outer compartment 5 cm in depth and the remainder uniformly 10 cm thickness to the centre of the tunnel.

Interaction between the tunnel and the porous media was through local coupling the boundary equations for evaporation of liquid water (equation 3.9) and continuity of water vapour (3.2). Coupling was achieved through using the relative humidity and water vapour density calculated in tunnel compartments adjacent to the tunnel wall to define the fluxes in the boundary equations; the water and water vapour fluxes are then conserved between the two sub-systems. It should be noted that the coupling mechanism employed used a fully implicit scheme such that both the tunnel and porous media hydro-mechanical equations were solved as a single set of equations, rather than using some form of operator splitting or sequential coupling method. In this context, the implementation of equations 3.2 and 3.9 are no longer boundary conditions, but internal continuity equations of a different form to those used in the sub-systems either side of the connection. It should be noted that one could have chosen to represent the liquid water evaporation linkage between the models through the pressure-based formulation (equation 3.10) as one done in Step 0 and this was examined as a sensitivity case.

Boundary conditions on the tunnel model consist of simple advective flows of water vapour at the inflow and outflow ends. Consistent with the formulation in the tunnel model, the advective flows on the boundaries are upwinded, hence the inflow of water vapour is the product of the experimentally applied vapour density (from relative humidity) and the air flow rate. Similarly, at the outflow end of the tunnel, the rate loss of vapour is given by the product of the calculated water vapour density in the upwind adjacent compartment to the boundary and the air flow rate.

Given that the reference model used a simple 1D discretisation, the whole 10 m length of the tunnel and circumference was represented using a single compartment (Figure 5-1). Investigations on the impact of the tunnel and host rock being discretised along the length of the tunnel are discussed in the following sections. The sub-system linking approach required that the discretisation on the tunnel surface be the same for both sub-systems. For example increasing the discretisation along the tunnel axis in the Opalinus Clay would require the same axial discretisation for tunnel sub-system.

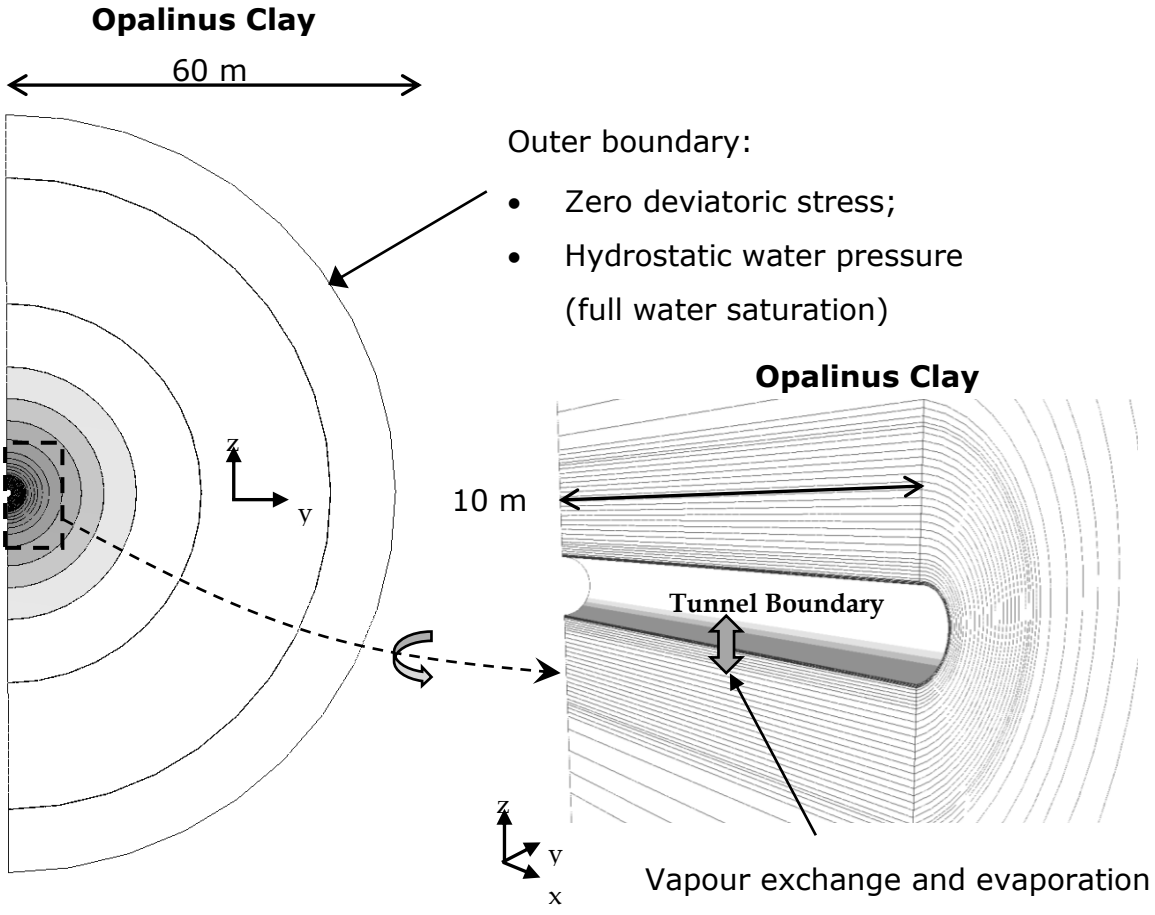

Figure 5-2. Porous medium grid geometry for the QPAC calculations. 1D cylindrical compartments are coloured by radius and shown for the Opalinus clay only. The 1D cylindrical compartments have a defined thickness (along the axis of the tunnel) of 10 m, and hence represents an average behaviour along the length of the tunnel.

5.3.2 Calibrated QPAC Step 2 Results

Using the new tunnel model a range of investigations were conducted to improve the host-rock calibration and understand the best approach for the parameterisation of the tunnel system. Only small changes were made to the host-rock parameterisation, the only significant change being the adjustment of the capillary pressure curve from the curve that was fixed across teams during Step 0 to be consistent with the observed water contents and suctions. The parameterisation is given in Table 5-1.

The comparisons made in this section use the tunnel relative humidity data released mid-way through Step 2 but do not include the host-rock data made available *after* the blind comparison in November 2011. Thus the tunnel relative humidity and mass balance comparisons for Step 2 (discussed below) for QPAC were predictive, because the data were released ahead of the inter-comparison meetings, they cannot be described as strictly controlled blind predictions.

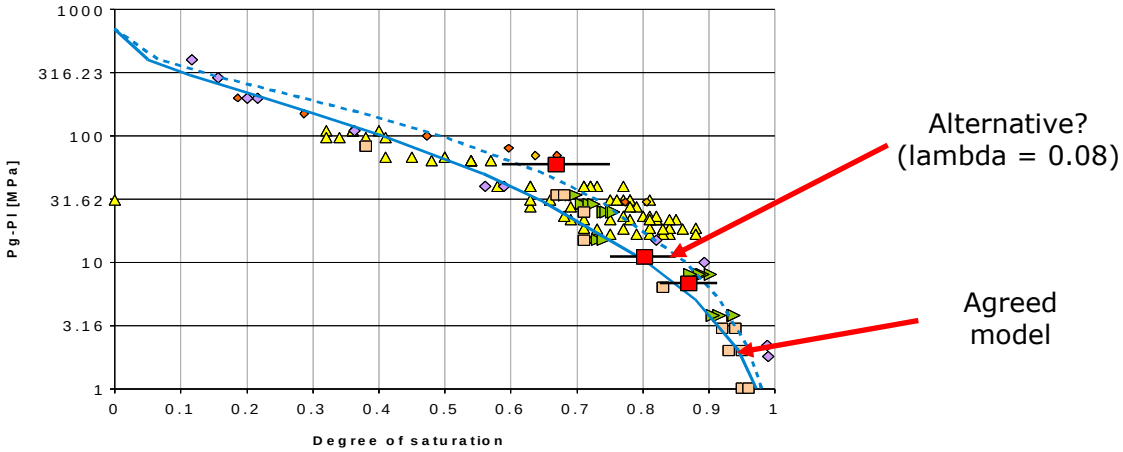

Figure 5-3. Updated suction curve for Step 2 calculations. Field measurements are shown as red squares with black error bars.

Table 5-1. Parameterisation for the calibrated Step 2 calculations

Parameter	Unit	Value	Source
Acceleration due to gravity g	m s^{-2}	9.81	Gettys *et al.* (1989)
Young's Modulus (Clay) E	GPa	1	Calibrated value from Bock (2001)
Poissons Ratio (Clay) v	-	0.3	Estimated value
Failure Mode (Clay)	-	None – elastic only	Assumption
Reference Porosity (Clay) θ_0	-	0.165	Fitted to observed water content data (Garitte & Gens, 2008)
Initial Deviatoric Stress (Radial)	atmosphere (bar)	0	(Garitte & Gens, 2008)
Initial Deviatoric Stress (Axial)	atmosphere (bar)	0	(Garitte & Gens, 2008)
Initial Deviatoric Stress (Vertical)	atmosphere (bar)	0	(Garitte & Gens, 2008)
Initial Water Pressure	atmosphere (bar)	Hydrostatic	(Garitte & Gens, 2008)
Elastic Response Time	years	0.001 days	Assumption
Initial Temperature	degrees C	15	(Garitte & Gens, 2008)
Reference Water Density	kg m^{-3}	1000	Assumption
Reference Water Pressure	atmosphere (bar)	1	Assumption
Relative Permeability Air $k_{r,A}$	-	Sg	Gas is assumed to be largely passive to water saturation.
Relative Permeability Water $k_{r,w}$	-	$S_{wr}^{(1/2)}\ (1-(1-S_{wr}^{(1/\lambda)})^{\lambda})^{2}$ Where S_{wr} is the reduced saturation and λ is a fitting parameter = 0.3	λ was calibrated within the range given in Muñoz *et al.* (2003) in Step 0.

Parameter	Unit	Value	Source
Intrinsic Permeability k	m^2	k_0 $((\theta^3)/((1-\theta)^2))(((1-\theta_0)^2)/(\theta_0^3))$ where k_0 = 1.125e-19 m^2	k_0 is a fitting parameter bounded by the ranges discussed in Muñoz *et al.* (2003). Kozensky's model for porosity/permeability coupling.
Reference Vapour Diffusivity D_v	$m^2\ s^{-1}$	2.50E-006	Claesson & Sallfors (2005) and calibrated
Suction pressure Ψ	MPa	Determined by constraint solution to: $0 = S_{wr} - ((1 + (\Psi / P_0)^{(1/(1-\lambda))})^{-\lambda})$ $((1-(\Psi / P_S))^{\lambda_s})$ Where P_0 = 3.9 [MPa] λ = 0.08 [-] P_S = 700 [MPa] λ_s= 2.73	Muñoz *et al.* (2003)
Initial Water Saturation	-	0.99999	Floria *et al.* (2002)
Dry grain density ρ_m	$kg\ m^{-3}$	2700	Derived and calibrated value from initial conditions quoted in Floria *et al.* (2002). Consistent with Bock (2001)
Effective Pore Pressure (for calculating effective stress)	MPa	$P_w S_w^n + P_{air}(1-S_w^n)$ n=1	Modified version of the standard Bishop Effective Stress model.
Phase 0 Applied RH	-	0.6	Calibrated
Phase 0 Applied Air flow rate	m^3/h	30	Estimated
Tunnel Air Velocity Distribution	-	Uniform (Turbulent Flow)	Calibrated – best results with radially well-mixed tunnel water vapour. (see Bond *et al.*, 2010)
Radial tunnel dispersion	$m^2\ s^{-1}$		Calibrated – best results with radially well-mixed tunnel water vapour. (see Bond *et al.*, 2010)

A range of sensitivity analyses were conducted on the parameterisation of vapour migration and air movement in the tunnel. The first major conclusion was that in order for the observations on tunnel inflow/outflow mass balance and interaction with the host rock to be consistent with the known water content data in the Opalinus Clay, that the whole tunnel had to be contributing significantly, i.e. there could be no 'passive zone'. Such an observation is consistent with the small tunnel radius and relatively slow airflow rates through the tunnel. The second major conclusion was that there was relatively little sensitivity to the radial velocity distribution and the inclusion or exclusion of enhanced radial mixing (turbulence) in the model.

The comparison between the observed average relative humidity in the tunnel and the calculated values shown in Figure 5-4 are extremely close throughout the experiment. The results clearly show very similar magnitudes and transient behaviours even during the rapid changes in 2006. There is clearly a deviation between the curves at the end of 2006 and during 2007, but this appears to come about due to erroneous or missing data. Similarly good results were obtained for total mass balance (Figure 5-5), relative humidity, water pressure at the end of Phase 1, water content in the rock mass and rock-mass dimensional change with time (Figure 5-6 to Figure 5-9).

The bulk water mass balance shows the calculated results tracking the experimental estimates well with time. It is noted however that while the model shows similar drying rates during Phase 1 and 2, the experimental data may suggest a slower response during Phase 2, although the deviation is within the bounds of data uncertainty, and hence cannot be positively isolated as a trend. If present, this trend might be indicative of a bulk reduction in intrinsic permeability with time, potentially associated with healing of rock damage through creep.

The modelled mechanical evolution versus observations for Phase 1 is illustrated in Figure 5-9. The experimental data showed considerable variation, although not apparently structured variation, and hence for the 1D case used here, comparison is made versus the data of B47, which exhibited a reasonable median behaviour of the available data. The model results show the initial expansion of the rock mass through tunnel construction, and then progressive contraction through Phase 0 (for which we have no data) as drying takes place. The wetting and drying cycle during Phase 1 is well-captured in terms of the expansion and contraction of the extensiometers. It should be noted that the elastic modulus used for the model is towards the lower end of expected intact rock values, and this may be indicative of the effects of damage, or alternatively, that the poro-elastic model needs to subsume other processes such as clay swelling which will exaggerate dimensional change.

Overall, all the Phase 1 metrics showed improvement and the consistency with the limited Phase 2 data was also extremely good.

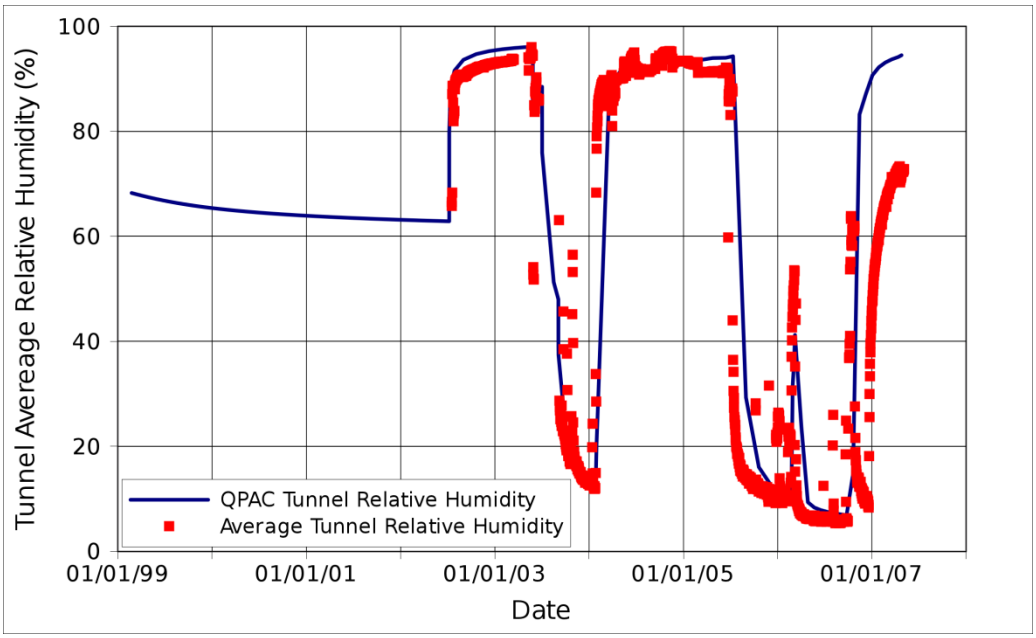

Figure 5-4. Comparison between the calculated and observed relative humidity of air in the experimental tunnel for Phase 1 and 2.

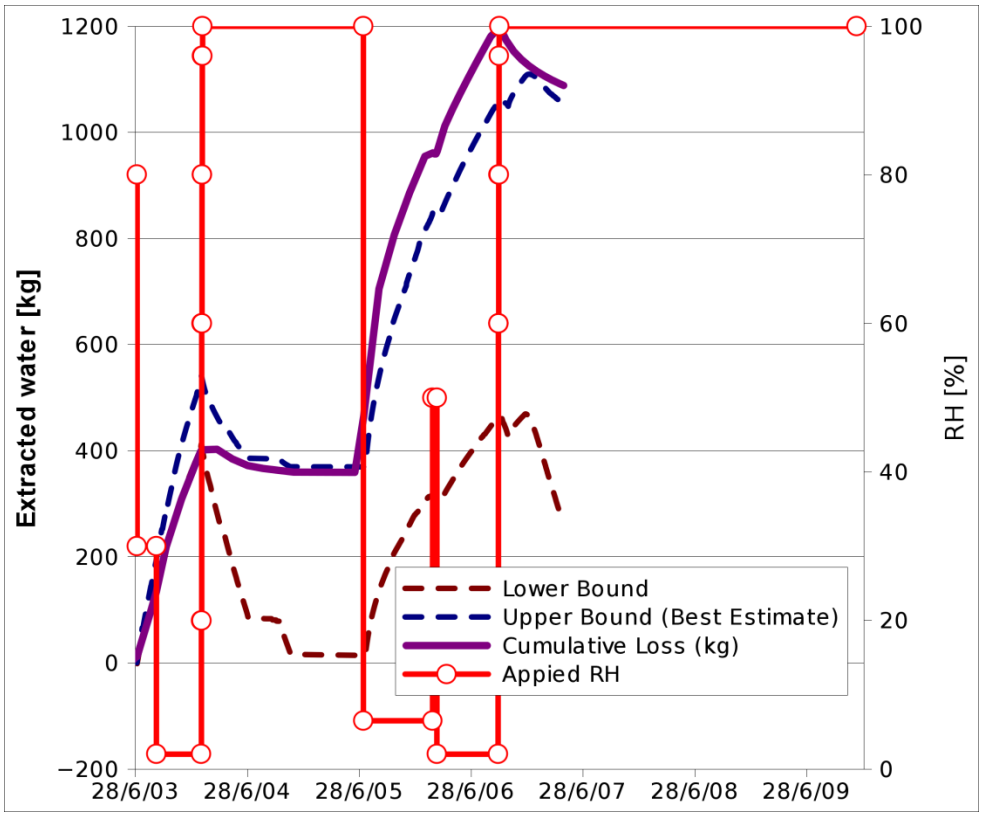

Figure 5-5. Comparison between the calculated and observed water balance in the ventilation experiment tunnel for Phase 1 and 2.

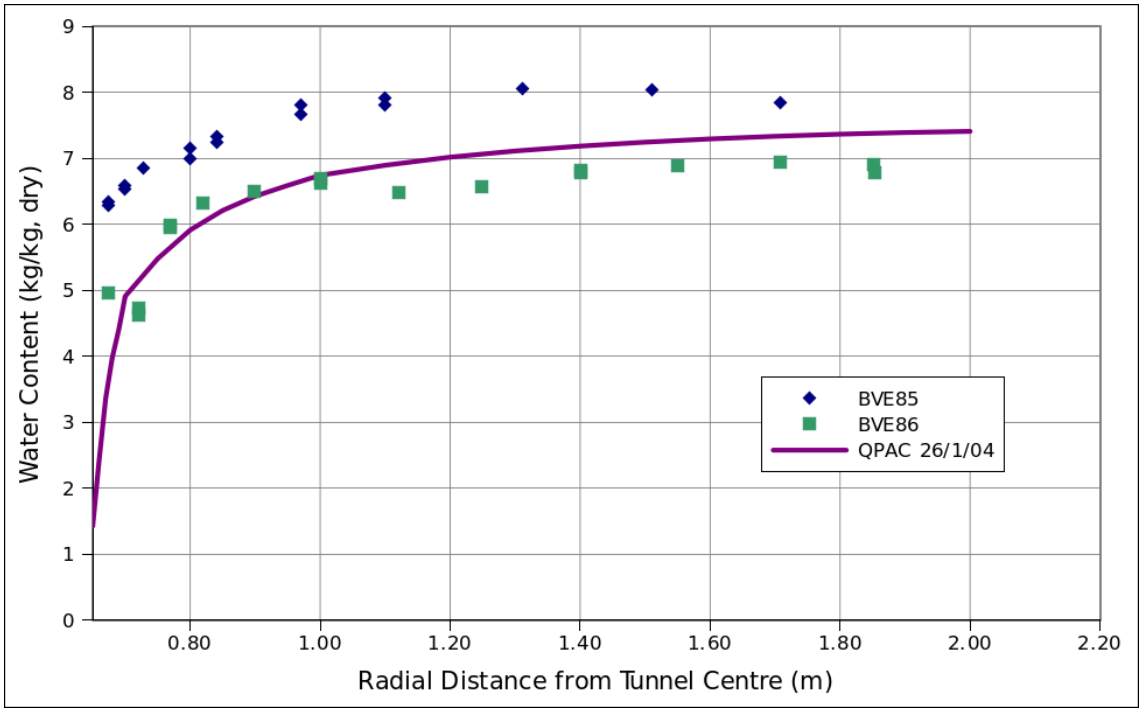

Figure 5-6. Observed and computed water contents for the start and end of Phase 1

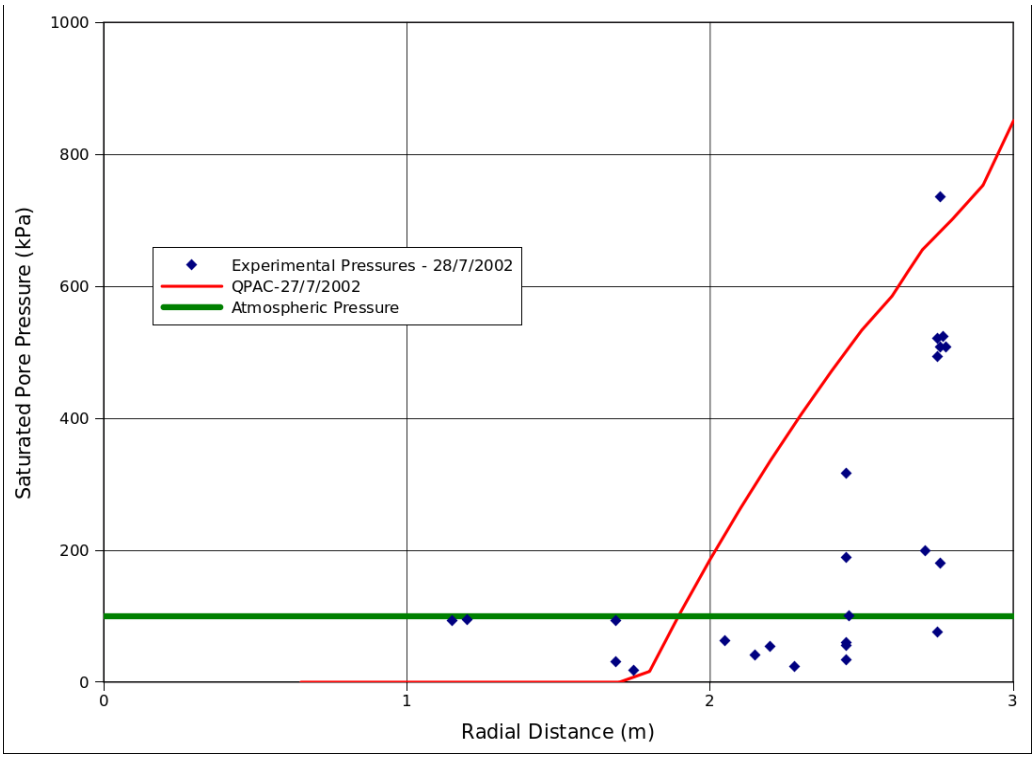

Figure 5-7. Comparison of modelled and experimental pressures at the start of Phase 1

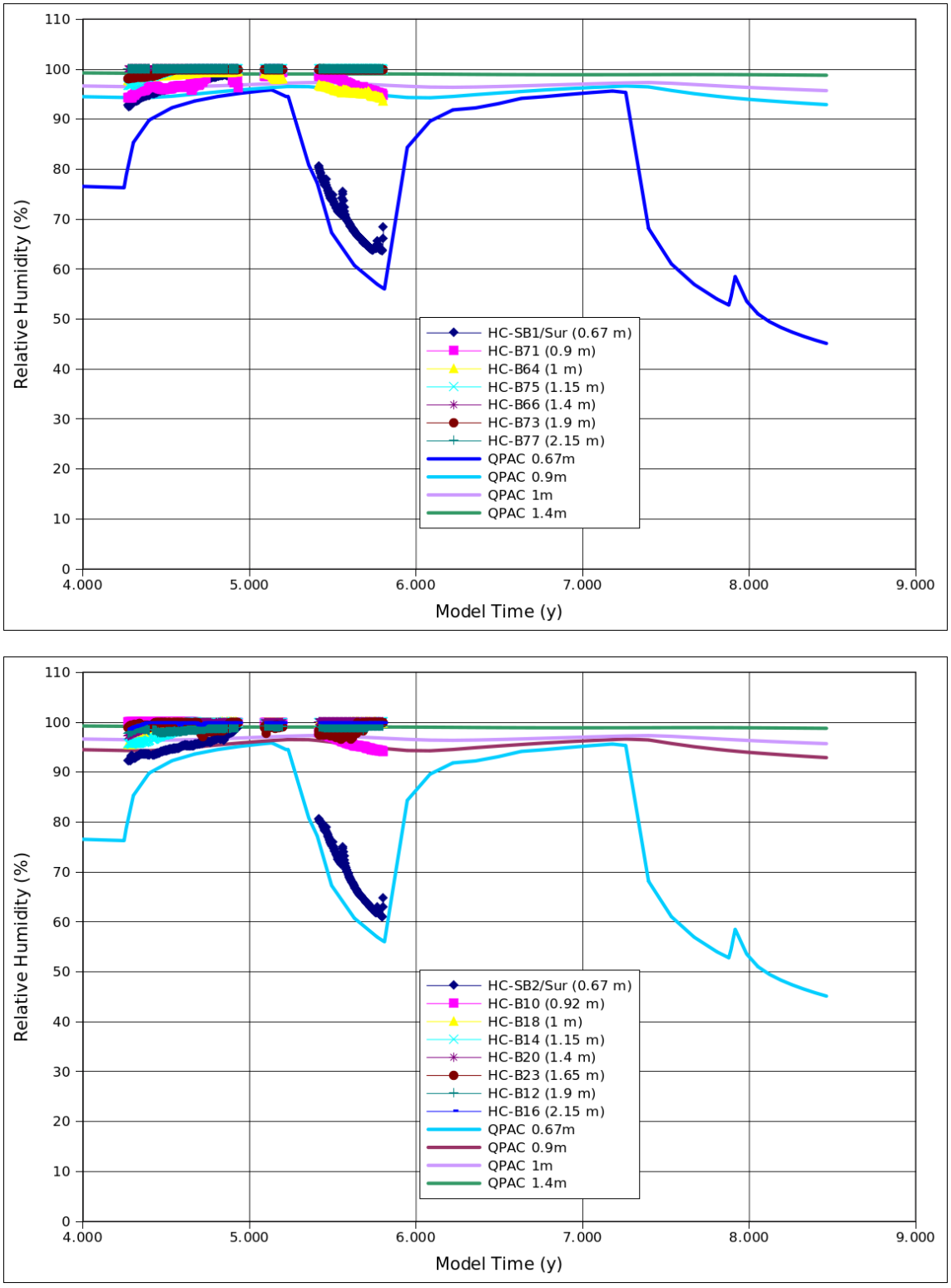

Figure 5-8. Relative humidity, experimental versus computed during Phase 1. The two plots refer to measurements taken close to the air inflow (top) and close to the air outflow (bottom). Calculated results during Phase 2 are also shown.

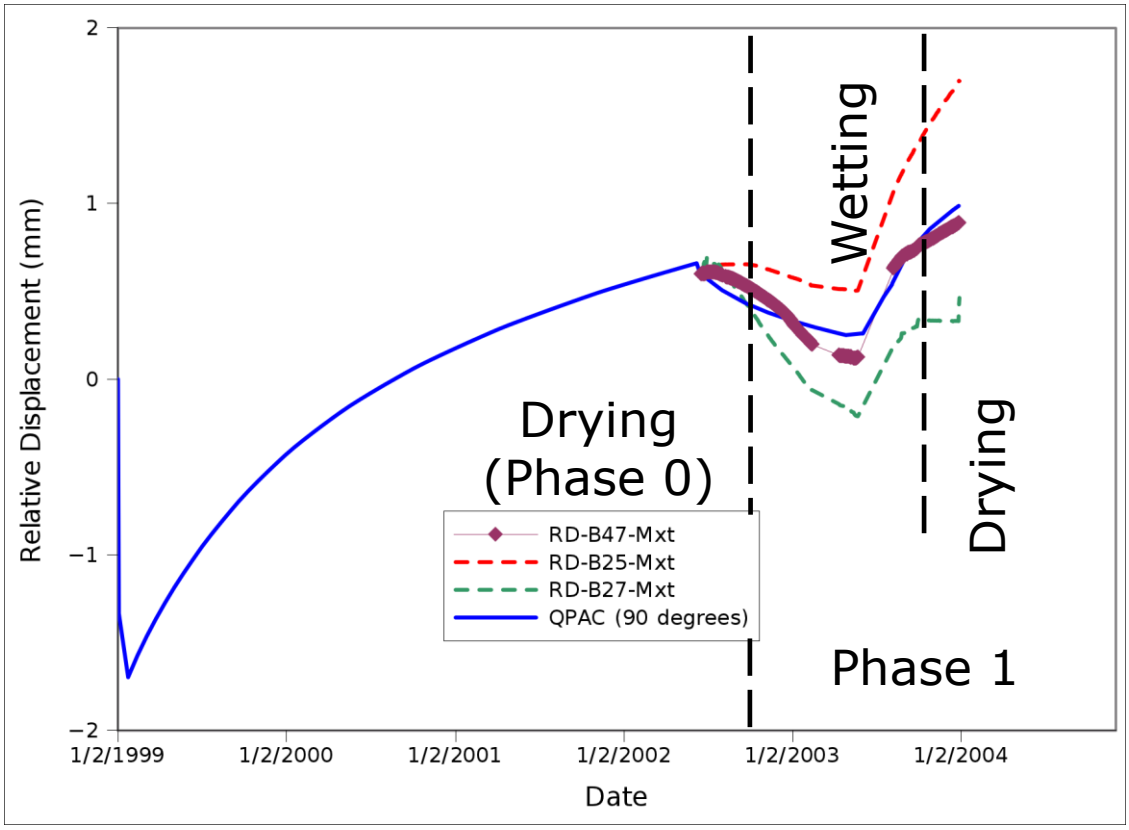

Figure 5-9. Comparison between the calculated and observed relative displacements during Phase 0 and Phase 1.

Overall, calibration has changed very little from the Step 1 results, but has improved the results overall. This tends to build confidence that the Step 0 analysis provided a sound basis for the hydraulic model in the full VE. The major change has been the full adoption of the tunnel subsystem model which, in this case, provides a robust mechanism of using the 'true' boundaries of the system rather than relying on direct measurements of the tunnel condition.

The bulk fluid results and the generalities of the displacements seem to match the system well, although perhaps the model is a little too dry adjacent to the tunnel, at the expense of having too much water at a greater radial distance. Some details of behaviour notably the spatial variability in the displacement response and the measured very fast fluid responses, as discussed as part of Step 1, still cannot be replicated and indeed there is no process or feature in the model to enable this response to occur.

5.3.3 QPAC Additional Investigations

In coordination with the other Task A members a set of sensitivity and uncertainty analyses were suggested for Quintessa to conduct in order to complement other investigations conducted by the remaining teams. The investigations fell into two broad categories; better understanding the assumptions around the tunnel evaporation condition; and investigations to reveal processes that may be giving rise to the rapid pressure transients in the host-rock, 2 m distant from the tunnel. To this end the following cases were run.

Surface Condition

- ▲ Impact of using the pressure based liquid water condition on the tunnel wall
- ▲ Discretisation along the axis of the tunnel

Rapid Host-Rock Pressure Responses

- ▲ Impact of modelling potentially leaking piezometers explicitly
- ▲ Impact of adopting anisotropic mechanical properties
- ▲ Impact of including rock failure mechanisms

5.3.4 Pressure-based surface condition

To test the conclusion of Section 4 that the sensitivity of the model result is small with respect to the choice of the type of surface boundary applied, the model described in the previous section was adjusted to use the pressure-based surface formulation. The result was quite striking. However during the major drying component of Phase 2, the drying effect is magnified, resulting in a peak loss of 1300 kg of water (compare with ~1100 kg shown in Figure 5-5). It appears that under strong drying conditions the pressure formulation was exerting a much greater control.

However, resolving this discrepancy could be readily achieved through one of two methods either;

- scaling intrinsic permeability by a factor of 3/4 and changing the λ factor in the relative permeability formulation (Table 2) from 0.35 to 0.3; *or*
- eliminating the enhanced lateral turbulent mixing in the tunnel to induce vapour density gradients across the tunnel radius (Figure 5-10 and Figure 5-11).

Figure 5-10 and Figure 5-11 show that the deviation of the wall tunnel relative humidity from the average tunnel relative humidity is quite small, even under strongly drying conditions. Neither change is especially large and is covered by the conceptual and parameter uncertainty inherent in the data model.

The conclusion must be that for the ventilation experiment formulation, the pressure-based approach for the surface condition is more sensitive to the assumptions regarding the distribution of water vapour in the tunnel than the flux-based approach, however small changes to the parameterisation of the porous media can overcome this sensitivity relative to the flux-based formulation. Unless additional data can constrain the characteristics of the system further from this analysis it must be concluded that the assumptions of the details of the behaviour of the tunnel with regard to water vapour distribution are of secondary importance in this system.

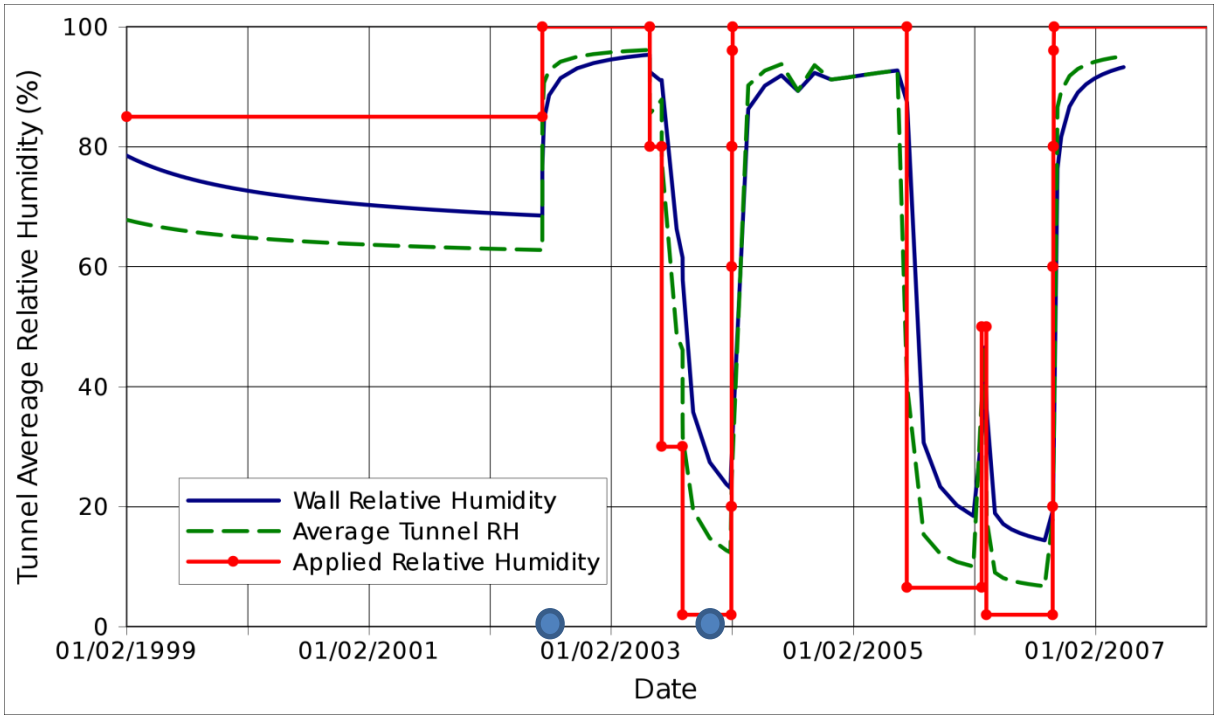

Figure 5-10. Comparison between the average and wall relative humidity calculated in the QPAC tunnel model when using the pressure formulation for the surface boundary and no enhanced radial mixing. The times for the relative humidity plots in the tunnel show in Figure 5-11 are highlighted by spots on the x axis.

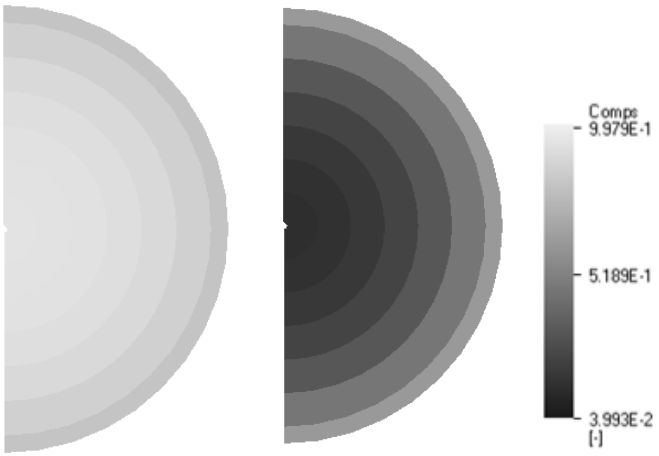

Figure 5-11. Relative humidity across the tunnel (shown as a half model) at 8/7/2002 (left) and 1/11/03 (right), showing the relative small amount of relative humidity change across the tunnel with no enhanced radial water vapour mixing.

Discretisation along the tunnel axis

In order to test the assumption that treating the tunnel and Opalinus clay with a single compartment in the tunnel axial direction was appropriate, and also to understand the modelled variation of relative humidity along the length of the tunnel, the reference case was divided into five compartments axially. The average relative humidity at each distance along the axis of the tunnel and the results are plotted together with the applied relative humidity. In addition comparison was made between the estimated mass balance from the outflowing water vapour and that produced from the 1D calculations.

The computed mass balance is visually indistinguishable from Figure 5-5, and as such is not discussed further, and the variation along the tunnel is shown in Figure 5-12. The difference between the upstream and downstream relative humidities is of the order of 10-15% under strongly drying conditions, which is similar to the variation along the tunnel shown in the experimental observations (Figure 5-13). The model shows slightly less variation than seen by the inflow and outflow data, especially at early times, but this can be understood by noting that the evaluation points in the model are 1 m away from the ends of the tunnel, and hence don't capture the full variation.

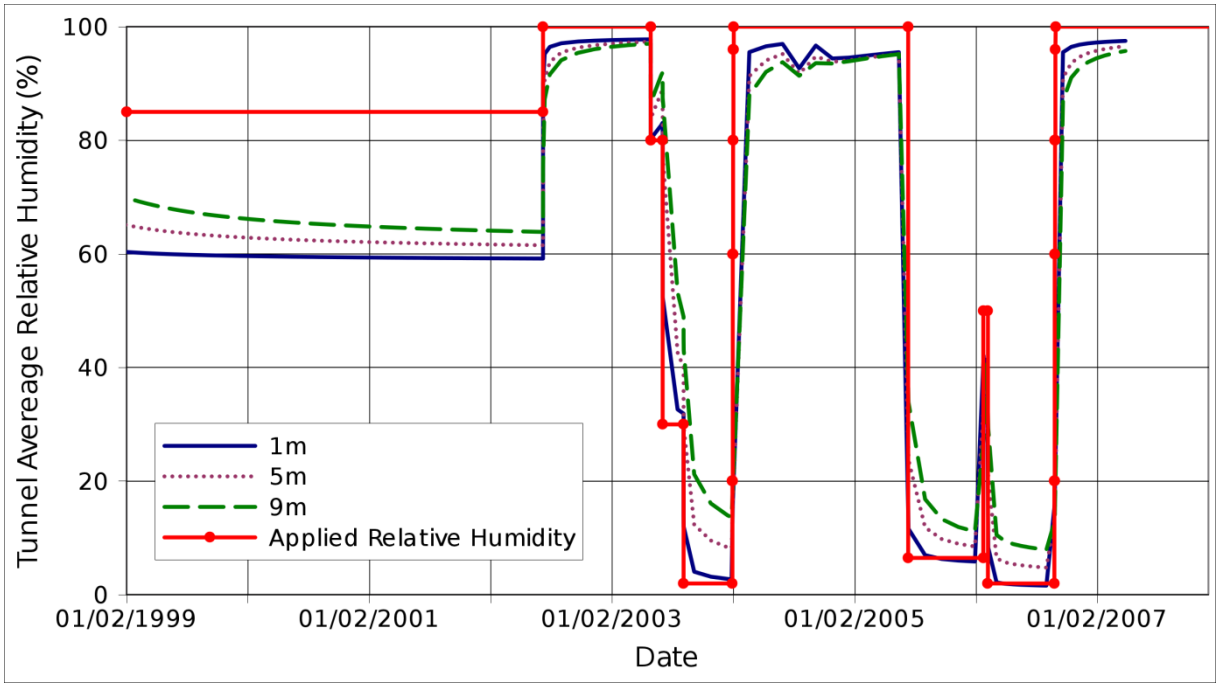

Figure 5-12. Plot of average relative humidity across the tunnel (%) with different distances along the tunnel axis from the air inlet, at 1 m, 5 m and 9 m.

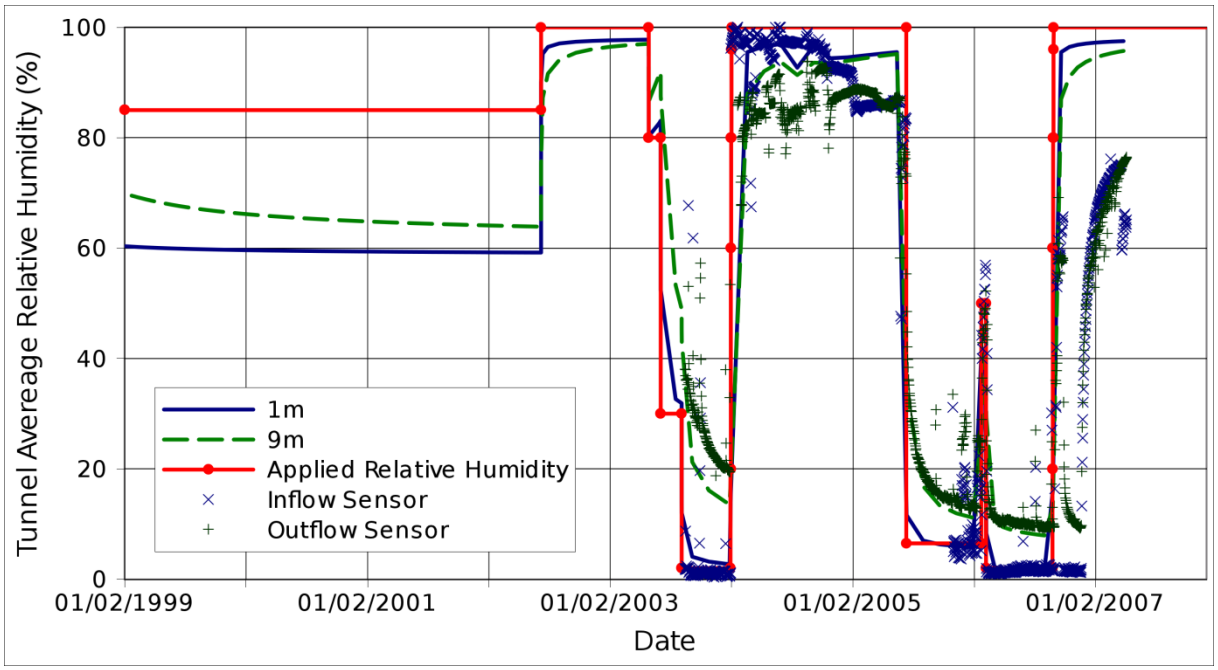

Figure 5-13. Plot of average relative humidity across the tunnel (%) plotted at 1 m and 9 m from the air injection, in comparison with the inflow and outflow relative humidity data.

Given the similarity in results between the 1D and 2D cases, but also that the model reproduces the observed variation in relative humidity along the axis of the tunnel, it appears that this abstracted approach gives a good representation of the tunnel for understanding the hydraulic mass balance of the system, and as a more complete 'boundary' to the porous medium hydro-mechanical model.

Explicit modelling of potentially leaky piezometers

In order to see whether the boreholes could be acting as fast pathways for the observed rapid pressure transfer into the host rock some numerical experiments were conducted. The reference model was modified to include a specialised 'well' compartment which represented one of the piezometers. This compartment is connected to the host-rock compartments horizontally out to 2 m radially from the tunnel and is assigned a permeability to represent the concrete backfill. The tunnel end of the well compartment has the same connection arrangement to the Tunnel subsystem as the ordinary compartments. Mechanical processes are disabled in the well compartment.

Cases were run for different permeabilities and porosities for the piezometer seals. The results aren't presented in detail here, but in general terms in order for the piezometers to act as fast pathways, the permeability of the piezometers needs to be greater than that of the rock, with a very low effective porosity (assumed to be small fracturing around the seals), and the net behaviour is very sensitive to the choice of piezometer

permeability. This means that the while hydraulic signals can be conducted quickly down the piezometer, the piezometer can become a major flow pathway for vapour and liquid water. This is not what is observed in the system (there is no evidence of damp patches around the borehole seals). Furthermore given that all the piezometers seem to behave in the same manner with respect to rapid changes in saturated water pressure, overall it seems unlikely that the piezometers seals are behaving as rapid conduits and they seem unlikely to be directly causing the pressure changes seen.

Anisotropic Mechanical Properties

The anisotropy of mechanical rock properties may be of interest to the 'fast pressure response' problem, because is creates the possibility of significant dilatancy (and hence implied porosity changes) of volumes of rock, which could imply significant pore pressure changes under bulk stress changes. This could therefore give a mechanism whereby changes in pore pressure 2 m into the rock could be caused almost instantaneously by changes in relative humidity at the tunnel wall.

Bock (2001) gives a range of anisotropic (transverse isotropy) values for the Opalinus Clay, covering Young's Modulus, Shear Modulus, Poissons Ratio and failure strengths. Looking at the available data it is clear that the Young's Modulus perpendicular to the bedding direction is of the order of a factor of 2.5 less than that aligned with the bedding planes.

A calculation was conducted which considered the following anisotropic elastic moduli, noting that consistent with the reference case we reduce the Young's modulus to a lower level than tabulated in Bock (2001), consistent with the observation given in Bock (2001) that moduli appear to be significantly lower at lower stress levels. The properties used were:

Perpendicular to bedding (z):

Young's Modulus = 0.5 GPa
Shear Modulus = 0.75 GPa

Parallel to bedding (xy plane):

Young's Modulus = 2 GPa
Shear Modulus = 0.75 GPa

Poisson's Ratio (x,z) = Poisson's Ratio (y,z) = 0.24
Poisson's Ratio (x,y) = 0.33

The reference model was discretised into 10 angular sections (i.e. 18 degrees each) to allow the mechanical anisotropy to be appropriately represented and the mechanical properties resolved onto the cylindrical grid appropriately.

The results showed that the overall bulk behaviour of the model (as observed through the general water balance, for example) is very similar to the isotropic case, however, as one would expect, significant differences were seen in the relative displacements around the tunnel (Figure 5-14).

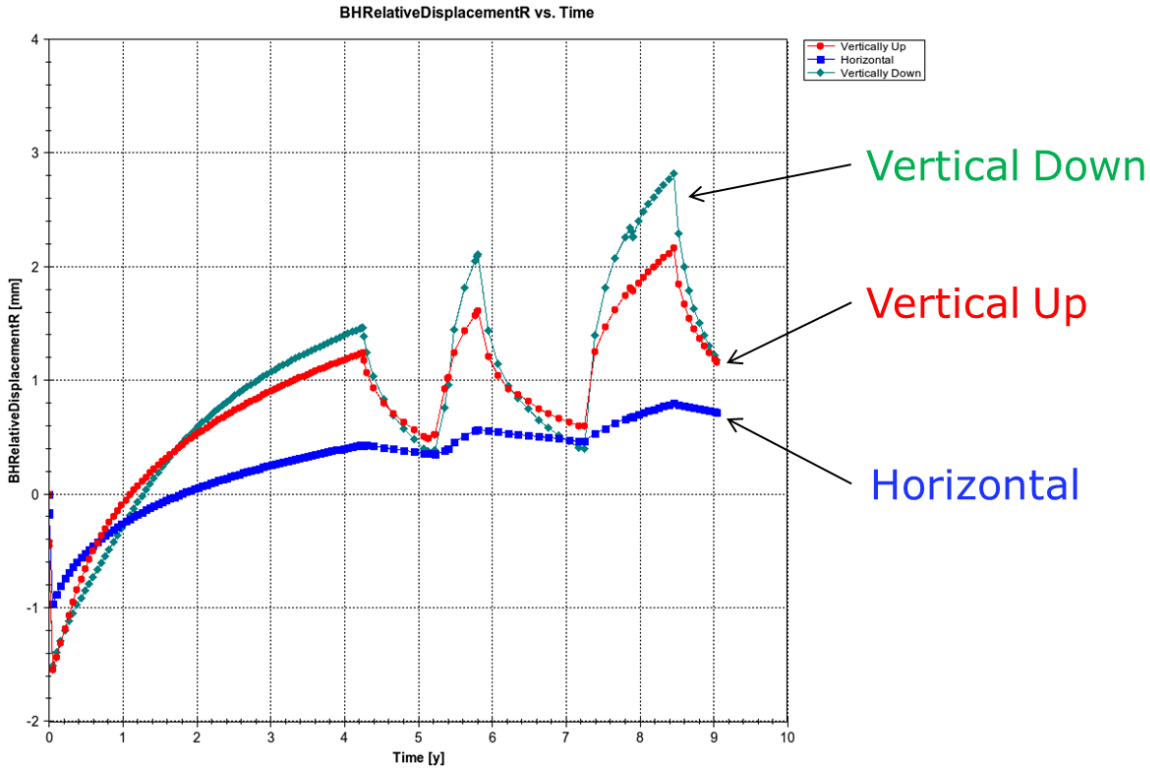

Figure 5-14. Variation in radial relative displacement for the anisotropic mechanical properties case.

Such variations in displacements are not observed, however there are no relative displacement measurements close to the horizontal, all are inclined or sub-vertical. Even if very small displacements were to be seen along the horizontal axis, there are no measurement points in place to make the observation.

In terms of the main issue, rapid changes in saturated fluid pressures, the results are more interesting. It can be seen that in the vertical directions small increases in pressure are associated with wetting and small decreases with drying. In the horizontal direction the association is reversed, as one might reasonably expect. It should be noted that the horizontal behaviour is restricted to a relatively narrow sub-horizontal arc and that boreholes with an inclination of approximately 20 degrees would see a behaviour closer to the vertical responses. Thus given all the piezometers are inclined at 45 degrees or greater to the horizontal, one would only expect to see the 'vertical' style responses in the experimental data, as is the case.

However, the responses observed are too small in comparison with the observations by at least a factor of five, so it seems unlikely that mechanical anisotropy alone can be responsible for the saturated pressure fluctuations seen. However it does illustrate the principal that such mechanical effects can have significant impacts on saturated water pressures, and this avenue of investigation should be pursued.

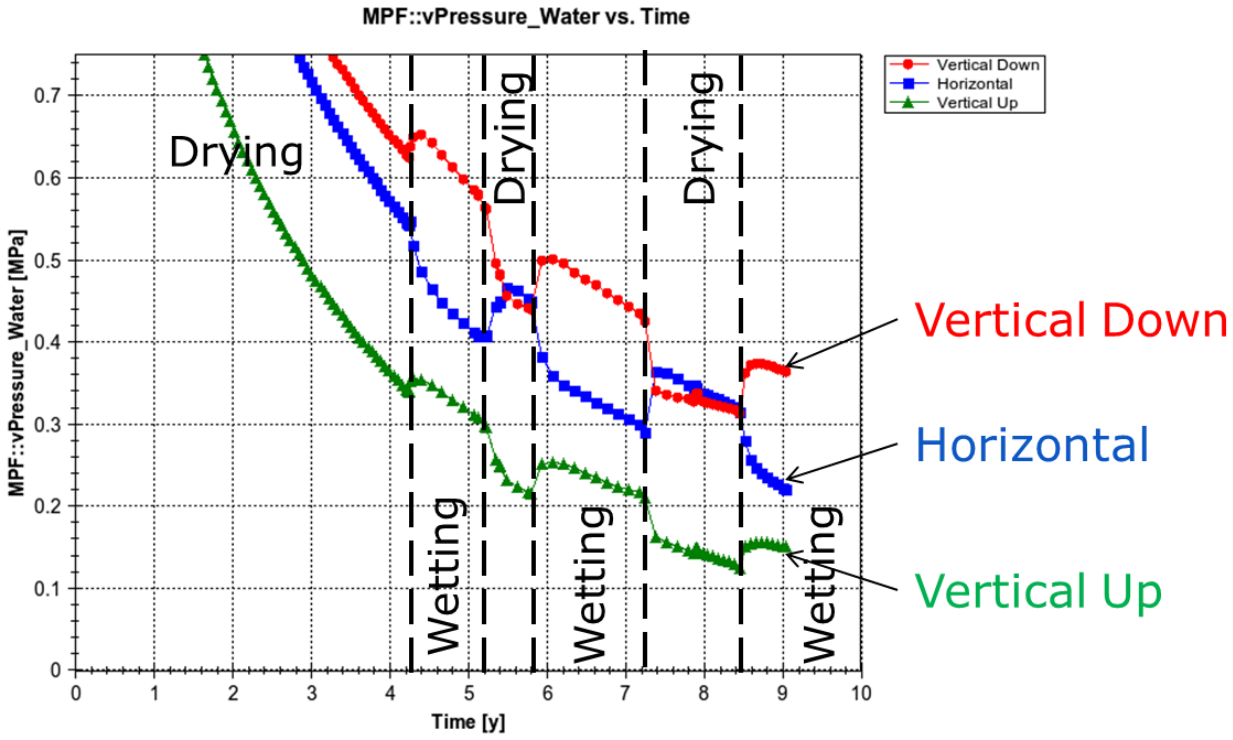

Figure 5-15. Variation in saturated water pressure at a distance of 2 m from the tunnel wall at three different orientations for the anisotropic mechanical properties case.

This avenue of investigation was developed further by other members of the task and the results are discussed by Millard *et al.* (2012). Some very recent analysis discussed in Garitte *et al.* (2012) may suggest that some external thermal effects from other experiments and natural thermal variation may be partially responsible; however the question is very much open.

Rock Failure

Failure of the rock mass provides another means by which dilatancy, and hence significant porosity change, can be introduced into the model. Failure caused by changes in bulk stress state therefore gives another means by which the rapid pressure changes in the saturated zone could be caused by the relative humidity changes in the tunnel.

Bock (2001) gives values for a number of failure modes for the Opalinus Clay. By default QPAC allows for anisotropic Mohr-Coulomb failure also including simple tensile failure. From Bock (2001) the following Mohr-Coulomb values were used:

Perpendicular to bedding (z):

Cohesive Strength = 5.5 MPa
Failure Angle = 25 degrees
Tensile Strength = 2 MPa

Parallel to bedding (xy plane):

Cohesive Strength = 2.2 MPa
Failure Angle = 25 degrees
Tensile Strength = 9 MPa

These were included in the anisotropic elasticity model sensitivity case. No attempt to represent damage in the material properties was attempted, due to a lack of suitable data.

The results showed that no failure was predicted to occur until very late in the experiment during the final wetting cycle. Failure was predicted to occur at the tunnel wall and would be relatively shallow on the tunnel surface (see Figure 5-16) and would occur after 7.4 years. Impacts of failure on fluid pressures were observed to be very small and in the wrong location and time to be consistent with the saturated piezometer data record.

It should be noted that at the time these calculations were conducted it was thought that no plastic failure had occurred in the microtunnel, however at the recent Decovalex Finland workshop, the Task A management confirmed that some surface failure of the Opalinus Clay in the tunnel wall had been seen later in Phase 2. No further data were made available. It is important not to overstate this 'prediction', however it appears that using the available laboratory and field data, a general prediction of the relative strength of the host rock under the loads caused by the variation in ventilation is broadly consistent with field observations.

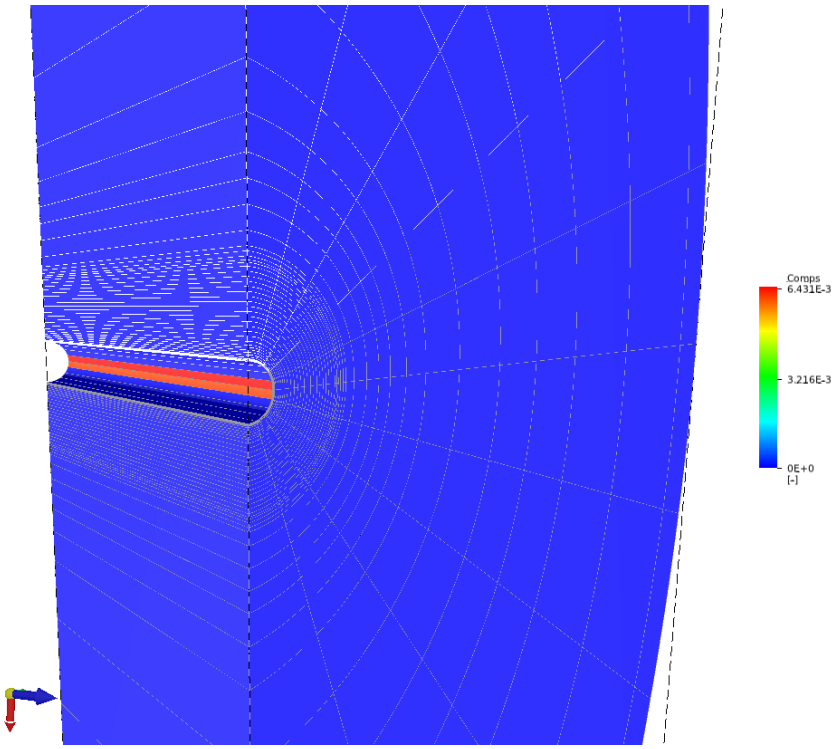

Figure 5-16. Magnitude of predicted plastic failure at approximately 7.3 y model time.

5.3.5 QPAC Step 2 Conclusions

Besides the addition of the tunnel model, relatively small changes have been made from the Step 1 models to get a good calibration for the available data. In general the performance of the model is very good, with the only outstanding issue remaining the behaviour of the saturated water pressures. However some scoping analysis using anisotropic mechanical properties have indicated that introducing dilatancy through mechanical processes may hold the answer to resolving this issue, without compromising the general hydraulic behaviour of the system.

In addition there is some evidence from the calibration exercises that the intrinsic permeability of the system is reducing with time. This could be attributed to mechanical creep and 'healing' of the EDZ.

There is clearly more scope for investigation in this area, hence Step 2 cannot be described as closed and it may be for a future project to progress this understanding further

5.4 University of Edinburgh Step 2 Analysis

5.4.1 Approach

As discussed at the beginning of Section 5, it was decided that the UoE Step 2 work would focus on producing the simplest physical model that could be used to replicate the hydro-mechanical response around the tunnel, as well as a simplified hydraulic representation of the tunnel itself. This focus was completely complementary to the Quintessa work during Step 1 and 2, which had already started to examine simplifications that could be made to the hydro-mechanical process models, and also complementary to work of other teams, who were tending to include more complex process models (e.g. Millard *et al.* 2012). Given the potential complexity of the models that could be produced for this experiment, attempting to understand what could be the simplest realistic model would be a valuable contribution.

Building on the Step 1 work it was decided that as a starting point UoE should attempt a model with the following processes and geometry:

1. The geometry should be as simple as possible, preferably 1D cylindrical.
2. The model should be isothermal.
3. It was noted by various teams during Step 0 and Step 1 that the gas phase played almost no role in the physical response, except to act as 'space' into which water could vaporise. To this end it was suggested that the UoE model should evaluate the use Richards' equation rather than full multi-phase flow. This means that in equation 3.1 gas pressure is assumed to be constant and hence that gas is rapidly mobile in comparison with water, thus gas fluxes, relative permeabilities, etc. do not need to be considered.
4. Vapour is included in the relative permeability formulation rather than being modelled explicitly.
5. Rather than perform a full poro-elastic analysis to calculate relative displacements in the clay, a simplified functional form should be developed that takes the changes in porosity (a function of pore pressure changes and rock compressibility) and integrates them across the 2 m extensiometer lengths to estimate rock expansion and compression.

While all of the models produced in this task were assumed to be isothermal, the other simplifications, especially points 3 and 5 are potentially very significant.

5.4.2 Process Model, Parameterisation and Boundary Conditions

Processes

As discussed in the previous section, rather than full multi-phase flow, Richards' equation was used for the hydraulic processes, which utilises equation 3.1, but gas pressure is assumed to be constant and hence fluxes for the gas are not calculated.

The mechanical behaviour of the rock may be inferred by post processing the water pressure and saturation results to infer a porosity change from the estimated rock compressibility. In one dimension, the linear displacement of all of the line elements may be calculated over each time step by summing the change in porosity that would have occurred if the rock strain state had achieved equilibrium with the water pressure and saturation conditions. Thus the change in radial length l (m) for a given node i at time t for a first order 1D element e, which has two nodes i and i+1, with the subscript 0 denoting reference values;

$$\theta_i = \theta_{i,0} \exp\left[\frac{S_{w,i}(P_{0,i}-P_i)\beta}{\theta_{i,0}}\right] \quad 5.1$$

$$\varepsilon_i = \theta_{i,0}\left(\left(\frac{{\theta_i}^{1/3}}{{\theta_{i,0}}^{1/3}}\right)-1\right) \quad 5.2$$

$$\Delta l_e = \frac{(\varepsilon_i+\varepsilon_{i+1})}{2}(x_{i+1}-x_i) \quad 5.3$$

Hence the total dimensional change between and including elements m and n

$$\Delta l_{m-n} = \sum_{e=m}^{e=n} \Delta l_e \quad 5.4$$

The compressibility β is obtained from the Young's modulus (Y) via the bulk modulus (B) and Poisson's ratio (v), in 3D:

$$\beta = \frac{1}{B} = \frac{(3(1-2v))}{Y} \quad 5.5$$

The main limitation of this method is that it is a simple post-processing step and so cannot be coupled with other processes or allow for changes in the stress field.

Parameterisation

To allow for the reduction in permeability to water with decreasing water content, the relative permeability is calculated as a function of water saturation. Following from the work in Step 0 and 1, the van Genuchten function (van Genuchten, 1980) formulation was used and a modified van-Genuchten function for capillary pressure (Munoz *et al.*, 2003 - Figure 3-14).

The remaining parameter set used in the final calibration for the Step0 report, were used as a starting point for the Step 2 calculations, having simplified the physical formulation from Step 1. Subsequently the intrinsic permeability was changed to fit the mass balance estimation, and this became the base case against which sensitivity analyses were carried out, but no other parameters were changed substantially. Final material properties are given below.

Table 5-2. Step 2 parameterisation for UoE Step 2

Parameter	Value	Units	Source
Porosity	0.19	-	Step 0 calibrated
Intrinsic Permeability	6.0×10^{-20}	m^2	Calibrated
Reference Grain density	2700	kg m^{-3}	(Fernández *et al.* 2007a)
Young's modulus	1	GPa	Bock (2001)

Boundary Conditions and Initial Conditions

Because no tunnel model was available to reflect the true boundary conditions of the system, the boundary condition of the rock domain at the tunnel wall is modelled as being capillary pressure as a function of (an average value of) relative humidity of the tunnel air (i.e. using equation 3.8). As discussed previously, the tunnel relative humidity data were provided by the task organisers mid way through Step 2 when it was recognised most teams would be unable to make fully predictive calculations.

Gauges RH-HyV-In, RH-HyV-Out, TS-RH1, TS-RH2 are assumed to be representative of the RH in the tunnel. The resulting time series plot is noisy and so the 20 day rolling mean is used as shown in Figure 5-17. The outer radial boundary condition is set as no-flow.

Initial water pressures are set at 1.85 MPa with water fully saturated.

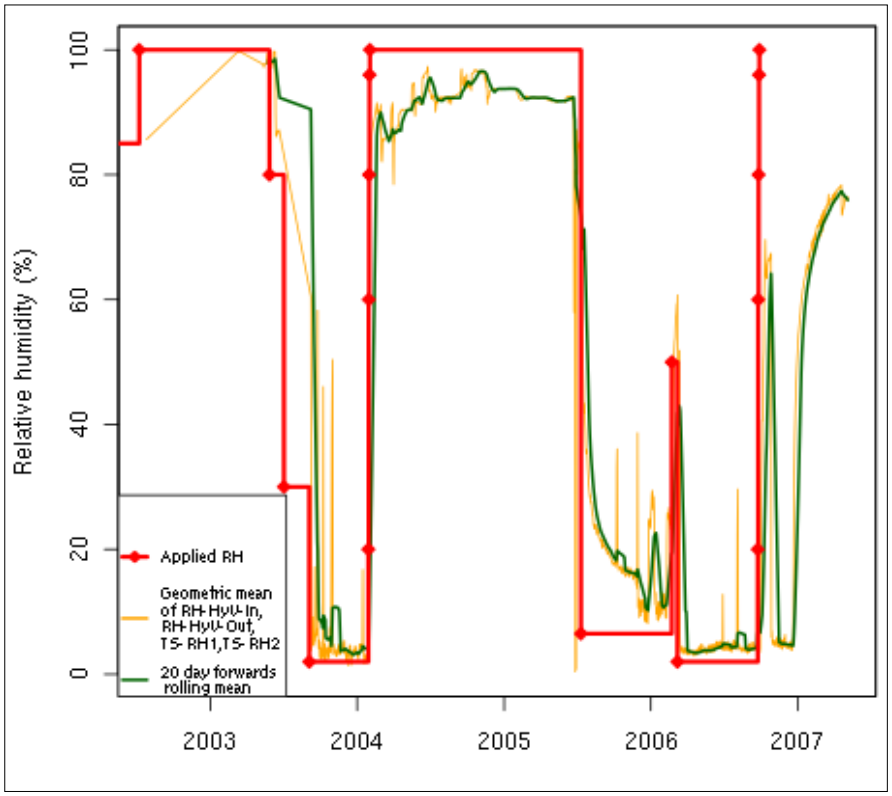

Figure 5-17. Applied relative humidity and selected gauges

5.4.3 Implementation

Using the domain outlined in Figure 4-12, a 1D axisymmetric (cylindrical) grid was developed (Figure 5-18). The 1D domain represents a horizontal portion of rock from the tunnel wall out to a distance (or depth) of 65 m. The finite element mesh comprised of 297 line elements with lengths ranging from 1 mm to 1.2 m. Most elements are concentrated within the first 2 m of the tunnel wall (Figure 5-19).

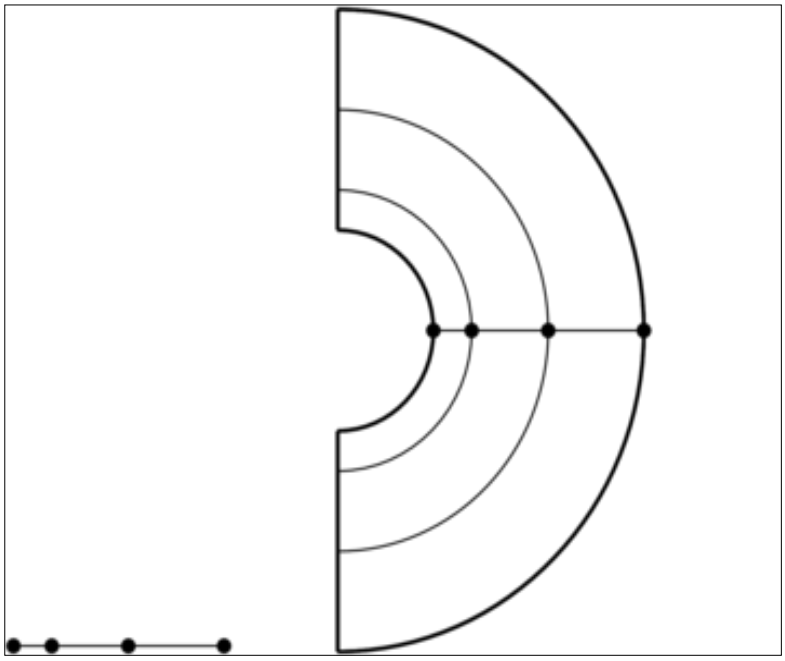

Figure 5-18. 1D model domain and mesh of line elements (left), and the axisymmetric variant (right) showing the increased element volumes associated with the line elements.

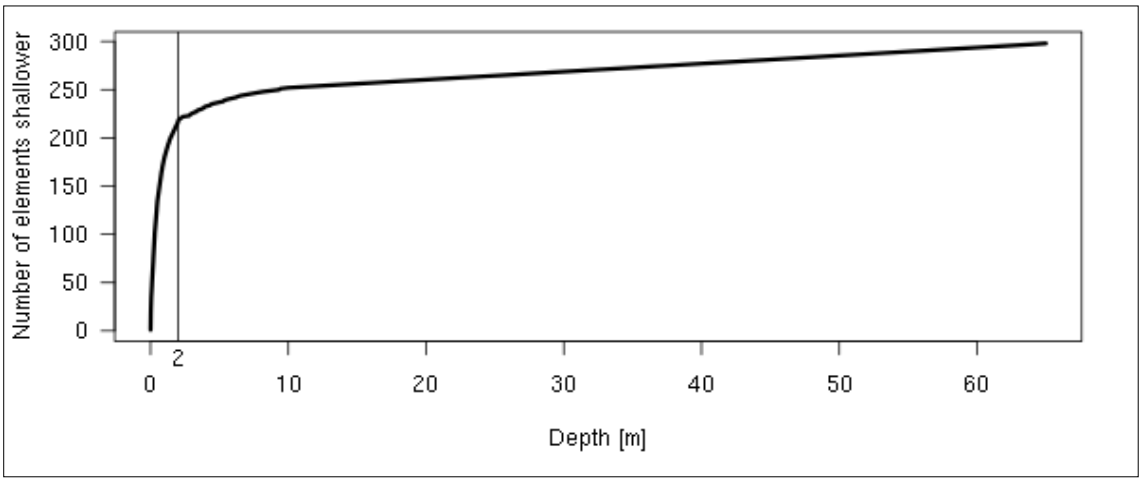

Figure 5-19. 1D mesh spacing, showing number of elements with a radial dimension less than the indicated radial depth. As shown, most elements are within 2 m of the tunnel wall.

As a consequence of the simplicity of the model, it takes only about 10 seconds to run – highly beneficial for uncertainty and sensitivity analysis.

5.4.4 Results and Sensitivity Analyses

As series of sensitivity analyses were conducted in addition to the reference case looking at variation in key results as a function of intrinsic permeability and reference porosity.

The porosity of 0.19 determined for the Drying Test (Step 0), shows a better fit to the water mass balance results (see Figure 5-20) than the lower porosities. The earlier part of the main desaturation event fits the results better than at later times, however the intrinsic permeability (shown in Figure 5-21) appears to be much less influential than porosity. In all cases the mass balance appears to be representative of the observed experimental data for Phase 1 and 2.

The water contents of samples taken from boreholes before and after the second desaturation period by Traber (2003) and Fernández *et al.* (2007) are assessed against model results in Figure 5-22 and Figure 5-23 respectively. In both cases the water contents determined in the laboratory have been recalculated according to the porosity of the base case model (0.19). The general level of consistency is reasonable, indicating that the distribution of water removal from the tunnel wall is approximately correct.

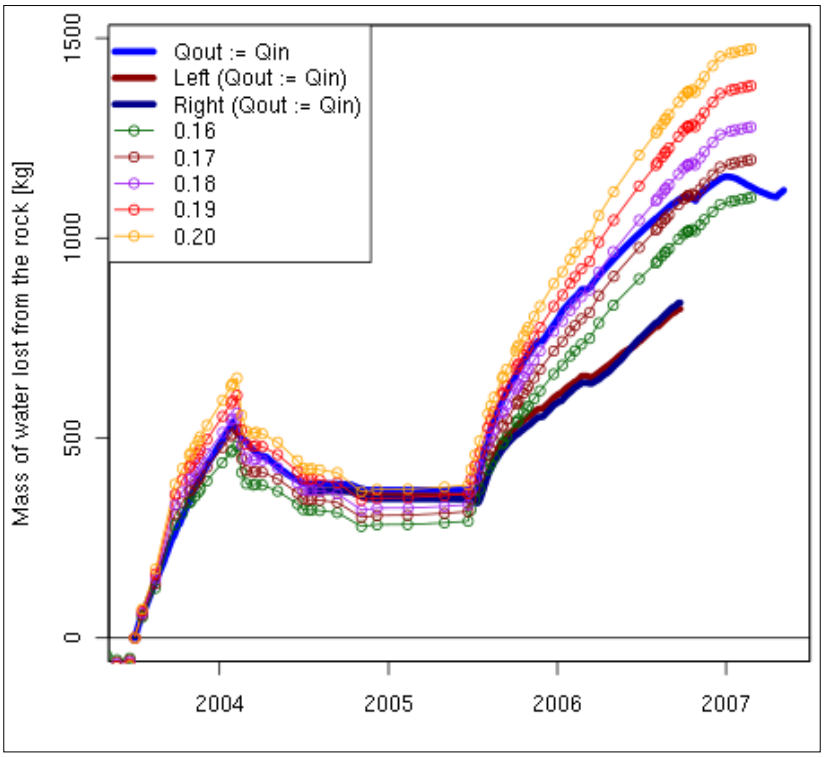

Figure 5-20. Sensitivity of water mass balance to porosity during Phase 1 and Phase 2 of the VE

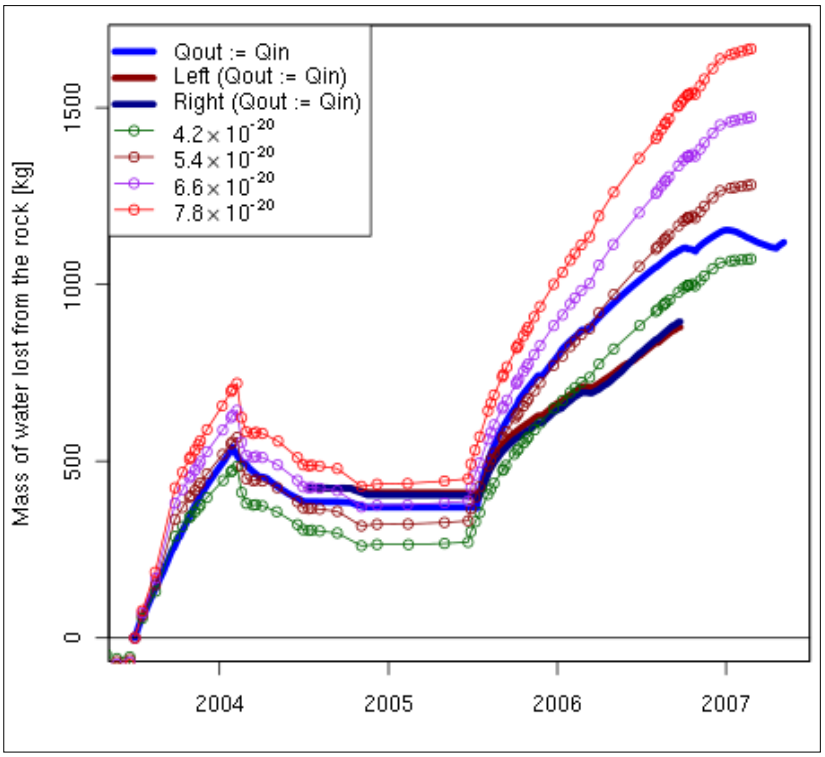

Figure 5-21. Sensitivity of water mass balance to intrinsic permeability during Phase 1 and Phase 2 of the VE

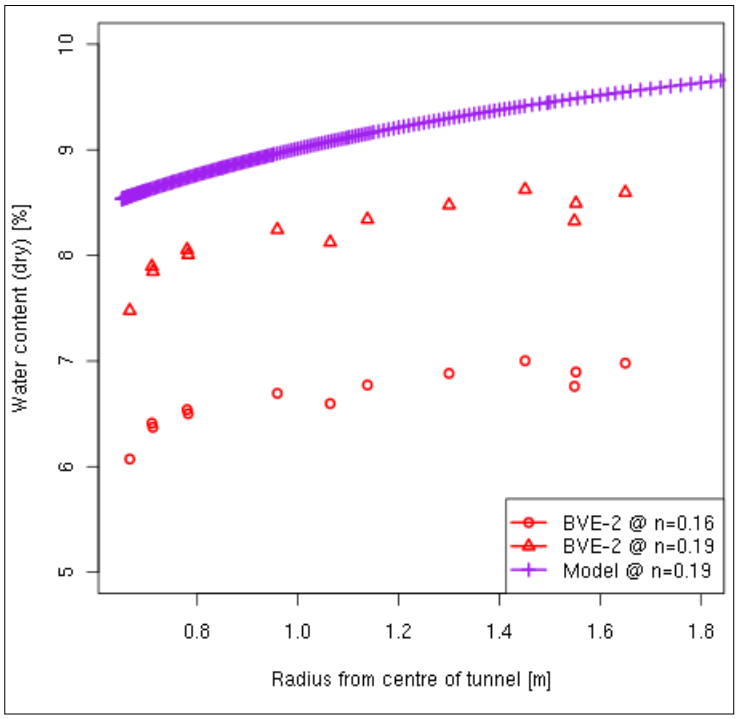

Figure 5-22. Water content (%) at 2002-07-05, start of Phase 1.

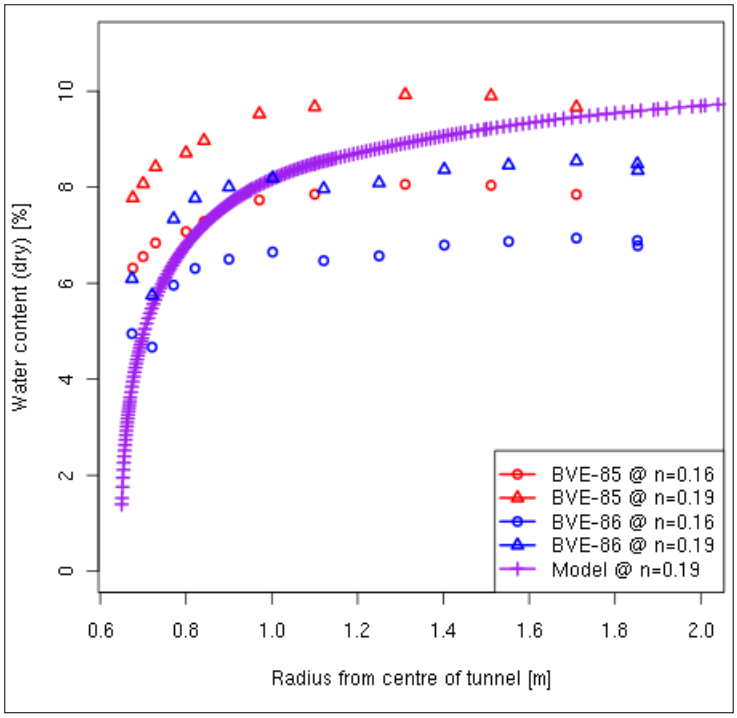

Figure 5-23. Water content (%) at 2004-01-26, end of Phase 1.

Overall, the modelled mechanical response of the rock shows an averaging effect inherent in the mathematical method used. The response has a particularly good fit to the sensor in borehole BVE-28 (Figure 5-24). The agreement is best with the sub-horizontal holes (i.e. in cylindrical coordinates, with a phi of around 90 or 270 degrees) listed in Table 5-3 and a less good agreement with those at steeper angles from the horizontal.

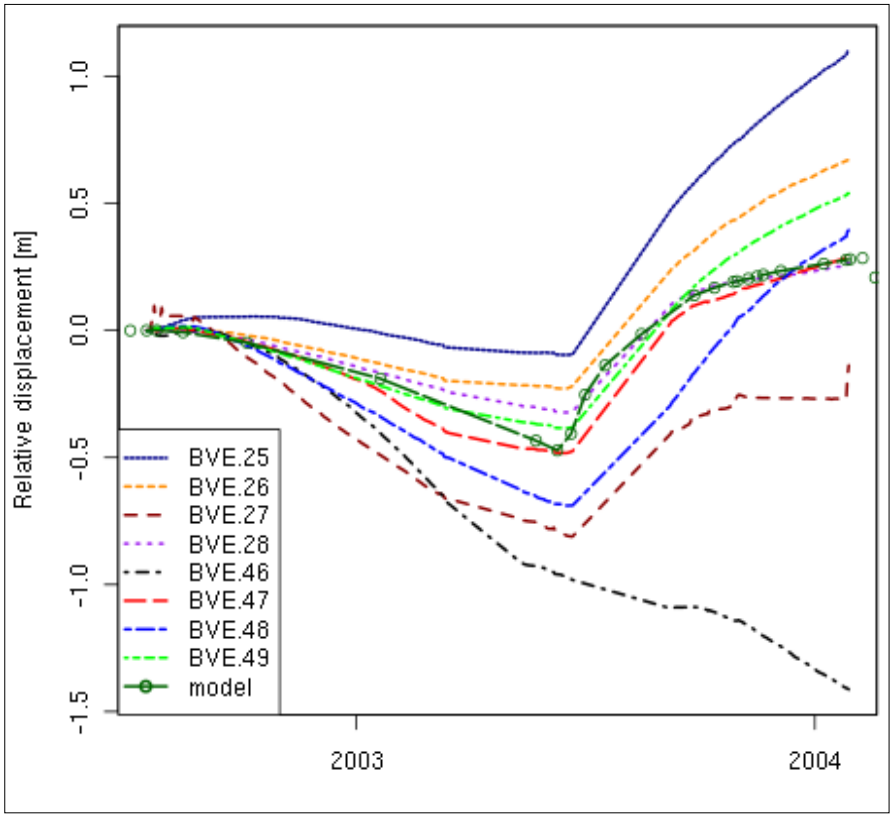

Figure 5-24. Mechanical deformation. Model results show good agreement with BVE-47.

Comparing the model with BE-47 it can be seen that:

- a slight positive displacement at the start of the data is not seen in the model
- the subsequent decreasing displacement is not quite steep enough
- the increase in displacement occurs too early
- the flattening out occurs to soon

The simplified mathematical model, although it neglects changes in the stress state of the rock and assumes equilibrium at all times, is a useful approximation of coupled hydraulic and mechanical processes.

Table 5-3 Boreholes whose sensors are in good agreement with the mechanical response. Rho is radial distance from the centre of the tunnel, z is distance down the tunnel, phi is angle from vertically upwards.

Borehole	rho	phi	z (m)
BVE-47	2.65	100	4.4
BVE-49	2.65	260	4.4
BVE-26	2.65	100	6.85
BVE-28	2.65	260	6.85

5.4.5 Prototype Tunnel Model

The problem of representing the tunnel wall interface in one model was addressed in OpenGeoSys using two separate models with domains arranged as Figure 5-25.

The flow of air and water vapour in the tunnel was assumed to be viscously dominated and for practical purposes this was represented as a saturated porous medium with very high porosity and permeability. Exchange of water mass with the rock was governed by the saturation of the rock and the concentration of water in the tunnel by coupling of the respective boundary conditions.

The exchange takes place between pairs of nodes on either side of the interface at the tunnel wall (Figure 5-26). The two models communicate via a shared memory segment and semaphores administrated by the operating system. The scheme and how it integrates with the finite element method is shown in Figure 5-27.

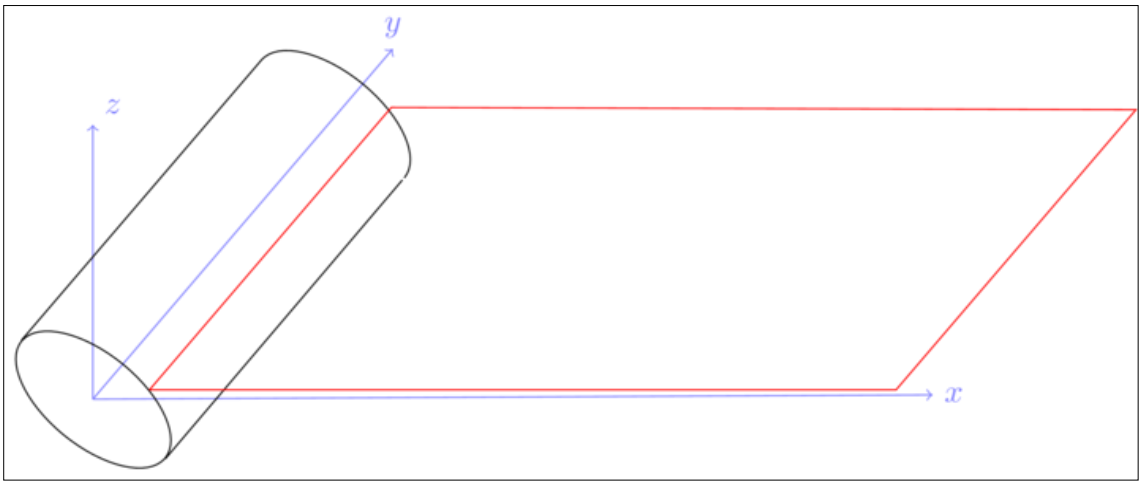

Figure 5-25. Tunnel (cylinder) and rock (plane) domains, each runs in a separate OGS instance.

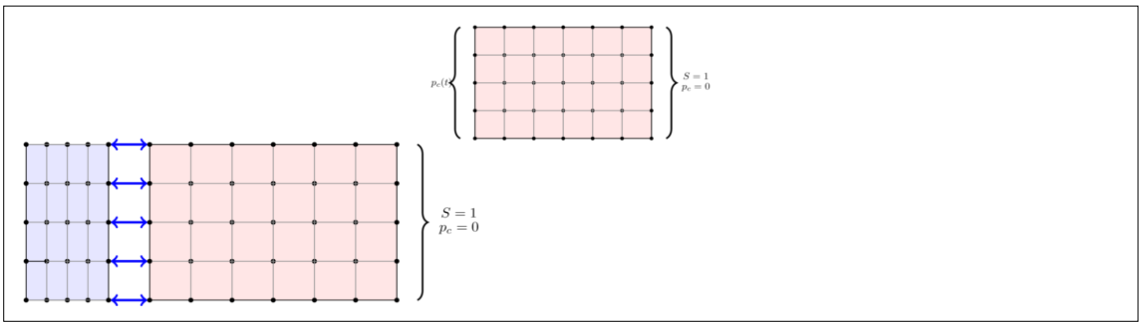

Figure 5-26: The uniformly distributed (denoted using braces) boundary condition of the rock model (top) at the tunnel wall is replaced with source terms by linking mesh nodes with those of the tunnel model (the blue rectangle).

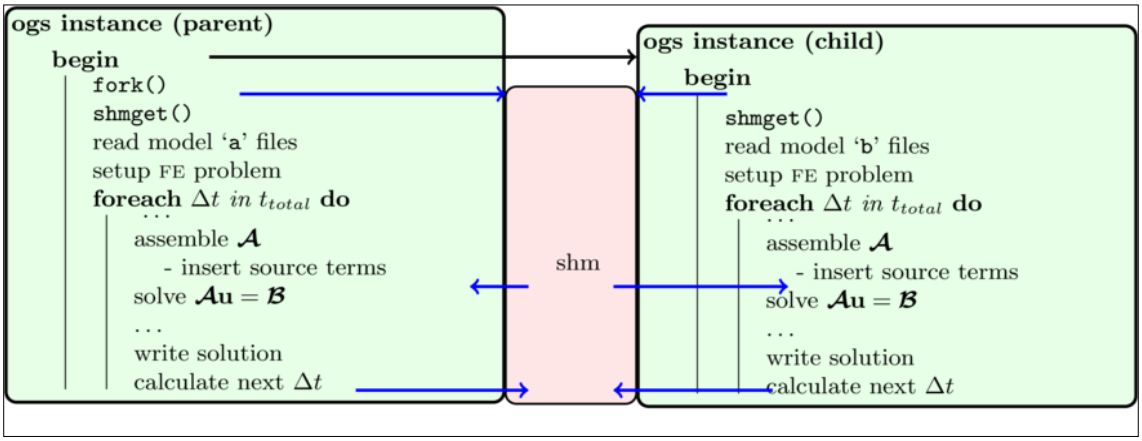

Figure 5-27. Abbreviated execution scheme of linked models showing separate memory address spaces and interaction via a third — the shared memory segment (labelled shm). The call to fork() copies the OGS process to a separate memory space. The calls to shmget() create, or attach to, a shared memory segment. Blue arrows indicate read or write operations depending on direction.

The advantages of using two separate models are that the it required little extra programming: if they were combined in OGS as a coupled model significantly more effort would be required, in this scheme all that was added to OGS was functionality to set up, write and read the shared memory, and semaphores that control when this happens. The semaphores cause each OGS instance (i.e. each model) to be either paused or continued, as appropriate and hence run different time-stepping strategies for each model, as required. This key disadvantage of this approach is that the two models are not fully coupled, greatly increasing the chances for numerical instability if the timestepping on one or both sides is not adequately conditioned.

The functions that define the behaviour at the tunnel interface, for both models, are implemented in a standalone module that is included by OGS. This allowed more rapid development and greatly simplified specific testing.

Consistent with the experience of a number of other teams in Task A, persistent stability and scaling issues were found when using this form of sequentially coupled model (rather than fully coupled as illustrated by the QPAC calculations), so no complete Phase 1 and 2 results using the tunnel model are available using OpenGeoSys, however work is continuing beyond the end of DECOVALEX-2011 to resolve these issues.

5.4.6 Summary

Many aspects of the Ventilation Experiment can be modelled satisfactorily within the uncertainties in the data using a simple 1D axisymmetric finite element approximation of Richards' Equation, implemented in OpenGeoSys. Of particular interest was the ability to model the mechanical response of the system. Very good agreement with the

horizontal VE results as a simple post-processing step rather than through fully-coupled analysis.

Representation of the tunnel using OGS has proven difficult thus far, although work is ongoing.

5.5 Blind Predictive Analysis

As referred to in Section 5.1, the hydro-mechanical data for the Opalinus Clay for Phase 2 was not released to the teams until after November 2011. Prior to the release of the data the organisers required that predictions for Phase 2 evolution be submitted for evaluation. These results were then presented publically without the participants prior knowledge.

The graphs below show selected comparisons for relative displacement, water pressure, water content and relative humidity for the teams as presented at the November 2011 meeting (current graphs in the draft Garitte *et al*, 2012). Results for Quintessa, CAS (Chinese Academy of Sciences), JAEA (Japanese Atomic Energy Agency) and CEA (Commissariat à l'Energie Atomique) were compared. However, due to technical difficulties, the results of UoE were not available sufficiently early before the meeting and hence are not shown because they cannot be considered a genuine blind prediction. The full compilation of Phase 2 results are currently being worked on and will be presented in Garitte *et al.* (2012), however the task organiser has not yet updated his graphs with the available UoE results at the time of writing. Given the good match between UoE's total mass balances over Phase 2 (compare Figure 5-28 and Figure 5-21), it is expected that the UoE results would have been consistent with the other teams' results. It must be emphasised that the results presented in Figure 5-28 to Figure 5-33 are interim and hence indicative only, and will be updated for the final DECOVALEX-2011 reporting.

Overall the results are coherent across teams, generally fall within the bounds of the observations, and reflect the temporal variations of the experiment. There are clearly some differences across the teams, particularly with respect to the CAS results and relative humidity. The only area where there was a consistent deviation was in the saturated fluid pressures (Figure 5-32), mainly in the inability to capture the rapid increase in pressure from unsaturated to saturated during the early high applied relative humidity during Phase 2 (early 2005). This should not be a surprise because all teams struggled to represent these rapid variations during Phase 1, and there would be no expectation that they would be replicated in Phase 2.

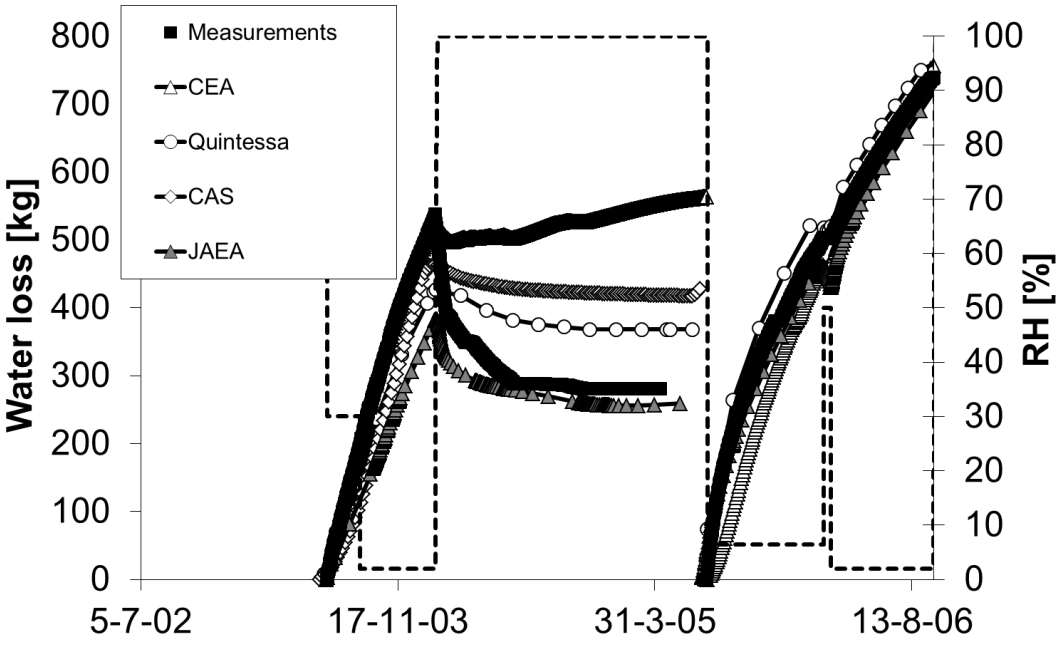

Figure 5-28. Comparison of mass balance across Task A team members involved in the blind prediction (draft from Garitte *et al*, 2012).

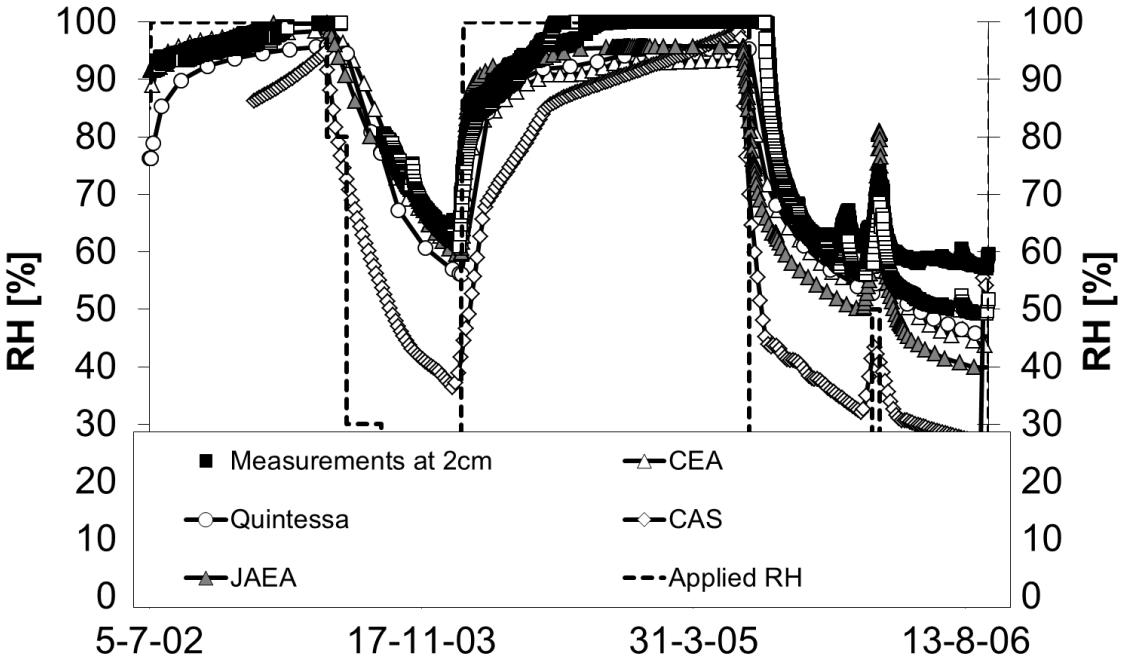

Figure 5-29. Comparison of relative humidity at 2cm depth into the tunnel wall across Task A team members involved in the blind prediction (draft from Garitte *et al*, 2012).

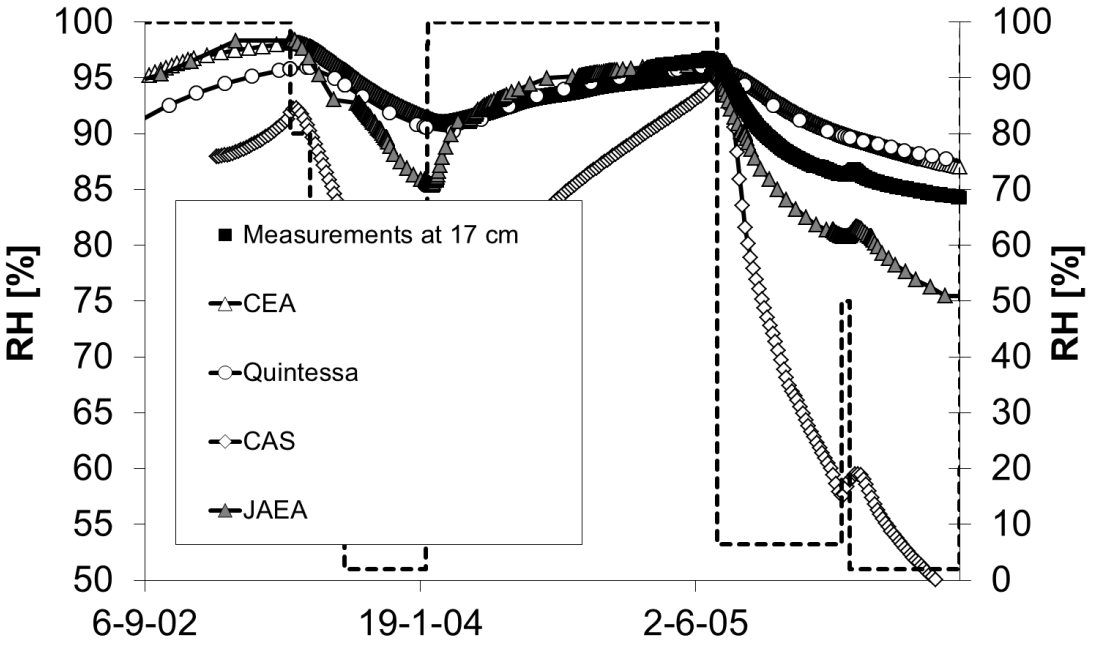

Figure 5-30. Comparison of relative humidity at 17cm depth into the tunnel wall across Task A team members involved in the blind prediction (draft from Garitte *et al*, 2012).

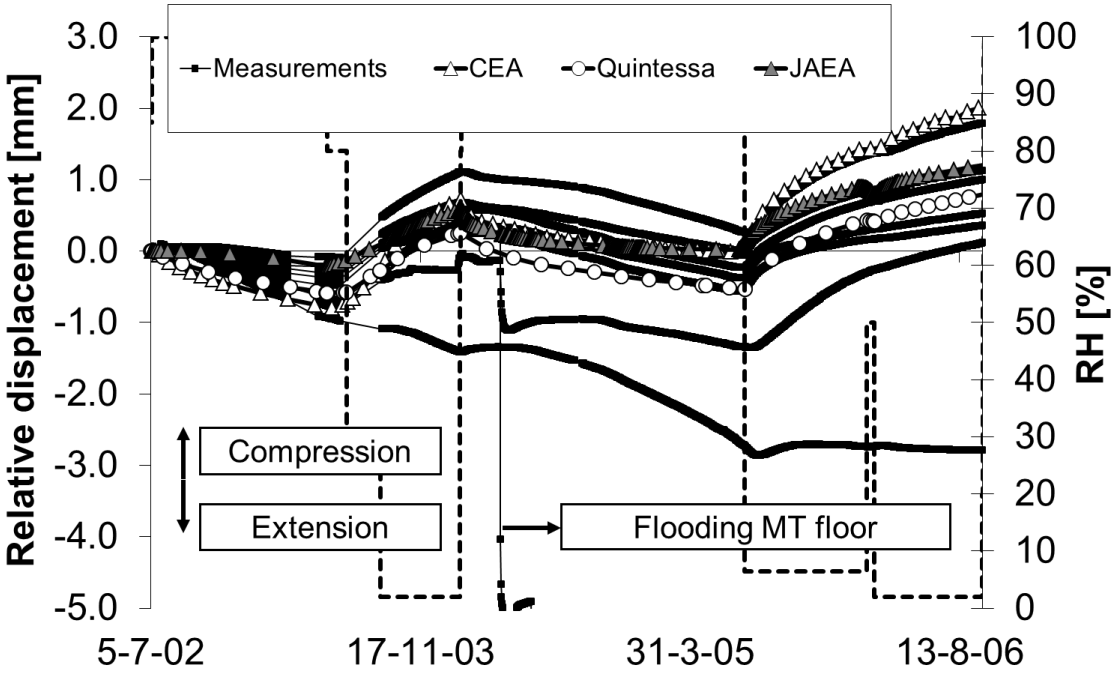

Figure 5-31. Comparison of relative displacement from the tunnel wall to 2 m depth into the clay across Task A team members involved in the blind prediction (draft from Garitte *et al*, 2012).

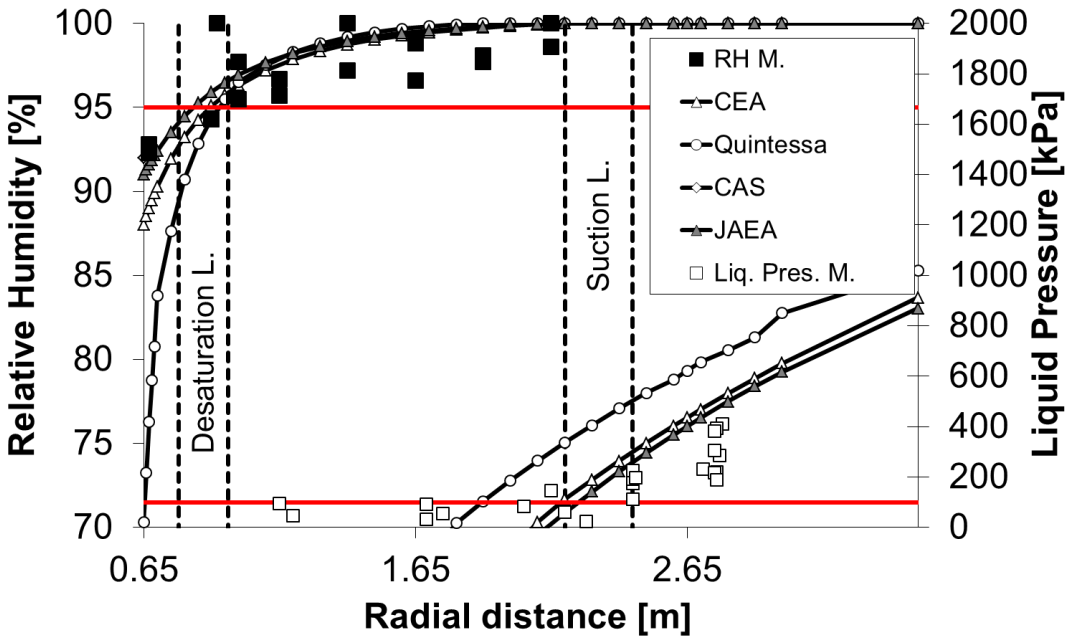

Figure 5-32. Comparison profile of relative humidity and water pressures at 5/7/2002 from the tunnel wall to 3m depth into the clay across Task A team members involved in the blind prediction (draft from Garitte *et al*, 2012).

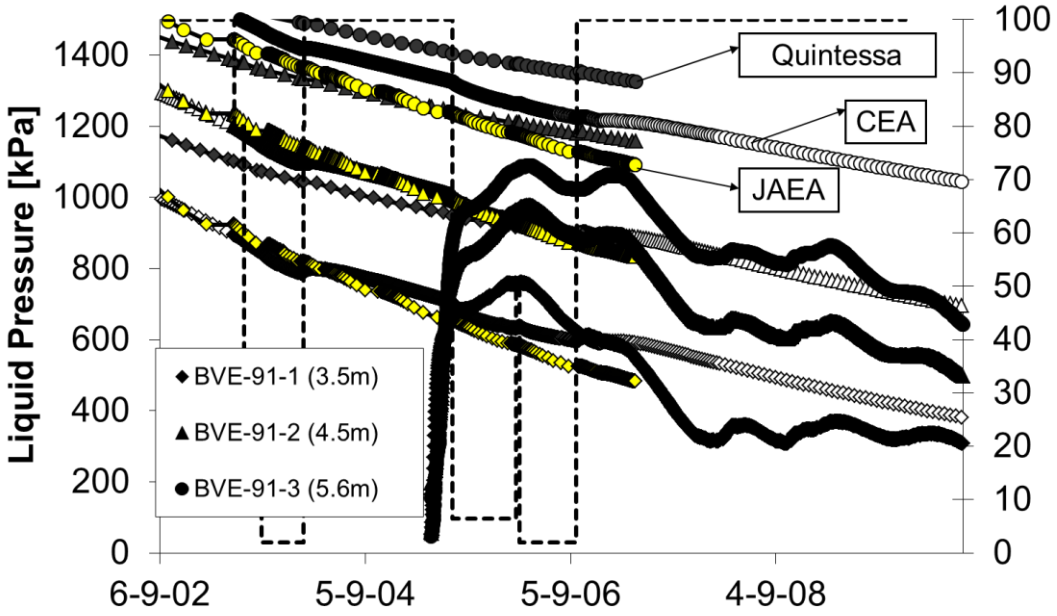

Figure 5-33. Comparison saturated water pressures and available data in the clay across Task A team members involved in the blind prediction (draft from Garitte *et al*, 2012) during Phase 2.

6 Step 3: Non-reactive Transport Modelling

In order to progress modelling the reactive chemical system, with all the attendant uncertainties in process and parameterisation, it was first necessary to gain confidence in the basic transport processes by understanding and representing the significantly simpler non-reactive system. Hence the first area of work considered just the chloride system which is independent of the reactive system.

6.1 Chloride Geochemical Data and Conceptual Model

The primary discussion of the geochemical analysis is provided by Fernandez *et al.* (2007 a, b) which describes the results of four campaigns of data collection. Boreholes were drilled and rock-core taken for geochemical and whole-rock analysis on or around the following dates, note that these are a subset of the boreholes drilled during these campaigns:

Table 6-1 . Boreholes used for geochemical analysis and their excavation date

Borehole	Date
BVE 82	5/7/2002
BVE 85	26/1/2004
BVE 86	26/1/2004
BVE 97	2/5/2005
BVE 99	2/5/2005
BVE 100	2/5/2005
BVE 105	9/10/2006
BVE 106	9/10/2006
BVE 107	9/10/2006
BVE 109	9/10/2006
BVE 110	9/10/2006

The pore water analysis was conducted using two techniques. The majority of data was obtained through whole-rock analysis, whereby core samples were crushed and then leached using a solid to liquid ratio of 1:4, and the resulting fluid analysed. Some data were also obtained through squeezing and the extracted fluid analysed. In all cases consistency in the squeezing results and the whole-rock analysis was good, sufficient to give confidence that the obtained results were representative. These two

different forms of measurement give rise to two natural, but different, ways to describe the concentration of chloride in the porous medium. The whole-rock analysis produces concentration per dry rock mass (mg/kg rock) while the squeezing analysis tends to give concentration in the water extracted (mg/l or mol/l). Conversion between the two requires knowledge of the absolute water content, fluid saturations, total porosity and any geochemical porosity exclusion effects for the species in question. Indeed the estimation of geochemical porosities for the Opalinus clay, as discussed by Fernandez *et al.* (2007a,b) in the context of chloride exclusion, can be achieved through the comparison of these different analyses for similar samples. Fernandez *et al.* (2007 a, b) discuss the analysis and interpretation in full detail, however the following key points can be established:

1. The Opalinus Clay water is marine in origin and has a background salt concentration of approximately 0.3-0.4 mol/l.
2. From supporting work cited in Fernandez *et al.* (2007b), chloride is expected to be present in between 0.62 and 0.55 of the free porosity – this is termed the 'chloride porosity ratio' and was assumed to occur primarily from anion exclusion processes.
3. There is a considerable increase in concentration, and the absolute amount of chloride salts close to the tunnel wall (see Figure 6-1). While the boreholes are constructed at different locations in the tunnel, at each time, the profile of chloride is quite consistent.

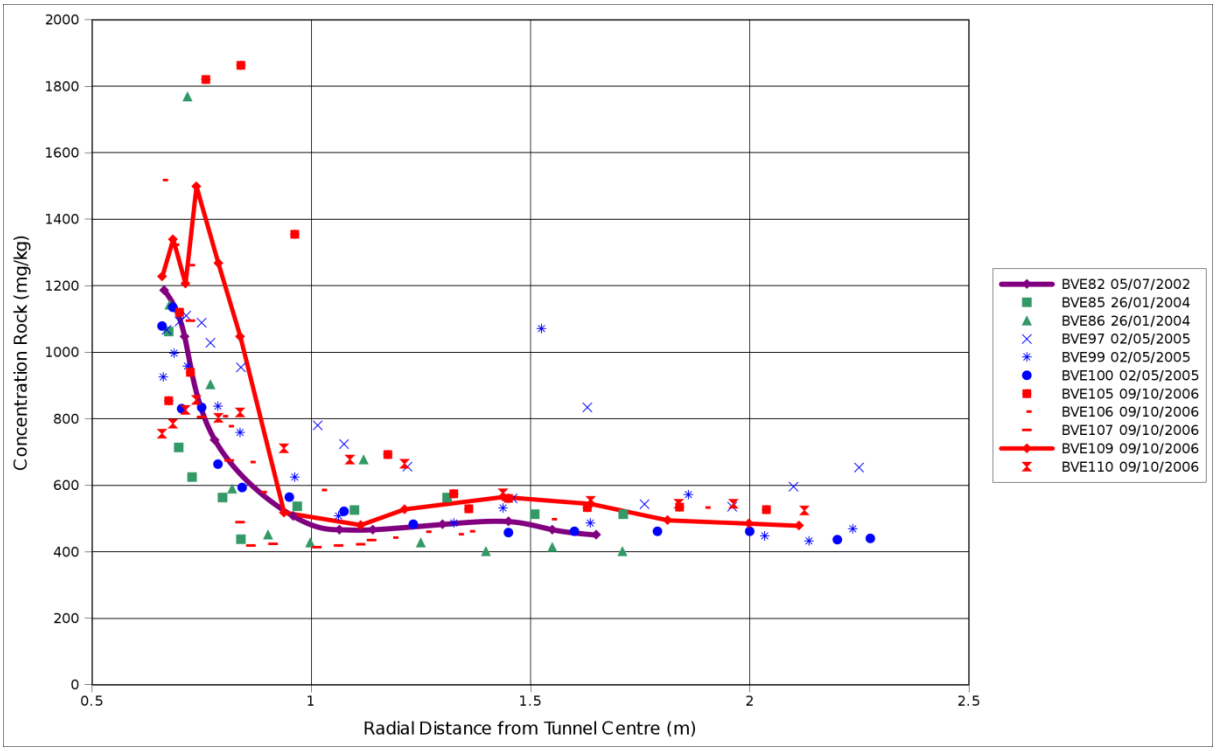

Figure 6-1. Chloride borehole data plotted for all available boreholes and coloured by the four sampling times. Curves show representative behaviour for two selected boreholes. Data are shown as mg chloride/kg rock, consistent with the measurement technique and are reproduced from Fernandez *et al.* (2007a,b)

The conceptual interpretation of the chloride evolution is relatively simple, assuming that chloride can be treated as a fully conservative tracer. Evaporation of water at the tunnel wall and within the pores causes the chloride to become locally concentrated as the solutes do not leave the rock with the water vapour. The desaturation and lower water pressures at the tunnel wall causes more water containing chloride to flow towards the tunnel by advection. This inflowing water causes not only the chloride concentration in pore water to rise through reduction in the volume of water in which the chloride is dissolved, but also the relative amount of chloride relative associated with a given rock mass. The creation of a concentration gradient of chloride in pore water generates back-diffusion of solutes into the host rock away from the tunnel. The two competing processes of advective inflow and diffusive outflow will tend to move the chloride system to a steady state and create the relatively stable profile of concentration seen from the tunnel wall. There is clearly scatter in the data between boreholes at given times, but given the relatively few data points, the uncertainties in the measurement techniques and the apparent scatter in each profile, it is difficult to construct an argument for structured heterogeneity in the system on the basis of these results.

6.2 Chloride porosity and migration

The conceptual model for chloride migration was taken directly from the interpreted behaviour described by Fernandez *et al.* (2007b) and restated in Section 3. However, one area of particular concern was the representation of the so-called 'chloride porosity'. An often reported feature of argillaceous materials is that the water-filled porosity of the system is not the same as the porosity estimated from other methods, most notably geochemical methods (e.g. Pearson, 1998). The reason for this disparity can come from a number of sources but fall into two general classes. The first is an electrochemical exclusion process whereby charged anions (such as chloride) become excluded from part of the total available water due to the net negative charge on clay surfaces. The second process is related, and comes from the observation that all of the water in a claystone is not present as free water in open porosity. Instead, depending on the clay, saturation, geochemistry and stress state, water may be present in the interlayers between clay layers, or may be adsorbed to the surface of the clay. In these alternative physical forms of water, ions may also be excluded.

Fernandez *et al.* (2007b) gives an Opalinus Clay 'chloride porosity ratio' ranging between 0.55 and 0.62, this being the scaling factor applied to the total porosity to estimate the effective geochemical porosity for chloride. Thus for the Opalinus Clay and other claystones, a conceptual evaluation must be made and reflected in the mathematical representation of charged species migration through advection and diffusion. Consistent with Fernandez *et al.* (2007a,b) concentrations of chloride in groundwater are calculated using the non-excluded water volume, rather than the total water volume.

6.3 Mathematical model

The mathematical model comprises two processes; advection and diffusion. In addition to the hydro-mechanical model the equations assumed to governing the basic model are:

$$g_{diff,i} = -\mathrm{AD}_{\mathrm{Eff,i}} \nabla C_i$$

$$g_{adv,i} = q_{\mathrm{liquid}_{\mathrm{water}}} C_i \qquad 6.1$$

$$D_{\mathrm{Eff,i}} = D_{w,i} S_w \frac{\theta}{\tau}$$

where $g_{diff,i}$ is the diffusive flux of species 'i' (mol s^{-1}), $g_{adv,i}$ is the advective flux of species 'i' (mol s^{-1}), C_i is the concentration of species 'i' in water (mol m^{-3}), $D_{\mathrm{Eff,i}}$ is the effective diffusion coefficient (m^2 s^{-1}), A is the total area of porous medium transfer (m^2), $q_{\mathrm{liquid}_{\mathrm{water}}}$ is the volumetric flux of liquid water (m^3 s^{-1}), θ is the available porosity (including any geochemical porosity effects), τ is the tortuosity (-), S_w is the water saturation (-) and $D_{w,i}$ is the free water diffusivity of species 'i' (m^2 s^{-1}).

The principal uncertainty in the formulation is in the specification of the correct liquid water flow rate with regard to the potential conceptual importance of multiple 'types' of porosity. Because the chloride exclusion porosity implicitly includes a number of different processes, including having water bound by interaction with swelling clays and anion exclusion, the effective advective water flux for chloride transport could be:

- **Non-chloride water 'bound'; physical partitioning dominates**: advective water transport takes water from only the 'chloride' porosity. This model assumes that the water not associated with chloride is physically bound to the rock matrix, dominantly as inter-layer water (as one might expect in a fully saturated bentonite). Therefore in this model all the advective migration of water is associated with the chloride transport leading to proportionally higher transport velocities.
- **Non-chloride water 'free'; electro-chemical partitioning dominates**: all water is advected, hence the flux of water calculated applies to all water, not just the chloride associated water. This model assumes the partitioning is essentially an electro-chemical process related to chloride and does not involve any differing physical forms of water. Therefore in this model the advective migration of water is proportionally partitioned between the water associated with the chloride and non-chloride porosity, leading to slower transport velocities than physical exclusion model, i.e. the conventional D velocity calculated using the total available porosity.
- **Combination Model**: some interpolation between the two end-members above using some form of mixed dual porosity model.

The working assumption adopted by Quintessa and UoE, given the available information presented by Fernandez *et al.* (2007a,b), was that the anion exclusion process would dominate the observed chloride porosity, hence for a starting point the electro-chemical exclusion model should be the reference assumption and that other models should be investigated as process sensitivities. It should be noted that when considering only concentrations of chloride in groundwater as the principal output from the analysis (rather than mass of chloride per unit rock mass, for example), and when using the electro-chemical exclusion model that the chloride porosity scales out of the equations (6.1) and hence can be neglected.

Some consideration was given to the potential for was transport through osmotic effects (Bader and Kooi, 2005), however through simple hand calculations of potential water flux rates versus those seen in the hydro-mechanical modelling, showed that osmotic water fluxes would only contribute significantly less than 1% of the hydro-mechanical flow rates for the concentration contrasts observed. For this reason the osmotic water fluxes were not considered and hence any coupling between the chloride concentration and water migration could also be neglected.

6.4 General Modelling Approach

Given the relative simplicity of the process model associated with non-reactive transport, it was considered a good test of the Quintessa and UoE Step 2 models to attempt to replicate the chloride disposition results. This approach gave an opportunity to compare numerical implementations, and understand the potential sensitivity of the chloride results to the difference in the hydro-mechanical behaviours seen in Step 1 and 2.

The equations given in formula 6.1 were already available in QPAC and OGS, and hence calculations were relatively simple to perform for both teams. Two general approaches were adopted for implementation:

1. Direct addition of the tracer transport process model to the hydro-mechanical formulation utilising common timesteps.
2. Re-use of the same grid as used for the hydro-mechanical calculations, but simply transposing the liquid water fluxes and water saturations from the hydro-mechanical calculations as input to the tracer transport model.

Given there is little opportunity for coupling between the process models, both methods are functionally equivalent provided the flux transposition for the second method is at sufficiently fine intervals. QPAC used the first approach and OGS used the second.

Chloride results were calculated by both Quintessa and UoE using the respective Step 2 models (see previous section) and both are presented.

6.5 Representative Inputs and Results

The reference Quintessa Step 2 1D cylindrical model implemented in QPAC (Section 5.3) which includes an explicit representation of the tunnel are presented here as a reference point, having already been demonstrated to give a good predictive mass balance and representation of tunnel relative humidity across Phases 1 and 2 of the ventilation experiment . The QPAC model used a monolithic approach in this case and appended the Tracer Transport (TT) module to the existing 1D multiphase flow (MPF) and mechanical (M) calculations, using the liquid water flows and water saturations from the MPF directly. As discussed previously the model contained 45 compartments in the cylindrical representation of the host rock, down to sub-cm scales close to the tunnel, increasing approximately geometrically to 10s of metres at the outer radial boundary.

The input parameterisation is tabulated below.

Table 6-2. Input parameters for the Quintessa QPAC chloride model.

Parameter	Unit	Value	Source
Chloride Porosity Ratio	-	0.575	Fernandez *et al.* (2007a,b)
Background Chloride Concentration	mol/l	0.35	Fernandez *et al.* (2007a,b)
Free water diffusion coefficient	$cm^2\ s^{-1}$	$2x10^{-5}$	Boudreau (1997)
Tortuosity	-	3.6	Estimate – various sources. Minor calibration parameter

Boundary conditions were purely advective on the outer cylindrical boundary of the model (with no-flow in the axial directions, consistent with the hydraulic model) and no-flow across the tunnel boundary, assuming that no chloride is lost through evaporation.

The results at the time of the four drilling campaigns are compared with the equivalent experimental results in Figure 6-2 to Figure 6-5. Note that in order to avoid any inconsistencies between the interpreted water concentration inferred from whole rock analysis, we use a direct comparison between the whole-rock concentration measurements (kg chloride per kg dry rock – as measured), rather than the inferred pore-water concentrations.

The consistency between the numerical results and the experimental data is clearly very good, and it is encouraging that features such as the localised peak seen in 6/10/2006 (compare Figure 6-4 and Figure 6-5) is replicated by the model. This result lends considerable support to the hydro-mechanical results, and provides a high degree of confidence that the process representations are well captured by the numerical tool.

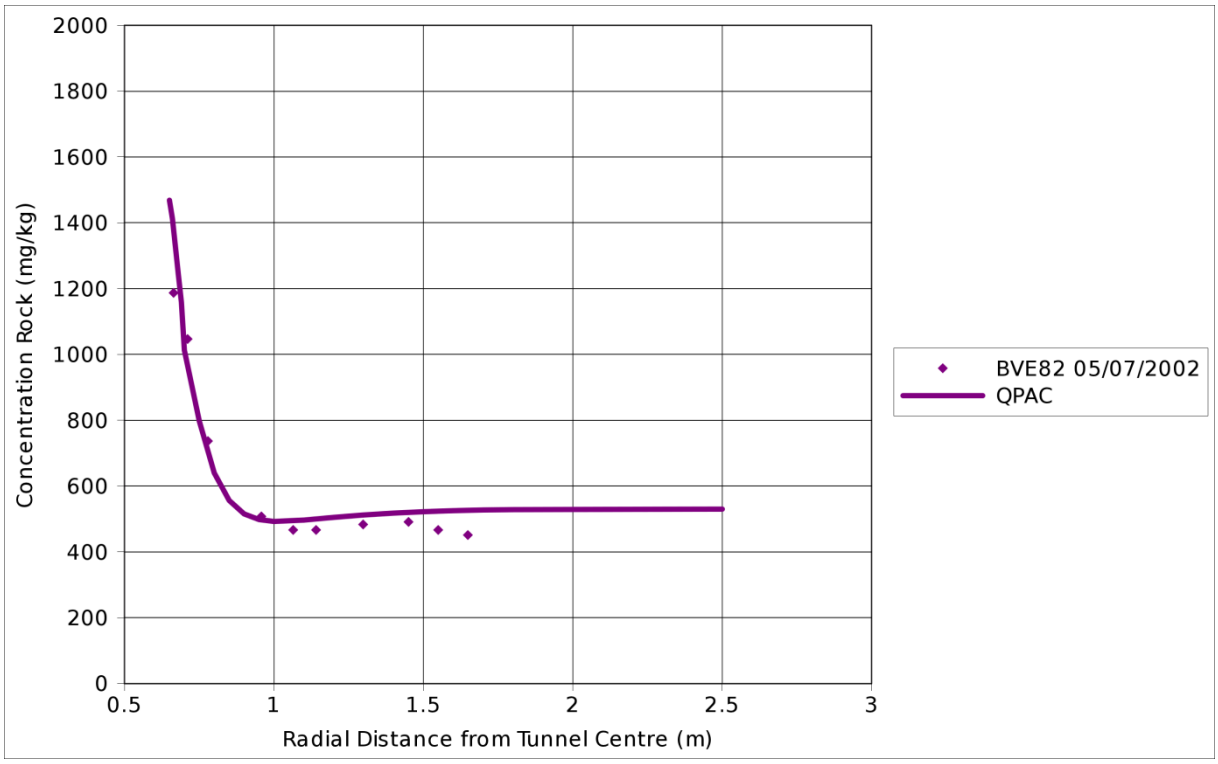

Figure 6-2. Comparison of calculated chloride mass concentrations (mg/kg rock) versus the experimental data at 5/7/2002 for QPAC.

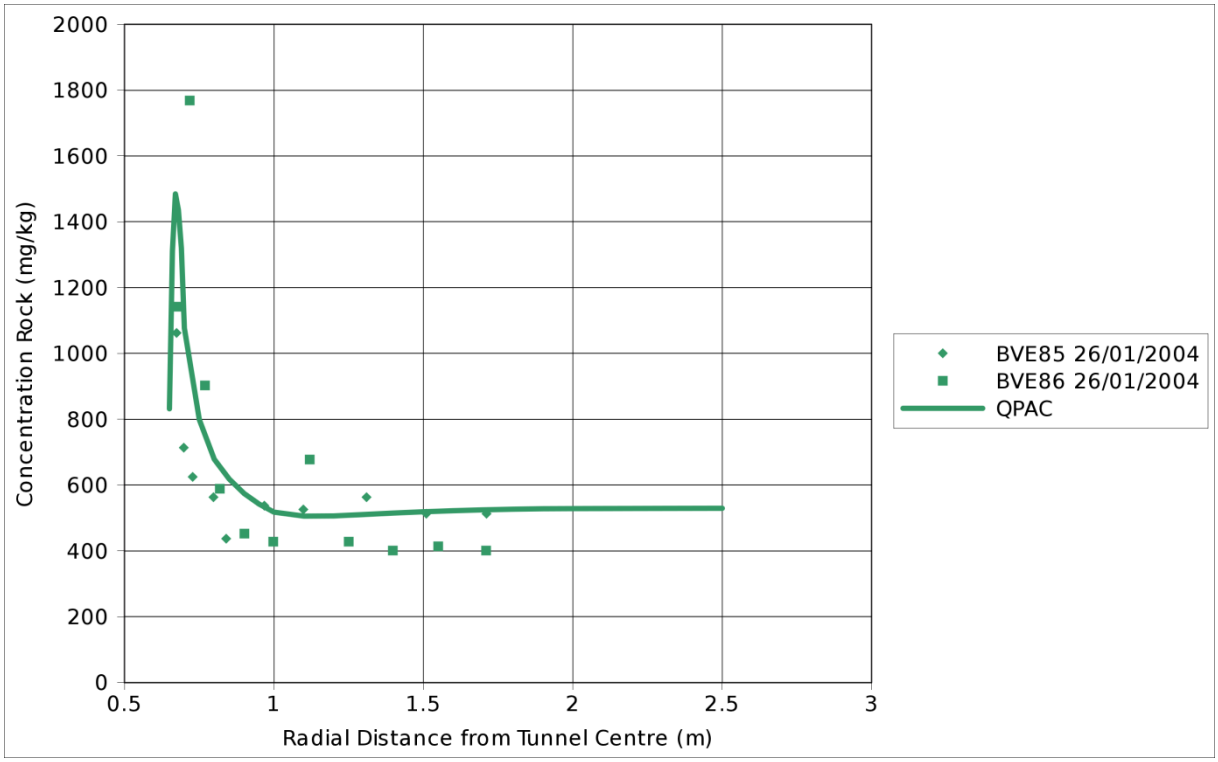

Figure 6-3. Comparison of calculated chloride mass concentrations (mg/kg rock) versus the experimental data at 26/1/2004 for QPAC.

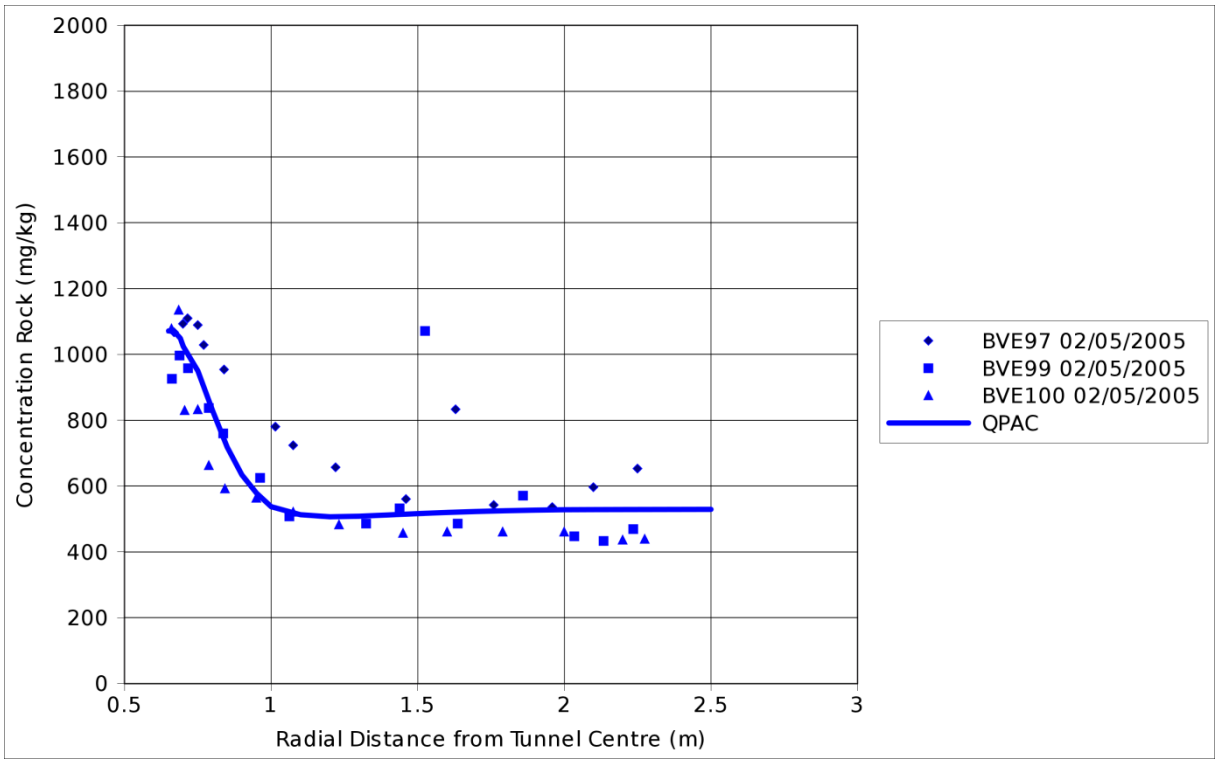

Figure 6-4. Comparison of calculated chloride mass concentrations (mg/kg rock) versus the experimental data at 2/5/2005 for QPAC.

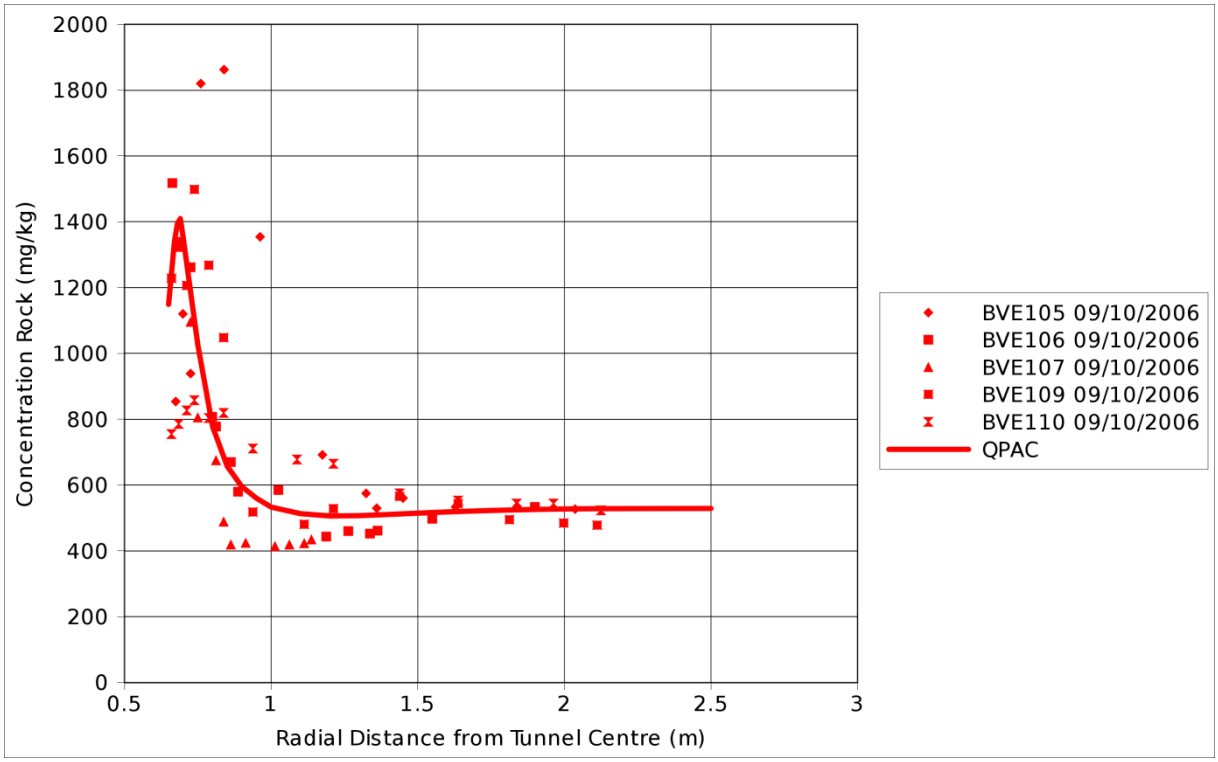

Figure 6-5. Comparison of calculated chloride mass concentrations (mg/kg rock) versus the experimental data at 9/10/2006 for QPAC.

The full UoE results with the parameterisation given in Table 6-3 are shown in Figure 6-6 to Figure 6-9.

Table 6-3. Input parameters for the OGS chloride model.

Parameter	Unit	Value	Source
Chloride Porosity Ratio	-	0.565	Fernandez (2007a,b)
Background Chloride Concentration	mol/l	0.28	Fernandez (2007a,b)
Free water diffusion coefficient	$cm^2\ s^{-1}$	$2.03x10^{-5}$	Boudreau (1997)
Tortuosity	-	2	Estimate – various sources.

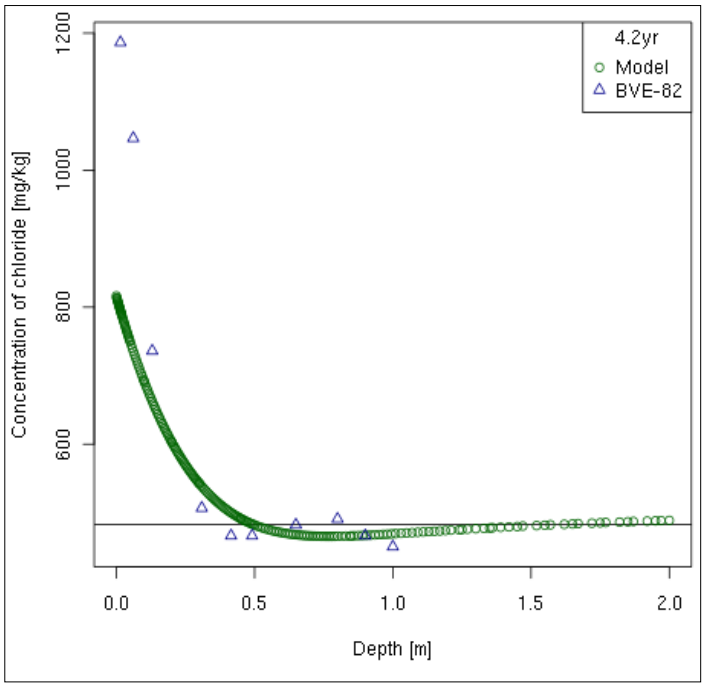

Figure 6-6. Comparison of calculated chloride mass concentrations (mg/kg rock) versus the experimental data at 5/7/2002 for OGS.

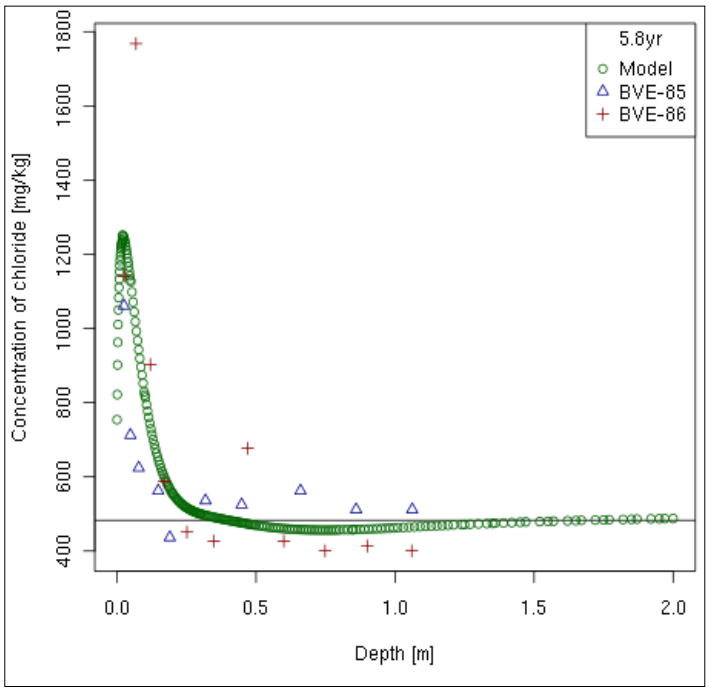

Figure 6-7. Comparison of calculated chloride mass concentrations (mg/kg rock) versus the experimental data at 26/1/2004 for OGS.

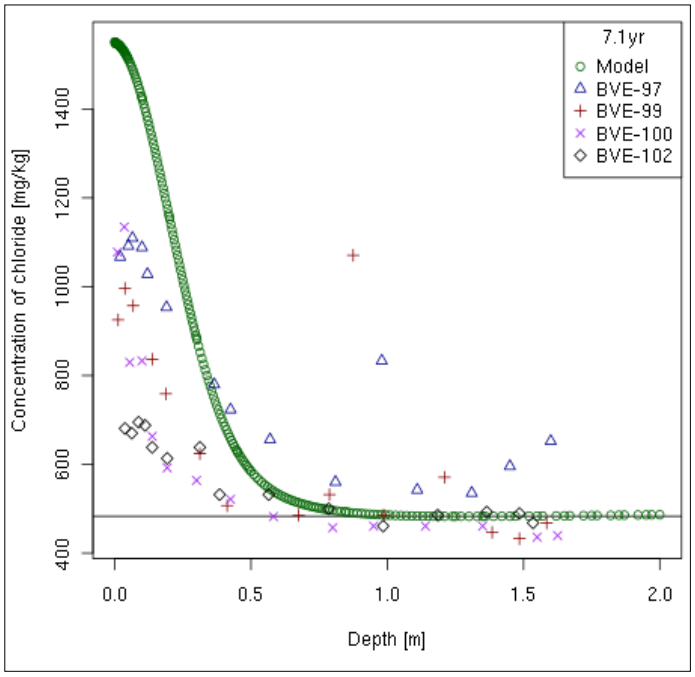

Figure 6-8. Comparison of calculated chloride mass concentrations (mg/kg rock) versus the experimental data at 2/5/2005 for OGS

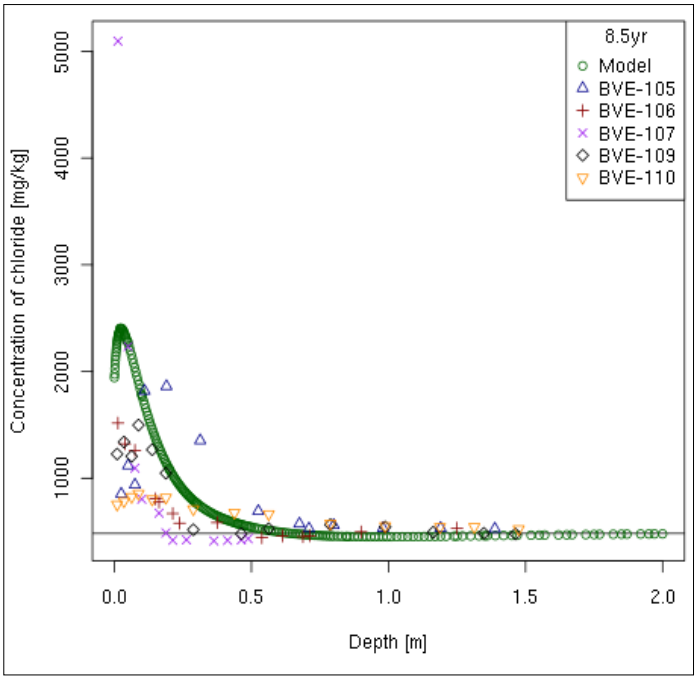

Figure 6-9. Comparison of calculated chloride mass concentrations (mg/kg rock) versus the experimental data at 9/10/2006 for OGS.

As an illustration of the level of agreement between the codes a cross comparison is shown for 2/5/2005, this time using the comparison against chloride water concentration.

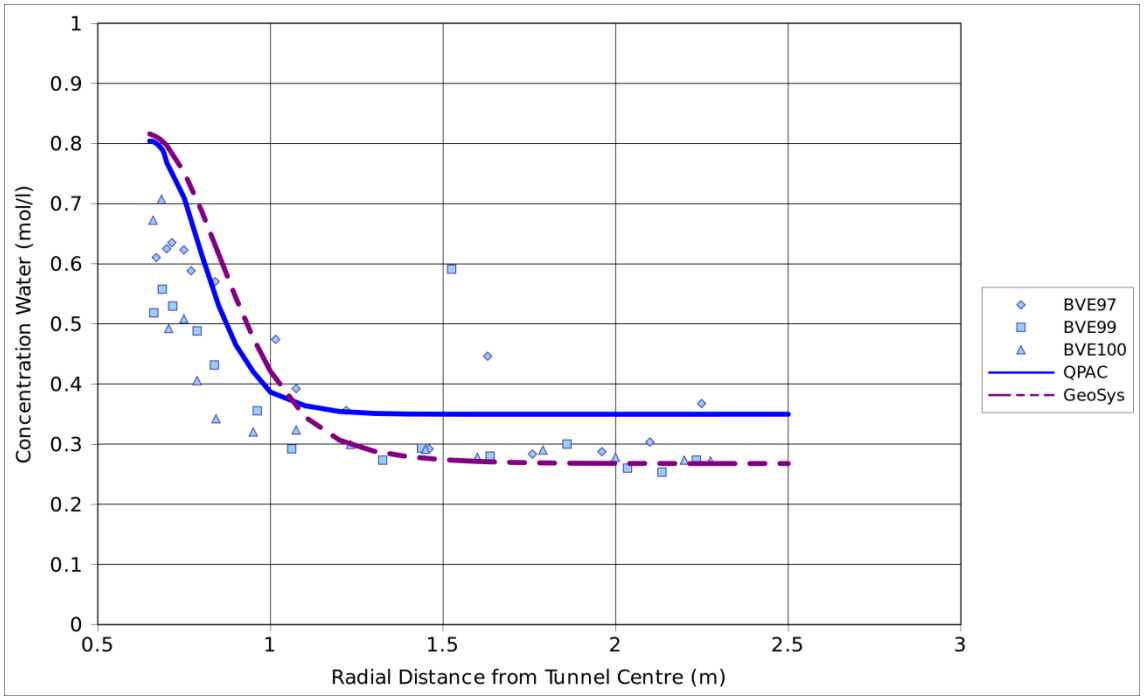

Figure 6-10. Comparison of calculated chloride water concentrations (mol/l) at 2/5/2005.

The two models make slightly different assumptions regarding what constitutes a suitable background concentration due to differing porosities, and show a slightly different width of peak. The wider peak for the UoE model is consistent with the slightly lower tortuosity (and hence higher effective diffusion coefficient) used in their model (Table 6-2, Table 6-3) and the comparison is good despite such minor differences.

6.6 Sensitivity Analyses

A series of sensitivity and uncertainty analyses were performed to confirm the general consistency noted in the previous section. A large number of cases were run so the results are discussed in outline only. The main areas of investigation were:

1. Higher dimensionality: 2D or 3D models.
2. Alternative conceptual treatment of the chloride porosity.
3. General parameter sensitivity.
4. Sensitivity to hydraulic changes.

The general results of the analyses can be summarised as follows:

1. The primary parameter sensitivity was to the effective diffusion coefficient, primarily through the assumed free water diffusion coefficient and the tortuosity (equation 6.1). Increasing the effective diffusivity tended to spread the zone of increased chloride while reducing the peak value at, or adjacent to, the tunnel wall. This result is consistent with the differences in results between the two models (Figure 6-10) and the related minor parameterisation differences.
2. In cases where the hydraulic system was changed, provided the basic water balance was kept broadly consistent with the experimental measurements, the chloride response remained consistent. This illustrates the importance of the advective component of water flow concentrating chloride at the tunnel wall. Changing the conceptual model to the 'bound water' model for the chloride porosity gave the expected result. This process model effectively increases the advective velocity for the chloride transport. This tends to narrow the chloride peak close to the tunnel wall and create higher bulk rock and dissolved water concentrations of the order of 1.25 to 1.5 times those seen in the reference QPAC reference results (Figure 6-2 to Figure 6-5). This is not a major change and within the bounds of conceptual and parametric uncertainty arising from tortuosity in the diffusion model, for example.
3. Higher dimensionality models were run looking at the likely variation along the axis of the tunnel and spatially around the tunnel perimeter, to consider whether we would expect to see a structured variation in the concentration data. The conclusion of such analyses were that while structural variation could clearly be induced in the models, the magnitude of expected variation was relative small (factor of ~1.5 in peak rock mass concentrations at the tunnel surface (Figure 6-11), most obviously along the axial direction of the tunnel, and much less for water chloride concentrations (Figure 6-12)). It was considered that it would be difficult to distinguish such a trend in the available data, given the observed 'scatter' through various uncertainties in the analysis approach and the relatively small amount of data available, especially at early times.

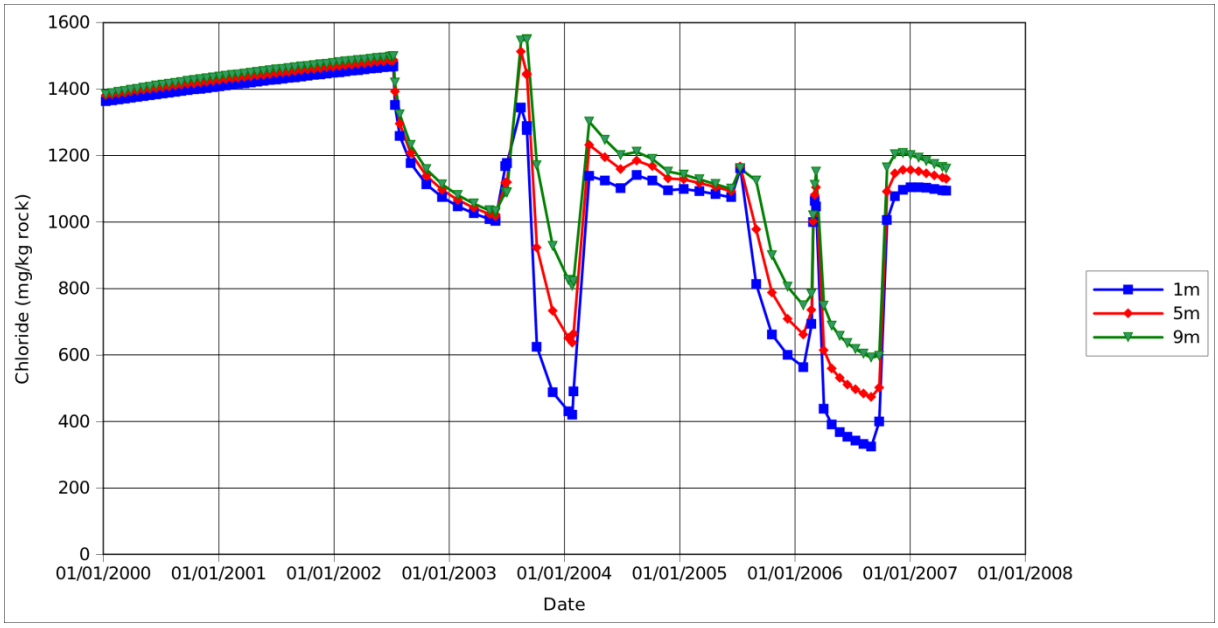

Figure 6-11. Comparison of calculated chloride rock mass concentrations (mg/kg rock) at 1 m, 5 m and 9 m along the long axis of the tunnel using a 2D (radial, axial) representation of the system in QPAC with 10 axial compartments.

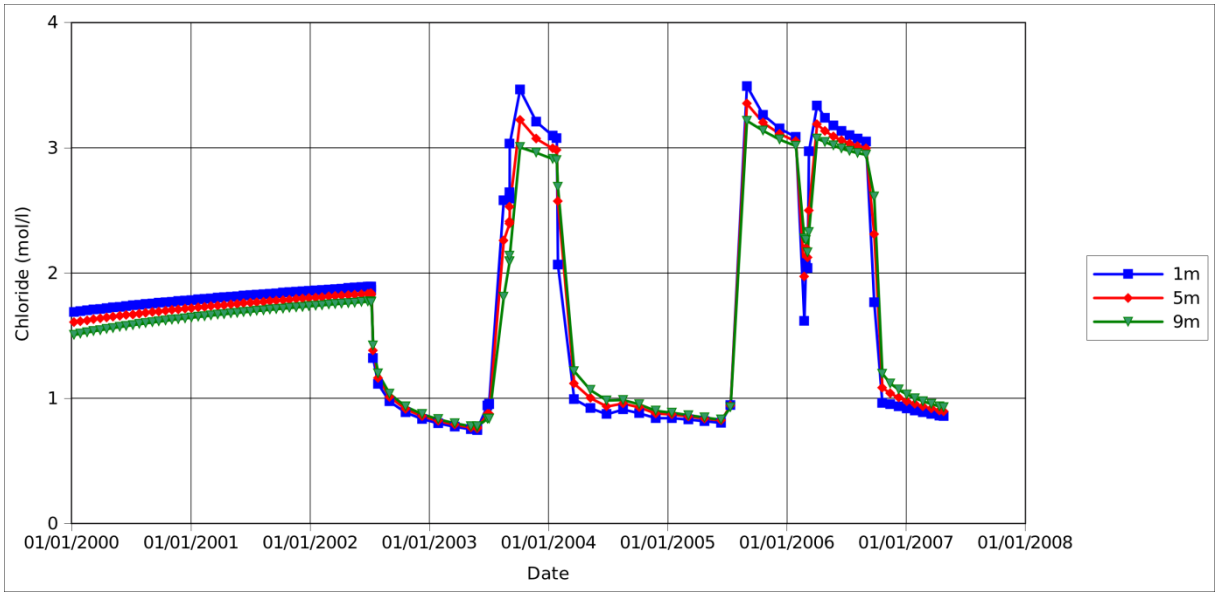

Figure 6-12. Comparison of calculated chloride concentrations (mol/l) at 1 m, 5 m and 9 m along the long axis of the tunnel using a 2D (radial, axial) representation of the system in QPAC with 10 axial compartments.

6.7 Summary Comments

Using the available data it was relatively straightforward to produce a transport model that reflects the conceptual understanding of the system. This indicates that the basic hydraulic model and chloride conceptual model is robust and adds confidence to the overall performance of the model. The results do indicate that in general the results a largely insensitive to the major transport parameters, being more influenced by the underpinning hydraulic model.

Such a result gave sufficient confidence in the non-reactive transport calculation to attempt the significantly more complex and less well constrained reactive transport analysis.

7 Step 4: Reactive Transport Modelling

The work of Fernandez *et al.* (2007a,b) indicated that while the chloride results could be understood relatively simply, and the transport analysis coupled with the hydro-mechanical model in the previous section has borne this out, some aspects of the geochemistry showed anomalous behaviour. In particular the measurements of dissolved sulphate concentrations were inconsistent with conservative transport behaviour, and as such, appeared to be the product of reactive transport phenomena. The objective of Step 4 was to build on the work of the previous steps and the initial work of Fernandez *et al.* (2007a,b) to help understand the apparently anomalous behaviour of sulphate.

7.1 Data and Conceptual Model

In addition to the chloride data discussed in Section 6 and Appendix B, a broad geochemical analysis was conducted including sulphate concentrations. It should be noted that there is considerable uncertainty in the sulphate analysis because of the tendency for additional oxidation of the samples under laboratory conditions. Comments by Fernandez *et al.* (2007a,b) indicate that this effect was minimised as far as practicable and the results are considered not to be invalidated by this effect.

Consistent with the chloride data there was observed a significant increase in sulphate also close to the tunnel wall. However, because the ratio of sulphate to chloride is constant in water saturated samples at approximately 0.05 (the value for seawater), it is clear that the increase in sulphate is in excess of the relative increase seen in chloride concentration – see Figure 7-1 and Figure 7-2.

For the sulphate system it was considered likely that an oxidation reaction is occurring due to the ingress of air into the region around the tunnel, in addition to the advective/diffusion processes seen for chloride. Incoming air induces an oxidation reaction in which the pyrite and gypsum found in the rock mass produce an increase of the sulphate concentration. The geochemical arguments relating to this process are discussed in the following section and Fernandez *et al.* (2007b).

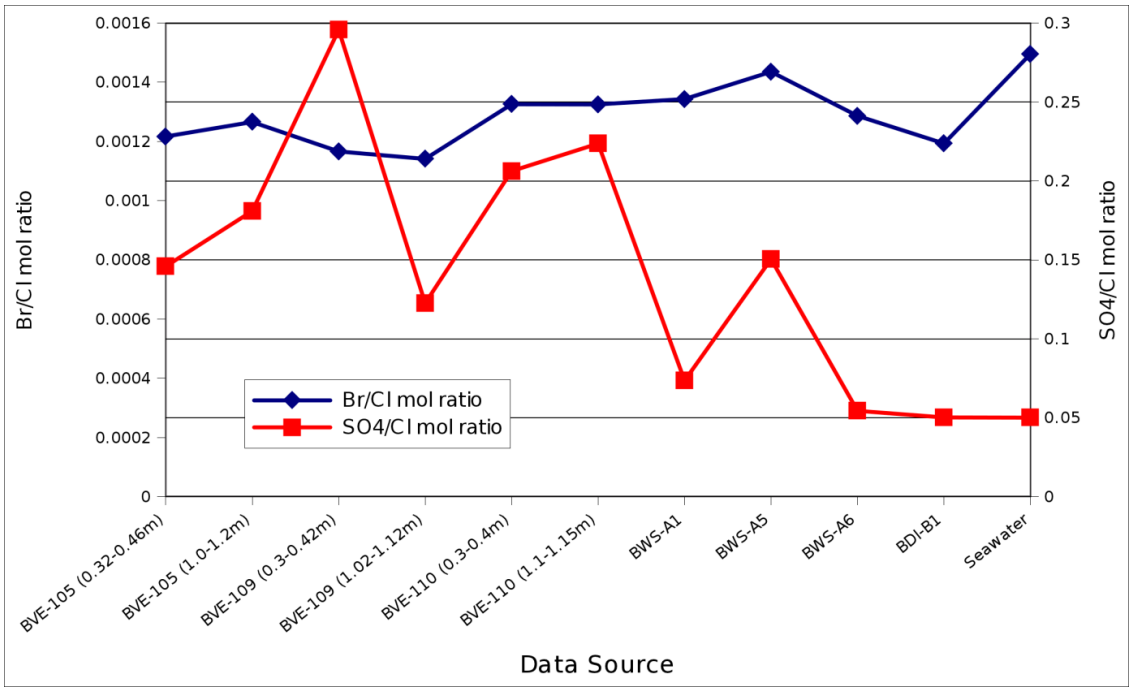

Figure 7-1. Br/Cl and SO4/Cl ratio in pore waters obtained in boreholes from the VE-Experiment. BVE boreholes are from the ventilation tunnel with depth from the tunnel wall indicated, BWS and BDI boreholes are water saturated and from elsewhere in the URL (from Fernandez *et al.* 2007b)

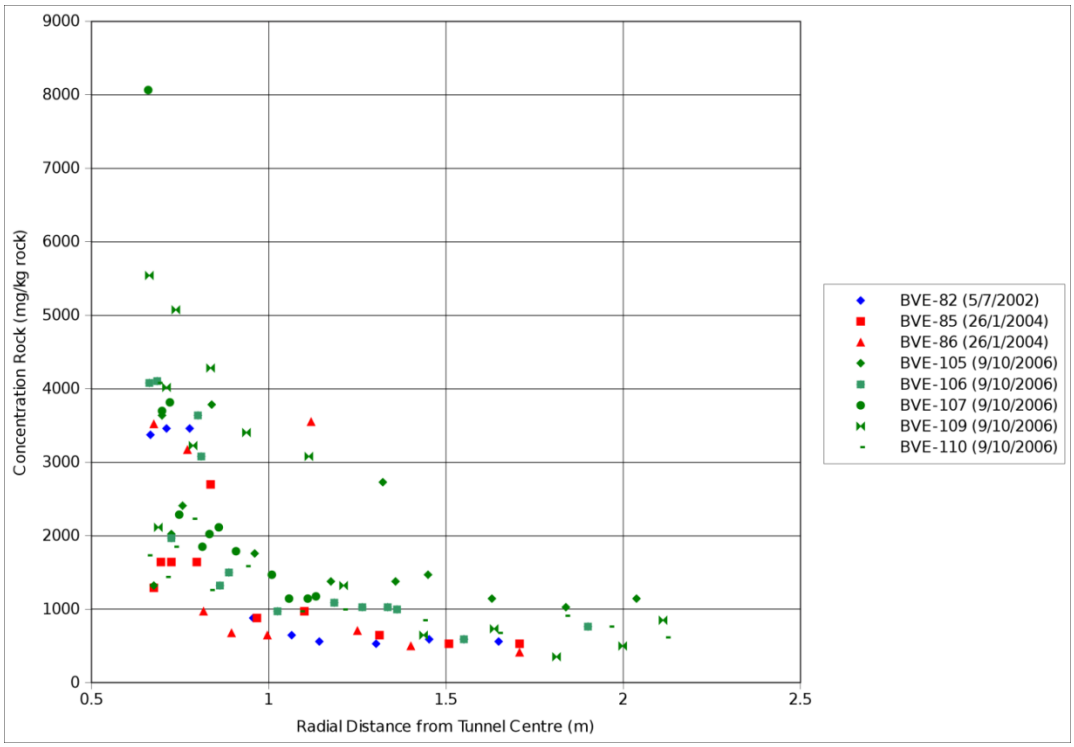

Figure 7-2. Sulphate concentration expressed as mg/kg rock (total rock concentration). Transcribed from Fernandez *et al.* (2007b).

7.2 Approach

Of the teams that participated in modelling the Ventilation Experiment for DECOVALEX, only Quintessa attempted the full reactive transport modelling component. The model developed was a reconnaissance or prototype model using QPAC, designed to investigate the plausibility of a redox-pyrite-gypsum model in describing the observed evolution of the sulphate.

For these initial calculations it was assumed that the feedback of the chemical processes on the hydraulic calculations was weak. In particular, it was assumed that the rates at which oxygen is dissolved into the water and takes part in redox reactions are not sufficient to significantly alter the O_2 partial pressure in the pores due to a relatively rapid re-supply of O_2 through the connected gas (air) body to the tunnel (which is assumed to homogenise quickly compared to other processes in the system.) Since there is no assumed coupling back to the hydraulic calculations, the reactive transport calculations can simply use the reported fluxes, air pressures and saturations from pre-existing runs as input (similarly to the chloride calculations), with oxygen partial pressures calculated assuming 21% O_2 in the gas phase.

The geochemical sub-system was deliberately kept simple for these prototype calculations. The key process of interest is the oxidation of pyrite (FeS_2), since this is likely to exert the strongest control over O_2 concentrations in the pore water. The pyrite oxidation reaction can be represented as

$$FeS_{2(s)} + 3.75O_{2(aq)} + 0.5H_2O = H^+ + 2SO_4^{2-} + Fe^{3+}.$$

Pyrite oxidation will release sulphate to the pore water and reduce pH.

Sulphate concentrations in the pore water will vary according to the rate at which sulphate is supplied from oxidation of pyrite and the rate at which it is transported through the system. Transport is a consequence of advection by the bulk movement of water through the pore space and diffusion in the bulk water. Sulphate concentrations will be expected to be highest where oxygen is abundant, leading to the greatest amounts of dissolution of pyrite, and so are expected near the tunnel wall where there is a strongly connected gas phase. Concentrations will also become more elevated as a consequence of evaporation at the tunnel wall, although this process is not represented in the prototype model.

Dissolved O_2 concentrations will be transported similarly but are also subject to a source of oxygen from dissolution wherever free gas is present in the pore space. Dissolution is represented as a kinetic process that attempts to achieve a target equilibrium activity of dissolved O_2 in the pore water that is calculated from the O_2 fugacity.

In addition to pyrite, calcite ($CaCO_3(s)$), quartz ($SiO_2(s)$) and albite ($NaAlSi_3O_8$) were included in the model to represent the solids present in the host rock. All minerals were modelled kinetically. Calcite will tend to buffer pH in the model by dissolving. Quartz and albite are expected to be relatively inert.

Although the intention was to keep the geochemical system simple, in order to properly represent the redox system, several aqueous species were included in the model. 12 basis species were included in the model together with 31 complex and redox species, resulting in around 50 geochemical species per compartment.

The reactive transport module in QPAC has been designed to enable interactions of groundwater and other subsurface fluids with rocks and man-made materials to be modelled. In an open system (i.e. systems other than 'closed-box' batch-type systems) the interactions in the water-rock system are represented by non-linear reactive transport equations, which couple the fluid flow and transport equations to equations representing the geochemical reactions between the pore water components and the solid materials. The model is 'fully coupled' (rather than being implemented as a two-step process as in some other modelling codes) and allows alteration processes in the rock and man-made materials feed back into the fluid flow equations through variations in porosity and other material properties such as permeability and tortuosity (although this option is not used in the current calculations).

Effects on other rock properties can be inferred, such as the loss in the swelling capacity of bentonite clays as monovalent sodium ions are replaced by divalent calcium ions.

The module includes models for both homogeneous reactions within the fluid and heterogeneous interactions between the fluid and minerals. In fluids the following processes were simulated:

- Aqueous complexation - the process by which significant fractions of the dissolved species can occur as complex aqueous species. These reactions are fast compared to fluid flow, and are represented by equilibrium equations expressing laws of mass action.
- Activity of species - the module incorporates models for low activity solutions (for example, the Davies equation (e.g., Zhu and Anderson, 2002)) as well as the Pitzer virial equations for higher concentration solutions (Harvie *et al.*, 1984), which augment the standard Debye-Hückel activity model (e.g., Zhu and Anderson, 2002) with the addition of terms that describe the interaction between individual ion pairs and triples.

The model includes several potential fluid-rock interaction processes, including solid solutions, ion-exchange, surface complexation and precursor cannibalisation. However in the simple simulation considered here the only relevant processes were

mineral dissolution and precipitation reactions, which are simulated in the model using kinetics. In each case, a kinetic rate was defined as a function of the in-situ pore water conditions, typically depending on the saturation of the mineral (a measure of its tendency to dissolve or precipitate at the in-situ conditions), activities of key species (e.g. H+,OH- or O2(aq)) and a rate constant. The precise treatment of the kinetics in this modelling study is discussed in Section 7.4. As minerals precipitate / dissolve, corresponding amounts of their component aqueous species are removed / introduced to the pore water to conserve the total mass.

Aqueous species are free to diffuse in the pore water and be transported by advection and dispersion when the water is flowing. In this study, Darcy pore water fluxes are obtained from the hydro-mechanical flow modelling, and use the same flows used for the chloride calculations.

7.3 Geochemical Model and Parameterisation

7.3.1 Pore Chemistry

For the purposes of this simple model, the Opalinus clay was assumed to be composed of albite (71 wt. %), quartz (14 wt.%), calcite (13 wt.%) and pyrite (2 wt.%). As previously mentioned, albite and quartz are expected to be relatively inert. The initial porewater composition in the model was calculated in a separate PHREEQC calculation using the llnl.dat thermodynamic database assuming calcite and pyrite equilibrium, with Na and Cl concentrations reported by Fernandez *et al.* (2007b, BVE-102) with charge being balanced on pH. The composition is given in Table 7-1 and is consistent with the previous PHREEQC modelling reported by Fernandez *et al.* (2007b), which itself is consistent with the available groundwater composition data.

Table 7-1. Opalinus clay pore water composition

Property	Value
Temperature (C)	25
pH	6.99
pe	-2.93
Eh (V)	-0.17
Log $pO_{2(g)}$	-66.94
Log $pCO_{2(g)}$	-2
	(molal)
Na	3.309×10^{-1}
Cl	3.669×10^{-1}
HCO_3	3.214×10^{-3}
Fe	1.664×10^{-4}
Ca	1.945×10^{-2}
SO_4	3.329×10^{-4}
Equilibrium minerals	Calcite, Pyrite

7.3.2 Subsystem Couplings Domain and Boundary Conditions

As stated earlier, couplings between the hydraulic subsystem, in which the Multiphase Flow Module (MPF) calculates flows, and the reactive geochemical subsystem, in which the reactive transport module (RT) simulates geochemical reactions and solute transport, were assumed to be one-way with chemical reactions and alteration having no direct feedback on hydraulic properties in this preliminary version of the model. The key couplings are that:

- Porewater fluxes calculated by MPF are used by RT in its solute advection formulation ;
- Air pressures calculated by MPF are used to derive $O_{2(g)}$ fugacities and hence dissolved $O_{2(aq)}$ activities, which are then used as 'targets' for dissolution processes;
- Air saturations calculated by MPF are used to identify regions with negligible gas in the pores (dissolution processes are not simulated in regions with air saturations less than 0.01).

The implementation of these relationships is as follows. The diffusive-advective transport flux in the RT module is given by

$$J_{RT,i} = -\rho_w(D\nabla c_i - q_{RT}c_i)$$

for each solute species $i$in the geochemical subsystem. Here $\rho_w$is the porewater density (kg m^{-3}), D(m^2 s^{-1}) is the diffusion coefficient, q_{RT}(m s^{-1}) is the Darcy velocity and c_i(mol/kg) is the molality of the solute species. The RT Darcy velocity can be related to the MPF water fluxes, $q_{MPF,w}(r,t)$(kg/y), by

$$\rho_w A(r) q_{RT}(r,t) = q_{MPF,w}(r,t),$$

where $A(r)$is the 'transport area' in the discretisation, which is given by the area of the common interface over which the flux applies.

O_2 fugacity was derived from the MPF air pressure using an ideal gas assumption,

$$f_{O_2}(r,t) = 0.21 \times P_{MPF,g}(r,t),$$

where $P_{MPF,g}(r,t)$is the MPF gas (air) phase pressure in bars. The target dissolved $O_{2(aq)}$ molality that is implied by the MPF gas phase pressure is then

$$c^{\text{target}}_{O_{2(aq)}}(r,t) = f_{O_2}(r,t)K_{O_{2(g)}}$$

where $K_{O_{2(g)}}$is the $O_{2(g)}$ equilibrium constant at the in-situ temperature (taken to be 25°C due to availability of thermodynamic data for Fe species). The introduction of O_2 into the porewater is represented by a source term for $O_{2(aq)}$ in the geochemical subsystem driven by the difference between the target and actual in-situ $O_{2(aq)}$ molality, given by

$$S_{O_{2(aq)}}(r,t) = f(s_{MPF,g}(r,t))k_{\text{dissolve}}(c^{\text{target}}_{O_{2(aq)}}(r,t) - c^{\text{actual}}_{O_{2(aq)}}(r,t)).$$

Here $k_{\text{dissolve}}$is the dissolution rate (y^{-1}), $s_{MPF,g}(r,t)$is the MPF gas saturation and $f(s_{MPF,g}(r,t))$is a "cut-off function" that is used to disable dissolution in regions where the gas saturation is lower than 1%, since there are trace quantities of gas present at all locations in the multiphase flow formulation in MPF that would not contribute towards a genuine source of dissolved gas.

To fully couple the RT and MPF processes, all that would be necessary would be to insert a sink term into the MPF model corresponding to the RT source term and to implement a coupling to represent loss of solvent in the RT module due to evaporation, that would reflect the rise in concentrations as evaporation occurs near the tunnel walls. These couplings would be relatively simple to introduce into a future version of the model, should this be desirable. Evaporation processes have been implemented in bespoke models in previous applications of the RT module (e.g. Savage *et al.*, 2010).

The modelling domain was the same 1D cylindrical domain of 45 compartments used for the chloride calculations (see Section 5.3). Reactive transport boundary conditions

at the tunnel wall assumed a zero solute concentration gradient in the pore water. This means that all transport out through the tunnel wall is purely advective, i.e. solutes are carried out through the tunnel wall in any (liquid) water that leaves the system via that route, which in the current parameterisation is zero, i.e. all water exchange with the tunnel is through evaporation/precipitation and water vapour migration processes.

At the boundary in the host rock (60 m into the rock; see Figure 5-2), a fixed Opalinus clay pore water composition was applied, leading to an advective boundary condition when MPF water flows are inwards and a diffusive flux when the boundary solute concentrations differ from the solute concentrations in the adjacent cells in the model. The fixed pore water composition was calculated in a separate PHREEQC calculation using the llnl.dat thermodynamic database (thermo.com.V8.R6.230; Johnson *et al.*, 2000) assuming calcite and pyrite equilibrium, with Na and Cl concentrations reported by Fernandez *et al.* (2007b, BVE-102) and charge balance on pH. The computed composition is shown in Table 7-1. This composition was also used as the initial pore water composition in the rock at the start of the calculations.

7.3.3 Reference Parameterisation

The model includes mineral reactions for pyrite, calcite, quartz and albite as shown in Table 7-2. The aqueous species included in the pore water chemistry model are listed in Table 7-3. Log K data for all aqueous and mineral species were taken from the database thermo.com.V8.R6.230 (Johnson *et al.*, 2000). A temperature of 25°C was assumed throughout to ensure availability of thermodynamic data, noting that this temperature is not very different from the 15°C observed at the tunnel wall, and in the context of all the other uncertainties regarding the geochemical system this is a relatively minor issue.

Table 7-2. Mineral reactions and equilibrium constants

Reaction	**Log K (25°C)**
$FeS_{2(s)} + 3.75O_{2(aq)} + 0.5H_2O = H^+ + 2SO_4^{2-} + Fe^{3+}$	225.89
$CaCO_{3(s)} + H^+ = Ca^{2+} + HCO_3^-$	1.85
$SiO_{2(s)} = SiO_{2(aq)}$	-4
$NaAlSi_3O_{8(s)} + 4H^+ = Al^{3+} + Na^+ + 3SiO_{2(aq)} + 2H_2O$	2.76

Table 7-3. Aqueous species included in the model. Basis species are shown in bold text, redox species are shown in bold italic text. Log K data for all redox and complex species are taken from thermo.com.V8.R6.230 (Johnson *et al.*, 2000) at 25 °C.

Reaction
$SiO_{2(aq)}$
$Na^+, NaSO_4^-, NaHCO_{3(aq)}, NaCl_{(aq)}$
$Ca^{2+}, CaHCO_3^+, CaCO_{3(aq)}, CaSO_{4(aq)}, CaCl^+$
$HCO_3^-, CO_3^{2-}, CO_{2(aq)}$
$SO_4^{2-}, HS^-, HSO_4^-, H_2S_{(aq)}$
$Mg^{2+}, MgSO_{4(aq)}, MgHCO_3^+, MgCO_{3(aq)}, MgCl^+$
K^+, KSO_4^-
$Fe^{2+}, Fe^{3+}, FeCO_{3(aq)}, FeHCO_3^+, FeOH^+, Fe(OH)_2^+, Fe(OH)_{3(aq)}, FeOH_4^-,$ $Fe(OH)_{2(aq)}, Fe(OH)_3^-, Fe(SO)_{4(aq)}, FeCl^+$
$Al^{3+}, Al(OH)_4^-, Al(OH)_3$
$O_{2(aq)}$
Cl^-
H^+, OH^-, H_2O

The aqueous reaction subsystem was modelled assuming instantaneous equilibrium in the aqueous phase for all species. Mineral evolution was simulated with kinetics. For pyrite, the rate law of Willamson and Rimstidt (1994) was used:

$$r_{\text{pyrite}} = -A(t)k\frac{m_{O_2}^{0.5}}{m_{H^+}^{0.11}}$$

where the rate constant $k = 10^{-8.19}$mol m^{-2} s^{-1}, $m_i$is the molality of the subscripted species and $A(t)$(m^2) is the time-dependent reactive surface area of pyrite. The fit of this model for pyrite oxidation to measured data, and the variation of the rate with O_2 and H^+ in the pore water is shown in Figure 7-3.

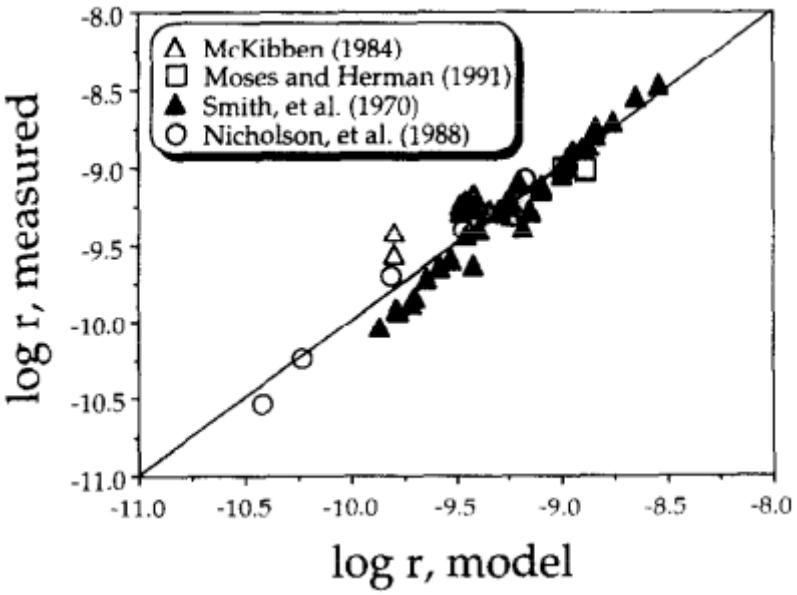

Small failure immediately adjacent to tunnel wall during late wetting

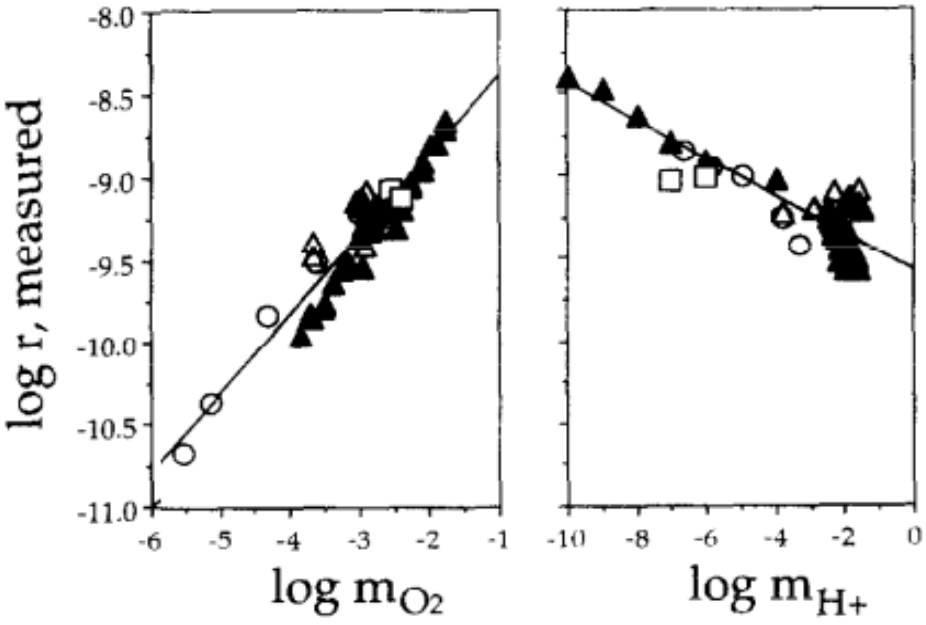

Figure 7-3. Pyrite oxidation model fit to measured data (top) and variation with porewater O_2 and H^+ (bottom). From Williamson and Rimstidt (1994) "The kinetics and electrochemical rate-determining step of aqueous pyrite oxidation", Geochimica et Cosmochimicha Acta, 58

Calcite dissolution and precipitation was modelled using a reaction based on departure from equilibrium from Busenberg and Plummer (1981):

$$r_{\text{calcite}} = A(t)k(\frac{Q}{K} - 1)^{\alpha},$$

where the rate constant $k = 10^{-5.2}$ mol m^{-2} s^{-1} and

$$\alpha = \begin{cases} 0.9 & \text{when } Q < K \text{(dissolving)}, \\ 1.0 & \text{when } Q > K \text{(precipitating)}. \end{cases}$$

Quartz and albite are both simulated using transition state theory-(TST) based reactions with pH-dependent dissolution and precipitation rates:

$$r_i = A_i(t)\left(k_{i,\text{H}^+}10^{-n_i pH} + k_{i,\text{OH}^-}10^{-m_i(14-pH)}\right)\left(\frac{Q}{K} - 1\right)$$

where the subscript $i$refers to the mineral (albite or quartz) with the values of the terms as given in Table 7-4. The rates are a fit to various experimental datasets, as shown in Figure 7-3.

Table 7-4. Coefficients in the reaction rate expression for albite and quartz

	k_{i,H^+} mol m^{-2} s^{-1}	k_{i,OH^-} mol m^{-2} s^{-1}	n_i	m_i
Albite	2.38 x 10^{-10}	2.31 x 10^{-10}	0.4	0.38
Quartz	4.34 x 10^{-12}	6.06 x 10^{-10}	0.31	0.41

Effective diffusion coefficients for all aqueous species was set to be

$$D_e = \theta \times 10^{-10}\ \text{m}^2\text{s}^{-1}$$

where θ is the in-situ evolving porosity, which is within 10% of the model used for the chloride calculations.

Note that in the default model as, a simplifying assumption, there is no concept of a chloride porosity or other geochemical porosity, so the full porosity is available for reactive transport, however as shown in the non-reactive transport modelling, in this case the geochemical porosity appears not to show a major effect.

7.4 Numerical implementation

In this study, aqueous activities are represented using the Davies model, in which the activity coefficient $\gamma_i$of species $i$is given by

$$\log\gamma_i = \frac{-Az_i\sqrt{I}}{1+\sqrt{I}} + 0.2Az_i^2 I. \qquad 7.1$$

Here A is the Debye-Hückel constant (see for example Zhu and Anderson, 2002), $z_i$is the charge of species i. The ionic strength $I$is defined as,

$$I = \frac{1}{2}\sum_i l_i z_i^2, \qquad 7.2$$

where $l_i$is the molality (mol/kg) of species species i. The activity $a_i$of species $i$is then given by

$$a_i = \gamma_i l_i. \qquad 7.3$$

Equilibrium conditions between the porewater species are represented by laws of mass action. These relate the equilibrium constant $K_j$of the j^{th} species to the activities by

$$K_j = \prod_i a_i^{\alpha_{ij}},$$

where $\alpha_{ij}$is the stoichiometry of species $i$in the equation for species j. For this study, equilibrium constants have been taken from the thermodynamic database thermo.com.V8.R6.230 (Johnson *et al.*, 2000).

The aqueous species are organised in the thermodynamic database so that reactions for all redox species can be expressed in terms of a collection of aqueous "basis" species, and reactions for all aqueous complex species and minerals can be expressed in terms of only basis and redox species. With sequences $B_1,\ldots,B_{N_B}$, $R_1,\ldots,R_{N_R}$and $C_1,\ldots,C_{N_C}$used to index the basis, redox and complex species respectively, the mass action equations for the redox and complex species become

$$K_{Rj} = a_{Rj}^{-1}\prod_{i=1}^{N_B} a_{Bi}^{\alpha_{BiRj}}, \text{ and} \qquad 7.4a$$

$$K_{Cj} = a_{Cj}^{-1}\prod_{i=1}^{N_B} a_{Bi}^{\alpha_{BiCj}}\prod_{i=1}^{N_R} a_{Ri}^{\alpha_{RiCj}}. \qquad 7.4b$$

(The activities of the redox and complex species appear with power -1 in (7.4a,b) because the reactions are written so that the redox and complex species always have stoichiometry 1 in their defining reactions.)

The model includes several potential fluid-rock interaction processes, including solid solutions, ion-exchange, surface complexation and precursor cannibalisation. However in this study the only relevant fluid-rock processes are mineral dissolution and precipitation reactions, which are simulated in the model using kinetics. A kinetic rate G_j(mol m^{-3} y^{-1}) for the rate of change of the concentration m_j(mol m^{-3} of total volume) of the j^{th} mineral in the system is specified for $j = 1,\ldots,N_M$. Then

$$\frac{dm_j}{dt} = G_j. \qquad 7.5$$

$G_j$can be defined as a function of the in-situ porewater conditions, typically depending on the saturation of the mineral (a measure of its tendency to dissolve or precipitate at the in-situ conditions), activities of key species (e.g. H^+,OH^- or $O_{2(aq)}$) and a rate constant. Hence $G_j$typically varies with time. The precise treatment of the kinetics in this modelling study are discussed in Section 7.3.3.

For each aqueous species $i$the rate of change of the molality of the pore water species is coupled to the kinetic change in the abundance of the j^{th} mineral by a source/sink term S_{ij}(mol kg^{-1} y^{-1}) with magnitude

$$S_{ij} = \frac{-\mu_{ij} G_j}{\rho_w \theta}. \qquad 7.6$$

Here, $\mu_{ij}$is the stoichiometry of the i^{th} aqueous species in the j^{th} mineral species, ρ_w(kg m^{-3}) is the density of water and $\theta$is the porosity.

If we now distinguish the molalities of the aqueous basis, redox and complex species by $b_{j.}(= l_{Bj})$, $c_{j.}(= l_{Cj})$and $r_{j.}(= l_{Rj})$respectively, then the mass conservation equations for the aqueous basis, redox and complex species can be written as

$$\frac{\partial}{\partial t}\rho_w \theta b_j = T_{Bj} \tilde{G}_{Cj} - \sum_{i=1}^{N_R} \alpha_{BjRi} \tilde{G}_{Ri} - \sum_{i=1}^{N_C} \alpha_{BjCi} \tilde{G}_{Ci} - \sum_{i=1}^{N_M} \mu_{BjMi} G_i \qquad 7.7a$$

$$\frac{\partial}{\partial t}\left(\rho_w \theta r_j\right) = T_{Rj} + \tilde{G}_{Rj} - \sum_{i=1}^{N_R} \alpha_{BjRi} \tilde{G}_{Ri} - \sum_{i=1}^{N_C} \alpha_{RjCi} \tilde{G}_{Ci} - \sum_{i=1}^{N_M} \mu_{RjMi} G_i \qquad 7.7b$$

$$\frac{\partial}{\partial t}\left(\rho_w \theta c_j\right) = T_{Cj} + \tilde{G}_{Cj} \qquad 7.7c$$

Here, the terms T_{*j}(mol m^{-3} y^{-1}) are transport operators for the basis, redox and complex species, which will be discussed shortly. The terms $\tilde{G}_{*j}$(mol m^{-3} y^{-1}) denote the rates of reaction of the redox and complex species. As noted above, aqueous pore water reactions are assumed to be in equilibrium at all times, so these rates are effectively infinite. They can be eliminated from the mass conservation equations (7a-c) to give the following mass conservation equation for basis species j,

$$\begin{aligned} &\frac{\partial}{\partial t}\left(\rho_w \theta\left(b_j + \sum_{i=1}^{N_C} \alpha_{BjCi} c_i + \sum_{i=1}^{N_R} \alpha_{BjRi} r_i + \sum_{i=1}^{N_R} \alpha_{BjRi} \sum_{k=1}^{N_C} \alpha_{RiCk} c_k\right)\right) = \\ &\quad T_{Bj} + \sum_{i=1}^{N_C} \alpha_{BjCi} T_{Ci} + \sum_{i=1}^{N_R} \alpha_{BjRi} T_{Ri} + \sum_{i=1}^{N_R} \alpha_{BjRi} \sum_{k=1}^{N_C} \alpha_{RiCk} T_{Ck} \\ &\qquad - \sum_{i=1}^{N_M} \mu_{BjMi}\, G_i - \sum_{i=1}^{N_R} \alpha_{BjRi} \sum_{k=1}^{N_M} \mu_{RiMk} G_k \end{aligned} \qquad 7.8$$

The system of equations 7.4(a,b), 7.5 and 7.8 provide $N_C + N_R$equations (from 7.4a, 7.4b), $N_M$equations (from 7.5) and $N_B$equations (from 7.8), which are sufficient to characterise the system.

The transport terms $T_j$are of the form

$$T_j = \nabla \cdot F_j, \qquad 7.9$$

where the F_j(mol m^{-2} y^{-1}) are diffusive-dispersive-advective fluxes,

$$F_j = \rho_w \left(\left(D_j^{(\text{eff})} + \widetilde{D}_j q\right) \nabla l_j + q l_j\right). \qquad 7.10$$

Here, $D_j^{(\text{eff})}$(m^2/y) is the effective diffusion coefficient of the j^{th} aqueous species, $\widetilde{D}_j$(m) is the (longitudinal) dispersion coefficient and q(m s^{-1}) is the Darcy velocity of the fluid.

For the purposes of this study, dispersion coefficients are assumed to be zero for all species, effective diffusion coefficients are assumed equal for all species and Darcy

fluxes are obtained from the multiphase flow calculations (as described in Section 5.3). If different effective diffusion coefficients are chosen for each species then additional electrochemical flux terms are required to ensure charge balance.

7.5 Summary of main reactive transport results

O_2 dissolution takes place in the model as the gas saturation (from the MPF calculations) migrates into the host rock. The progress of the gas saturation front is mirrored in the evolving O_2(aq) concentration, which is plotted against time in Figure 7-4. O_2 dissolution is only assumed to take place at gas saturations above 1%. The location of the free gas front equates to the position of the sharp front in the O_2(aq) curves, since dissolution is assumed to be rapid. By the end of 2006 a sharp front has migrated approximately 1.25 m into the rock (1.9 m from the tunnel centre). The smoother low concentration front beyond the sharp front is a consequence of diffusion of small quantities of the dissolved O_2(aq) beyond the free gas front.

Pyrite dissolution takes place in the model wherever the O_2(aq) concentration is elevated (Figure 7-5). Hence by late 2006 some pyrite dissolution is seen at distances up to 1.25 m in the rock. Adjacent to the tunnel boundary, where O_2 dissolution takes place for the longest duration, approximately 10% of the initial pyrite inventory is dissolved.

Pyrite dissolution leads to a reduction in pH in the pore-water (Figure 7-6). By late 2006 the pH falls to around 4.75 over short distances adjacent to the tunnel wall and to 5-5.5 over the first 1.1 m of rock. A relatively small amount of calcite dissolution takes place to buffer pH at these levels (Figure 7-7). Around 1.5% of the calcite is lost over the first 0.35 m of rock. In the compartment immediately adjacent to the tunnel there is a small amount of calcite precipitation. This is most likely an artefact of the choice of the zero gradient boundary conditions. There is no significant alteration of albite and quartz over the timescales that are simulated

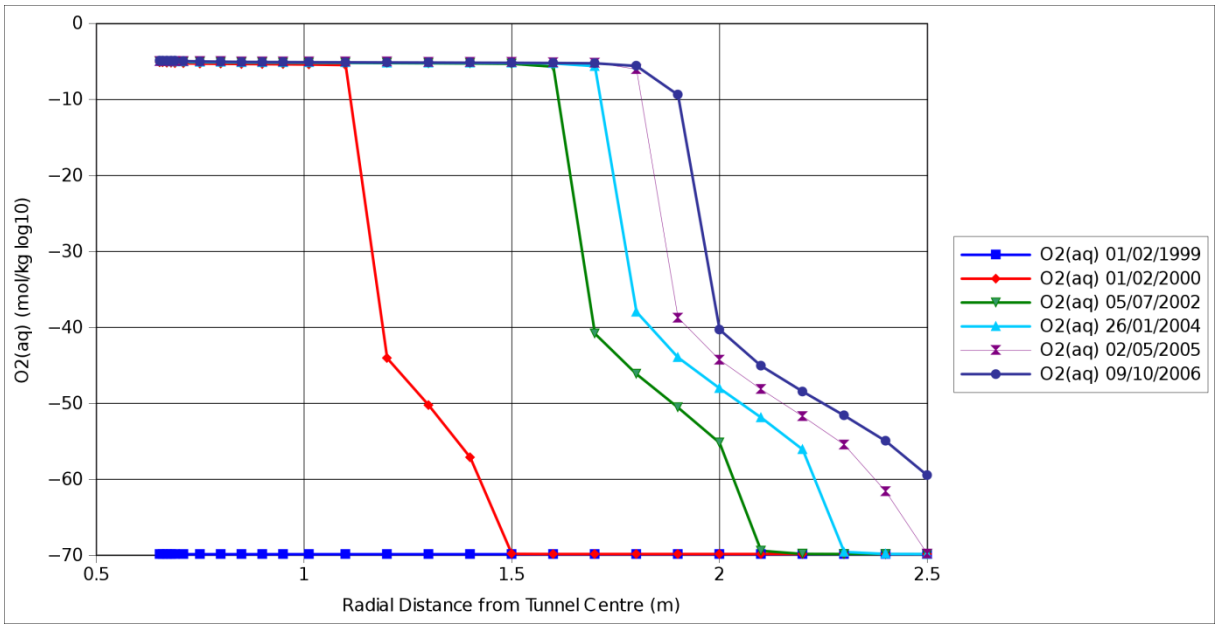

Figure 7-4. Progress of the O2(aq) front from dissolution of the free gas phase.

Figure 7-5. Pyrite concentration profiles.

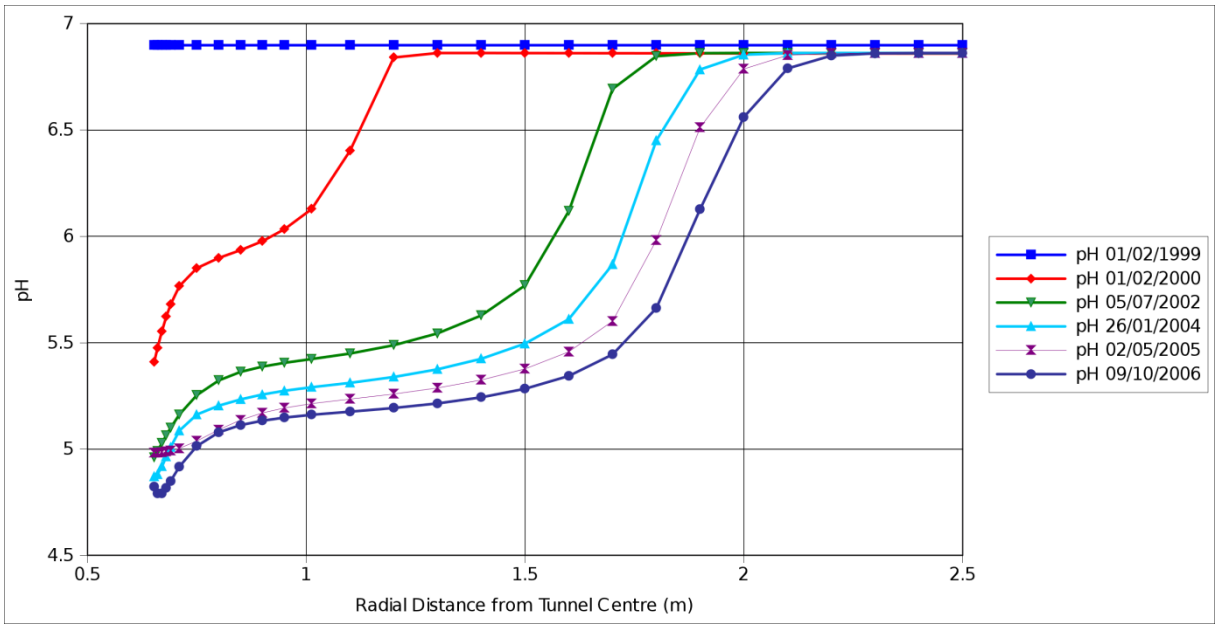

Figure 7-6. pH concentration profiles.

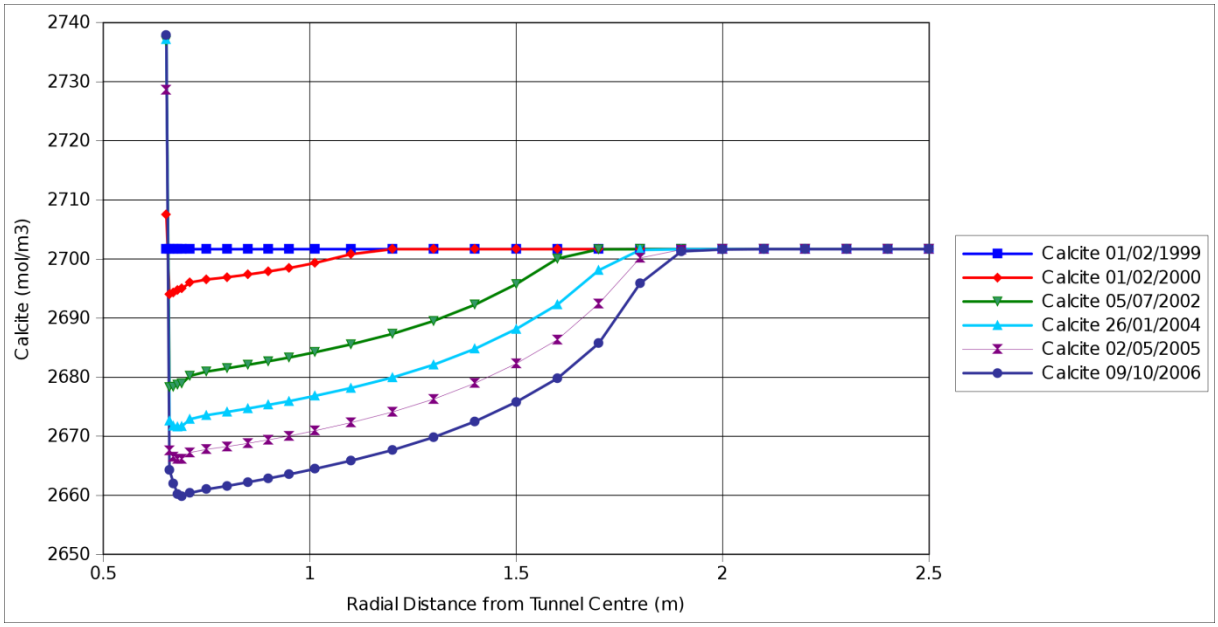

Figure 7-7. Calcite profiles.

The key output of interest is the sulphate content in the porewater, since this can be directly compared to measured data from Fernández and Melón (2007). Measured and simulated sulphate concentrations (mg / kg rock) are shown in Figure 7-8 to Figure 7-10 . Given the scatter in the measured data, the fit provided by the numerical model is reasonably good and is well within the range of the measured data. There are few datapoints at 5/7/2002 with the simulated sulphate content underestimating concentrations at the tunnel boundary but matching reasonably well in the 0.3-0.8 m range. At 26/1/2004 the model over-predicts concentrations with respect to the bulk of the datapoints in the 0.2-0.9 m range, but falls about mid-way between the measurements in the first 0-0.2 m. By 9/10/2006 the spread in the measured data is significant. The simulated results fall approximately in the middle of the envelope of datapoints, although the majority of the datapoints lie below the simulated values, although the simulated concentrations near the tunnel boundary fit closer to the larger of the measured datapoints in this range.

The reasonable fit despite ignoring the concept of a reduced geochemical porosity may lead to the conclusion that multi-component transport processes are occurring, with different aqueous species being advected at different rates. However, sulphate concentrations are likely to be affected mostly by mineral interactions (notably pyrite dissolution) with transport being a secondary effect. This can be seen in the concentration profiles in Figure 7-8 to Figure 7-10, where the 'hump' in the profile is mostly a consequence of localised pyrite dissolution (and mirrors the pyrite dissolution profiles in Figure 7-5) with the localised peak near the tunnel boundary being primarily a consequence of advective transport. If a similar 'sulphate porosity' assumption was made, it would be likely to most markedly affect results where advection processes dominate, i.e. near the tunnel boundary. It would have the effect of reducing the local peak, which might lead to a better fit to the non-peak sulphate concentrations that were measured, but would not be expected to have a large effect on the main sulphate peak close to the tunnel wall.

Hence a single porosity scaling (for anions and cations to ensure charge balance) may be adequate to improve the advection model for all aqueous species and improve both the sulphate fit near the tunnel walls and the chloride fit in general. 'Fine-tuning' of the pyrite dissolution kinetics (such as surface area term) may lead to a better fit in the next 1 m of rock. These factors could be investigated in any future updates to the models.

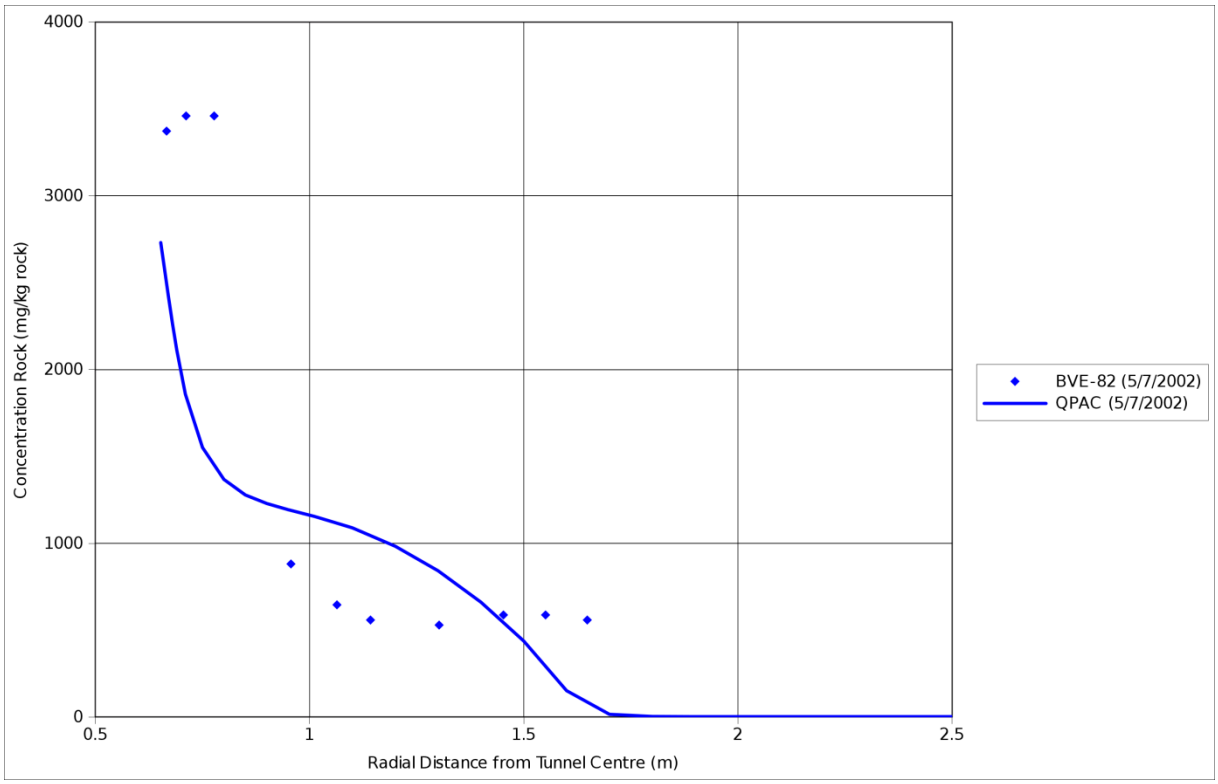

Figure 7-8. Sulphate concentration expressed as mg/kg rock (total rock concentration) at 5/7/2002 – comparison against numerical results.

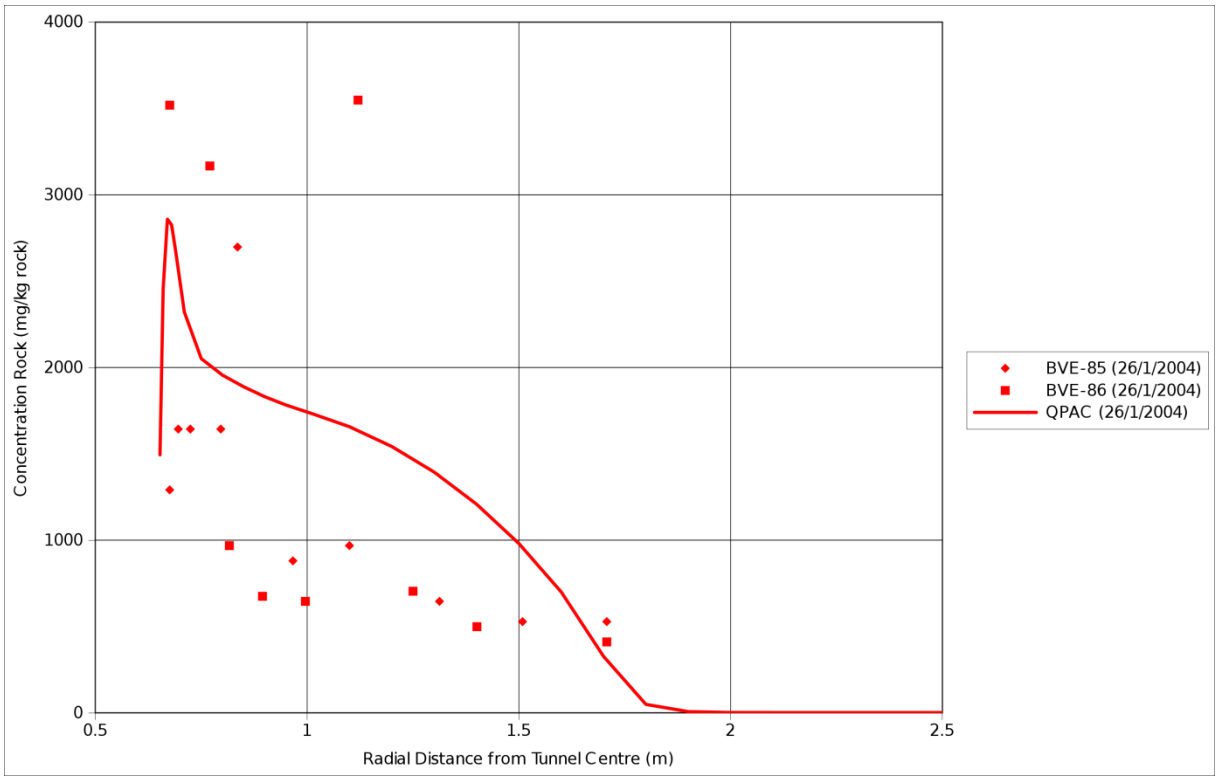

Figure 7-9. Sulphate concentration expressed as mg/kg rock (total rock concentration) at 26/1/2004 – comparison against numerical results.

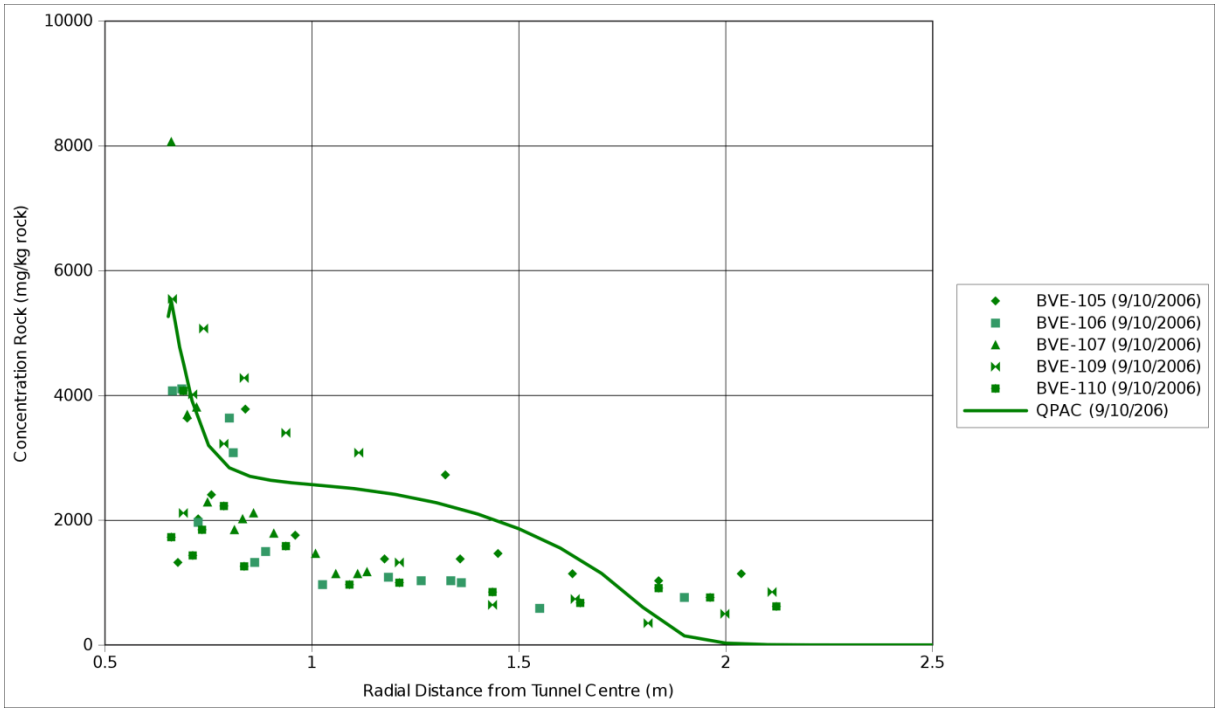

Figure 7-10. Sulphate concentration expressed as mg/kg rock (total rock concentration) at 9/10/2006 – comparison against numerical results.

7.6 Summary Comments

Building on the chloride analysis, a relatively simple representation of the key geochemical properties that are likely to have operated has been developed, namely, kinetic treatments of pyrite dissolution (releasing dissolved sulphate and reducing pH), calcite dissolution (pH buffering); and solute transport of reactive and non-reactive species. The model includes a simplified representation of mineralogy and pore water compositions and a relatively simple treatment of reactive mineral surface area. However, based on the comparison of measured with simulated data, the models provide a good representation of key processes.

8 Conclusions

Quintessa and the University of Edinburgh have participated in Task A of DECOVALEX-2011. Through a coordinated approach using two complementary codes, Quintessa and UoE, along with the other participants in Task A, have demonstrated that it is possible to model the coupled hydro-mechanical-chemical processes associated with the Opalinus Clay and reproduce nearly all of the experimental observations.

The work by Quintessa using QPAC demonstrated a technique to represent the hydraulic behaviour of the tunnel sufficient that the true boundary conditions of the experiment could be represented, and a genuine blind predictive analysis could be made. QPAC was also used to perform a full reactive geochemical analysis of the redox front advancing ahead of the water desaturation zone around the tunnel.

The complementary work by UoE showed that a relatively simple model using 1D axisymmetric elements, Richards' equation for hydraulic evolution (rather than full multi-phase flow) and a simple post-processing step to calculate mechanical evolution (rather than coupled poro-elasticity) could give a good representation of the observations.

Some uncertainties do remain however. The most significant is the failure of the models to be able to reflect the rapid saturated water pressure changes seen during Phase 1. Some initial work presented here and continued by Millard *et al.* (2012), suggests that a combination of hydro-mechanical interactions with anisotropic mechanical properties may provide a mechanism to reproduce these observations. Some very recent analysis discussed in Garitte *et al.* (2012) may suggest that some external thermal effects may be partially responsible, however the question is very much open.

Overall the work has demonstrated that it is possible to move from laboratory scale analysis into the field scale, and make good predictions on hydro-mechanical-chemical evolution of a ventilated tunnel in an argillaceous rock.

9 References

Bader, S. and H. Kooi (2005) Modelling of solute and water transport in semi-permeable clay membranes: comparison with experiments, Advances in Water Resources, 28, 203-214.

Bishop A.W. (1959). The principle of effective stress. Tecnisk Ukeblad 39, pp 859-863

Bock H. (2001). RA Experiment. Rock Mechanics Analyses and Synthesis: Data report on Rock Mechanics. Q+ S Consult. Technical Report 2000-02.

Boudreau DP (1997). Diagenetic models and their implementation: modelling transport and reactions in aquatic sediments, volume 414. Springer.

Bond AE (2010). A Thermal Module for QPAC. Quintessa Report QRS-QPAC-THM-1.

Bond AE and Benbow. (2009). QPAC Multi-Phase Flow Module Functional Specification and Architectural Design. Quintessa Report. QRS-QPAC-HYD-2.

Bond, A.E., Maul, P.R., Savage, D. and Wilson, J. (2009). The Use of QPAC-EBS for Project THERESA Full-Scale Tests. Quintessa Report QRS-3009A-2 version 2.0.

Bond AE, Millard A, Nakama S, Zhang C, B Garitte (2012a). Approaches for representing hydro-mechanical coupling between engineered caverns and argillaceous porous media at Ventilation Experiments, Mont Terri. International Journal of Rock Mechanics and Geotechnical Engineering. *In preparation.*

Bond AE, Benbow SJ, Wilson J, Millard A, Nakama S, English E, McDermott C and Garitte B. (2012b). Reactive and non-reactive transport modelling in partially water saturated argillaceous porous media around the Ventilation Experiment, Mont-Terri. International Journal of Rock Mechanics and Geotechnical Engineering. *In preparation.*

Bossart P., Nussbaum C., (2007)**.** Mont Terri project – Heater Experiment, Engineered Barrier Emplacement and Ventilation Experiment Swiss Geological Survey, n°1.

Brooks RH & Corey AT. 1966. Properties of porous media affecting fluid flow. *J. Irrig Drain. Div. Am. Soc. Civil Eng*. **92(IR2)**. 61-68.

Busenberg, E., Plummer, L.N., (1986). "*A comparative study of the dissolution and crystal growth kinetics of calcite and aragonite.*" In: Mumpton, F.A. (Ed.), Studies in Diagenesis, U.S. Geol. Surv. Bull., Vol. 1578, pp. 139–168.

Carranza-Torres C. and J. Zhao. (2009). Analytical and numerical study of the effect of water pressure on the mechanical response of cylindrical lined tunnels in elastic and elasto-plastic porous media. International Journal of Rock Mechanics & Mining Sciences 46 (2009) 531–547.

Claesson J and Sällfors G (2005). Drying and Resaturation of the Bentonite Barrier. New Tools for Modeling and Analysis. In SKI report "Engineered Barrier System – Long-term Stability of Buffer and Backfill", 2005:48.

Fernandez AM, Melon, AM, Villar MV and Turrero. (2007a). Geochemical characterisation of the rock samples for the VE-Test before a second cycle of drying. NF PRO RTD CR WP4.3 Deliverable 4.3.5

Fernandez AM and AM Melon. (2007b). Geochemical characterisation of the rock samples for the VE-Test after a second cycle of drying. NF PRO RTD CR WP4.3 Deliverable 4.3.6

Floría, E., Sanz, F.J. & García-Siñeriz, J.L. (2002). AITEMIN. Drying test: evaporation rate from core samples of "Opalinus clay" under controlled environmental conditions Project Deliverable 6 EC contract FIKW-CT2001-00126.

Garitte B and Gens A. 2008. DECOVALEX-2011: DESCRIPTION OF TASK A HMC PROCESSES IN ARGILLACEOUS ROCKS.

Garitte, B., Gens, A., Liu Q., Liu, X., Millard, A., Bond, A., McDermott, C., Fujita T. & Nakama, S.. 2010. Modelling benchmark of a laboratory drying test in Opalinus Clay. In Rock Mechanics in Civil and Environmental Engineering – Zhao, Labiouse, Dudt & Mathier (eds) © 2010 Taylor & Francis Group pp 767-770.

Garitte B., Bond .A, Millard A., Zhang C., English M., Nakama S., Gens A. (2012). Analysis of hydro-mechanical processes in a ventilated tunnel in an argillaceous rock on the basis of different modelling approaches. International Journal of Rock Mechanics and Geotechnical Engineering. *In preparation.*

M.J. van Genuchten (1980) A closed-form equation for predicting the hydraulic conductivity of unsaturated soils. Soil Sci. Soc. Am. J., vol. 44,

Gens, A. (2000), HE Experiment; Complementary Rock Laboratory Tests. Technical Note TN 2000-47. Mont Terri Project.

Gettys W, Skove I, Keller I and Frederick J (1989). Physics: Classic and Modern. McGraw-Hill, Inc.

Harvie, C. E., Moller, N. and Weare, J. H. (1984). "The prediction of mineral solubilities in natural waters: The Na-K-Mg-Ca-H-Cl-SO4-OH-HCO3-CO3-CO2 H2O system to high ionic strengths at 25oC" Geochimica et Cosmochimica Acta, 48, 723-751.

Johnson, J, Anderson, G and Parkhurst, D (2000), "Database 'thermo.com.V8.R6.230,' Rev. 1.11", Lawrence Livermore Natl. Lab., Livermore, Calif.

Ippisch, O., *et al.* (2006), Validity limits for the van Genuchten-Mualem model and implications for parameter estimation and numerical simulation, *Advances in Water Resources*, *29*, 1780-1789.

Lewis, R. W., and B. A. Schrefler (1998), *The Finite Element Method in the Static and Dynamic Deformation and Consolidation of Porous Media*, 2 ed., 492 pp., John Wiley & Sons, Chichester, England.

Martin, C.D., Lanyon, G.W. (2003). Measurement of in-situ stress in weak rocks at Mont Terri Rock Laboratory, Switzerland, International Journal of Rock Mechanics & Mining Science 40: 1077–1088

Millard, A., Bond A.E., Nakama S., Zhang C., Barnichon J-D., and B., Garitte. (2012). Accounting for anisotropic effects in the prediction of the hydro-mechanical response of a ventilated tunnel in an argillaceous rock. International Journal of Rock Mechanics and Geotechnical Engineering. *In preparation.*

Muñoz, JJ, Lloret A and E Alonso. (2003). C.I.M.N.E., UPC. "VE" Experiment, Laboratory Report: Characterization of hydraulic properties under saturated and non saturated conditions. Project Deliverable 4. EC contract FIKW-CT2001-00126.

Nagra (2002a), (Nationale Genossenschaft für die Lagerung radioaktiver Abfälle (National Coorperative for the Disposal of Radioactive Waste) Project Opalinus Clay. Demonstration of disposal feasibility for spent fuel, vitrified high-level waste and long-lived intermediate-level waste (Entsorgungsnachweis). Technical Report 02-05, 472 pp.

Nagra (2002b), (Nationale Genossenschaft für die Lagerung radioaktiver Abfälle (National Coorperative for the Disposal of Radioactive Waste) Synthese der geowissenschaftlichen Untersuchungsergebnisse

NDA (2010). Geological Disposal: An overview of the generic Disposal System Safety Case. NDA Report no. NDA/RWMD/010

Pearson, F.J. (1998). Geochemical and other porosity types in clay-rich rocks. Water-Rock interaction, Arehart and Hulston (eds.), pp. 259-262. Balkema. Rotterdam.

Quintessa (2010). QPAC: Quintessa's General Purpose Modelling Code (General Overview). QRS-QPAC-11.

Rutqvist J, Noorishad J and Tsang C-F (1999). Coupled Thermohydromechanical Analysis of a Heater Test in Unsaturated Clay and Fractured Rock at Kamaishi Mine. SKI Report 99:50.

Sanavia, L., *et al.* (2006), Finite element analysis of non-isothermal multiphase geomaterials with application to strain localization simulation, *Computational Mechanics*, *37*, 331-348.

Savage D, Benbow S, Watson C, Takase H, Ono K , Oda C and Honda A (2010). "*Natural systems evidence for the alteration of clay under alkaline conditions: An example from Searles Lake, California*", Applied Clay Science 47, 72-81.

Traber. (2003). Geochemical characterisation of samples from drill core BVE82. Project Deliverable D5b EC contract FIKW-CT2001-00126.

Villar, MV., Martin, PL. and JM. Barcala. 2005. Infiltration tests at isothermal conditionsand under thermal gradient. Technical report CIEMAT/DMA/M2140/1/05.

Williamson, M.A. and Rimstidt, J.D. (1994). "*The kinetics and electrochemical rate-determining step of aqueous pyrite oxidation*" Geochimica et Cosmochimica Acta, 58.

Zienkiewicz, O.C.; Taylor, R.L. (2005). Finite Element Method for Solid and Structural Mechanics (6th Edition). Elsevier.

Zhang, C. L., and T. Rothfuchs (2005), Report on instrument layout and pre-testing of large lab VE-tests. Deliverable 4.3.11.

Zhang *et al.* [authors to be confirmed] (2012) A THM formulation for modeling water transport around a ventilation tunnel in an argillaceous rock. In preparation. International Journal of Rock Mechanics and Geotechnical Engineering. In preparation.

Zhu, C and Anderson, G (2002). "*Environmental Applications of Geochemical Modelling*" Cambridge University Press.

10 Acknowledgements

The authors would like to acknowledge the interaction and support with all the other Task A team members, however particular thanks are reserved for Benoit Garitte of UPC and Alain Millard of CEA.

Appendix A: Laboratory Drying Test

The Step 0 experimental data is described in detail by Floria *et al.* (2002), the information provided here is purely for reference.

The experiment consisted of three nearly identical samples of Opalinus Clay, each at near-full water saturation. The three samples were placed in a drying chamber (Figure A 1 and Figure C 2)

Figure A 1. Sample inside a drying chamber (left) and the drying chamber itself (right)

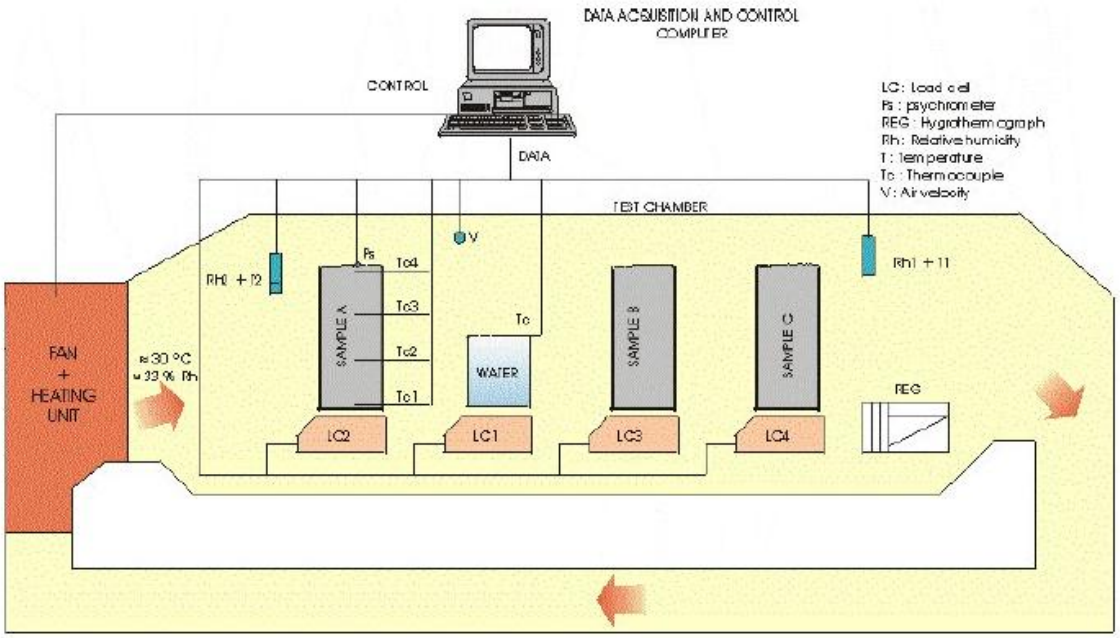

Figure A 2. Schematic layout of the drying chamber

The three samples together with a container of water were monitored throughout the experiment, which ran for approximately 142 days. During this time the following measurements were made:

- ▲ relative humidity in the drying chamber at two locations;
- ▲ temperature in the drying chamber at two locations;
- ▲ airflow through the chamber;
- ▲ temperature at different elevations in Sample A;
- ▲ weight of each sample with time during the experiment, and hence directly inferred water loss with time; and
- ▲ water content (by mass) for samples at different elevations when the samples were removed from the drying chamber. Sample A was removed at 142 days, Sample C at 99 days and Sample C at 21 days.

The various measurements are shown in the following figures (from Floria *et al.*, 2002).

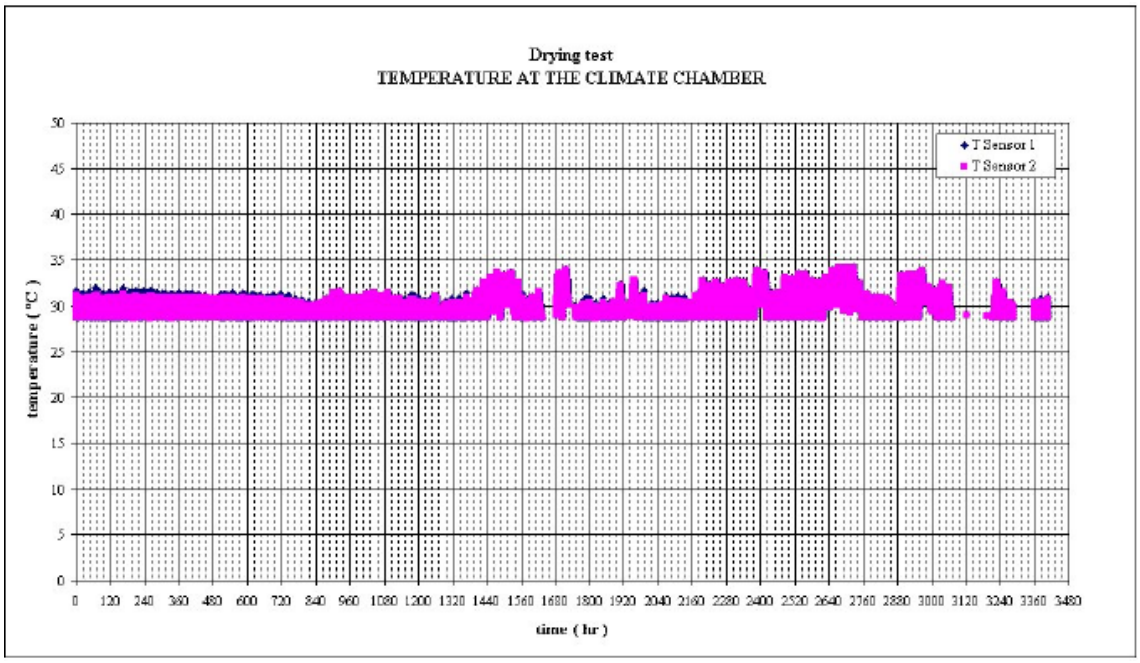

Figure A 3. Temperature measured from the two probes in the drying chamber.

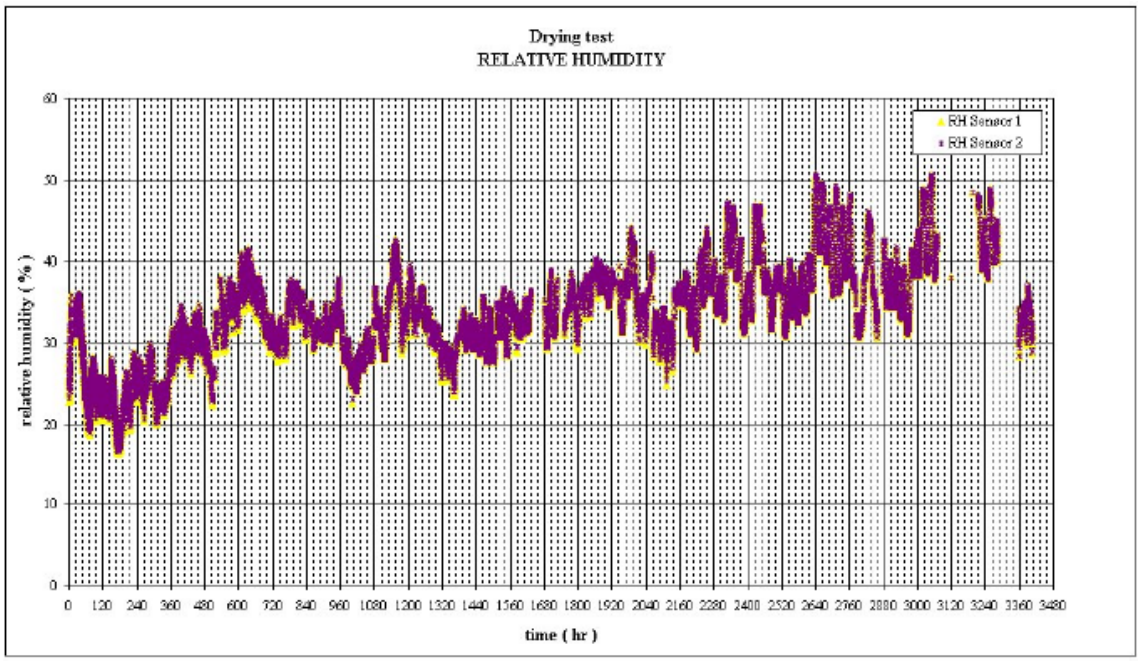

Figure A 4. Relative humidity measured from the two probes in the drying chamber.

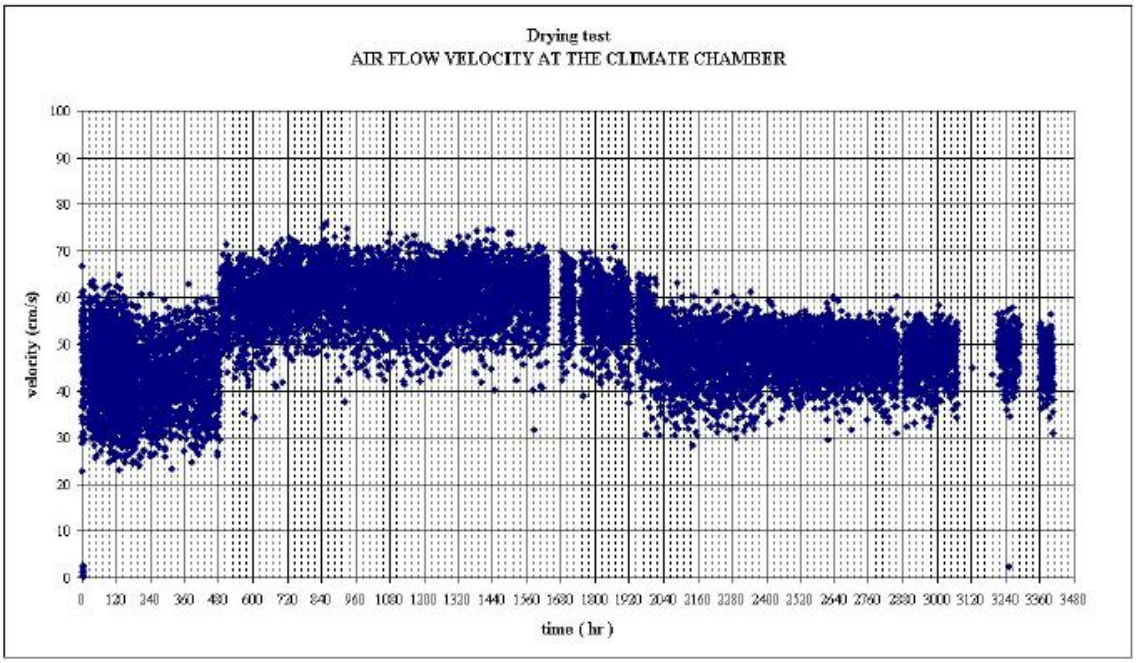

Figure A 5. Airflow through the drying chamber.

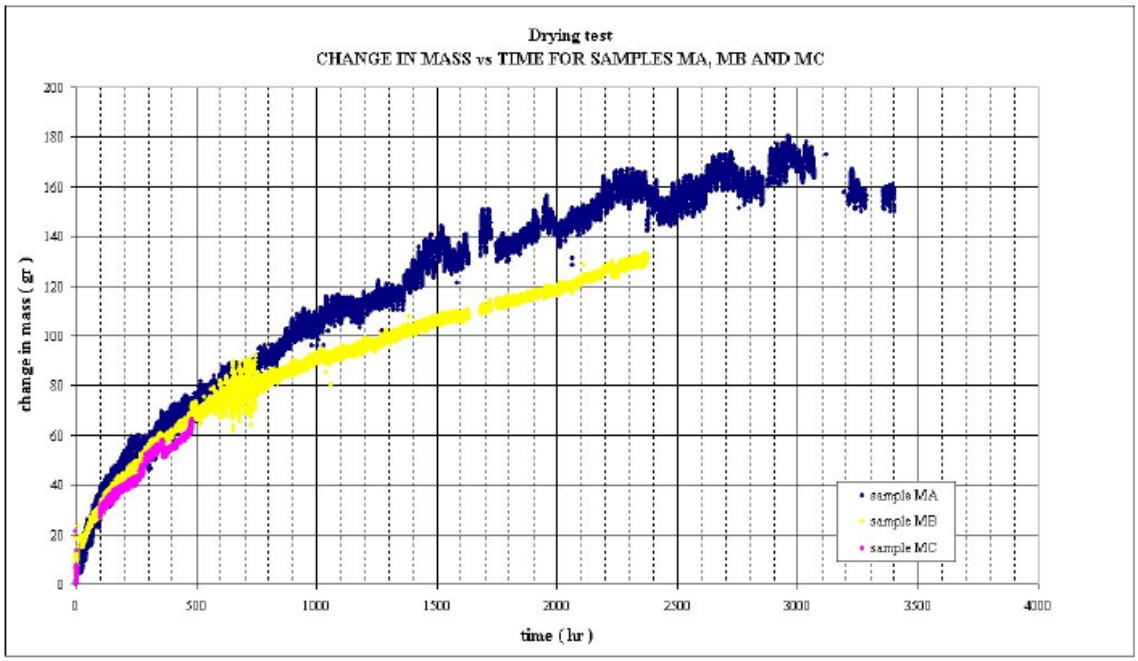

Figure A 6. Inferred water loss from the three samples.

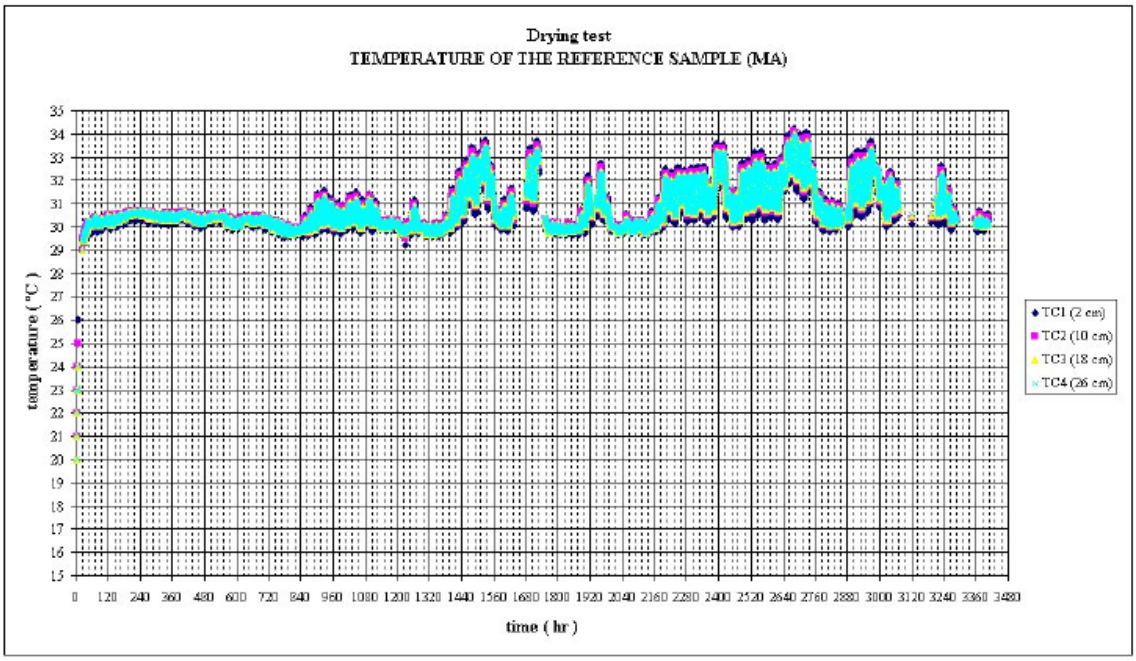

Figure A 7. Temperature in Sample A at the four measurement locations (note thermal equilibrium in the sample).

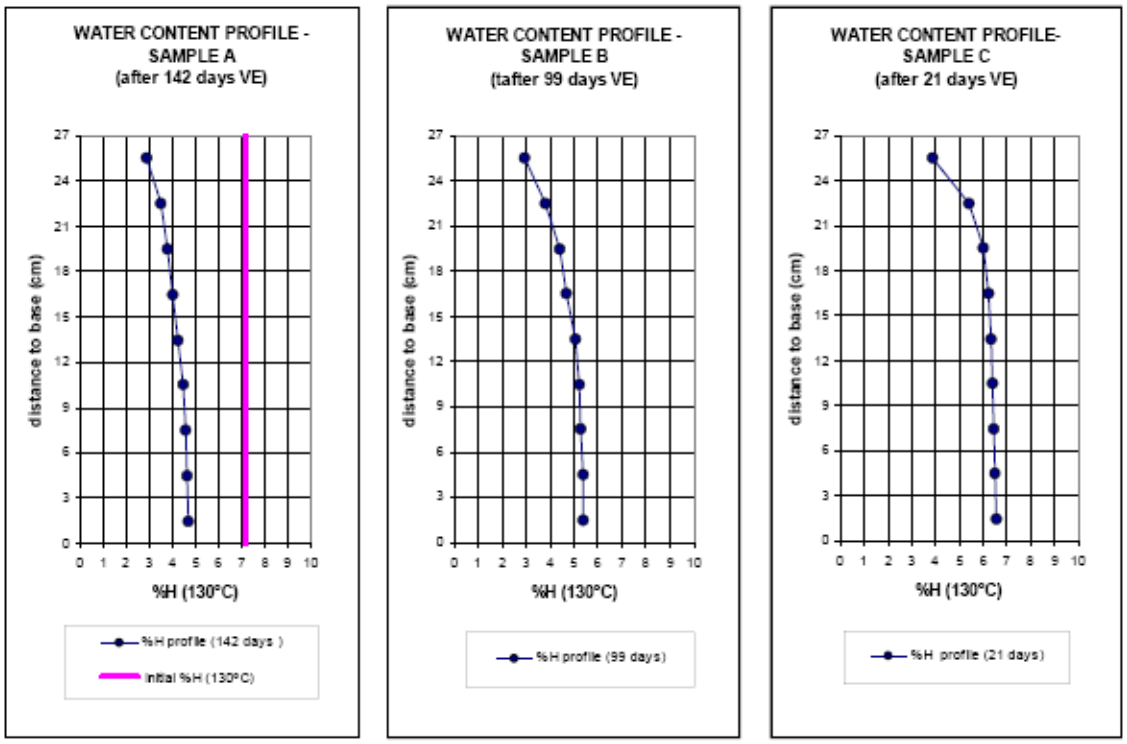

Figure A 8. Measured water contents at elevations from the base, for the three samples.

Appendix B: Ventilation Experiment Data

The following text and figures have been adapted from Garitte and Gens (2008).

B.1 Objectives and significance

The main objective of Task A is to examine the hydromechanical and chemical changes that may occur in argillaceous host rocks, especially in relation to the ventilation of drifts.

The significance of the study lies in the fact that all drifts and tunnels in the repository will be subjected to ventilation effects to some extent during the operational phase of the facility. It is believed that argillaceous rocks may be especially sensitive to this type of action Specifically the following issues are potentially involved in this task:

1. Desaturation/resaturation of the rock.
1. Air/rock interface
2. Damage/microcracking of the host rock due to hydromechanical and/or chemical effects
3. Evolution of the EDZ

B.2 Definition of the problem and approach

The Task is based on the performance and results of the Ventilation (VE) Test carried out in the Mont Terri underground laboratory involving Opalinus clay. The VE test has been performed in a 10 m long section of the unlined Rock Bored (RB) microtunnel (MT - diameter = 1.3 m), excavated in 1999 in the shaly facies section. In the summer of the year 2002, the test section was sealed off by means of two double doors and monitored. Figure B 1 shows the location of the tunnel in the Mont Terri URL and Figure B 1 shows a schematic layout of the experiment.

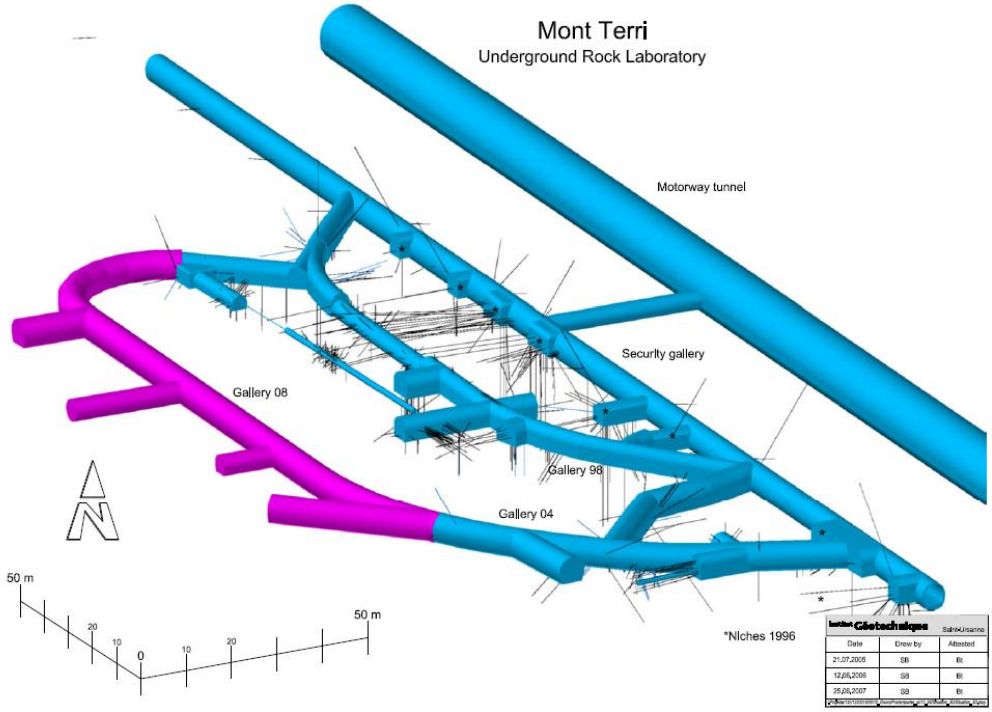

Figure B 1: Location of the VE microtunnel (MT) at the Mont Terri URL

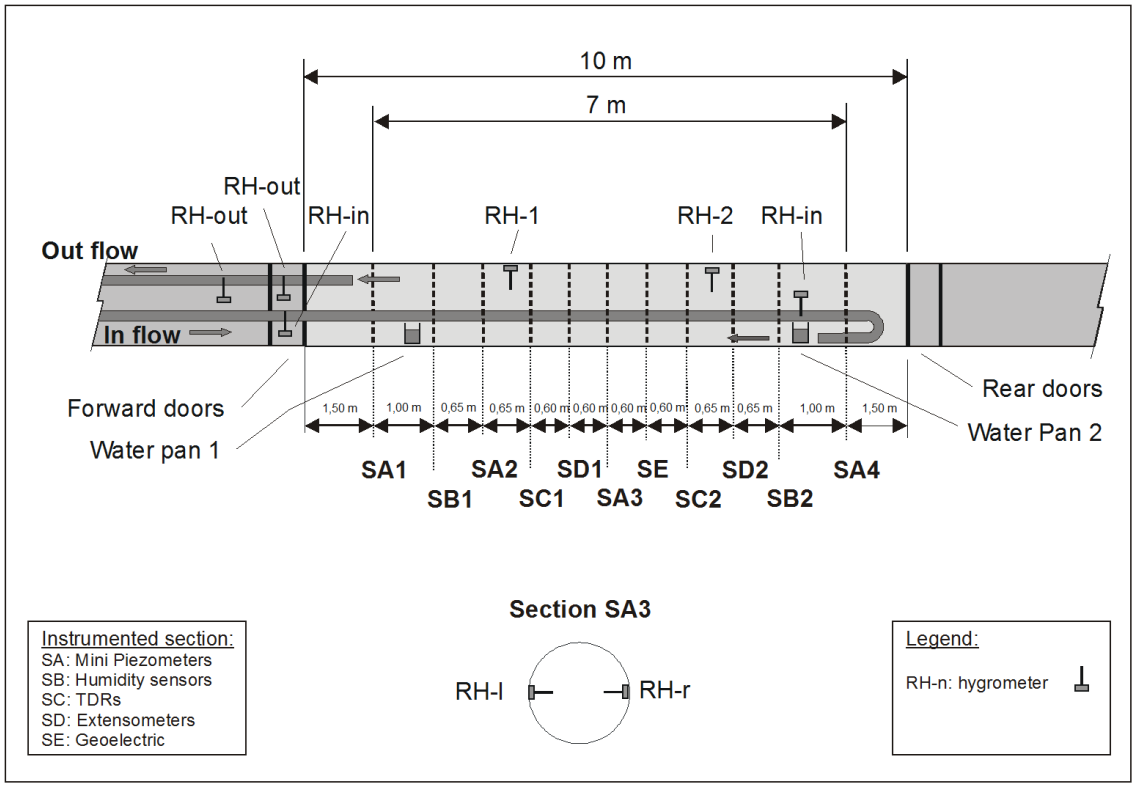

Figure B 2: Schematic layout of the VE experiment

Subsequently the test section was subjected to a number of desaturation-resaturation episodes by means of forced ventilation injecting air with controlled values of relative humidities. The relative humidity was measured in the incoming air and also on the tunnel wall (Figure B 2). Monitoring the relative humidity of the outgoing air allowed the determination of the water mass balance in the test section of the tunnel.

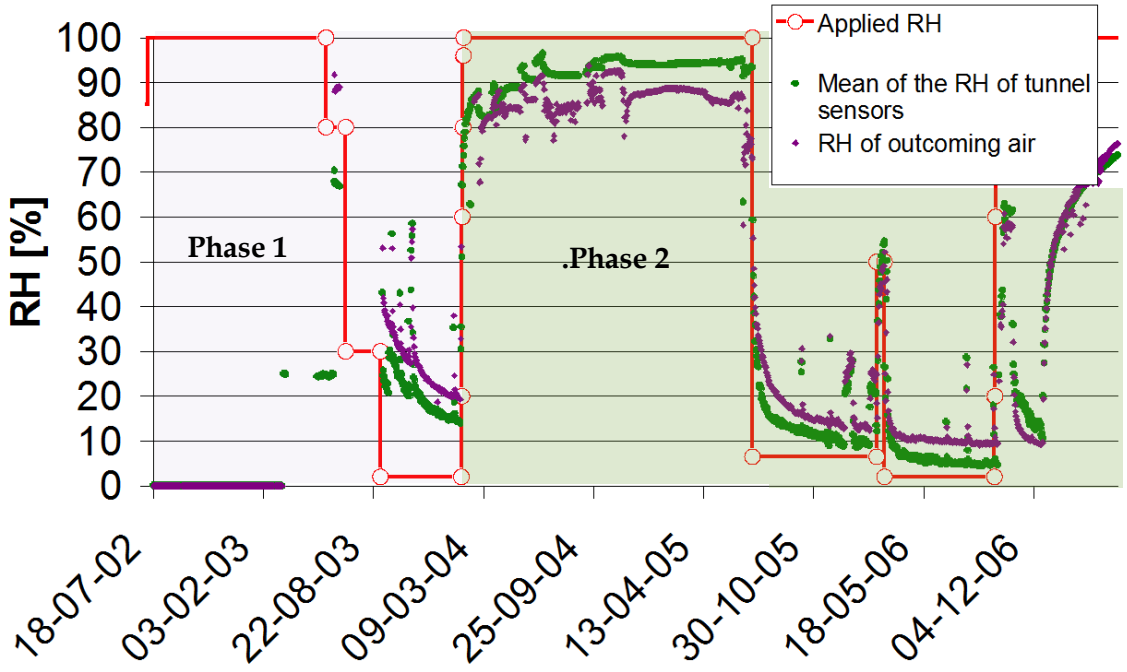

Figure B 3: Measured relative humidity in the incoming air, at tunnel wall and in the outpipe.

Several different phases of the test can be usefully distinguished:

- Phase 0 in which the VE tunnel was excavated and left open without controlled ventilation conditions (from February 1999 to July 2002).
- Phase 1 in which the VE tunnel was subjected to controlled ventilation conditions resulting in rock resaturation (from July 8th 2002 to May 28th 2003) and subsequent desaturation (from May 28th 2003 to January 29th 2004).
- Phase 2 in which an additional episode of controlled resaturation (from January 29th 2004 to July 11th 2005) and desaturation (from July 11th 2005 to September 24th 2006) was performed. Finally, a last resaturation stage was applied.

The approach will be based on the performance of hydromechanical and geochemical modelling of the test and comparison with experimental observations. This will allow checking the capabilities of the various modelling tools and to advance in the understanding of ventilation effects on argillaceous host rock.

B.3 Step 1 Data

The input data (Table B 1) outlined below has been specified to be used by the teams to create the boundary condition at microtunnel wall, while the output data (Table B 1) is that to which model results are to be compared with. Due to the complexity of the task, no blind prediction was expected from this step and all the available data has been provided to the teams.

Initial Conditions

The initial water pressure (before the excavation of the microtunnel) is about 1.85 MPa. According to Martin and Lanyon (2003), the determination of the stress state in the Opalinus Clay in Mont Terri is not straightforward. The most consistent data are those from hydraulic fracturing that indicates a stress of 4MPa normal to the bedding plane (at the VE test site, the trace of the bedding is perpendicular to the axis of the microtunnel and the bedding planes plunge with a small angle of 25^{o} towards the South-East). The minor stress is not well determined and was attributed a low value of 2 MPa or less. Its orientation is approximately perpendicular to the vertical plane containing the microtunnel axis. The major stress has a value of 6-7MPa.

Table B 1: Input and output data for step 1.

Input data	Output data
Figure B 4	Figure B 7: RH measurements in the rock mass
Figure B 5	Figure B 8: water balance
Figure B 6	Figure B 9: water content profiles
	Figure B 10: water pressure evolution
	Figure B 11: water pressure profile
	Figure A 12 relative displacements

Input Data

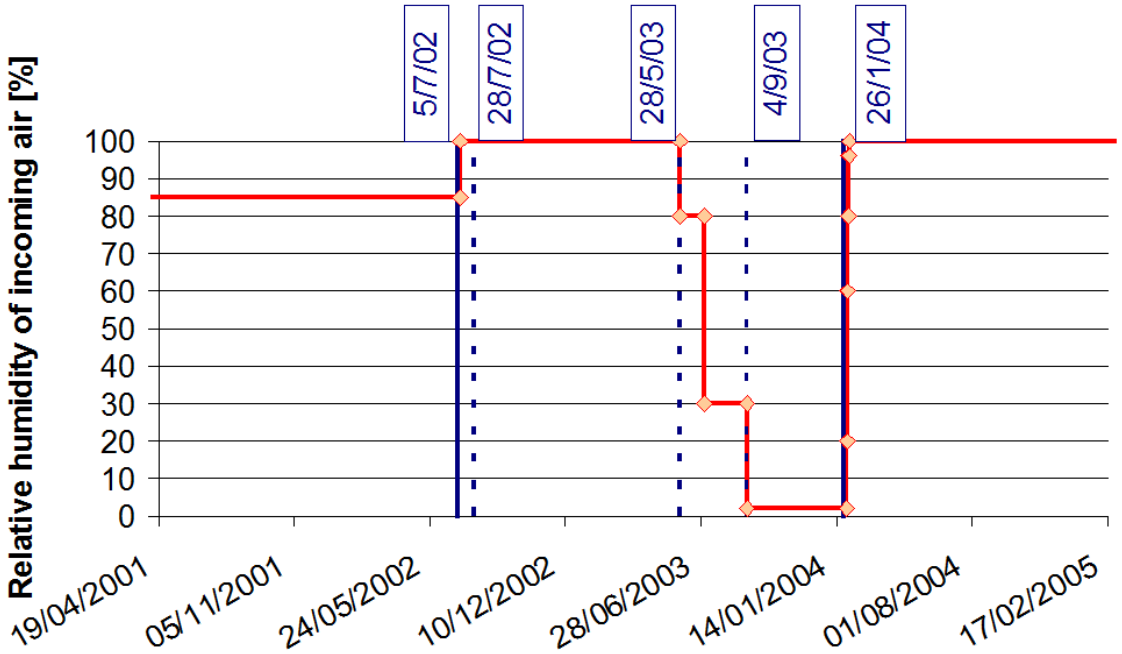

Figure B 4: RH of the incoming air and some important dates. The RH value of 85% before 08/07/02 is purely indicative.

Figure B 4 summarizes the main events of phase 0 and 1 of the VE, the modelling of which is the aim of step 1 of task A. The history of the microtunnel between its excavation and the isolation of the ventilated section is unknown. The value of the microtunnel RH during this period should be estimated from the data collected at the start of the controlled ventilation period (e.g. water pressure profile: Figure B 11, water content profile in BVE-82: Traber, 2003). The value appearing in Figure B 4, before July 7th 2002, is purely indicative.

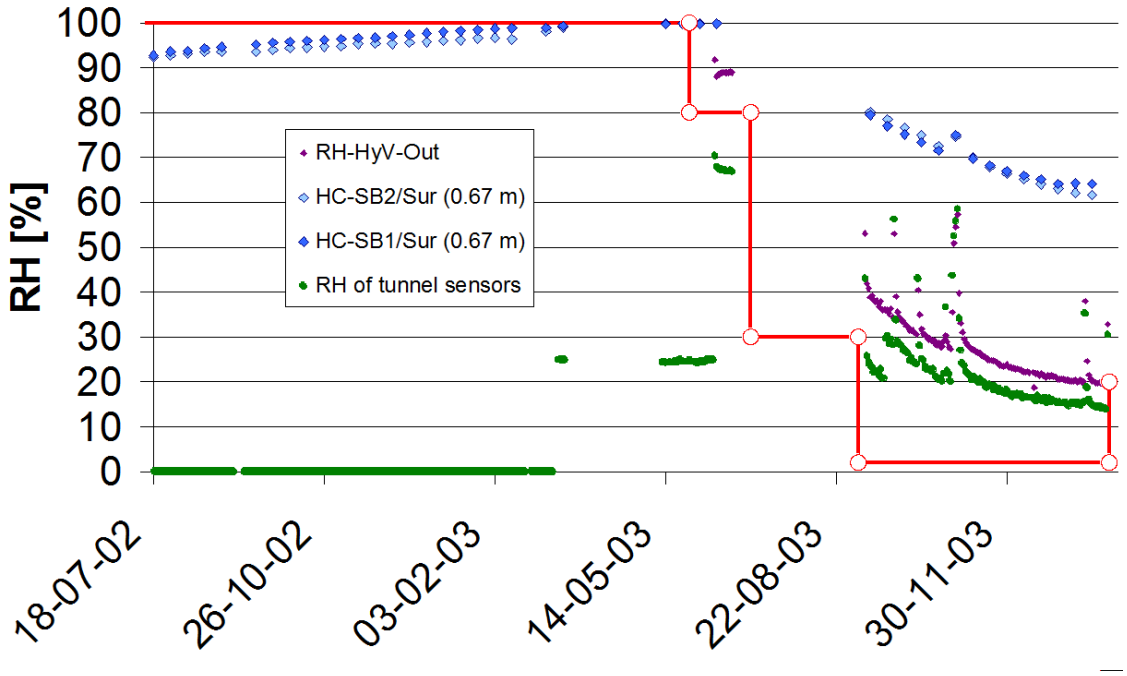

Figure B 5: Evolution of the RH in the microtunnel and in the skin layer (2 cm from the wall and separation from the microtunnel by a thin concrete layer.

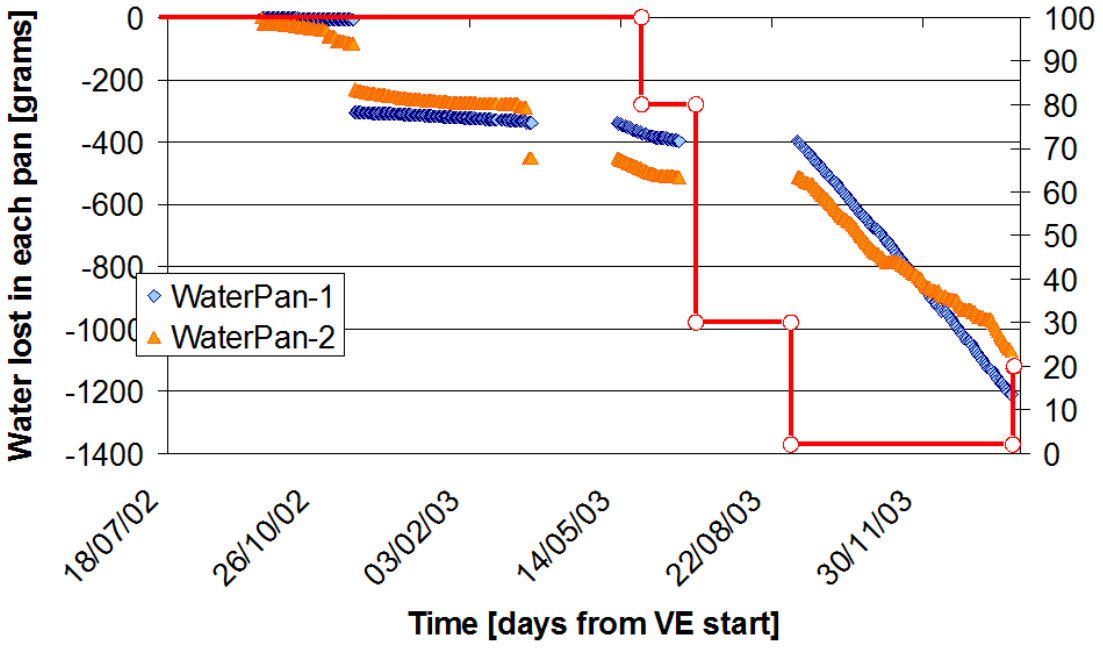

Figure B 6: Loss of water in the water pans (diameter of 10cm).

Output Data

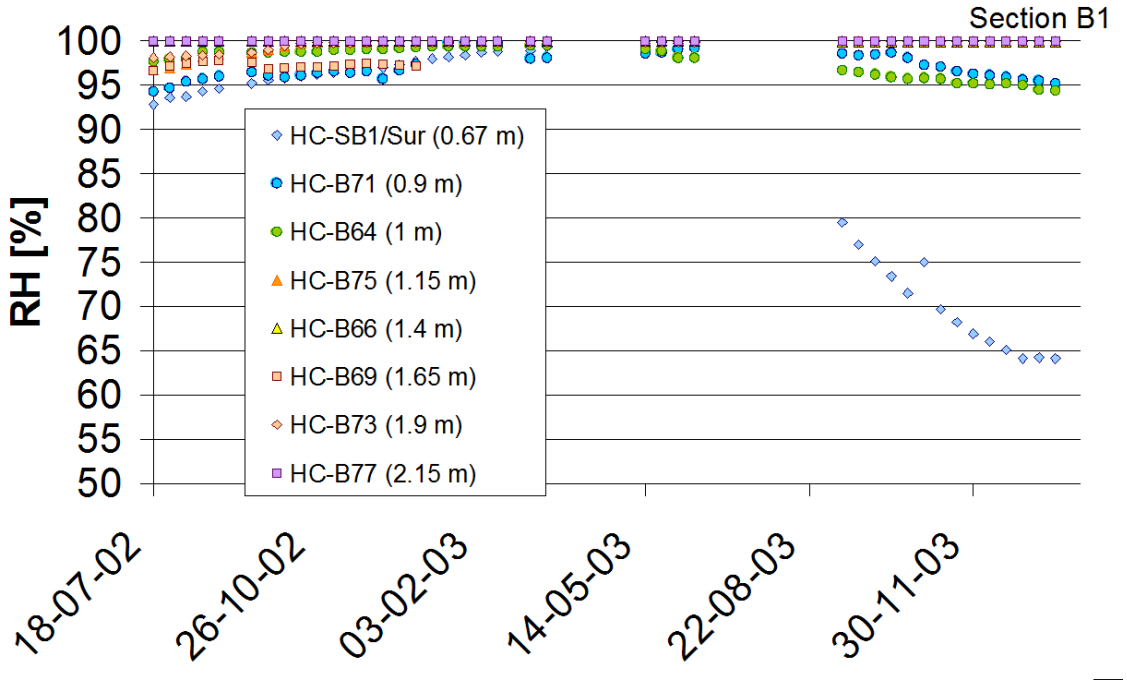

Figure B 7: Measurements of RH in the rock mass and in the skin layer (Distances from the microtunnel centre).

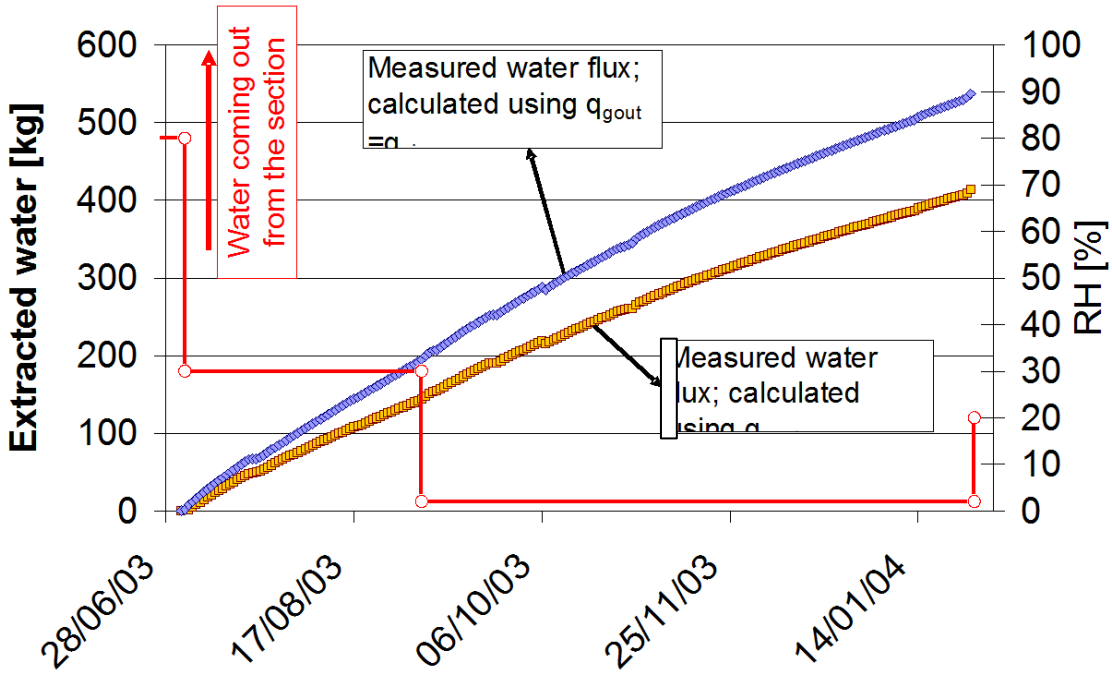

Figure B 8: Accumulated extracted water calculated from the RH of incoming and outgoing air and the air flow (adpated from Garitte and Gens 2008).

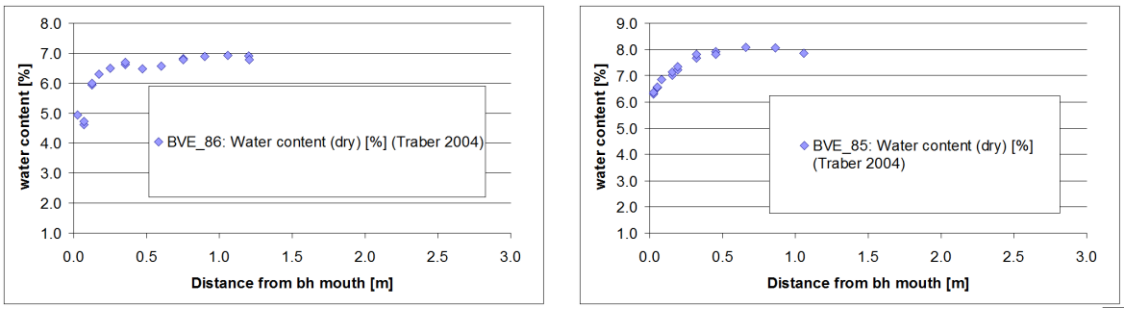

(a) (b)

Figure B 9: Water content profiles in a horizontal (a) and a vertical (b) borehole after the desaturation of phase 1.

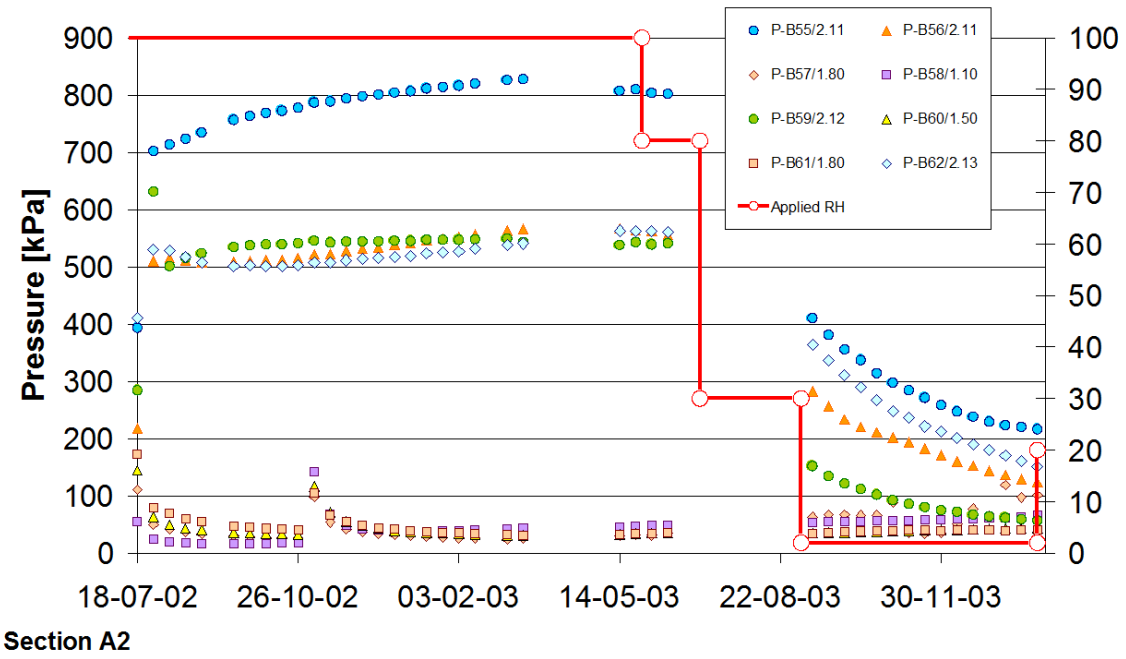

Figure B 10: Water pressure evolution. Values lower than 100 kPa indicate a suction state (adapted from Garitte and Gens 2008).

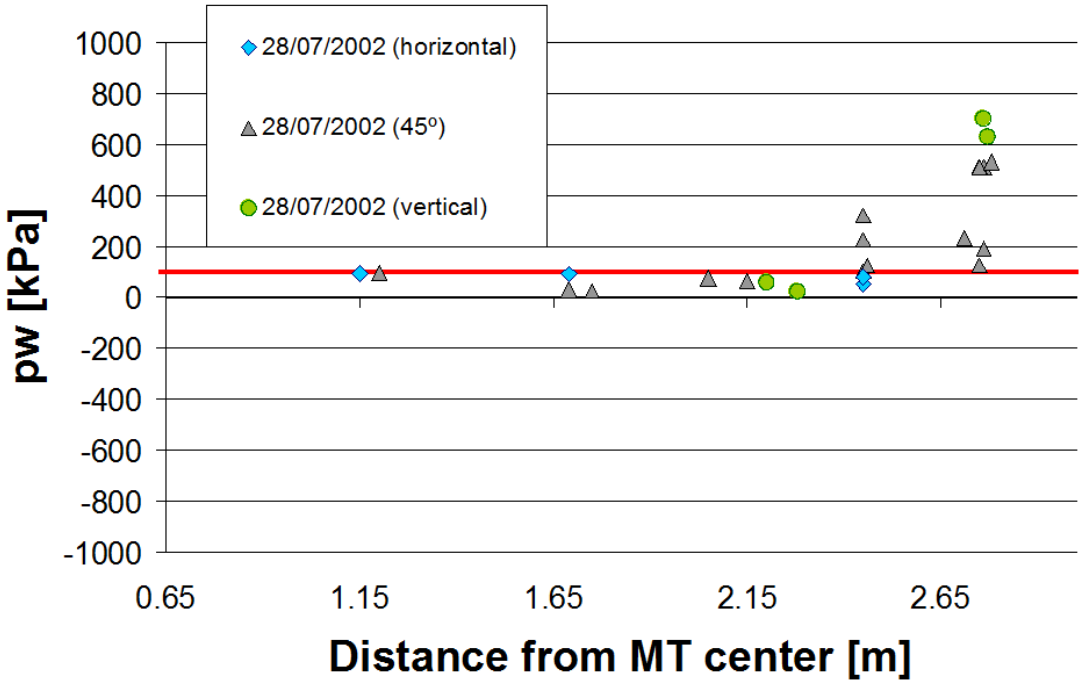

Figure B 11: Water pressure profile at the start of the controlled period.

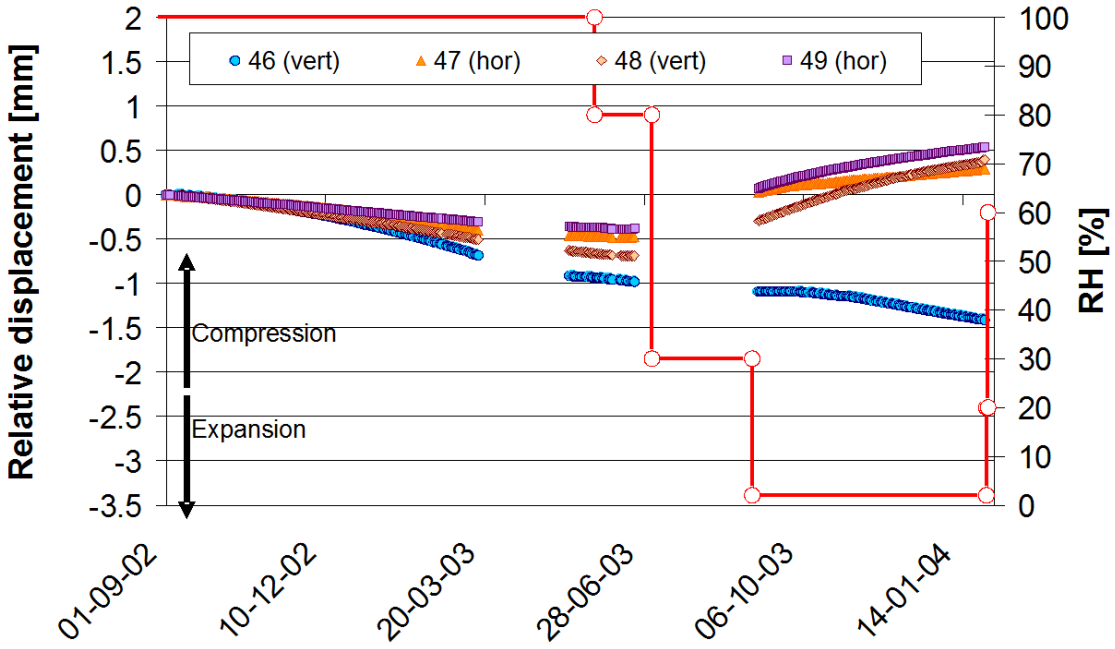

Figure B 12: Relative radial displacement between wall points and points 2 m inside the rock mass.

B.4 Step 2 Data

The only additional data given for Phase 2 was the applied and observed relative humidities in the VE tunnel and the airflow through the tunnel. The data could be used to derive a further mass balance depending on the assumptions made on how much of the 'lost' air interacted with the tunnel. It was expected that the true mass balance would like between the blue and green lines on the figure below. The orange line is an interpretation that was presented by the Task A organisers, but because it does not account for air loss explicitly, it is felt to be unreliable, especially during the resaturation phases.

B.5 Step 3 Data

The two reports by Fernandez *et al.* (2007a,b) discuss the sampling, measurement and interpretation of core data from the VE before during Phase 1 and Phase 2, with particular reference to the inferred pore water geochemistry. One of the key outputs of the interpretation is the construction of a series of chloride profiles away from the VE tunnel. These results are significant because chloride should act as a conservative tracer, hence if the chloride profiles can be reproduced through physical modelling, it

will considerably add to the confidence in the underpinning hydro-mechanical models and the conceptualisation of tracer transport in the pore water.

The available profiles consist of four time periods of data (4.24, 5.8, 7.06 and 8.5 years since VE Tunnel construction) each with 1, 2 3 and 5 borehole cores respectively. The measured data were mg/kg rock, reflecting the analysis approach chosen. From this analysis and other measurements of rock properties inferred molar concentrations per unit volume of pore water can be derived. This latter conversion is somewhat problematic, requiring assumptions to be made about the porosity and inferred saturation state of each of the samples. Therefore it is proposed that the data for cross-comparison be the basic measured data of mg/kg rock. This prevents further uncertainty being included in the cross-comparison.

A summary plot of the available data is shown in Figure B 14. The plot also shows two 'type' profiles at different times, indicating the general form of the chloride profiles with time. It is clear that the profiles overlap considerably but there is a tendency to create local peaks away from the tunnel boundary at 5.8y and 8.5y

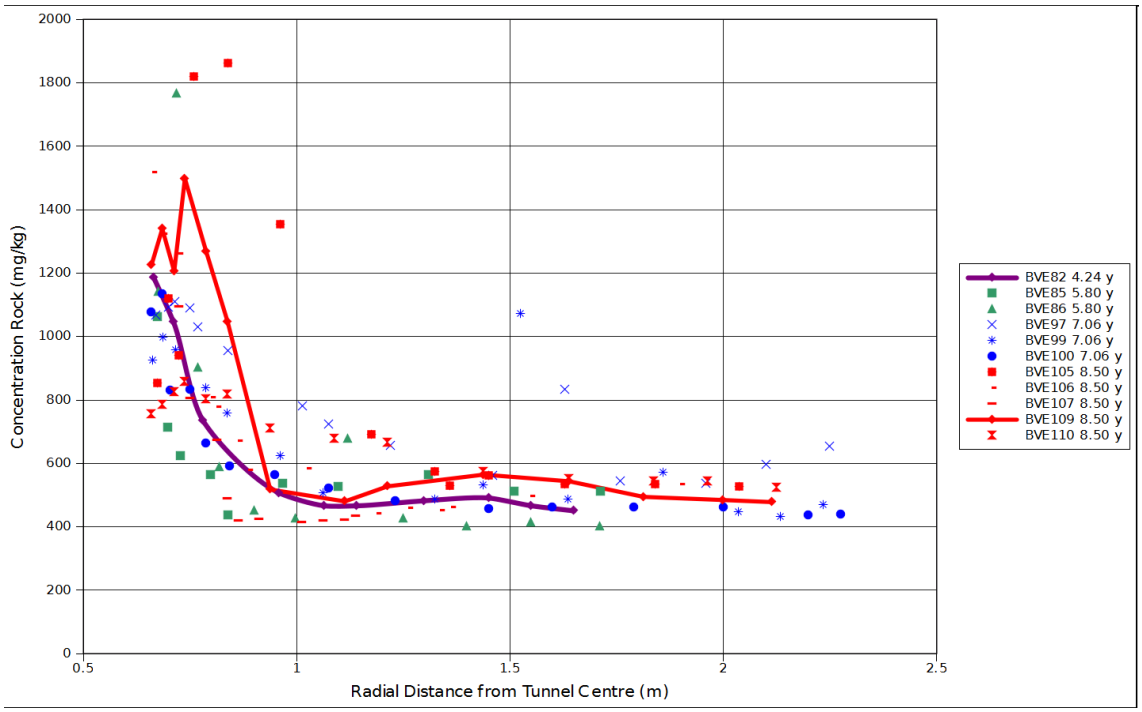

Figure B 14: Summary plot of chloride data taken from Fernandez *et al.* (2007a,b)

B.6 Step 4 Data

Fernández and Melón (2007) report sulphate concentrations measured after the second ventilation test (Figure B 15). As described by Fernández and Melón (2007), the 'background' concentrations of solid sulphate in the Opalinus clay are ~400-500 mg/kg, which are lower than those observed after the ventilation experiments, thereby suggesting that significant pyrite oxidation occurred (although it is not clear exactly when). Sulphate contents from different boreholes show some variation. However, sulphate concentrations similar to 'background' levels were generally measured in samples collected from boreholes at a depth of 0.4m from the gallery. The degree of oxidation in the samples taken closer to the gallery (up to a depth of 0.17 m) is similar, or slightly higher than that associated with samples taken prior to the second evaporation test (Fernández and Melón, 2007). The maximum sulphate concentrations are associated with samples taken at a distance of 0.05 to 0.1 m from the gallery surface.

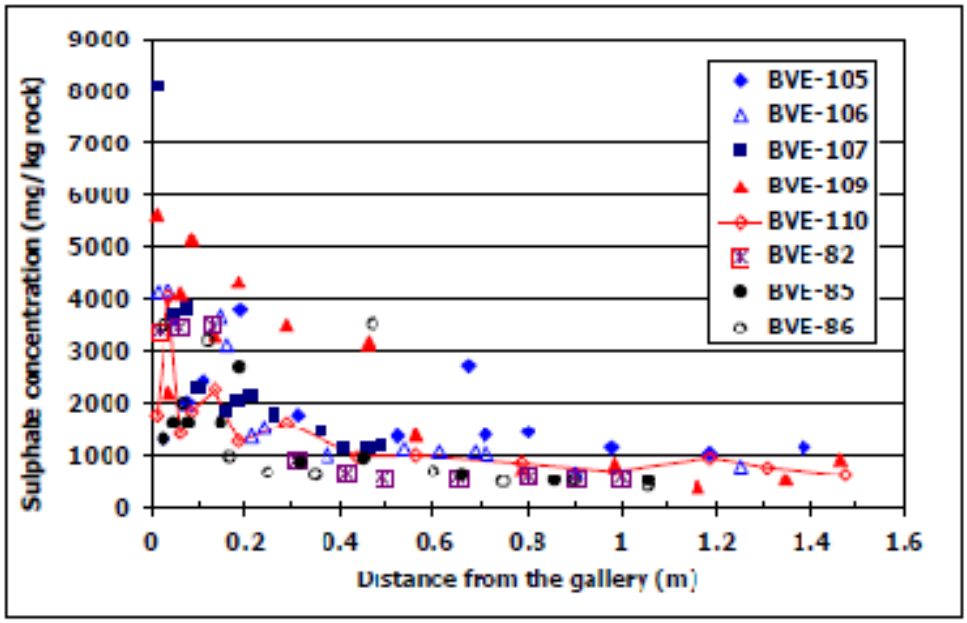

Figure B 15: sulphate concentrations (mg / kg of rock) in borehole samples taken after the second ventilation test (reproduced from Figure 78 of Fernández and Melón, 2007). The plot includes data for BVE-82 (pre-ventilation) and after the first VE tests (BVE-85, BVE-86).

Appendix C: Relevant Details of the OpenGeoSys Processes and Numerical Approach

C1 Calculation of isothermal flow in porous media

Definition of symbols

C_p	Effective specific heat of porous medium $\left(Jkg^{-1}K^{-1}\right)$
C_p^g	Specific heat of gas mixture $\left(Jkg^{-1}K^{-1}\right)$
C_p^w	Specific heat of liquid pahse $\left(Jkg^{-1}K^{-1}\right)$
$\mathbf{D}_g^{gw}$	Effective diffusivity tensor of water vapour in dry air $\left(m^2s^{-1}\right)$
$\mathbf{D}_g^{ga}$	Effective diffusivity tensor of dry air in water vapour $\left(m^2s^{-1}\right)$
g	Accelertion due to gravity $\left(ms^{-2}\right)$
$\mathbf{k}$	intrinsic permeability tensor $\left(m^2\right)$
k_{rel}	relative permeability of phase
M_a	molar mass of dry air $\left(gmol^{-1}\right)$
M_w	molar mass of water $\left(gmol^{-1}\right)$
M_g	molar mass of gas phase $\left(gmol^{-1}\right)$
n	porosity
p^c	capillary pressure $\left(Pa\right)$
p^g	gas pressure $\left(Pa\right)$
p^w	liquid water pressure $\left(Pa\right)$
p^{ga}	dry air partial pressure $\left(Pa\right)$
p^{gw}	water vapour partial pressure $\left(Pa\right)$
p^{gws}	saturated water vapour pressure $\left(Pa\right)$
R	gas constant $\left(8314.41\ Jkmol^{-1}K^{-1}\right)$
RH	Relative Humidity
S_w	liquid phase volumetric saturation
S_g	gas phase volumetric saturation
T	absolute temperature
v_g^{gw}	diffusion velocity of water vapour in dry air $\left(ms^{-1}\right)$
v_g^{ga}	diffusion velocity of dry air in water vapour $\left(ms^{-1}\right)$
t	time $\left(s\right)$
b_s	cubic thermal expansion coefficienct of solid $\left(K^{-1}\right)$
l_{eff}	effectuve thermal conductivity of the porous medium
m	dynamic viscosity $\left(Pas\right)$
r^g	density of gas phase $\left(kg/m^3\right)$
r^w	density of liquid phase $\left(kg/m^3\right)$

Following Sanavia, *et al.*, (2006), the macroscopic balance equations for water and vapour in a solid non deforming skeleton can be expressed as

$$n\left[\rho^{w}-\rho^{gw}\right]\left[\frac{\partial S_{w}}{\partial T}\frac{\partial T}{\partial t}+\frac{\partial S_{w}}{\partial p^{c}}\frac{\partial p^{c}}{\partial t}\right]+\left[1-S_{w}\right]n\left[\frac{\partial \rho^{gw}}{\partial T}\frac{\partial T}{\partial t}+\frac{\partial \rho^{gw}}{\partial p^{c}}\frac{\partial p^{c}}{\partial t}\right]$$
$$-div\left(\rho^{g}\frac{M_{a}M_{g}}{M_{g}^{2}}D_{g}^{gw}grad\left(\frac{\partial \rho^{gw}}{\partial p^{c}}\right)\right)+div\left(\rho^{w}\frac{\mathbf{k}k_{rel}^{rw}}{\mu^{w}}\left[-grad\left(p^{g}\right)+grad\left(p^{c}\right)+\rho^{w}\mathbf{g}\right]\right) \quad \text{C.1}$$
$$+div\left(\rho^{w}\frac{\mathbf{k}k_{rel}^{rg}}{\mu^{w}}\left[-grad\left(p^{g}\right)+\rho^{g}\mathbf{g}\right]\right)-\beta\frac{\partial T}{\partial t}=0$$

The relationship between the gas pressure, the capillary pressure and the water pressure is given by

$$p^{c}=p^{g}-p^{w} \quad \text{C2}$$

The mass balance equations for the dry air in the same skeleton is expressed as

$$n\rho^{ga}\left[\frac{\partial S_{w}}{\partial T}\frac{\partial T}{\partial t}+\frac{\partial S_{w}}{\partial p^{c}}\frac{\partial p^{c}}{\partial t}\right]+\left[1-S_{w}\right]n\left[\frac{\partial \rho^{ga}}{\partial T}\frac{\partial T}{\partial t}+\frac{\partial \rho^{ga}}{\partial p^{c}}\frac{\partial p^{c}}{\partial t}+\frac{\partial \rho^{ga}}{\partial p^{g}}\frac{\partial p^{g}}{\partial t}\right]$$
$$-div\left(\rho^{g}\frac{M_{a}M_{g}}{M_{g}^{2}}D_{g}^{ga}grad\left(\frac{p^{ga}}{p^{g}}\right)\right)+div\left(\rho^{ga}\frac{\mathbf{k}k_{rel}^{rg}}{\mu^{g}}\left[-grad\left(p^{g}\right)+\rho^{g}\mathbf{g}\right]\right) \quad \text{C.3}$$
$$-\beta_{s}\rho^{ga}\left[1-n\right]\left[1-S_{w}\right]\frac{\partial T}{\partial t}=0$$

The energy balance equation can be expressed as

$$\left(\rho C_{p}\right)_{eff}\frac{\partial T}{\partial t}+\rho^{w}C_{p}^{w}\left[\frac{\mathbf{k}k_{rel}^{rw}}{\mu^{w}}\left[-grad\left(p^{g}\right)+grad\left(p^{c}\right)+\rho^{w}\mathbf{g}\right]\right]grad\left(T\right)$$
$$+\rho^{g}C_{p}^{g}\left[\frac{\mathbf{k}k_{rel}^{rg}}{\mu^{g}}\left[-grad\left(p^{g}\right)+\rho^{g}\mathbf{g}\right]\right]grad\left(T\right)-div\left(\lambda_{eff}grad\left(T\right)\right)=-\dot{m}_{vap}\Delta H_{vap} \quad \text{C.4}$$

C2 Constitutive equations

Using the ideal gas law for the mixture of water vapour and dry air, and applying the equation of state of a perfect gas (the Clapeyron equation) and Dalton's law applied to dry air (ga), water vapour (gw) and moist air (g) allows the following expressions to be derived.

$$p^{ga} = \rho^{ga} \frac{RT}{M_a} \quad \text{C.5}$$

$$p^{gw} = \rho^{gw} \frac{RT}{M_w} \quad \text{C.6}$$

$$p^{g} = p^{ga} + p^{gw} \quad \text{C.7}$$

$$\rho^{g} = \rho^{ga} + \rho^{gw} \quad \text{C.8}$$

In partially saturated zones the equilibrium water vapour pressure is established from the Kelvin-Laplace equation

$$p^{gw} = p^{gws}(T)\, e^{\left(-\frac{p^c M_w}{\rho_w RT}\right)} \quad \text{C.9}$$

Where p^{gws} is the water vapour saturation pressure depending only on temperature. The term required for the solution of C1 is then given by differentiation of C.9 as

$$\frac{\partial p^{gw}}{\partial p^{c}} = -\frac{M_w}{\rho_w RT} p^{gws}(T)\, e^{\left(-\frac{p^c M_w}{\rho_w RT}\right)} \quad \text{C.10}$$

The saturated water vapour density is given by

$$\rho^{gw} = 10^{-3} e^{\left(19.891 - \frac{4975}{T_{abs}}\right)} \quad \text{C.11}$$

The relative permeability and capillary pressure correlation with saturation may either be provided by experimental data or by an empirical formula based on experimental results. In this case we use the experimental results best fitted by an empirical function to provide the capillary pressure formulation, and several approaches were taken to derive the best fitting permeability function. This is discussed later.

For the binary mixture of the dry air and water vapour, Fick's law gives the following relative velocities of the diffusing species

$$v_g^{ga} = -\frac{M_a M_w}{M_g^2} D_g^{ga} grad\left(\frac{p^{ga}}{p^g}\right) = \frac{M_a M_w}{M_g^2} D_g^{ga} grad\left(\frac{p^{gw}}{p^g}\right) = -v_g^{gw} \quad \text{C.12}$$

The molar mass of the gas mixture, M_g is given by

$$\frac{1}{M_g} = \frac{\rho^{gw}}{\rho^g}\frac{1}{M_w} + \frac{\rho^{ga}}{\rho^g}\frac{1}{M_a} \quad \text{C.13}$$

The effective diffusivity coefficient of water vapour in air is

$$D_g^{ga} = \tau\left(1 - S_w\right) 2.16 \times 10^{-5}\left(\frac{T_{abs}}{273}\right)^{1.8} \quad \text{C.14}$$

C3 Finite element formulation

The finite element formulation is derived by applying the Galerkin procedure for the spatial integration and the finite difference approach for the time integration of the integral form of the balance equations Lewis and Schrefler (1998); Zienkiewicz and Taylor (2005). After spatial discretisation within the isoparametric formulation, the following non linear and coupled system of equations is obtained.

$$\begin{bmatrix} 0 & \mathbf{C}_{cc} & \mathbf{C}_{ct} \\ \mathbf{C}_{gg} & \mathbf{C}_{gc} & \mathbf{C}_{gt} \\ 0 & \mathbf{C}_{tc} & \mathbf{C}_{tt} \end{bmatrix} \frac{\partial}{\partial t}\begin{bmatrix} \overline{p}^c \\ \overline{p}^g \\ \overline{T} \end{bmatrix} + \begin{bmatrix} \mathbf{K}_{cg} & \mathbf{K}_{cc} & \mathbf{K}_{ct} \\ \mathbf{K}_{gg} & \mathbf{K}_{gc} & \mathbf{K}_{gt} \\ \mathbf{K}_{tg} & \mathbf{K}_{tc} & \mathbf{K}_{tt} \end{bmatrix}\begin{bmatrix} \overline{p}^c \\ \overline{p}^g \\ \overline{T} \end{bmatrix} = \begin{bmatrix} f_c \\ f_g \\ f_t \end{bmatrix} \quad \text{C.15}$$

Referring to Sanavia *et al.*, (2006) a further coupled process of mechanical deformation was also included, and the full formulation of the FE matrices are given in this paper. Although implemented in the code at this stage, calculations for Step 0 of the task A were performed without any mechanical alteration being considered hence the shortened formulation. Additionally although temperature is given as a field variable, the evaluation of the experimental results was carried out assuming a constant temperature.

Once the field variables of capillary pressure and air pressure had been evaluated using the finite element approach, the saturation of the phases was evaluated via the capillary pressure function. The flux throughout the system was then determined as presented in C15.